

**BOILING HEAT TRANSFER FOR  
AN IMPINGING JET ON A HOT PLATE  
AND  
THE DEVELOPMENT OF A NEW CORRELATION**

**BY**

**SHANNON L. SUMMERFIELD**

**A Thesis**

**Submitted to the Faculty of Graduate Studies**

**In Partial Fulfillment of the Requirements**

**For the Degree of**

**MASTER OF SCIENCE**

**Department of Mechanical and Manufacturing Engineering**

**University of Manitoba**

**Winnipeg, Manitoba**

**© Copyright by Shannon Lee Summerfield, August 2004**

**THE UNIVERSITY OF MANITOBA**

**FACULTY OF GRADUATE STUDIES**

**\*\*\*\*\***

**COPYRIGHT PERMISSION**

**BOILING HEAT TRANSFER FOR  
AN IMPINGING JET ON A HOT PLATE  
AND  
THE DEVELOPMENT OF A NEW CORRELATION**

**BY**

**SHANNON L. SUMMERFIELD**

**A Thesis/Practicum submitted to the Faculty of Graduate Studies of The University of**

**Manitoba in partial fulfillment of the requirement of the degree**

**Of**

**MASTER OF SCIENCE**

**Shannon L. Summerfield © 2004**

**Permission has been granted to the Library of the University of Manitoba to lend or sell copies of this thesis/practicum, to the National Library of Canada to microfilm this thesis and to lend or sell copies of the film, and to University Microfilms Inc. to publish an abstract of this thesis/practicum.**

**This reproduction or copy of this thesis has been made available by authority of the copyright owner solely for the purpose of private study and research, and may only be reproduced and copied as permitted by copyright laws or with express written authorization from the copyright owner.**

## **Abstract**

Jet impingement heat transfer for a stationary plate is investigated to provide a better understanding of the cooling process that occurs in a hot steel mill. Various effects on heat transfer are presented, some of which are jet velocity, water temperature, nozzle-to-surface spacing, wall superheat, nozzle diameter, planar versus circular jets, nozzle configuration, and surface oxidation. Correlations presented by other researchers, which are used to determine the heat flux within the single-phase forced convection, nucleate boiling, and critical heat flux (CHF) regimes, were compared with experimental data obtained from the University of British Columbia (UBC) facility for a circular jet. Only one single-phase forced convection correlation was found to match well with the data. All of the nucleate boiling correlations reviewed highly overestimated the heat flux data. A few CHF correlations can be used to accurately represent the experimental data. A new heat transfer correlation was developed, which can be used to ascertain the heat flux within the single-phase forced convection and nucleate boiling regimes.

---

## Table of Contents

<b>Abstract</b> .....	<b>ii</b>
<b>Table of Contents</b> .....	<b>iii</b>
<b>List of Figures</b> .....	<b>vi</b>
<b>List of Tables</b> .....	<b>x</b>
<b>Nomenclature</b> .....	<b>xi</b>
<b>Acknowledgements</b> .....	<b>xiv</b>
<b>1. Introduction</b> .....	<b>1</b>
<b>2. Literature Review</b> .....	<b>3</b>
2.1 The Hot Rolling Process .....	3
2.2 Hydrodynamics of Jet Impingement .....	4
2.2.1 Jet Configurations.....	4
2.2.2 Hydrodynamic Regions .....	6
2.2.3 Jet Impingement Velocity.....	7
2.2.4 Diameter at Jet Impingement.....	7
2.2.5 Water Pressure at Jet Impingement .....	8
2.3 Jet Impingement Heat Transfer for a Stationary Plate .....	8
2.3.1 Single-phase Forced Convection .....	10
2.3.2 Nucleate Boiling .....	13
2.3.3 Two-phase Convection .....	17
2.3.4 Critical Heat Flux .....	22
2.3.5 Transition Boiling.....	29
2.3.6 Film Boiling.....	29
2.3.7 Modes of Heat Transfer During Impingement .....	30
2.3.8 Heat Transfer Within and Outside the Stagnation Region .....	31
2.3.9 Visual Representation of Heat Transfer .....	32
2.3.10 Wetting Zone .....	33
2.4 Variables Affecting Jet Impingement Heat Transfer .....	33
2.4.1 Effect of Nozzle Configuration .....	34
2.4.2 Effect of Wall Superheat .....	35
2.4.3 Effect of Jet Velocity .....	35
2.4.4 Effect of Nozzle Diameter .....	40
2.4.5 Effect of Subcooling .....	40
2.4.6 Effect of Nozzle-to-Surface Spacing.....	43
2.4.7 Effect of Surface Variations .....	44
2.4.8 Effect of Jet Angle.....	45
2.4.9 Effect of an Intermittent Jet.....	46
2.4.10 Effect of Adding Air Bubbles to the Jet .....	47
2.5 Water Jet Impingement on a Moving Plate.....	48

---

<b>3. Experimental Apparatus and Procedure.....</b>	<b>50</b>
3.1 ROTC Facility Apparatus .....	50
3.2 Test Sample .....	52
3.2.1 Chemical Composition .....	52
3.2.2 Thermo-physical Properties.....	52
3.3 Thermocouples .....	53
3.3.1 Thermocouple Installation.....	54
3.4 Experimental Procedure .....	57
<b>4. Test Conditions, Selection, and Observations .....</b>	<b>59</b>
4.1 Experimental Conditions.....	59
4.2 Calculating the Heat Flux.....	61
4.3 Selecting the Tests to use for the Analyses.....	62
4.4 Experimental Data Observations.....	68
4.4.1 Boiling Regimes Defined .....	69
4.4.2 Single-phase Forced Convection Region .....	70
4.4.3 CHF Region.....	70
4.4.4 Time Interval for the Boiling Regimes.....	73
<b>5. Single-phase Forced Convection Analysis and Results .....</b>	<b>81</b>
5.1 Summary of Correlations Used .....	81
5.2 Determining the Single-phase Forced Convection Heat Flux.....	82
5.3 Effect of Water Flow rate.....	86
5.4 Effect of Water Temperature .....	91
5.5 Comparison with the Experimental Data .....	91
5.5.1 Results for Equation 2.8 .....	92
5.5.2 Results for Equation 2.9 .....	93
5.5.3 Results for Equation 2.10 .....	100
5.5.4 Results for Equation 2.11 .....	106
5.5.5 Results for Equation 2.12 .....	112
5.5.6 Results for Equation 2.13 .....	115
5.5.7 Results for Equation 2.14 .....	119
5.5.8 Comparison Between Equations 2.13 and 2.14.....	125
5.5.9 Summary of Results .....	126
<b>6. Nucleate Boiling Analysis and Results .....</b>	<b>129</b>
6.1 Results .....	129
<b>7. Two-phase Analysis and Results .....</b>	<b>132</b>
7.1 Modification of the Chen Correlation.....	132
7.1.1 Macroconvective Heat Transfer Coefficient .....	132
7.1.2 Microconvective Heat Transfer Coefficient.....	133
7.1.3 The New Correlation .....	137
7.2 Comparison with Experimental Data .....	138
7.3 Comparison with Other Researcher's Data.....	146

<b>8. CHF Analysis and Results.....</b>	<b>149</b>
8.1 Determining the Correlation CHF .....	153
8.2 Effect of Heater Diameter .....	155
8.3 Effect of Water Flow Rate .....	156
8.4 Effect of Water Temperature.....	158
8.5 Comparison with the Experimental Data .....	160
8.5.1 Results for Equation 2.41 .....	160
8.5.2 Results for Equation 2.42.....	164
8.5.3 Results for Equation 2.43.....	168
8.5.4 Results for Equation 2.45.....	170
8.5.5 Results for Equation 2.46.....	173
8.5.6 Results for Equation 2.47.....	174
8.5.7 Results for Equation 2.48.....	178
8.5.8 Results for Equation 2.49.....	180
8.5.9 Results for Equation 2.50.....	181
8.5.10 Results for Equation 2.51 .....	185
8.5.11 Summary of Results.....	186
<b>9. Conclusion .....</b>	<b>187</b>
<b>10. Recommendations for Future Work.....</b>	<b>190</b>
<b>11. References.....</b>	<b>192</b>
<b>Appendix A: Thermocouple Conduction Error Literature Review .....</b>	<b>197</b>
<b>Appendix A References.....</b>	<b>216</b>
<b>Appendix B: Hauksson’s and Meng’s Observations.....</b>	<b>217</b>

---

## List of Figures

Figure 2.1: Basic layout of a hot rolling table [4].....	3
Figure 2.2: Cooling configurations used in a hot rolling mill [2].....	4
Figure 2.3: Jet configurations [6].....	5
Figure 2.4: Hydrodynamic regions [6].....	7
Figure 2.5: Boiling curve for a saturated liquid [6].....	10
Figure 2.6: Nucleate boiling in a horizontal tube [17].....	13
Figure 2.7: Enhancement factor F [21].....	20
Figure 2.8: Suppression factor S [21].....	21
Figure 2.9: Transition boiling [17].....	29
Figure 2.10: Film boiling [17].....	30
Figure 2.11: Heat transfer regimes for a stationary plate [2, 3, 7, 33, and 34].....	31
Figure 2.12: Surface temperature curves for SS316 steel at a water temperature of 30°C and 30L/min flow rate [3].....	32
Figure 2.13: The effects of nozzle configuration at different locations [42].....	34
Figure 2.14: Plate temperature cooling for jet velocities of 6.52 m/s (test 10) and 4.63 m/s (test 13) [39].....	35
Figure 2.15: The effects of jet velocity on the rewetting front [41].....	36
Figure 2.16: The effect of jet velocity on heat flux [46].....	37
Figure 2.17: The influence of jet velocity on heat flux [47].....	38
Figure 2.18: The effect of jet velocity on the CHF [35].....	39
Figure 2.19: Surface temperature graphs at water temperatures of 13°C (test 10) and 30°C (test 11) [39].....	41
Figure 2.20: The effect of subcooling on heat flux [47].....	42
Figure 2.21: The effect of surface roughness on heat flux in the stagnation region [50].....	44
Figure 2.22: Inclination angles tested by Tong [53].....	45
Figure 2.23: The effect of jet inclination angle on Nusselt number [53].....	46
Figure 2.24: The effect of adding air bubbles to a water jet on heat flux [55].....	48
Figure 3.1: ROTC facility apparatus.....	51
Figure 3.2: Thermocouple pair installation.....	54
Figure 3.3: Thermocouple layout at water temperatures up to 50°C.....	55
Figure 3.4: Thermocouple layout at water temperatures of 60°C to 95°C.....	56
Figure 3.5: Schematic view of test plate setup.....	57
Figure 4.1: Experimental heat flux at 15 l/min.....	64
Figure 4.2: Experimental heat flux at 30 l/min.....	65
Figure 4.3: Single-phase forced convection heat flux at 30 l/min.....	66
Figure 4.4: Experimental heat flux at 45 l/min.....	67
Figure 4.5: Single-phase forced convection heat flux at 45 l/min.....	68
Figure 4.6: Boiling regimes for test H5030.....	69
Figure 4.7: Single-phase forced convection heat flux at 15 l/min.....	70
Figure 4.8: Determining the CHF for test H4030.....	71
Figure 4.9: Experimental data CHF.....	72
Figure 4.10: Wall superheat CHF occurred at.....	73
Figure 4.11: Regimes defined for test H3045.....	74
Figure 4.12: Regimes defined for test M9545.....	75

---

Figure 4.13: Time interval for transition boiling regime for test H3045 .....	77
Figure 4.14: Time interval for nucleate boiling regime for test H3045 .....	78
Figure 4.15: Time interval for single-phase forced convection regime for test H3045....	78
Figure 5.1: Effect of flow rate for Equation 2.8 .....	86
Figure 5.2: Effect of flow rate for Equation 2.12 .....	87
Figure 5.3: Proportional Factors to h Values at Different Flow Rates for Equations a) 2.9, 2.10, 2.11 b) 2.12, 2.13, 2.14.....	90
Figure 5.4: Heat flux for Equation 2.14 at different water temperatures .....	91
Figure 5.5: Equation 2.8 compared with the data of test H5045 .....	93
Figure 5.6: Percent of the experimental data that fell within $\pm 30\%$ of Equation 2.9 .....	94
Figure 5.7: Equation 2.9 compared with the data of test M7015.....	95
Figure 5.8: Equation 2.9 compared with the data of test M8015.....	96
Figure 5.9: Equation 2.9 compared with the data of test H5030 .....	97
Figure 5.10: Equation 2.9 compared with the data of test M7045.....	98
Figure 5.11: Equation 2.9 compared with the data of test M9545.....	98
Figure 5.12: Percent of the experimental data that fell within $\pm 30\%$ of Equation 2.10..	100
Figure 5.13: Equation 2.10 compared with the data of test M9515.....	101
Figure 5.14: Equation 2.10 compared with the data of test H5030 .....	102
Figure 5.15: Equation 2.10 compared with the data of test M9530.....	102
Figure 5.16: Equation 2.10 compared with the data of test H3045 .....	103
Figure 5.17: Equation 2.10 compared with the data of test H4045 .....	104
Figure 5.18: Equation 2.10 compared with the data of test M9545.....	104
Figure 5.19: Percent of the experimental data that fell within $\pm 30\%$ of Equation 2.11..	106
Figure 5.20: Equation 2.11 compared with the data of test H3015 .....	108
Figure 5.21: Equation 2.11 compared with the data of test M7015.....	108
Figure 5.22: Equation 2.11 compared with the data of test M8015.....	109
Figure 5.23: Equation 2.11 compared with the data of test M9515.....	109
Figure 5.24: Equation 2.11 compared with the data of test H4030 .....	110
Figure 5.25: Equation 2.11 compared with the data of test M7045.....	111
Figure 5.26: Equation 2.11 compared with the data of test M9545.....	111
Figure 5.27: Percent of the experimental data that fell within $\pm 30\%$ of Equation 2.12..	113
Figure 5.28: Equation 2.11 compared with 2.12 at 15 l/min and $T_{\text{water}} = 30^{\circ}\text{C}$ .....	114
Figure 5.29: Percent of the experimental data that fell within $\pm 30\%$ of Equation 2.13..	116
Figure 5.30: Equation 2.13 compared with the data of test H3045 .....	117
Figure 5.31: Equation 2.13 compared with the data of test M7045.....	118
Figure 5.32: Equation 2.13 compared with the data of test M9545.....	118
Figure 5.33: Percent of the experimental data that fell within $\pm 30\%$ of Equation 2.14..	120
Figure 5.34: Equation 2.14 compared with the data of test M8015.....	121
Figure 5.35: Equation 2.14 compared with the data of test H4030 .....	122
Figure 5.36: Equation 2.14 compared with the data of test M9530.....	122
Figure 5.37: Equation 2.14 compared with the data of test H3045 .....	123
Figure 5.38: Equation 2.14 compared with the data of test H4045 .....	124
Figure 5.39: Equation 2.14 compared with the data of test M9545.....	124
Figure 6.1: Nucleate boiling correlations compared with the data of test M9545.....	130
Figure 6.2: Nucleate boiling correlations compared with the data of test H3045 .....	131
Figure 7.1: Subcooled correlation with $S=1$ compared with the data of test H4030.....	134

---

Figure 7.2: Subcooled correlation with calculated S compared with the data of test H4030 .....	135
Figure 7.3: Calculated suppression factor for test H4030 .....	136
Figure 7.4: Calculated suppression factors for all the tests .....	137
Figure 7.5: Percent of the experimental data that fell within $\pm 30\%$ of the correlation... ..	139
Figure 7.6: Two-phase correlation compared with the results of test H5015 .....	140
Figure 7.7: Two-phase correlation compared with the data of test M7015 .....	141
Figure 7.8: Suppression factor comparison at $T_{\text{water}} = 70^{\circ}\text{C}$ and 15 l/min .....	141
Figure 7.9: Two-phase correlation compared with the data of test M7045 .....	142
Figure 7.10: Suppression factor comparison at $T_{\text{water}} = 70^{\circ}\text{C}$ and 45 l/min .....	143
Figure 7.11: Two-phase correlation compared with the data of test M9545.....	143
Figure 7.12: Suppression factor comparison at $T_{\text{water}} = 95^{\circ}\text{C}$ and 45 l/min .....	144
Figure 7.13: Two-phase correlation compared with the data of test M9530.....	145
Figure 7.14: Suppression factor comparison at $T_{\text{water}} = 95^{\circ}\text{C}$ and 30 l/min .....	145
Figure 7.15: The two-phase correlation compared with data from Hall et. al [64] .....	148
Figure 8.1: CHF calculated at $D=d_{\text{ji}}$ and $D=1.1*d_{\text{ji}}$ at $T_{\text{water}} = 30^{\circ}\text{C}$ , flow rate of 15 l/min, and wall superheat of $200^{\circ}\text{C}$ .....	154
Figure 8.2: CHF at $T_{\text{water}} = 30^{\circ}\text{C}$ , 15 l/min, and $\Delta T_{\text{sat}}$ of $200^{\circ}\text{C}$ .....	156
Figure 8.3: CHF for Equations 2.41 and 2.48 at $T_{\text{water}} = 30^{\circ}\text{C}$ and $\Delta T_{\text{sat}}$ of $200^{\circ}\text{C}$ at ....	157
Figure 8.4: CHF for all other equations at $T_{\text{water}} = 30^{\circ}\text{C}$ and $\Delta T_{\text{sat}}$ of $200^{\circ}\text{C}$ at different flow rates.....	158
Figure 8.5: CHF for Equations 2.41, 2.43, 2.49, 2.50, and 2.51 at 15 l/min at different water temperatures.....	159
Figure 8.6: CHF for Equations 2.42, 2.45, 2.46, 2.47, and 2.48 at 15 l/min at different water temperatures.....	159
Figure 8.7: Percent error for Equation 2.41 .....	161
Figure 8.8: Equation 2.41 compared with the experimental data at 15 l/min.....	162
Figure 8.9: Equation 2.41 compared with the experimental data at 30 l/min.....	162
Figure 8.10: Equation 2.41 compared with the experimental data at 45 l/min.....	163
Figure 8.11: Percent error for Equation 2.42 .....	165
Figure 8.12: Equation 2.42 compared with the experimental data at 15 l/min.....	166
Figure 8.13: Equation 2.42 compared with the experimental data at 30 l/min.....	166
Figure 8.14: Equation 2.42 compared with the experimental data at 45 l/min.....	167
Figure 8.15: Percent error for Equation 2.43 .....	168
Figure 8.16: Equation 2.43 compared with the experimental data at 15 l/min.....	169
Figure 8.17: Equation 2.43 compared with the experimental data at 30 l/min.....	169
Figure 8.18: Equation 2.43 compared with the experimental data at 45 l/min.....	170
Figure 8.19: Percent error for Equation 2.45 .....	171
Figure 8.20: Equation 2.45 compared with the experimental data at 15 l/min.....	172
Figure 8.21: Equation 2.45 compared with the experimental data at 30 l/min.....	172
Figure 8.22: Equation 2.45 compared with the experimental data at 45 l/min.....	173
Figure 8.23: Percent error for Equation 2.46.....	174
Figure 8.24: Percent error for Equation 2.47 .....	175
Figure 8.25: Equation 2.47 compared with the experimental data at 15 l/min.....	176
Figure 8.26: Equation 2.47 compared with the experimental data at 30 l/min.....	176
Figure 8.27: Equation 2.47 compared with the experimental data at 45 l/min.....	177

---

Figure 8.28: Percent error for Equation 2.48.....	178
Figure 8.29: Equation 2.48 compared with the experimental data at 15 l/min.....	179
Figure 8.30: Equation 2.48 compared with the experimental data at 30 l/min.....	179
Figure 8.31: Equation 2.48 compared with the experimental data at 45 l/min.....	180
Figure 8.32: Percent error for Equation 2.49.....	181
Figure 8.33: Percent error for Equation 2.50.....	182
Figure 8.34: Equation 2.50 compared with the experimental data at 15 l/min.....	183
Figure 8.35: Equation 2.50 compared with the experimental data at 30 l/min.....	184
Figure 8.36: Equation 2.50 compared with the experimental data at 45 l/min.....	184
Figure 8.37: Percent error for Equation 2.51.....	185
Figure A.1: The Seebeck Voltage.....	197
Figure A.2: Basic Thermocouple [A3].....	199
Figure A.3: Thermocouple Circuit [A5].....	201
Figure A.4: Beaded Thermocouple Compared to the End of a Needle [A2].....	202
Figure A.5: Diagram for Analytical Model from [A7].....	206
Figure A.6: Analytical Model Setup used by Henning and Parker [A10].....	210
Figure A.7: Setup used by Boelter et. al [A13].....	214
Figure B.1: Cooling of internal and surface thermocouples [3].....	218
Figure B.2: Heat flux versus time at a water temperature of 30°C and jet impingement velocity of 5.7 m/s [3].....	219
Figure B.3: Heat flux versus wall superheat at a water temperature of 30°C and jet impingement velocity of 5.7 m/s [3].....	220
Figure B.4: Cooling of a hot steel plate [3].....	221
Figure B.5: Boiling curves at location 2 for different subcoolings at a flow rate of 45 l/min [2].....	223
Figure B.6: CHF at different subcoolings [2].....	224
Figure B.7: MHF at different subcoolings [2].....	224
Figure B.8: CHF at different jet velocities at 5°C subcooling [2].....	225
Figure B.9: MHF at different jet velocities at 5°C subcooling [2].....	226
Figure B.10: Effect of surface oxidation [2].....	227

## List of Tables

Table 2.1: $F_1$ , $F_2$ , $F_3$ , and $F_4$ functions for the Bowring correlation [20] .....	29
Table 3.1: Chemical composition of the steel alloys used in weight %.....	52
Table 3.2: Thermocouple Locations.....	56
Table 4.1: Test Conditions.....	60
Table 4.2: Summary of tests chosen to compare with the correlations.....	68
Table 4.3: Experimental data CHF.....	72
Table 4.4: Wall superheat CHF occurred at .....	73
Table 4.5: Wall superheat ranges for the regimes.....	76
Table 4.6: Time intervals for each boiling regime and percent of total cooling time.....	79
Table 5.1: Single-phase forced convection equations presented by other researchers .....	82
Table 5.2: Corrected Parameters for Equation 2.8.....	84
Table 5.3: Corrected Parameters for Equations 2.13 and 2.14 .....	84
Table 5.4: Proportional factors to $h$ at each of the flow rates.....	89
Table 5.5: Percent of the experimental data that fell within $\pm 30\%$ of Equation 2.9.....	94
Table 5.6: Percent of the experimental data that fell within $\pm 30\%$ of Equation 2.10.....	100
Table 5.7: Percent of the experimental data that fell within $\pm 30\%$ of Equation 2.11 .....	106
Table 5.8: Percent of the experimental data that fell within $\pm 30\%$ of Equation 2.12.....	113
Table 5.9: Percent of the experimental data that fell within $\pm 30\%$ of Equation 2.13.....	116
Table 5.10: Percent of the experimental data that fell within $\pm 30\%$ of Equation 2.14... ..	120
Table 5.11: Number and percentage of tests with = 70% of the experimental data falling with $\pm 30\%$ of the correlation.....	126
Table 5.12: Given and Theorized Applicable Conditions for Each Correlation .....	128
Table 6.1: Summary of nucleate boiling correlations analyzed.....	129
Table 7.1: Calculated suppression factor at $T_{\text{water}} = 40^\circ\text{C}$ and 30 l/min.....	136
Table 7.2: New two-phase forced convection correlation.....	138
Table 7.3: Percent of the experimental data that fell within $\pm 30\%$ of the correlation ....	139
Table 7.4: Parameters for the two-phase equation.....	147
Table 8.1: CHF equations presented by other researchers .....	150
Table 8.2: Heater diameters used for the analysis .....	154
Table 8.3: $D$ used to examine effect of heater diameter.....	155
Table 8.4: Percent error for Equation 2.41 .....	161
Table 8.5: Percent error for Equation 2.42 .....	165
Table 8.6: Percent error for Equation 2.43 .....	168
Table 8.7: Percent error for Equation 2.45 .....	171
Table 8.8: Percent error for Equation 2.46 .....	174
Table 8.9: Percent error for Equation 2.47 .....	175
Table 8.10: Percent error for Equation 2.48 .....	178
Table 8.11: Percent error for Equation 2.49 .....	181
Table 8.12: Percent error for Equation 2.50 .....	183
Table 8.13: Percent error for Equation 2.51 .....	185
Table 8.14: Conditions when the CHF equations can represent the data.....	186
Table A.1: Thermocouple Types [A4] .....	203

---

## Nomenclature

$C_{pf}$	Specific heat of liquid water
$C_{ps}$	Specific heat of the steel plate
$d_j$	Diameter of the jet at nozzle exit
$d_{jcor}$	Corrected diameter of the jet at nozzle exit
$d_{ji}$	Diameter of the jet at impingement
$D$	Heater diameter
$D_{tube}$	Diameter of the tube
$F$	Enhancement factor for the Chen correlation
$g$	Gravitational acceleration
$G$	Mass velocity, $\rho v$
$h$	Heat transfer coefficient
$\bar{h}$	Average heat transfer coefficient
$h_{FC}$	Forced convection heat transfer coefficient
$h_{mac}$	Macroconvective heat transfer coefficient
$h_{mic}$	Microconvective heat transfer coefficient
$h_{NB}$	Nucleate boiling heat transfer coefficient
$h_{TP}$	Two-phase heat transfer coefficient
$h_f$	Enthalpy of water
$h_{fg}$	Latent heat of vapourization of water
$h_{sat}$	Enthalpy of water enthalpy at saturation temperature
$k_f$	Thermal conductivity of liquid water
$k_g$	Thermal conductivity of water vapour
$k_s$	Thermal conductivity of the steel plate
$L$	Length of the tube
$Nu_j$	Nusselt number at nozzle exit
$Nu_{ji}$	Nusselt number at jet impingement
$p_{atm}$	Atmospheric pressure
$p_{bar}$	Water pressure in bars
$p_s$	Water pressure at stagnation point

$p_{\text{sat}}$	Water saturation pressure
$p_{\text{surf}}$	Water pressure at the surface temperature
$\Delta p_e$	The difference in vapour pressure corresponding to $\Delta T_e$
$Pr$	Prandtl number
$Pr_f$	Prandtl number of a liquid
$Q_{\text{air}}$	Volumetric flow rate of air
$Q_{\text{water}}$	Volumetric flow rate of water
$q''$	Heat flux
$q''_{CHF}$	Critical heat flux
$q''_{data}$	Experimental heat flux
$q''_{FNB}$	Heat flux for fully developed nucleate boiling
$q''_{forced}$	Single-phase forced convection heat flux
$q''_{NB}$	Nucleate boiling heat flux
$q''_{ONB}$	Heat flux at the onset of nucleate boiling
$q''_{SUB}$	Subcooled two-phase heat flux
$q''_{TP}$	Two-phase heat flux
$r$	Radial distance from the stagnation point
$Re_f$	Reynold's number of a liquid
$Re_j$	Reynold's number at nozzle exit
$Re_{jcor}$	Reynold's number at the corrected nozzle velocity and diameter
$Re_{ji}$	Reynold's number at jet impingement
$Re_{TP}$	Two-phase Reynold's number
$t$	Time increment
$T_{\text{film}}$	Water film temperature
$T_{\text{sat}}$	The saturation temperature of the water
$T_{\text{surf}}$	Plate surface temperature
$T_{\text{water}}$	Initial water temperature
$T_{\text{wet}}$	Rewetting temperature
$\Delta T_e$	The effective wall superheat with flow

$\Delta T_{\text{sat}}$  The difference between the surface and saturation temperature (wall superheat)

$$\Delta T_{\text{sat}} = T_{\text{surf}} - T_{\text{sat}}$$

$\Delta T_{\text{sub}}$  Subcooled temperature ( $\Delta T_{\text{sub}} = 100 - T_{\text{water}}$ )

$v_j$  Jet velocity at nozzle exit

$v_{j\text{cor}}$  Corrected jet velocity at nozzle exit

$v_{ji}$  Jet velocity at impingement

$X_{\text{tt}}$  Martinelli parameter

$Z$  Nozzle-to-plate spacing

$Z_{\text{cor}}$  Corrected nozzle-to-plate spacing

### Greek

$\alpha$  Void fraction

$\epsilon_{\text{sub}}$  Subcooling correction factor

$\mu_f$  Dynamic viscosity of liquid water

$\nu_f$  Specific volume of a liquid

$\nu_g$  Specific volume of a vapour

$\rho_f$  Density of liquid water

$\rho_g$  Density of water vapour

$\rho_s$  Density of the steel plate

$\sigma$  Surface tension of water

## Acknowledgements

I would like to thank the National Sciences and Engineering Research Council of Canada (NSERC) for funding my research.

I would also like to thank the following people for providing help with my research:

- My advisor Dr. Daniel Fraser for giving me the opportunity to do this research and providing me a tremendous amount of guidance and support throughout my studies.
- Ágúst Torfi Hauksson and Qi Meng for performing the experiments.
- Dr. Eric Bibeau and Dr. Marolo Alfaro for taking the time to evaluate my thesis and serve as the examiners.
- Dr. Vladan Prodanovic at the University of British Columbia for providing help along the way.
- Andrew Roncin and Chris Harrower for teaching me how to use Matlab.

## 1. Introduction

Crude steel production of the world exceeded 900 million tonnes in 2002 and continues to grow [1]. Roughly 25-30% of this incorporates the hot rolling process [2]. Hot rolled sheets can be used for piping and tubing, automotive parts, rail cars, and various equipment for construction and agriculture.

Despite the long-term usage of water jet cooling in hot rolling steel mills, little is fully understood about the actual heat transfer process that occurs. It is important to better understand jet impingement cooling during the hot rolling process because properties such as the final chemical composition, hardness, and malleability of the steel depend on the cooling rates and temperatures involved. This process needs to be better understood so the properties desired can be better accomplished and controlled.

Many researchers have reported data on jet impingement for stationary surfaces for different jet configurations. However, more data needs to be accumulated to better predict the heat transfer process. Thus, an ongoing experimental program is working on characterizing this process at the University of British Columbia using the run out table cooling (ROTC) facility, also of which researchers at the University of Manitoba collaborate with.

One or more correlations are needed in order to calculate the heat being removed from the plate, which could then be used to estimate the cooling rates that occur in a steel mill. Once this is known, the properties of the steel desired can be better controlled. Many equations have been provided by other researchers. However, there is an uncertainty as to their acceptable use under conditions that would occur in a steel mill. Therefore, this thesis provides correlations presented by other researchers for single-

phase forced convection, two-phase forced convection, nucleate boiling, and critical heat flux and compares them with data gathered by A. Hauksson [3] and Q. Meng [2] on stationary plate circular free-surface jet experiments performed at the ROTC facility. A new correlation has also been developed to represent the single-phase forced convection and nucleate boiling regimes.

There are many variables that influence the heat transfer characteristics in jet impingement cooling. Understanding their effects will help comprehend how the heat transfer process would be altered if one or more of these variables are changed in a hot steel mill. Therefore, the effects of nozzle configuration, wall superheat, jet velocity, nozzle diameter, subcooling, nozzle-to-surface spacing, surface variations, jet angle, intermittent jets, and adding air bubbles to the jet on jet impingement heat transfer will be discussed. Heat transfer for a moving plate will also be presented.

## 2. Literature Review

### 2.1 The Hot Rolling Process

Hot rolling usually follows the continuous casting process at a finishing temperature of 800°C to 950°C. Water jets at room temperature (18°C to 50°C) cool the sheet to 500°C to 750°C before it enters the coil. Multiple top and bottom headers at distances less than 1200 mm and 100 mm above and below the table, respectively, are distributed such that the strip cools as evenly as possible (Figure 2.1). The steel surface travels at an average speed of 10 m/s on motorized rollers approximately 18" apart on a table that can be up to 150 m long [2 and 3].

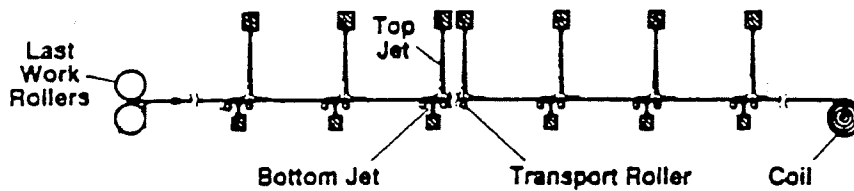


**Figure 2.1: Basic layout of a hot rolling table [4]**

When the water strikes the surface beneath the strip, the water falls away immediately due to gravity, resulting in a lower residence time compared to the water emitting from the top jets. Therefore, more flow (about 1.5 times) is needed on the bottom surface compared to the top surface in order to maintain symmetric cooling above and below the strip [5].

The three main types of cooling configurations used in the hot rolling process are circular jets (or laminar jets), planar jets (or water curtain) and spray cooling as shown in Figure 2.2.

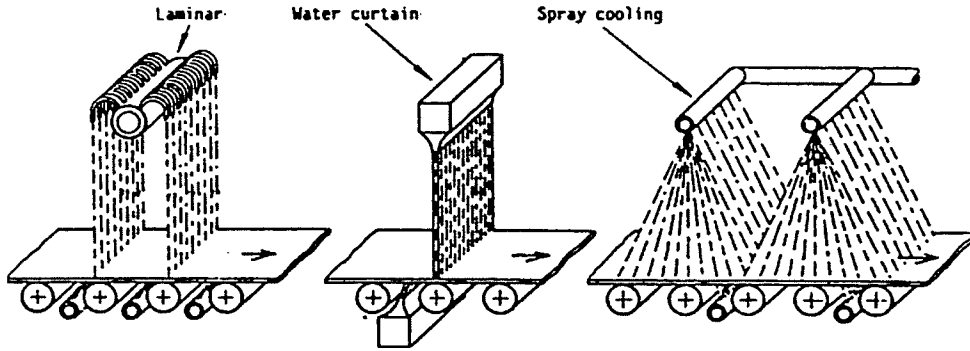


**Figure 2.2: Cooling configurations used in a hot rolling mill [2]**

It is important that the cooling process is understood so the metallurgical properties of the steel can be readily controlled. However, little is understood about the cooling that takes place in the hot rolling process. Research is on-going in this area to characterize the heat transfer that occurs.

## **2.2 Hydrodynamics of Jet Impingement**

### **2.2.1 Jet Configurations**

There are five different hydrodynamic jet configurations that can be used as shown in Figure 2.3. Depending upon the layout, free surface and plunging jets are commonly used on the runout table. With a free surface jet, the water jet travels through air and hits the surface unconstrained, allowing the water to freely flow off the surface edge. This prevents pooling on the surface and helps provide maximum heat transfer.

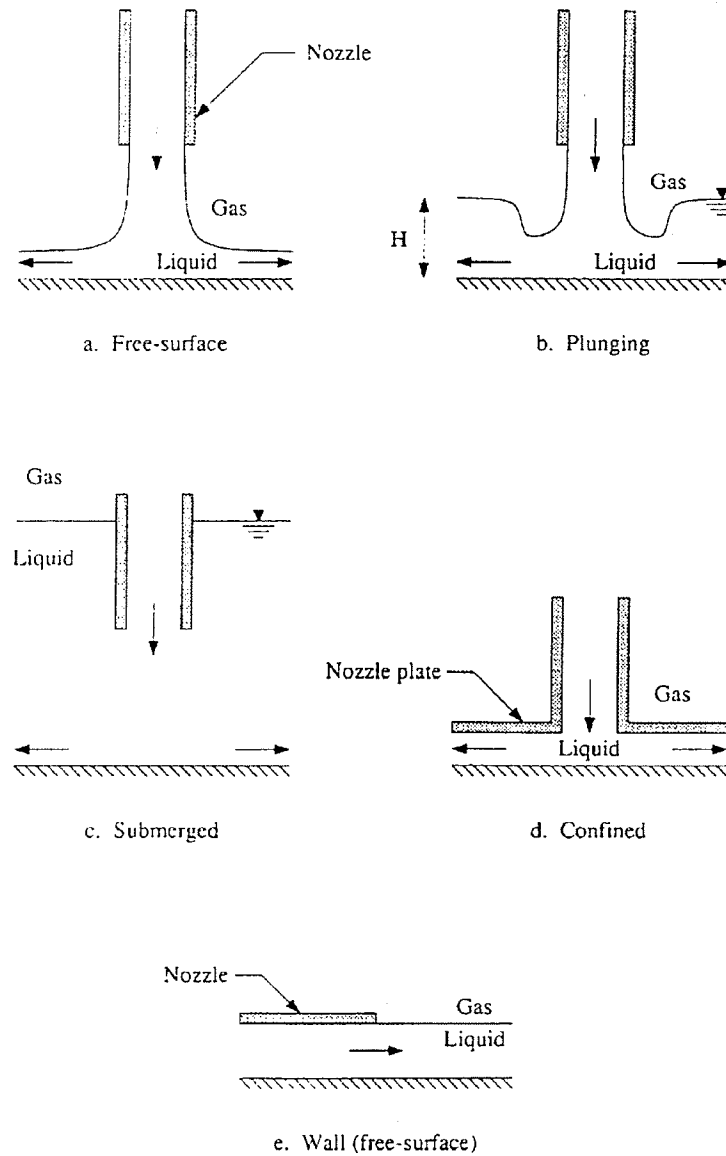


**Figure 2.3: Jet configurations [6]**

The moving strip on a steel runout table is cooled by an array of water jets as shown in Figure 2.1. In this situation, the first row resembles free surface jets but further downstream the water impinges as plunging jets because a thicker water layer flows on the surface resulting from the motion. Usage of plunging jets is less desirable than free surface jets because the thicker water layer limits the cooling process.

Jets can strike obliquely or normally to the plate on the top and bottom surfaces. The plate can be flat, convex, or concave and can be moving or stationary. The main focus of the experiments is on a free surface circular jet impinging normal to a flat surface. Runout table mills apply both upward and downward facing jets. However, the experiments performed at the ROTC facility only employed a downward facing jet to simplify the analysis. Later research should incorporate jet impingement on both the upside and downside of the plate.

### **2.2.2 Hydrodynamic Regions**

The three hydrodynamic regions for a planar free surface jet are the stagnation, acceleration and parallel flow regions as depicted in Figure 2.4 for a stationary plate. For a stationary plate, the stagnation region is at least the size of the jet diameter ( $r/d_{ji} < 0.5$ ) and is where the maximum pressure occurs. The streamwise velocity is zero at the stagnation point and increases radially outwards.

The acceleration region ranges from  $0.5 < r/d_{ji} < 2$  [2]. As the acceleration region expands outwards, the pressure decreases and the streamwise velocity increases. The impingement region or impingement zone refers to the stagnation and acceleration regions. In the parallel flow region ( $r/d_{ji} \geq 2$ ), the pressure approaches zero and the streamwise velocity approaches the impingement jet velocity [2 and 3].

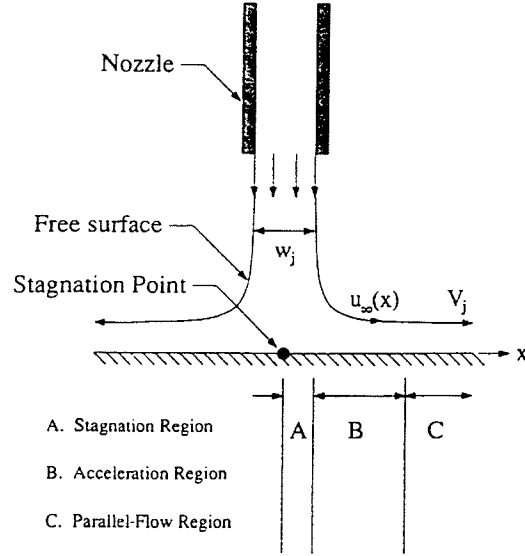


**Figure 2.4: Hydrodynamic regions [6]**

### 2.2.3 Jet Impingement Velocity

The jet impingement velocity is different for downward (plus sign) and upward jets (negative sign) due to gravitational acceleration and can be deduced from Bernoulli's equation [2, 3, and 7]. The relationship between the velocity at nozzle exit and jet impingement is provided in Equation 2.1. All variables presented in this report are defined in the nomenclature section.

$$v_{ji} = \sqrt{v_j^2 \pm 2 \cdot g \cdot Z} \quad (2.1)$$

### 2.2.4 Diameter at Jet Impingement

The diameter of the jet at impingement is related to the diameter from the nozzle exit, and the velocity at nozzle exit and impingement by:

$$d_{ji} = d_j \cdot \sqrt{\frac{v_j}{v_{ji}}} \quad (2.2)$$

### 2.2.5 Water Pressure at Jet Impingement

The water pressure at jet impingement depends upon the atmospheric pressure and density of water and nozzle jet velocity by:

$$p_s = p_{am} + \frac{1}{2} \cdot \rho_f \cdot v_j^2 \quad (2.3)$$

### 2.3 Jet Impingement Heat Transfer for a Stationary Plate

Considerable research has been performed on jet impingement heat transfer, especially when the plate is stationary. The heat transfer process that occurs will be discussed and some correlations developed from other researchers will be presented.

Most researchers have examined the effects of planar and circular jets cooling a plate. The use of planar and circular jets incorporates almost half the heat removed in the run out table operation [8]. Zumbrunnen et al. [9] and Chen and Tseng [5] reported that planar jets have an advantage over circular jets because they provide more uniform cooling in the transverse direction of the strip, while nonuniform cooling of circular jets occurs on the runout table in between the jet arrays because of the radial symmetry of the jet.

Blazevic [10] performed a comparison of aspirated sprays, sprays, and planar and circular jets by using the same volume of water per unit of strip width. They determined that using 4 rows in a circular jet array was more effective in cooling than planar jets. On the contrary, planar jets were more effective if only 1 row of circular jets was used. However, they compared the jets using different conditions, such as areas of cooling, depth of cooling, impact time, and surface temperature, and each provided conflicting results.

In summary, not enough research has been completed on the heat transfer results of planar and circular jets to conclude which is more effective. However, the heat transfer that occurs for each of these is different. Since this report compares results to data for a circular jet, only correlations provided by other researchers for a circular jet or those that can be adapted to represent a circular jet will be presented.

It is important to understand pool boiling heat transfer before an analysis can be performed for a cooling jet, especially when observing the heat flux deviations during the impingement process. Figure 2.5 shows the different modes of pool boiling heat transfer that occur during jet impingement. These are single phase forced convection, nucleate boiling, transition boiling, and film boiling. Each of these concepts will be explained. Applicable correlations from other researchers for single-phase forced convection, two-phase forced convection, nucleate boiling, and the critical heat flux will also be presented.

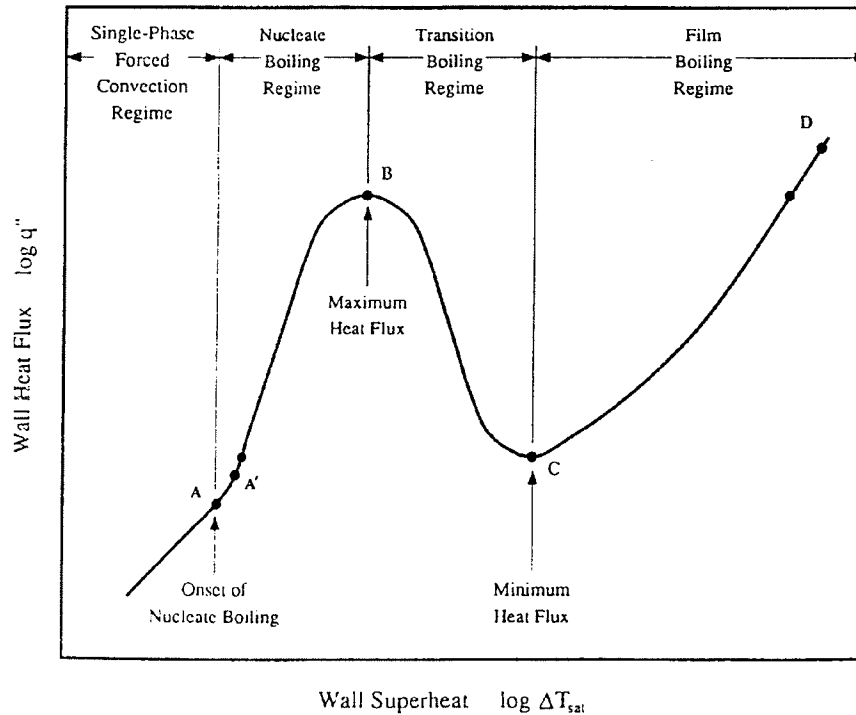


**Figure 2.5: Boiling curve for a saturated liquid [6]**

### 2.3.1 Single-phase Forced Convection

Single-phase forced convection involves the exchange of heat in a single-phase. This is when the wall surface temperature is less than or equal to the liquid saturation temperature at a given pressure. No phase change occurs until the wall superheat is positive. Figure 2.5 shows single-phase forced convection up to point A. This occurs when  $\Delta T_{\text{sat}}$  ( $\Delta T_{\text{sat}} = T_{\text{surf}} - T_{\text{sat}}$ ) is less than zero (i.e. when the plate temperature is less than the saturation temperature).

#### 2.3.1.1 Single-phase Forced Convection Correlations

Some researchers have studied single-phase forced convection for jet impingement heat transfer. They provided correlations for the Nusselt number which can in turn be translated into the heat transfer coefficient. Usually they are in the form of

$Nu = C \cdot Re^m \cdot Pr^n$ . Thus they depend upon the water properties which in turn are related to the surface temperature of the plate.

The Nusselt and Reynold's numbers at nozzle exit are calculated as:

$$Nu_j = \frac{h \cdot d_j}{k_f} \quad (2.4)$$

$$Re_j = \frac{\rho_f \cdot v_j \cdot d_j}{\mu_f} \quad (2.5)$$

The Nusselt and Reynold's numbers at jet impingement are defined as:

$$Nu_{ji} = \frac{h \cdot d_{ji}}{k_f} \quad (2.6)$$

$$Re_{ji} = \frac{\rho_f \cdot v_{ji} \cdot d_{ji}}{\mu_f} \quad (2.7)$$

Martin (1977) [11] recommended the follow equation for a circular gas jet. It should be noted that this is calculated at the nozzle exit:

$$\bar{Nu}_j = C_1 \cdot C_2 \cdot Re_j \cdot Pr^{0.42} \quad (2.8a)$$

where:

$$C_1 = \frac{d_j}{r} \cdot \frac{1 - 1.1 \cdot \frac{d_j}{r}}{1 + 0.1 \cdot (Z/d_j - 6) \cdot d_j / r} \quad (2.8b)$$

$$C_2 = 2 \cdot Re_j^{0.5} \cdot (1 + 0.005 \cdot Re_j^{0.55})^{0.5} \quad (2.8c)$$

This applies for  $2,000 \leq Re_j \leq 400,000$ ,  $2.5 \leq r/d_j \leq 7.5$ , and  $2 \leq Z/d_j \leq 12$ .

Barsanti et. al (1989) [12] examined the stagnation Nusselt number for a circular jet whose diameter extends from  $4d_j$  up to  $8d_j$ . They developed the following correlation for a stainless steel plate:

$$\bar{Nu}_{ji} = 0.0136 \cdot Re_{ji}^{0.837} \cdot Pr^{0.42} \quad (2.9)$$

This is applicable for  $3.26 < Pr < 6.04$  and  $53,025 < Re_{ji} < 210,709$ , jet diameters ranging from 10 to 20 mm, and water temperatures of 13°C to 40°C.

Faggiani and Grassi (1990) [13], presented the following correlation for the the stagnation Nusselt number for a circular jet up to two jet diameters:

$$\bar{Nu}_{ji} = 0.025 \cdot Re_{ji}^{0.8} \cdot Pr^{0.4} \quad (2.10)$$

This is applies to  $Z/d_{ji}=5$ ,  $Re > 77,000$ , and  $0.5 \leq Pr \leq 50$ .

Liu et al. (1991) [14] suggested that the following expressions be used for the stagnation zone Nusselt number for a circular jet at impingement:

$$Nu_{ji} = 0.715 \cdot Re_{ji}^{0.5} \cdot Pr^{0.4} \quad \text{when } 0.15 \leq Pr \leq 3 \quad (2.11a)$$

$$Nu_{ji} = 0.797 \cdot Re_{ji}^{0.5} \cdot Pr^{1/3} \quad \text{when } Pr > 3 \quad (2.11b)$$

This is within the region of  $0 \leq r/d_{ji} \leq 0.787$ .

Stevens and Webb (1991) [15] reviewed Wang's laminar flow solution (1989). They provided the following correlation for the stagnation point Nusselt number for a circular jet at impingement, which is applicable for  $0.5 \leq Pr \leq 50$ :

$$Nu_{ji} = 0.717 \cdot Re_{ji}^{0.5} \cdot Pr^{0.37} \quad (2.12)$$

Stevens and Webb (1991) [15] provided the following correlation for the stagnation point Nusselt number, which depends upon the ratio between the nozzle-to-plate spacing and jet diameter at nozzle exit:

$$Nu_j = 1.51 \cdot Re_j^{0.44} \cdot Pr^{0.4} \cdot \left( \frac{Z}{d_j} \right)^{-0.11} \quad (2.13)$$

This was determined under the conditions when  $2.2 \leq d_j \leq 8.9$  mm and

$$0.56 \leq Z/d_j \leq 18.5.$$

Stevens and Webb (1991) [15] also provided the following correlation for the stagnation point Nusselt number, which is applicable under the same conditions as Equation 2.13:

$$Nu_j = 2.67 \cdot Re_j^{0.567} \cdot Pr^{0.4} \cdot \left(\frac{Z}{d_j}\right)^{-0.0336} \cdot \left(\frac{v_j}{d_j}\right)^{-0.237} \quad (2.14)$$

### 2.3.2 Nucleate Boiling

Nucleate boiling occurs between points A and B in Figure 2.5. In this regime, isolated bubbles start to form at nucleation sites. The nucleate sites usually are where there are tiny pits or scratches on the surface [16]. The bubbles transport the phase change latent heat. As the liquid becomes more agitated, fluid circulation is improved, resulting in increased heat transfer [3]. Most heat transfer occurs directly from the surface to the moving liquid, and not through the vapour bubbles rising in the liquid [17].

Figure 2.6 shows nucleate boiling of methanol in a horizontal tube.

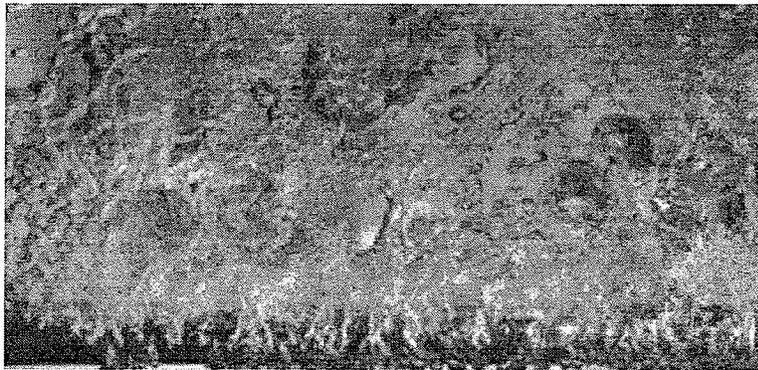


**Figure 2.6: Nucleate boiling in a horizontal tube [17]**

At the onset of nucleate boiling, shown from points A to A' in Figure 2.5, discrete bubbles start to form and detach from the surface [6]. From points A' to B fully developed nucleate boiling (bulk boiling) occurs where the liquid is more agitated, allowing the bubbles to form at a faster rate, hence increasing the heat transfer.

Nucleate boiling is a preferred region of boiling for many high heat flux cooling applications such as jet impingement heat transfer. This is due to a large increase in heat transfer that results from relatively small variations in surface temperature [6]. Thus its use is desired in industrial applications [18]. Fully developed nucleate boiling is highest at the stagnation point.

### **2.3.2.1 Nucleate Boiling Correlations**

#### **2.3.2.1.1 Circular Jet**

Many researchers have derived heat flux correlations in the nucleate boiling region. For impinging jets, all determined that nucleate boiling mainly depends upon wall superheat. Heat flux relationships given by other researchers incorporating wall superheat in the fully developed nucleate boiling regime for jet impingement cooling usually come in the form:

$$q_{FNB}'' = C \times \Delta T_{sat}''^n \quad (2.15)$$

Where C and n are experimentally determined constants.

Wolf et. al [6] reviewed Monde and Katto's paper [19] (1978) and derived the following equation for fully developed nucleate boiling from the graphical representation of their results. This is applicable for a circular saturated water jet:

$$q_{FNB}'' = 450 \cdot (\Delta T_{sat})^{2.7} \quad (2.16)$$

Katsuta and Kurose (1981) reported that fully developed nucleate boiling depends upon wall superheat. They derived the following equation for an R-113 saturated circular jet as presented by Wolf et. al [6]:

$$q''_{FNB} = 2.93 \times 10^{-6} \cdot (\Delta T_{sat})^{7.4} \quad (2.17)$$

### 2.3.2.1.2 Other Nucleate Boiling Correlations

There are also many generalized correlations for nucleate boiling. They will be provided in this section. McAdams et. al (1949), as investigated by Tong [16], provided the following correlation for fully developed nucleate flow boiling. This applies for water at pressures ranging from 30 to 90 psia:

$$q''_{FNB} = 0.074 \cdot (\Delta T_{sat})^{3.86} \quad (2.18)$$

Jen and Lottes (1951) [20] presented the following equation for the onset of subcooled nucleate boiling within a tube. This is pertinent for  $3.63 < D_{tube} < 5.74$  mm,  $7 < p_{bar} < 172$  bars,  $115 < T_{water} < 340^\circ\text{C}$  and mass velocities ranging from 11 to  $1.05 \times 10^4$  kg/(m<sup>2</sup>s).

$$\Delta T_{sat} = 25 \cdot (q''_{ONB})^{0.25} \cdot e^{-p_{bar}/62} \quad (2.19)$$

Rohsenow (1952) [20] determined the following generalized equation for fully developed saturated nucleate pool boiling of water on a stainless steel surface:

$$\frac{C_{pf} \cdot \Delta T_{sat}}{h_{fg}} = 0.013 \cdot \left[ \frac{q''_{FNB}}{\mu_f \cdot h_{fg}} \cdot \left( \frac{\sigma}{g \cdot (\rho_f - \rho_g)} \right)^{1/2} \right]^{0.33} \cdot \left[ \frac{C_{pf} \cdot \mu_f}{k_f} \right]^{1.7} \quad (2.20)$$

Hsu (1962) [6] provided the following incipience equation for the onset of nucleate boiling:

$$q''_{ONB} = \frac{h_{fg} \cdot k_f}{16 \cdot \sigma \cdot T_{sat} \cdot (v_g - v_f)} \cdot (\Delta T_{sat})^2 \quad (2.21)$$

Bergles and Rohsenow's generalized equation (1963) [20] for the onset of nucleate boiling in subcooled boiling heat transfer. This is valid for water only at pressures ranging from 1 to 138 bars.

$$\Delta T_{sat} = 0.556 \cdot \left[ \frac{q_{ONB}''}{1082 \cdot p_{bar}^{1.156}} \right]^{0.463 \cdot p_{bar}^{0.0234}} \quad (2.22)$$

Thom et. al (1965) [20] provided the following correlation for fully developed subcooled nucleate boiling of water within a tube, which is similar to Jen and Lottes' Equation 2.19:

$$\Delta T_{sat} = 22.65 \cdot (q_{ONB}'')^{0.5} \cdot e^{-p_{bar}/87} \quad (2.23)$$

Chen (1966) [21] provided the following relation by Forster and Zuber for fully developed nucleate pool boiling:

$$h = 0.00122 \cdot \left( \frac{k_f^{0.79} \cdot C_{pf}^{0.45} \cdot \rho_f^{0.49} \cdot g^{0.25}}{\sigma^{0.25} \mu_f^{0.29} \cdot h_{fg}^{0.24} \cdot \rho_g^{0.24}} \right) \cdot \Delta T_{sat}^{0.24} \cdot \Delta p_{sat}^{0.75} \quad (2.24)$$

Davis and Anderson (1966) [20] presented the following equation for the onset of subcooled nucleate boiling:

$$q_{ONB}'' = \frac{k_f \cdot (\Delta T_{sat})^2}{4 \cdot B} \quad (2.25a)$$

where:

$$B = \frac{2 \cdot \sigma \cdot T_{sat} \cdot v_{fg}}{h_{fg}} \quad (2.25b)$$

Frost and Dzakowic's (1967) [20] equation for the onset of subcooled nucleate boiling. As it can be seen, this is an extension of Equation 2.25:

$$q_{ONB}'' = \frac{k_f \cdot (\Delta T_{sat} / Pr_f)^2}{4 \cdot B} \quad (2.26)$$

### 2.3.3 Two-phase Convection

There is also the two-phase convection, where water is in both the liquid and vapour state during boiling. Rohsenow and Griffith (1955) [22] recommended that the two-phase heat flux be determined by adding the heat fluxes within the nucleate and single-phase forced convection regions together:

$$q_{TP}'' = q_{forced}'' + q_{NB}'' \quad (2.27)$$

Another particular correlation for two-phase convection was developed by Chen (1966) [21]. It is applicable for stable two-phase axial flow within a vertical tube for water and organic fluids under saturated conditions. It is assumed that the heat flux is less than the critical heat flux.

Chen defined two mechanisms of heat transfer within the two-phase region. The first is the macroconvective mechanism, which pertains to heat transfer due to forced convection. There is also the microconvective mechanism, which is due to bubble nucleation and growth. These two mechanisms can be added to determine the total heat transfer. Therefore, the two-phase heat transfer coefficient can be determined by adding the microconvective and macroconvective heat transfer coefficients:

$$h_{TP} = h_{mic} + h_{mac} \quad (2.28)$$

The macroconvective heat transfer coefficient is define as:

$$h_{mac} = h_{FC} \cdot F \quad (2.29)$$

Where  $h_{FC}$  is the heat transfer coefficient due to single-phase forced convection. Since Chen analyzed flow within a tube, this was suggested to be represented by the well-known Dittus-Boelter equation:

$$h_{FC} = 0.023 \cdot \text{Re}^{0.8} \cdot \text{Pr}^{0.4} \cdot \frac{k_f}{D_{tube}} \quad (2.30)$$

The function  $F$  in Equation 2.29 was introduced as the enhancement factor, which is always greater than unity. This enhancement is due to the flow of the liquid which causes the bubbles to grow and depart faster from the surface which in turn enhances the amount of heat being extracted from the surface. This takes into account the enhanced heat transfer that occurs due to increased velocities in two-phase flow. It is defined as the ratio of the two-phase Reynold's number to the liquid Reynold's number:

$$F = \left( \frac{\text{Re}_{TP}}{\text{Re}_f} \right)^n \quad (2.31)$$

The exponent  $n$  is determined depending upon the exponent for the Reynold's number for the forced convection equation. For the Dittus Boelter equation, this is equal to 0.8.

Combining Equation 2.29 through to 2.31 the macroconvective heat transfer coefficient becomes:

$$h_{mac} = 0.023 \cdot \text{Re}_f^{0.8} \cdot \text{Pr}^{0.4} \cdot \frac{k_f}{D_{tube}} \cdot F \quad (2.32)$$

Where  $\text{Re}_f$  is the liquid Reynold's number defined as:

$$\text{Re}_f = \frac{\rho_f \cdot D_{tube} \cdot (1-x)}{\mu_f} \quad (2.33)$$

The microconvective component of Equation 2.28 is due to nucleate boiling.

Chen defined this as:

$$h_{mic} = h_{NB} \cdot S \quad (2.34)$$

Where  $h_{NB}$  is defined as the heat transfer coefficient due to nucleate boiling. Chen suggested that the Forster and Zuber correlation be used to represent this value:

$$h_{NB} = 0.00122 \cdot \left( \frac{k_f^{0.79} \cdot C_{pf}^{0.45} \cdot \rho_f^{0.49} \cdot g^{0.25}}{\sigma^{0.25} \mu_f^{0.29} \cdot h_{fg}^{0.24} \cdot \rho_g^{0.24}} \right) \cdot \Delta T_e^{0.24} \cdot \Delta p_e^{0.75} \quad (2.35)$$

The function S in Equation 2.34 is a suppression factor due to the reduction in thermal boundary layer thickness, hence reduced heat transfer, from the contribution of forced convective boiling. There is a suppression in heat transfer for the nucleate boiling component because the heat is removed so fast due to the forced convective flow that bubble formation is inhibited, which thereby reduces heat transfer. It is defined as:

$$S = \left( \frac{\Delta T_e}{\Delta T_{sat}} \right)^{0.24} \cdot \left( \frac{\Delta p_e}{\Delta p_{sat}} \right)^{0.75} \quad (2.36)$$

The suppression factor S is always less than unity. It approaches unity at zero flow rate and approaches zero at infinite flow rate. Combining Equations 2.34 through to 2.36 the microconvective heat transfer coefficient becomes:

$$h_{mic} = 0.00122 \cdot \left( \frac{k_f^{0.79} \cdot C_{pf}^{0.45} \cdot \rho_f^{0.49} \cdot g^{0.25}}{\sigma^{0.25} \mu_f^{0.29} \cdot h_{fg}^{0.24} \cdot \rho_g^{0.24}} \right) \cdot \Delta T_{sat}^{0.24} \cdot \Delta p_{sat}^{0.75} \cdot S \quad (2.37)$$

Chen empirically determined the functions F and S. Chen tested approximately 600 data points under the conditions of  $0.5 \text{ bars} \leq p_{abs} \leq 34.8 \text{ bars}$ ,  $0.06 \text{ m/s} \leq v_{tube} \leq 4.5 \text{ m/s}$ , and quality x of 1% to 71%. The specific heat fluxes ranged from  $6.3 \text{ kJ/m}^2\text{s}$  to  $2394 \text{ kJ/m}^2\text{s}$ . Under these conditions F was estimated by plotting the ratio of the

experimental two-phase heat transfer coefficient as a function of the reciprocal of the Martinelli parameter,  $X_{tt}$ , which is defined as:

$$X_{tt} = \left( \frac{1-x}{x} \right)^{0.9} \cdot \left( \frac{\rho_g}{\rho_f} \right)^{0.5} \cdot \left( \frac{\mu_f}{\mu_g} \right)^{0.1} \quad (2.38)$$

Figure 2.7 shows the graphical results of the enhancement factor  $F$ . In the x-axis the variable  $z$  signifies  $1-x$ .

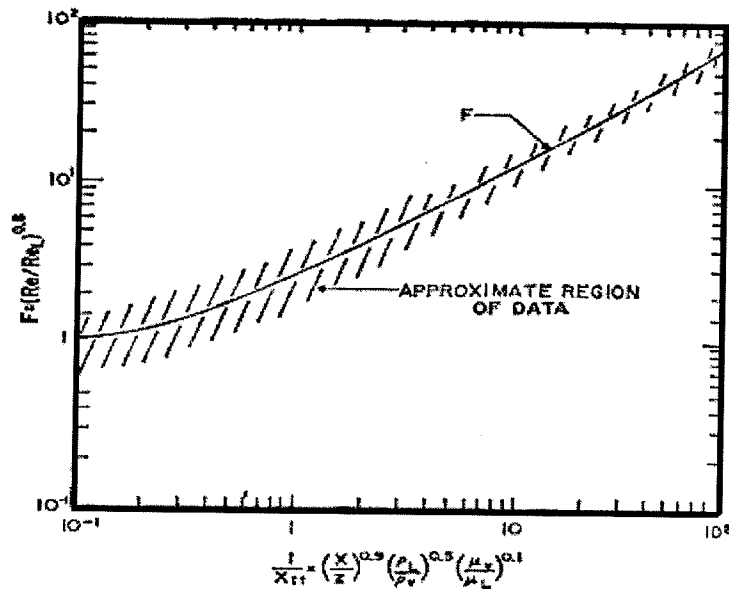


**Figure 2.7: Enhancement factor  $F$  [21]**

The suppression factor  $S$  was also determined graphically. Using the estimate of  $F$ , the results were plotted versus the two-phase Reynold's number, which is a function of the liquid Reynold's number and the enhancement factor, to get the graph in Figure 2.8. In the x-axis of the graph,  $Re$  represents the two-phase Reynold's number and  $Re_L$  represents the liquid Reynold's number.

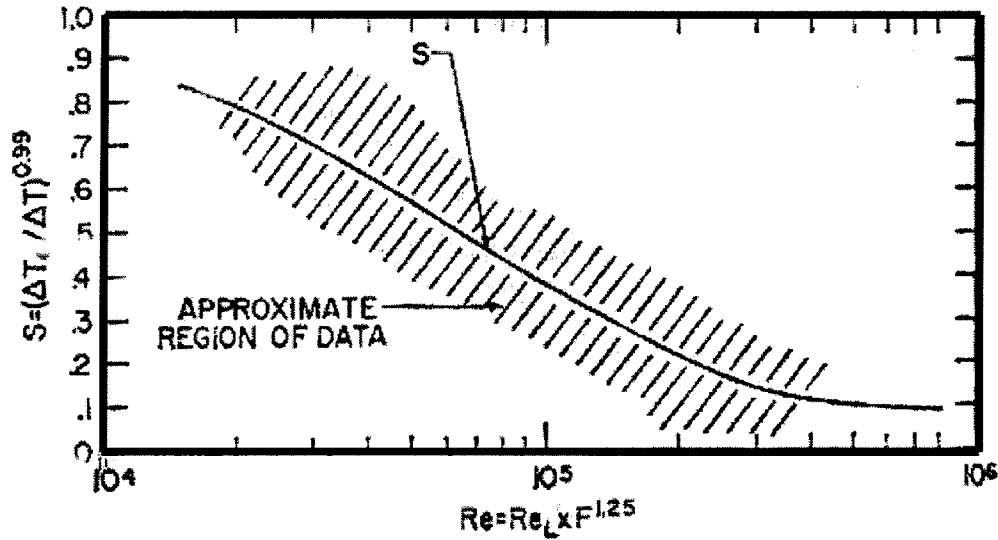


Figure 2.8: Suppression factor S [21]

Chen tested the correlation against the gathered 600 data points. From this the average deviation between the calculated and measured boiling heat transfer coefficients was  $\pm 12\%$ .

Once the two-phase heat transfer coefficient is determined, the corresponding two-phase heat flux for saturated boiling can be determined as:

$$q''_{TP} = h_{TP} \cdot (T_{surf} - T_{sat}) \quad (2.39)$$

Collier and Thome [20] reviewed Chen's work and added that the two-phase heat flux for subcooled boiling could be determined by:

$$q''_{SUB} = h_{mic} \cdot \Delta T_{sat} + h_{mac} \cdot (T_{surf} - T_{water}) \quad (2.40)$$

Collier and Thome suggested that that the enhancement factor F in the macroconvective term (see Equation 2.29) in Equation 2.40 be taken as unity.

### 2.3.4 Critical Heat Flux

The critical or maximum heat flux (CHF) occurs at point B in Figure 2.5. This is where the heat flux is the highest just after nucleate boiling.

#### 2.3.4.1 Critical Heat Flux Correlations

##### 2.3.4.1.1 Circular Jet

As it will be seen, the CHF for a circular jet mainly depends upon the different properties of water, which in turn depend upon the water temperature. They also depend upon the heater diameter ( $D$ ), jet velocity (in most instances), and jet diameter. The three types of correlations presented here are in the V-, I-, and L-regimes. Each regime is determined by the dependence of the CHF on parameters such as jet velocity and density ratio ( $\rho_f/\rho_g$ ) and mass flow rate.

Equations in the V-regime are the most widely investigated of all the regimes. They depend upon jet velocity at atmospheric pressure at large mass flow rates. They are usually in the form  $q''_{CHF} \sim v_j^{1/3}$ . Equations in the I-regimes generally do not depend upon jet velocity and occur at moderate pressures. Equations in the L-regime take place at atmospheric pressure and low mass flow rates. They are usually in the form  $q''_{CHF} \sim v_j$ .

There is also the HP-regime which occurs at pressures greater than atmospheric and has little or no dependence upon jet velocity [6] [23]. There is little research pertaining to this regime. Unless otherwise noted, all equations provided in this section refer to the V-regime for a downward facing circular jet. All equations also apply to steady state conditions only.

Ishigai and Mizuno's research (1974) [2] expressed the following equation for the CHF for a circular jet. This is applicable for jet velocities between 1.3 m/s and 9.0 m/s and subcooling between 45°C and 80°C:

$$q_{CHF}'' = 1.42 \times 10^4 \cdot \left( \frac{v_j}{d_j} \right)^{0.34} \cdot \Delta T_{sub}^{1.15} \quad (2.41)$$

Monde and Katto (1978) [19] performed experiments of a water jet impinging on an electrically heated copper plate. The heater could provide a maximum heat flux of  $2 \times 10^7$  W/m<sup>2</sup>. Water temperatures ranging from  $30^\circ\text{C} \leq T_{\text{water}} \leq 80^\circ\text{C}$  and heater diameters from 11 to 21 mm were used. Nozzle diameters of 2 mm and 2.5 mm were used with jet velocities ranging from 3.9 m/s to 26 m/s. From their results, they empirically derived the following generalized expression for CHF in the saturated condition:

$$\frac{q_{CHF}''}{\rho_g \cdot h_{fg} \cdot v_j} = 0.0745 \cdot \left( \frac{\rho_f}{\rho_g} \right)^{0.725} \cdot \left[ \frac{2 \cdot \sigma}{\rho_f \cdot v_j^2 \cdot D} \right]^{1/3} \quad (2.42)$$

Monde and Katto (1978) [19] took Equation 2.42 and added a correction factor to incorporate the water subcooling:

$$\frac{q_{CHF}''}{\rho_g \cdot h_{fg} \cdot v_j} = 0.0745 \cdot \left( \frac{\rho_f}{\rho_g} \right)^{0.725} \cdot \left[ \frac{2 \cdot \sigma}{\rho_f \cdot v_j^2 \cdot D} \right]^{1/3} \cdot (1 + \varepsilon_{sub}) \quad (2.43a)$$

Where:

$$\varepsilon_{sub} = 2.7 \cdot \left( \frac{\rho_f}{\rho_g} \right)^{0.5} \cdot \left( \frac{C_{pf} \cdot \Delta T_{sub}}{h_{fg}} \right) \quad (2.43b)$$

Lienhard and Eichhorn (1979) [24] used dimensional analysis to derive the following general expression for CHF for a saturated jet:

$$q_{CHF}'' = f(\rho_f / \rho_g) \cdot \left( \frac{(D/d_j)^3}{We} \right)^{A(\rho_f / \rho_g)} \cdot \frac{1}{D/d_j} \quad (2.44a)$$

Where the functions A and f depend upon the density ratio and need to be determined.

The Weber number is the ratio of inertia to surface tension forces and is defined as:

$$We = \frac{\rho_f \cdot v_j^2 D}{\sigma} \quad (2.44b)$$

Lienhard and Hasan (1979) [25] gathered experimental data from Katto and Shimizu [26], Monde and Katto [19], and Katto and Monde [27]. Using their data they modified Lienhard and Eichhorn's equation (Equation 2.44) to get the following correlation. This is pertinent for a saturated jet at  $11 \text{ mm} \leq D \leq 21 \text{ mm}$ ,  $v_j \leq 60 \text{ m/s}$ , and  $6 \leq p_{\text{bar}} \leq 27.9 \text{ bar}$ .

$$\frac{q_{CHF}''}{\rho_g \cdot h_{fg} \cdot v_j} = f(\rho_f / \rho_g) \cdot \left[ \frac{\sigma}{\rho_f \cdot v_j^2 \cdot D} \right]^{A(\rho_f / \rho_g)} \cdot \left( \frac{D}{d_j} \right)^{3 \cdot A(\rho_f / \rho_g) - 1} \quad (2.45a)$$

Where:

$$f = \left( 0.744 + 0.0084 \cdot \frac{\rho_f}{\rho_g} \right) \quad (2.45b)$$

$$A = 0.4346 + 0.1027 \cdot \ln \left( \frac{\rho_f}{\rho_g} \right) - 0.0474 \cdot \left( \ln \left( \frac{\rho_f}{\rho_g} \right) \right)^2 + 0.00426 \cdot \left( \ln \left( \frac{\rho_f}{\rho_g} \right) \right)^3 \quad (2.45c)$$

Monde (1980) [28] performed similar experiments as Monde and Katto [19] for a saturated circular water jet on an electrically heated copper plate. The heater could provide a maximum heat flux of  $2 \times 10^7 \text{ W/m}^2$ . Experiments were performed at water

velocities ranging from  $0.3 \leq v_j \leq 15$  m/s, and a heater diameter versus jet diameter ratio between  $5 \leq D/d_j \leq 36.4$ . They modified Equation 2.42 derived earlier by Monde and Katto [19] and added on a factor to incorporate the  $D/d_j$  ratio at nozzle exit:

$$\frac{q_{CHF}''}{\rho_g \cdot h_{fg} \cdot v_j} = \frac{0.0601 \cdot \left(\frac{\rho_f}{\rho_g}\right)^{0.725} \cdot \left[\frac{2 \cdot \sigma}{\rho_f \cdot v_j^2 \cdot D}\right]^{1/3}}{1 + 0.00113 \cdot (D/d_j)^2} \quad (2.46)$$

Monde et. al (1982) [6], determined the CHF at water pressures ranging from 1 to 6 bars in the V-regime at jet velocities varying from 0.7 to 20 m/s. They modified Equation 2.42 to get:

$$\frac{q_{CHF}''}{\rho_g \cdot h_{fg} \cdot v_j} = 0.068 \cdot \left(\frac{\rho_f}{\rho_g}\right)^{0.725} \cdot \left[\frac{2 \cdot \sigma}{\rho_f \cdot v_j^2 \cdot D}\right]^{1/3} \cdot \left(1 + 7 \cdot \left(\frac{\rho_f}{\rho_g}\right)^{-1}\right) \quad (2.47)$$

Under the same conditions Monde et. al (1982) [6] also presented the following correlation for the CHF in the I-regime:

$$\frac{q_{CHF}''}{\rho_g \cdot h_{fg} \cdot v_j} = 2.02 \cdot \left(\frac{\rho_f}{\rho_g}\right)^{1/3} \cdot \left[\frac{\sigma}{\rho_f \cdot v_j^2 \cdot D}\right]^{1/2} \quad (2.48)$$

Monde (1985) [23] collected experimental data from other researchers such as Katto and Monde [27], Monde and Katto [19], and Monde [28]. They used dimensional analysis and least squares fit of the data to determine the constant 0.221 and the exponents in the following correlation. This is applicable for a broad range of conditions such as  $292 \leq \rho_f/\rho_g \leq 1603$ ,  $0.36 \leq v_j \leq 60$  m/s, and  $5 \leq D/d_{ji} \leq 57.1$  for a saturated water jet.

$$\frac{q_{CHF}''}{\rho_g \cdot h_{fg} \cdot v_j} = 0.221 \cdot \left(\frac{\rho_f}{\rho_g}\right)^{0.645} \cdot \left[\frac{2 \cdot \sigma}{\rho_f \cdot v_j^2 \cdot (D - d_{ji})}\right]^{-0.343} \cdot \left(1 + \frac{D}{d_{ji}}\right)^{-0.364} \quad (2.49)$$

Sharan and Lienhard (1985) [29] used experimental data from Monde and Katto [19], Katto and Monde [27], Katto and Shimizu [26], and Monde [28] to reformulate the circular jet CHF Equation 2.44 of Lienhard and Eichhorn (1979) [24]. This is applicable for a saturated jet at  $11 \text{ mm} \leq D \leq 21 \text{ mm}$ ,  $0.3 \leq v_j \leq 60 \text{ m/s}$ ,  $5 \leq D/d_j \leq 36.4$ , and  $6 \leq p_{\text{bar}} \leq 27.9 \text{ bar}$ .

$$\frac{q_{CHF}''}{\rho_g \cdot h_{fg} \cdot v_j} = f(\rho_f / \rho_g) \cdot \left[ \frac{1000 \cdot \sigma}{\rho_f \cdot v_j^2 \cdot D} \right]^{A(\rho_f / \rho_g)} \cdot \left( \frac{D}{d_j} \right)^{-1/3} \quad (2.50a)$$

Where the functions  $f$  and  $A$  were determined as:

$$f = \left( 0.21 + 0.00171 \cdot \frac{\rho_f}{\rho_g} \right) \quad (2.50b)$$

$$A = 0.486 + 0.06052 \cdot \ln \left( \frac{\rho_f}{\rho_g} \right) - 0.0378 \cdot \left( \ln \left( \frac{\rho_f}{\rho_g} \right) \right)^2 + 0.00362 \cdot \left( \ln \left( \frac{\rho_f}{\rho_g} \right) \right)^3 \quad (2.50c)$$

Later, Katto and Yokoya (1988) [30] formulated the following equation from experimental data from a variety of sources such as Monde [28], Katto and Monde [27], Monde and Katto [19], and Katto and Shimizu [26]. This applies to a saturated jet within the ranges of  $5.3 \leq p_f/p_g \leq 1603$ ,  $0.7 \leq d_j \leq 4.1 \text{ mm}$ ,  $0.3 \leq v_j \leq 60 \text{ m/s}$ ,  $10 \leq D \leq 60.1 \text{ mm}$ , and  $3.9 \leq D/d_j \leq 53.9$ :

$$\frac{q_{CHF}''}{\rho_g \cdot h_{fg} \cdot v_j} = \left( \frac{\rho_f}{\rho_g} \right) \cdot \left[ 0.0166 + 7 \cdot \left( \frac{\rho_f}{\rho_g} \right)^{-1.12} \right] \cdot \left[ \frac{\sigma}{\rho_f \cdot v_j^2 \cdot (D - d_j)} \right]^m \cdot \left( 1 + \frac{D}{d_j} \right)^{-m} \quad (2.51a)$$

Where,

$$m = 0.532 \cdot \left( \frac{\rho_f}{\rho_g} \right)^{-0.0794} \quad \text{for } \frac{\rho_f}{\rho_g} \leq 248 \quad (2.51b)$$

$$m = 0.374 \cdot \left( \frac{\rho_f}{\rho_g} \right)^{-0.0155} \quad \text{for } \frac{\rho_f}{\rho_g} \geq 248 \quad (2.51c)$$

All the CHF correlations provided above pertain to a saturated downward jet. Katto and Shimizu (1979) [26] analyzed the CHF for an upward facing jet impinging upon a copper block to get the following relation. This is applicable for within the ranges of  $6 \leq p_{\text{bar}} \leq 27.9$  bar,  $d_j = 2$  mm,  $v_j \leq 20$  m/s, and  $D = 10$  mm.

$$\frac{q_{CHF}''}{\rho_g \cdot h_{fg} \cdot v_j} = 0.188 \cdot \left( \frac{\rho_f}{\rho_g} \right)^{0.614} \cdot \left[ \frac{\sigma}{\rho_f \cdot v_j^2 \cdot D} \right]^{1/3} \quad (2.52)$$

Monde and Okuma (1985) [31] experimentally determined the CHF for a saturated upward jet in the L-regime. Experiments were performed at jet velocities ( $v_j$ ) ranging from 0.33 to 13.7 m/s and  $D/d_j$  ratio of 9.6 to 57.1,  $D$  of 40 mm and 60 mm, and  $d_j$  of 0.7 to 4.13 mm. They determined the CHF as:

$$\frac{q_{CHF}''}{\rho_g \cdot h_{fg} \cdot v_j} = \kappa \cdot \left( \frac{\rho_f}{\rho_g} \right) \cdot \left[ \frac{d_j}{D} \right]^2 \quad (2.53a)$$

Where  $\kappa$  is the ratio of the liquid consumed from evaporation on the surface to the liquid supplied by the jet.

$$\kappa = 25.7 \cdot \left( \frac{\rho_f}{\rho_g} \right)^{-0.674} \cdot \left[ \frac{g \cdot (\rho_f - \rho_g) \cdot d_j^2}{\sigma} \right]^{-0.62} \quad (2.53b)$$

### 2.3.4.1.2 Other CHF Correlations

There are other correlations derived by various researchers for a flat surface or flow within a tube. These will be presented here. Collier and Thome (1994) [20] provided the following generalized equation for the CHF in pool boiling of water on a flat surface:

$$q_{CHF}'' = 0.149 \cdot h_{fg} \cdot \rho_g^{0.5} \cdot [\sigma \cdot g \cdot (\rho_f - \rho_g)]^{0.25} \quad (2.54)$$

A modified form of Equation 2.54, see Collier and Thome [20], which incorporates the water subcooling is:

$$q_{CHF}'' = 0.149 \cdot h_{fg} \cdot \rho_g^{0.5} \cdot [\sigma \cdot g \cdot (\rho_f - \rho_g)]^{0.25} \cdot \left[ 1 + 0.1 \cdot \Delta T_{sub} \cdot \left( \frac{\rho_f}{\rho_g} \right)^{0.75} \cdot \left( \frac{C_{pf}}{h_{fg}} \right) \right] \quad (2.55)$$

Collier and Thome [20] gives the following relation for flow within a tube:

$$q_{CHF}'' = \frac{G \cdot D_{tube} \cdot h_{fg}}{4 \cdot L} \cdot \left[ 1 + \frac{C_{pf} \cdot \Delta T_{sub}}{h_{fg}} \right] \quad (2.56)$$

Where:

$$G = \rho_f \cdot v_{ji} \quad (2.57)$$

The Bowring correlation (1972) [20] expresses the CHF for flow within a tube as:

$$q_{CHF}'' = \frac{A' + D_{tube} \cdot G \cdot (\Delta h_{sub})_{inlet} / 4}{C' + L} \quad (2.58a)$$

Where,

$$A' = \frac{2.317 \cdot D_{tube} \cdot G \cdot h_{fg} \cdot F_1}{4 \cdot (1 + 0.0143 \cdot F_2 \cdot D_{tube}^{0.5} \cdot G)} \quad (2.58b)$$

$$C' = \frac{0.077 \cdot F_3 \cdot D_{tube} \cdot G}{1 + 0.347 \cdot F_4 \cdot \left( \frac{G}{1356} \right)^n} \quad (2.58c)$$

$$n = 2 - 0.00725 \cdot p_{bar} \quad (2.58d)$$

$F_1$ ,  $F_2$ ,  $F_3$ , and  $F_4$  are functions of the system pressure and are defined in the following table depending upon the water pressure.

**Table 2.1:  $F_1$ ,  $F_2$ ,  $F_3$ , and  $F_4$  functions for the Bowring correlation [20]**

Pressure in bar	$F_1$	$F_2$	$F_3$	$F_4$
1	0.478	1.782	0.4	0.0004
5	0.478	1.019	0.4	0.0053

### 2.3.5 Transition Boiling

Transition boiling occurs between points B and C in Figure 2.5. Otherwise known as partial film boiling, a vapour film or blanket forms on the surface due to rapid bubble formation (see Figure 2.9) [16]. The thermal conductivity of the vapor is less than that of the liquid and because of this the heat flux decreases with increasing excess temperature [17]. Transition boiling is the least understood of all the boiling regimes [2].

**Figure 2.9: Transition boiling [17]**

### 2.3.6 Film Boiling

Film boiling arises when the saturation temperature is at a minimum at point C in Figure 2.5. This is known as the Leidenfrost point. Here the surface is covered by a vapour blanket where heat conduction occurs as can be seen in Figure 2.10.

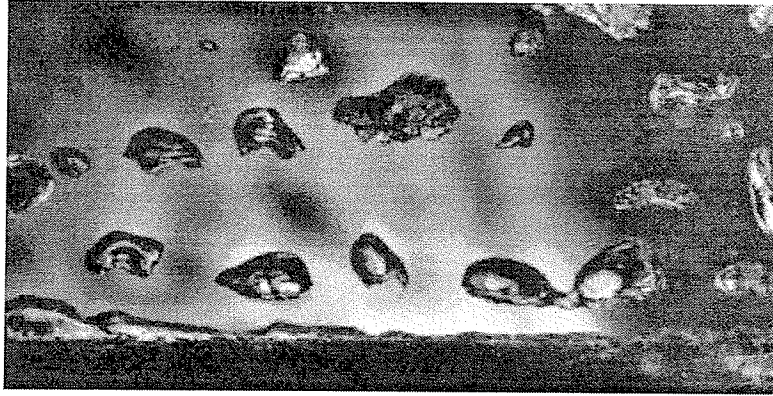


**Figure 2.10: Film boiling [17]**

The gas pressure from this vapour blanket prevents the rest of the water droplets from touching the plate. This layer thus protects the droplets from heat, which allows them to sit on top of the vapour layer for a while before it actually evaporates [32]. Heat transfer in this mode is dominated by conduction and convection through this vapour layer [20]. As the surface temperature increases radiation becomes the important form of heat transfer and the heat flux increases.

### **2.3.7 Modes of Heat Transfer During Impingement**

Figure 2.11 shows the different modes of heat transfer as they would occur with a planar jet on a stationary heated plate. Single-phase forced convection occurs in the stagnation region (Region I). As the liquid expands outwards symmetrically about the center of the jet, nucleate and transition boiling occur (Regions II). In Region III, film boiling occurs. In Region IV, due to surface tension effects, water agglomerates into pools, where convection and radiation occur. Some areas remain unwetted in this region and here radiation prevails. On the unwetted surface (region V in Figure 2.11), convection and radiation take heat away from the dry portion of the plate.

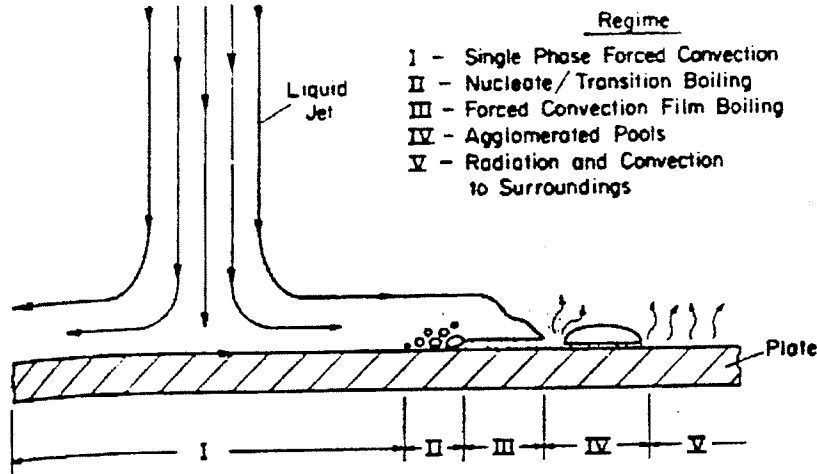
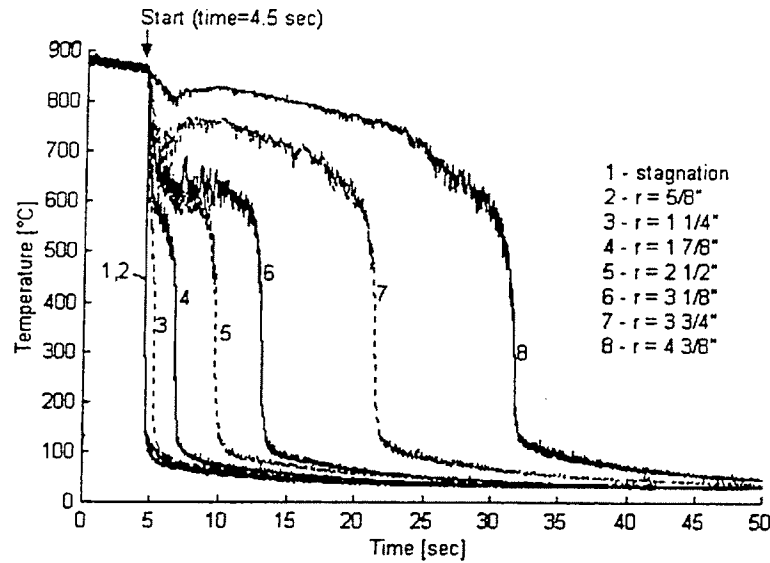


Figure 2.11: Heat transfer regimes for a stationary plate [2, 3, 7, 33, and 34]

### 2.3.8 Heat Transfer Within and Outside the Stagnation Region

Heat transfer in the stagnation region is the most widely researched topic in jet impingement heat transfer. The heat flux is highest at the stagnation point and the heat transfer downstream decreases radially from the stagnation point [35] [36].

Hauksson [3] studied heat transfer starting at the stagnation region out to a radial distance of  $4 \frac{3}{8}$  inches. Figure 2.12 shows his results of surface temperature varying with time. As it can be seen, the surface temperature dropped dramatically at the stagnation region. This cooling rate gradually decreased with increased radial distance from the center.



**Figure 2.12: Surface temperature curves for SS316 steel at a water temperature of 30°C and 30L/min flow rate [3]**

Wolf et. al [37] experimentally examined heat transfer in the stagnation region with a planar jet. They found that the heat transfer coefficient is constant in the stagnation region. Liu et. al [38] experimentally measured the heat transfer coefficient for a circular jet at the ROTC facility. They found a maximum heat transfer coefficient of  $34 \text{ kW}/(\text{m}^2 \text{ } ^\circ\text{C})$  in the stagnation region for an initial plate temperature of  $900^\circ\text{C}$ , 18.52 mm jet diameter, cooling water temperature of  $28^\circ\text{C}$ , and jet diameter of 30 mm, jet velocity of 6.52 m/s, and nozzle to plate distance of 15 cm.

### 2.3.9 Visual Representation of Heat Transfer

Liu et. al [39] studied jet impingement heat transfer at the ROTC facility for a circular jet. They video recorded the cooling process and saw that that the red hot steel surface at a temperature of around  $900^\circ\text{C}$  began to darken immediately in the stagnation region when the jet first hit the surface. Beyond the darkened region, the steel surface was still bright red even though water flowed over these areas. They could clearly see

vapour on the surface outside the darkened zone. They deduced that within the darkened area that a continuous or discontinuous vapour film should have formed on the surface initially for a very short time frame.

### **2.3.10 Wetting Zone**

Kokado et. al [40] defines the wetting zone as the effective forced water cooling region. In the non-wetting zone, the plate surface is exposed to a vapour film, which can be assumed to correspond to the film boiling area. Wetting occurs immediately within the stagnation region.

The rewetting temperature is otherwise known as the minimum film boiling temperature. This is where the transition occurs from a film boiling regime to when the liquid is in direct contact with a large portion of the surface [41]. Kokado et. al [40] defined the rewetting temperature as:

$$T_{wet} = 1150 - 8 * T_{water} \quad (2.59)$$

This applies only to a water temperature beyond 68°C; other conditions this applies to are not clearly stated.

## **2.4 Variables Affecting Jet Impingement Heat Transfer**

Jet impingement heat transfer is difficult to predict because it depends on many variables such as the effects of nozzle configuration, wall superheat, jet velocity, nozzle diameter, subcooling, nozzle-to-surface spacing, surface variations, and jet angle. Other research on intermittent jets, adding air bubbles to the jet, and moving plates and their effects on jet impingement heat transfer will also be summarized. It should be noted that since only trends are being examined, results pertaining to planar and circular jets will be discussed interchangeably.

### 2.4.1 Effect of Nozzle Configuration

Lee et. al [42] compared 3 different nozzle configurations and their effect on the Nusselt number in the cooling of an axisymmetric jet. These are square-edged, standard-edged, and sharp-edged orifices. They determined that sharp-edged nozzles provided the most effective heat transfer at the stagnation point than the other configurations at a Reynolds number of 30 000 as shown in Figure 2.13. The x-axis definition  $r/d$  stands for the radial distance divided by the jet diameter. The stagnation point is at  $r/d=0$ .

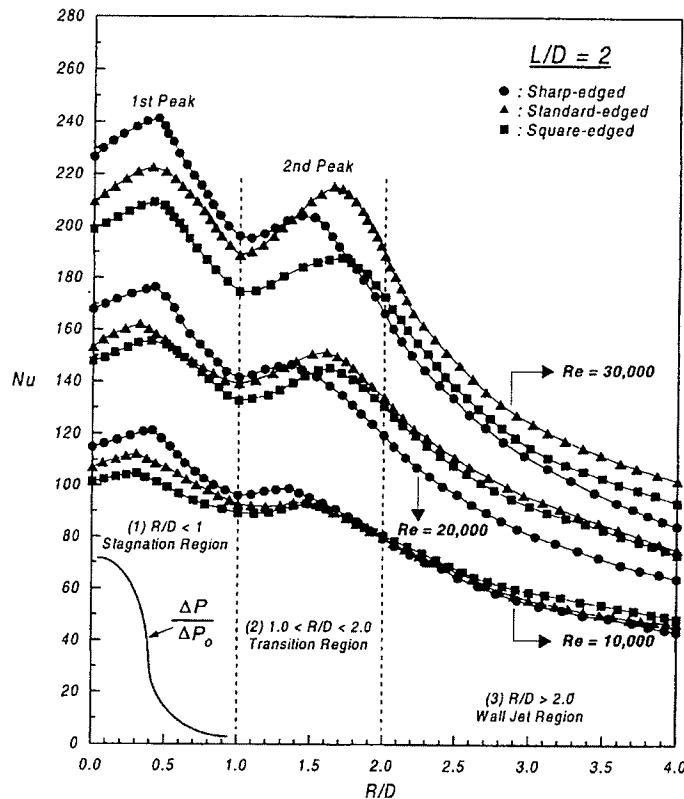


**Figure 2.13: The effects of nozzle configuration at different locations [42]**

Standard-edged was the second contender and square-edged was the least effective. However, in the wall jet region, which is at  $r/d > 2$ , standard-edged nozzles were most prominent, then square-edged, and sharp-edged.

### 2.4.2 Effect of Wall Superheat

As shown in Figure 2.5, the different modes of boiling heat transfer depend upon wall superheat. In the stagnation region, as the wall superheat is increased, the nucleate boiling heat flux increases. Many researchers [3, 6, 37, 43, and 44] support that heat transfer in the fully developed nucleate boiling region is affected by wall superheat only as discussed in Section 2.3.2.1.

### 2.4.3 Effect of Jet Velocity

Considerable research has been completed on the effects of jet velocity. Liu et. al [39] examined the effects of jet velocity at the ROTC facility. Figure 2.14 shows their graphical results for two different jet velocities. Test 10 in the figure had a jet impingement velocity of 6.52 m/s and test 13 had a velocity of 4.63 m/s. Outside the stagnation region, at a radial distance of 127 mm away from the center of the plate, they found that the cooling rate increased as the jet velocity increased.

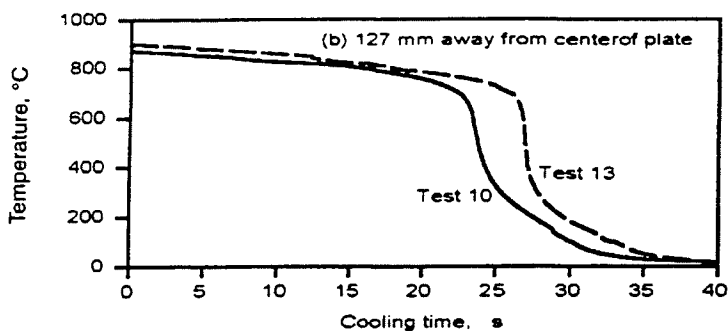


**Figure 2.14: Plate temperature cooling for jet velocities of 6.52 m/s (test 10) and 4.63 m/s (test 13) [39]**

Filipovic et. al [41] examined the outcome of varying the flow velocities on the spread of the rewetting front. As can be seen in Figure 2.15, increasing the flow velocity

increased the advancement of the rewetting front. In the figure, the wetting front speed is in mm/s. Jet velocities of 4, 3, and, 2 m/s were evaluated. Other researchers [2, 36, 39, and 45] reported similar results.

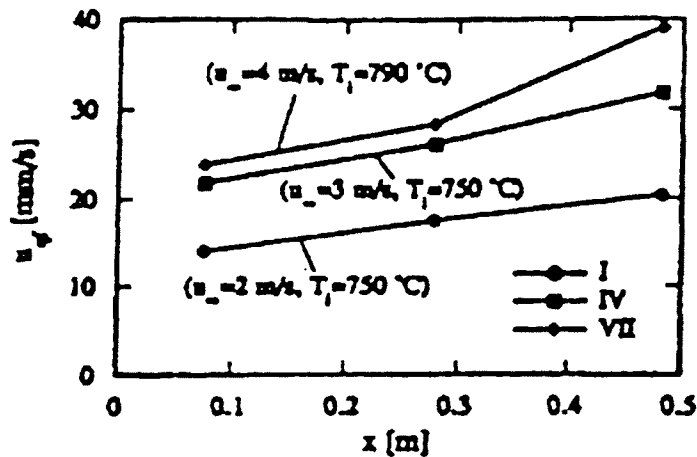
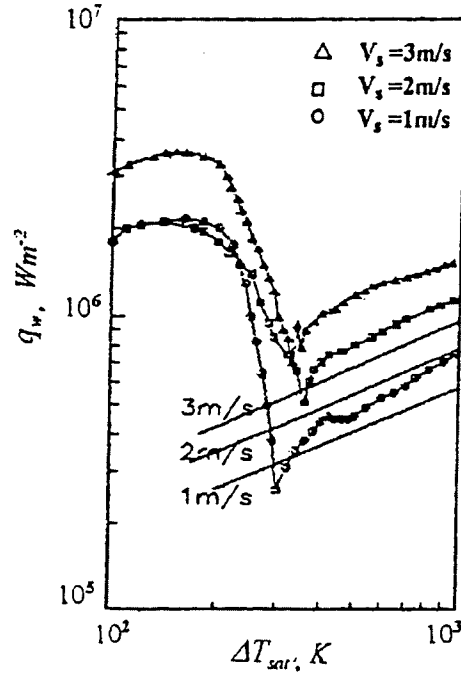


Figure 2.15: The effects of jet velocity on the rewetting front [41]

Liu and Wang [46] examined heat transfer of a circular jet in the stagnation region. The impinging velocity ranged from 1 to 3 m/s and liquid subcooling ranged from 5°C to 80°C. At a subcooling of 25°C and jet diameter of 10 mm, Figure 2.16 shows the effects of jet velocity on heat flux. It is shown that with increasing velocity, the critical heat flux and minimum heat flux increases along with increased heat transfer in the transition and film boiling regimes.



**Figure 2.16: The effect of jet velocity on heat flux [46]**

Ishigai et. al [47] studied the heat flux for a planar jet at an initial plate temperature of  $1000^\circ\text{C}$ . Figure 2.17 shows the heat flux as a function of wall superheat and jet velocity. For subcoolings of  $15^\circ\text{C}$ , the critical and minimum heat flux increased as well as increased heat flux with jet velocity in the transition and film boiling regimes. At higher subcoolings, the heat transfer curve was shifted to the left and therefore, film boiling did not occur. At higher subcoolings and jet velocity, a shoulder appeared in the transition regime where the heat flux remained constant.

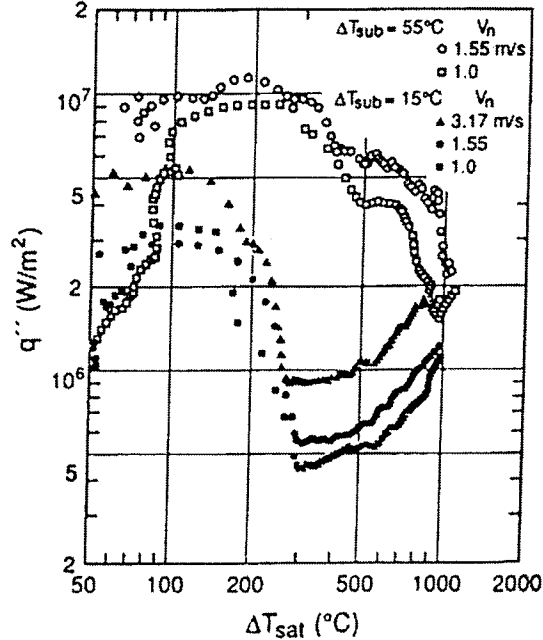


**Figure 2.17: The influence of jet velocity on heat flux [47]**

Kumagai et. al [35] performed planar jet impingement experiments to measure the transient heat flux as far as 56 jet widths from the stagnation region. As can be observed in Figure 2.18, they determined that increasing the jet velocity increased the critical heat flux. This was most pronounced in the stagnation region at  $L = 0$  mm and the level of influence of varying jet velocity decreased radially outwards. Monde et. al [48] experimentally determined the effects of jet velocity for an upward facing circular jet. They also determined that increasing the jet velocity increases the critical heat flux.

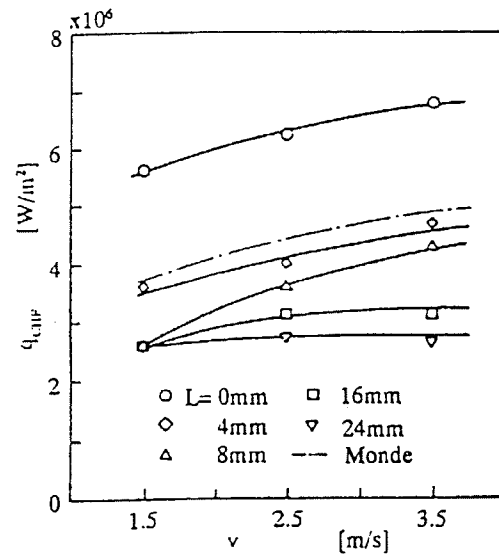


**Figure 2.18: The effect of jet velocity on the CHF [35]**

Robidou et. al [44] experimentally ascertained the effects of jet velocity for a planar jet on a copper plate. Heat flux was measured for jet velocities between 1.8 m/s and 4.5 m/s and subcoolings from 40°C to 70°C. Like Kumagai et. al [35], they discovered that the critical heat flux increased proportionally with jet velocity within the stagnation region. They also found that in the transition boiling regime, the heat fluxes shifted upwards with increasing jet velocity.

Figure 2.17 also shows that at lower subcoolings, that the film boiling heat flux increased with jet velocity. Filipovic et. al [8] completed experiments for a planar jet in the film boiling regime. They determined that within the stagnation region, the convection heat transfer coefficient increased with proportionally with jet velocity. Wolf et. al [37] studied single-phase convection heat transfer coefficient in the same region for a planar jet. Like Filipovic et. al [8], they found that the heat transfer coefficient increased proportionally with jet velocity within the stagnation region.

#### **2.4.4 Effect of Nozzle Diameter**

Many experiments on jet impingement heat transfer were performed at the ROTC facility [2, 3, and 38]. Their investigations concluded that in the stagnation region the heat transfer coefficient, hence the heat flux, increases with increasing nozzle diameter. This is because the size of the stagnation region depends upon the size of the jet. The larger the jet, the larger the stagnation region is, which increases heat transfer. Womac et. al. support these results [49].

Stevens and Webb [15] examined the effects of nozzle diameter on single-phase convection heat transfer within the stagnation region. With nozzle diameters ranging from 2.2 mm to 8.9 mm, they found that the stagnation region Nusselt number increased with increasing nozzle diameter. An increase in Nusselt number indicates an increase in heat transfer coefficient, which hence increases the heat flux.

#### **2.4.5 Effect of Subcooling**

Like jet velocity, the effects of subcooling on jet impingement heat transfer has been studied substantially. Subcooling is defined as the liquid saturation temperature minus the actual liquid temperature. Therefore, the lower the liquid temperature, the higher the subcooling is.

Liu et. al [39] performed circular jet experiments at the ROTC facility. As shown in Figure 2.19, the level of subcooling did not seem to affect heat transfer in the stagnation region. Test 10 was at a water temperature of 13°C and test 11 was at a lower subcooling, with a water temperature of 30°C. This applies to an initial steel plate temperature of 900°C, jet diameter of 18.92 mm, nozzle to plate distance of 1500 mm,

and jet velocity of 6.52 m/s. Earlier experiments performed by Liu et. al [38] at the same facility found similar results.

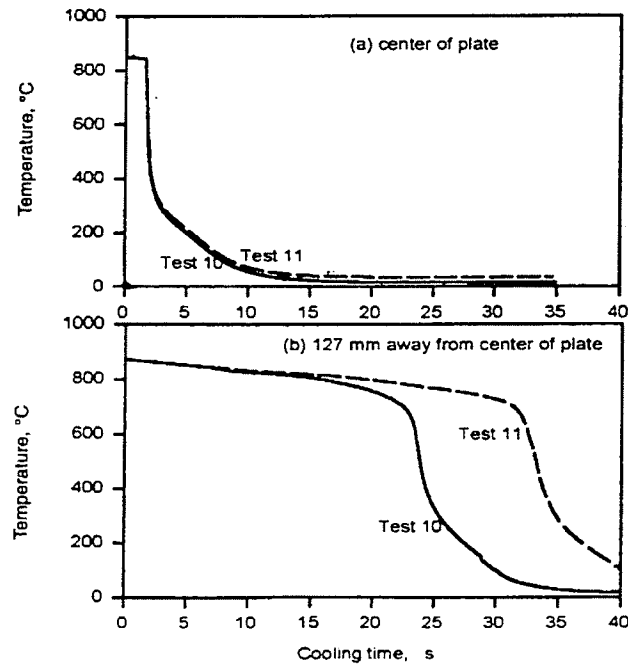


**Figure 2.19: Surface temperature graphs at water temperatures of 13°C (test 10) and 30°C (test 11) [39]**

However, outside the impingement region, Liu et. al [39] (see Figure 2.19), and Liu et. al [38] found that increasing the subcooling increases the heat flux. Other researchers support these results [35, 40, and 47]. Kumagai et. al [35] and Robidou et. al [44] added that the effects of subcooling on the heat flux was most pronounced within the stagnation region and was less influenced as the jet expanded radially outwards. Like jet velocity, varying the subcooling does not affect heat transfer in the fully developed nucleate boiling regime.

Figure 2.20 shows the heat flux for a planar jet at subcoolings evaluated between 5°C to 55°C at a jet velocity of 2.1 m/s, which shows the proportional relationship between subcooling and heat flux. As occurred in Figure 2.17, a shoulder appeared in the

transition boiling regime in Figure 2.20 when the subcooling was 25°C and higher. As the subcooling increased, the width of the shoulder expanded. It can also be seen that with higher subcoolings, the boiling curve shifted to higher superheats. Additionally, at subcoolings greater than 25°C, film boiling did not occur.

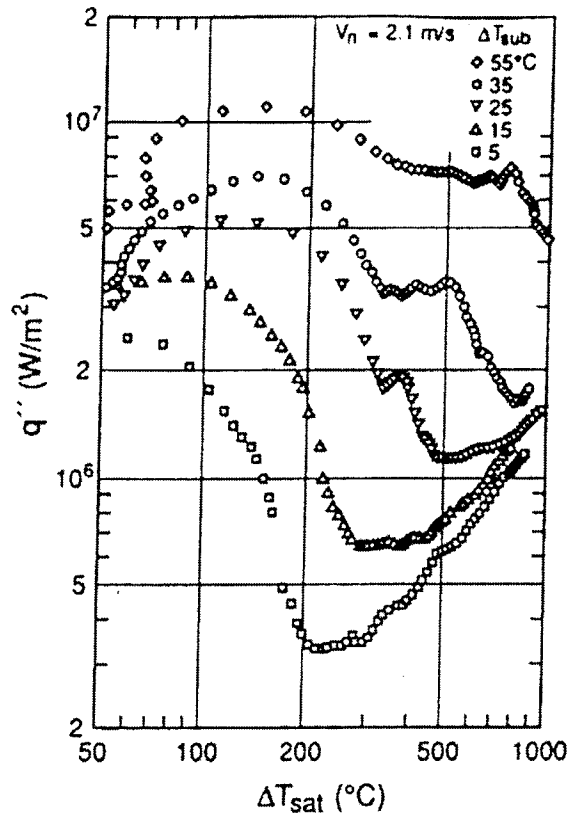


**Figure 2.20: The effect of subcooling on heat flux [47]**

Ochi et. al [36] performed similar experiments as Ishigai et. al [47] with a circular jet in the stagnation region. Their trends with subcooling closely resembled those in Figure 2.20. Figure 2.20 also shows that the critical heat flux increased with increased subcoolings. Other researchers [35, 36, 43, 44, and 48] also determined that the CHF increases with increasing subcooling temperatures.

Figure 2.20 also demonstrates that the minimum heat flux increases with subcooling (at lower subcoolings). Ishigai et. al [47] provided the following correlation for a planar jet, which reveals the influence of subcooling and jet velocity on the minimum heat flux. As it can be seen, as the subcooling and jet velocity increases, the minimum heat flux increases.

$$q_{\min}'' = 5.4 \times 10^4 \cdot v_j^{0.607} \cdot (1 + 0.527 \cdot \Delta T_{\text{sub}}) \quad (2.60)$$

#### 2.4.6 Effect of Nozzle-to-Surface Spacing

Wolf et. al [6] reviewed papers on jet impingement and all the ones examined reported that nozzle-to-plate spacings had little effect on the heat transfer within the stagnation region. Only spacings less than 5 mm were examined.

However, Stevens and Webb [15] found contradictory results. At a  $Z/d_{ji}$  range of 1.7 to 6.7, they found that there was a slight decrease in the Nusselt number for single-phase forced convection within the stagnation region.

Robidou et. al [44], on the other hand, determined that the effect of increasing the spacing increases the jet velocity due to gravitational acceleration. Hence as the distance is increased, the velocity increases, and heat transfer increases correspondingly. However, they interchangeably talked about free surface and immersed jets and did not make it clear which conditions, such as type of jet, nozzle to plate spacings, subcoolings, jet velocities, temperatures, etc. this applies to.

All the research above examined heat transfer at relatively small spacings and low height to diameter ratios. Therefore, more research needs to be performed by at a larger range of spacings, say up to 1.5 m, with higher  $Z/d_{ji}$  ratios, say over 100, to determine which is most accurate.

### 2.4.7 Effect of Surface Variations

Variations in surface roughness and oxidation can alter the heat transfer in jet impingement. Figure 2.21 provided by Chowdhury and Winterton [50], shows the heat flux versus surface roughnesses ranging from 0.25 to 4.75  $\mu\text{m}$ . They found that increasing the surface roughness provides better heat transfer in the stagnation region for nucleate boiling at a given wall superheat [50]. Gabour and Lienhard [51] also support these results. It can also be seen that surface roughness has little influence on heat transfer in the transition boiling region.

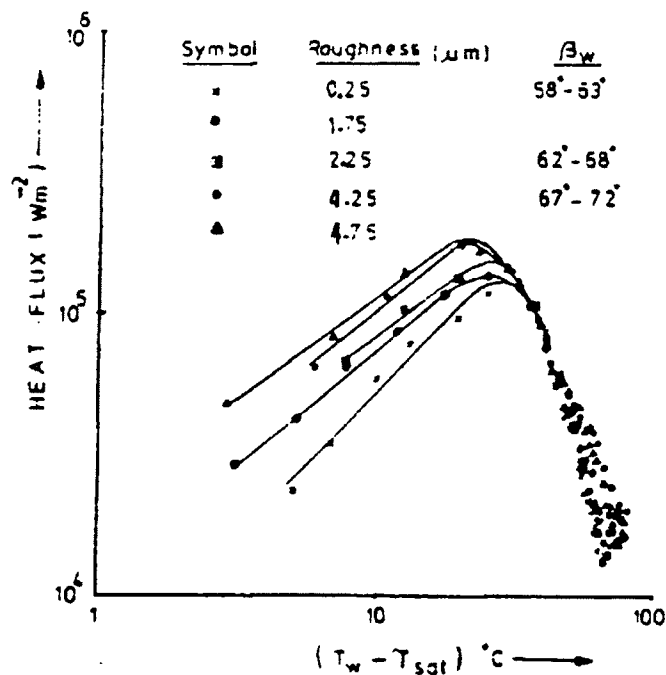


**Figure 2.21: The effect of surface roughness on heat flux in the stagnation region [50]**

Like surface roughness, Pan et. al [52] reported that surface oxidation increases the transition boiling heat flux. Therefore, while performing experiments, it is important to ensure that the test surface is smooth and free from oxidation so results will not be deviated. To do so, the plate needs to be cleaned before testing.

### 2.4.8 Effect of Jet Angle

Recently, Tong [53] experimentally studied heat transfer of an oblique planar jet. They evaluated the Nusselt number at inclination angles of 45°, 60°, 75°, and 90°, as displayed in Figure 2.22.

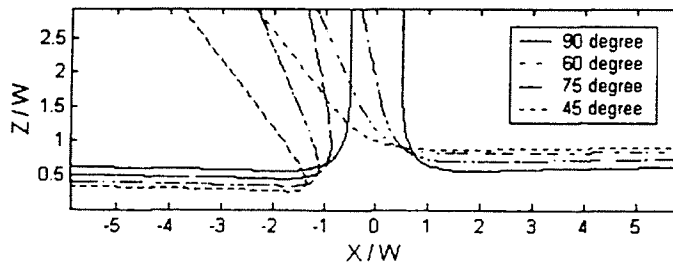


**Figure 2.22: Inclination angles tested by Tong [53]**

Figure 2.23 shows their results.  $X/W$  stands for the distance from the jet center divided by the jet width. They discovered that the Nusselt number increased as the angle decreased, where it was greatest at 45 degrees. It can also be seen in the figure that the peak Nusselt number shifted further upstream from the stagnation point compared to the perpendicular jet, where the Nusselt number was greatest at the center of the jet. These results apply to a Reynolds number of 10,000 and a uniform jet.

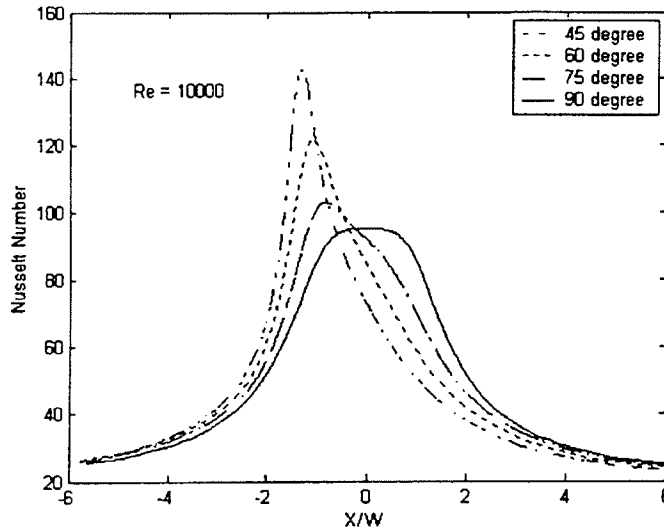


**Figure 2.23: The effect of jet inclination angle on Nusselt number [53]**

#### 2.4.9 Effect of an Intermittent Jet

Zumbrunnen and Aziz [54] determined the convective heat transfer of a planar intermittent jet, which can be regarded as a pulsating flow. They evaluated the Nusselt number at intermittent frequencies ranging from 30 hz to 130 hz, a Reynolds number of 9,450, and Prandtl number of 5.6.

At these conditions, they found that at intermittent frequencies below 94 hz, local Nusselt numbers were lower than that for a steady jet. However, at sufficiently high frequencies above 94 hz resulted in Nusselt numbers greater than that for a steady jet. At the highest frequency of 130 hz, Nusselt numbers exceeded values for a steady jet by two times.

On the contrary at higher velocities, with a Reynolds number of 16,000 and Prandtl number of 5.8, the Nusselt number in the stagnation region was lower with respect to a steady jet. They did not provide a clear explanation as to why this occurred.

Clearly, more research in this area needs to be performed to determine in which conditions using an intermittent jet could increase heat transfer.

#### **2.4.10 Effect of Adding Air Bubbles to the Jet**

Hall et. al [55] observed the heat transfer of a two-phase (water-air) jet. Compressed air is supplied to the nozzle. They evaluated the stagnation heat flux at void fractions ranging from 0 (single-phase liquid jet) to 0.3, constant jet velocity of 3 m/s, and subcooling of 75°C. The void fraction  $\alpha$  is defined as the ratio of the volumetric flow rates of the air and water:

$$\alpha = \frac{Q_{air}}{Q_{air} + Q_{water}} \quad (2.61)$$

Where Q standards for the volumetric flow rate. They provided Figure 2.24 to demonstrate the change in heat flux with respect to the void fraction  $\alpha$ . In the single phase convection boiling regime, the heat flux increased with increasing void fraction. However, varying the void fraction had no effects on critical heat flux and the heat flux in the nucleate boiling regime.

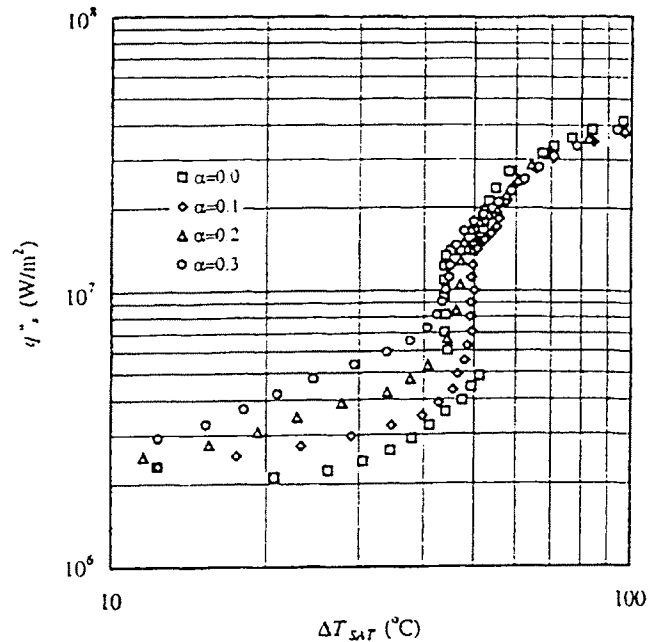


**Figure 2.24: The effect of adding air bubbles to a water jet on heat flux [55]**

One downfall of adding air bubbles to the jet is the water pumping power has to be increased to maintain the same liquid flow rate. However, alternate methods of bubble injection, such as extending capillary tubes into the jet at the nozzle jet, could be used.

### 2.5 Water Jet Impingement on a Moving Plate

The hydrodynamics and heat transfer are different for jet impingement if the plate were moving. In Figure 2.11, if the plate moves to the right, viscous forces close to the plate's surface increase the jet velocity to the right of the stagnation point (downstream). The opposite occurs upstream to the left of the stagnation point and the flow is decreased due to the plate motion [56]. Compared to a stationary plate, on the downstream side to the right of the stagnation zone, the vapour layer in regions III and IV would be stretched by the plate motion and the thickness would decrease. On the contrary, to the left of the

stagnation region on the upstream side, the vapour layer (in III and IV) would thicken because it is pulled toward the stagnation region by the movement of the plate [34].

Therefore, compared to stationary plates, in general, various researchers [4, 5, 34, 56, 57, 58, 59, 60, 61, and 62] speculate that increasing the plate motion promotes heat transfer on the downstream side due to the decreased vapour layer. This is especially so when the plate motion exceeds the jet velocity [5 and 34]. On the upstream side, heat transfer is reduced as a result of the thickened vapour layer.

All research so far has focused on the right side of the stagnation point if the plate is moving to the right (downstream side) in Figure 2.11. This is so because it is easier to study in detail. In the upstream direction, the fluid is entrained by the plate motion, making it much more difficult to perform an analysis. The experimental research reviewed had relatively slow plate speeds ranging from 0.008-0.83 m/s at values lower than the jet velocity [7, 60, and 63]. In an actual steel mill, the average plate speed is 10 m/s. Thus the speeds analyzed do not accurately represent what would actually happen in steel mill conditions. Consequently, their results would not correctly predict heat transfer with a moving plate in a mill.

### **3. Experimental Apparatus and Procedure**

Hauksson (2001) [3] and Meng (2002) [2] performed experiments on jet impingement heat transfer at the ROTC (run out table cooling) facility of the Advanced Materials Process Engineering Laboratories (AMPEL) in the Brimacombe building at the University of British Columbia. The boiling heat transfer of cooling a hot stationary steel plate with one downward facing circular water jet was analyzed. Various water temperatures ranging from 30°C to 95°C and flow rates ranging from 15 l/min to 45 l/min were used to determine the variation in their effects.

This thesis takes their experimental heat flux results and compares them with correlations provided by other researchers within the single-phase forced convection, nucleate boiling, two-phase forced convection, and CHF regimes. Here the apparatus and experimental procedure used will be discussed.

#### **3.1 ROTC Facility Apparatus**

The apparatus consists of an industrial scale run out cooling table that simulates cooling conditions which occur in an actual steel mill. A basic layout of the facility is depicted in Figure 3.1. An electric heating 22” wide by 50.5” long by 28” deep furnace (20 kW, 208 V, 3 phase, 92 amps) is used to heat up the steel plate. It is equipped with a nitrogen gas-filled pocket which was 19” x 48” x 5”. This pocket allows the specimen to be heated in an inert nitrogen environment to help prevent oxidation.

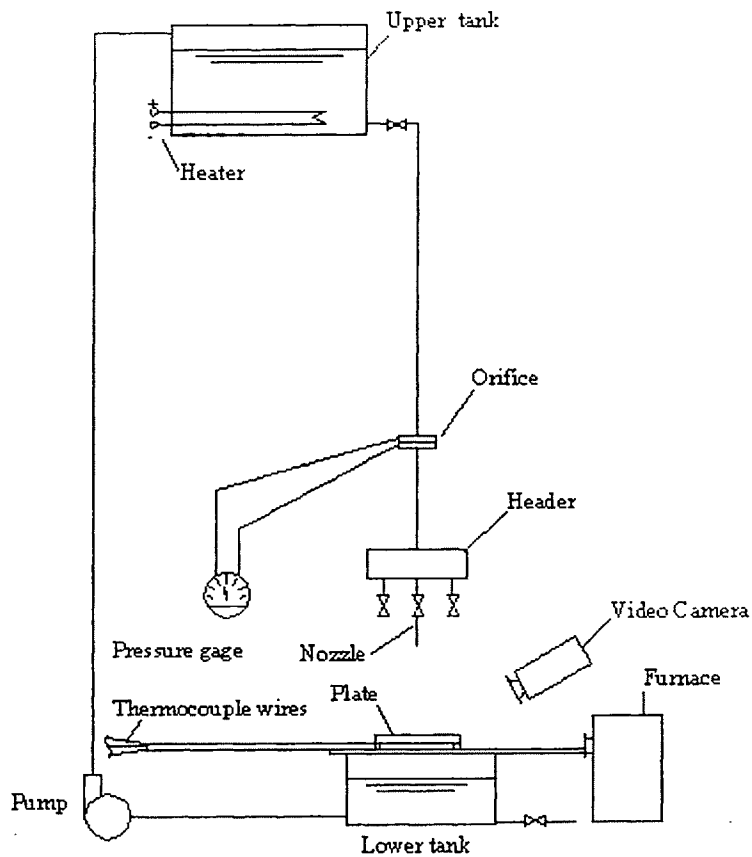


**Figure 3.1: ROTC facility apparatus**

A containment water tank (1.5 x 1.5 x 1 m) on the floor beneath the plate, which has an 8 kW heater, collects and heats the water used during each test. A float switch operated pump pushes the water up a 6.5 m high tower to the overhead primary water tank (1.5 x 1.5 x 1 m) that can hold up to 1350 litres of water. The water in the overhead tank contains a 30 kW heater to heat the water up to 95°C.

A header below the upper tank holds three circular water jets with spacings adjustable between 50 to 90 mm. This header can be placed 0.6 to 2 m above the plate. A valve below the header controls the water flow rate. An S-shaped tube connected (not

shown in the diagram) to the piping diverts the cooling water away from the plate until fully developed uniform flow develops, where it is then removed and the test begins.

### 3.2 Test Sample

Experiments performed at water temperatures up to and including 50°C used a steel plate with dimensions of 280 x 280 x 10 mm. For water temperatures ranging from 60°C to 95°C, a 280 x 280 x 7.6 mm plate was used.

#### 3.2.1 Chemical Composition

Experiments performed at water temperatures up to 50°C used SS316 and DQSK (Drawing Quality Special Killed) carbon steel plates in the as-rolled condition. Experiments ranging from 60°C to 95°C used DQSK plates. The chemical compositions of these materials are shown in Table 3.1.

**Table 3.1: Chemical composition of the steel alloys used in weight %**

<b>Alloy</b>	<b>C</b>	<b>Mn</b>	<b>P</b>	<b>S</b>	<b>Si</b>	<b>Al</b>	<b>Cr</b>	<b>Ni</b>	<b>Mo</b>	<b>N</b>
DQSK	0.06	0.24	0.005	0.011	0.006	0.041				0.0035
SS316	0.06	1.86					19.2	11.3	2.67	

For the analyses for this thesis, only data from DQSK steel plates was examined

#### 3.2.2 Thermo-physical Properties

The properties of AISI 1008 steel were used to represent the DQSK steel. Linear regression was used to get the following correlation for the thermal conductivity of AISI 1008 steel:

$$k_s = 60.571 - 0.03849 \cdot T_{surf} \text{ W / (m } ^\circ\text{C)}$$

Other properties for AISI 1008 steel are:

$$\text{Density: } \rho_s = 7,800 \text{ kg / m}^3$$

$$\text{Specific heat: } C_{ps} = 470 \text{ J / (kg } ^\circ\text{C)}$$

The properties for SS316 used in the data processing are:

$$k_s = 10.717 + 0.014955 \cdot T_{surf} \quad \text{for } T_{surf} < 780 \text{ } ^\circ\text{C}$$

$$k_s = 12.076 + 0.013273 \cdot T_{surf} \quad \text{for } 780 < T_{surf} < 1,672 \text{ } ^\circ\text{C}$$

$$\rho_s = 7,865 \text{ kg / m}^3$$

$$C_{ps} = 460 \text{ J / (kg } ^\circ\text{C)}$$

### 3.3 Thermocouples

Type K chromel-alumel thermocouples (Omega 304-K-Mo-1.5 mm) were used to measure the temperature of the inside and surface of the steel plate during the tests. They can tolerate temperatures up to 1250°C, which is within the range of the temperatures occurring during the analysis.

Due to their faster response, intrinsic thermocouples were used for all of the experiments. This is where the leads are welded to the plate surface very close together, but not touching. However, the thermocouple leads protrude out of the plate. They can in turn act as fins that conduct heat. This reduces the temperature at the base of the thermocouple where it is connected to the plate. Some researchers have examined the effects of this thermocouple conduction error. A literature review describing their findings is available in Appendix A.

### 3.3.1 Thermocouple Installation

8 thermocouple pairs were attached to the plate. Each pair consisted of a surface thermocouple and an internal thermocouple attached within the plate. Figure 3.2 shows the setup of the paired thermocouples. They were placed 1/8" apart. If the wires come into contact with each other or the plate, a premature connection occurs and gives an inaccurate measurement. To prevent this, alumina insulation encompassed the wires. Having thermocouples placed at varying depths allows the temperature gradient through the plate to be calculated which in turn was used to calculate the heat flux.

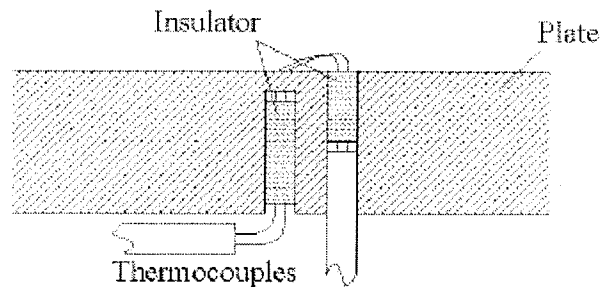


**Figure 3.2: Thermocouple pair installation**

Each of the pairs were distributed at locations starting at the center of the plate to radial distances distributed 5/8" increments apart. They were staggered to compensate for small flow disturbances that could occur if they are not installed precisely or if they move during the test. Figure 3.3 shows the thermocouple layout used for water temperatures up to 50°C. The 'r' variable signifies the radial distance from the center in inches.

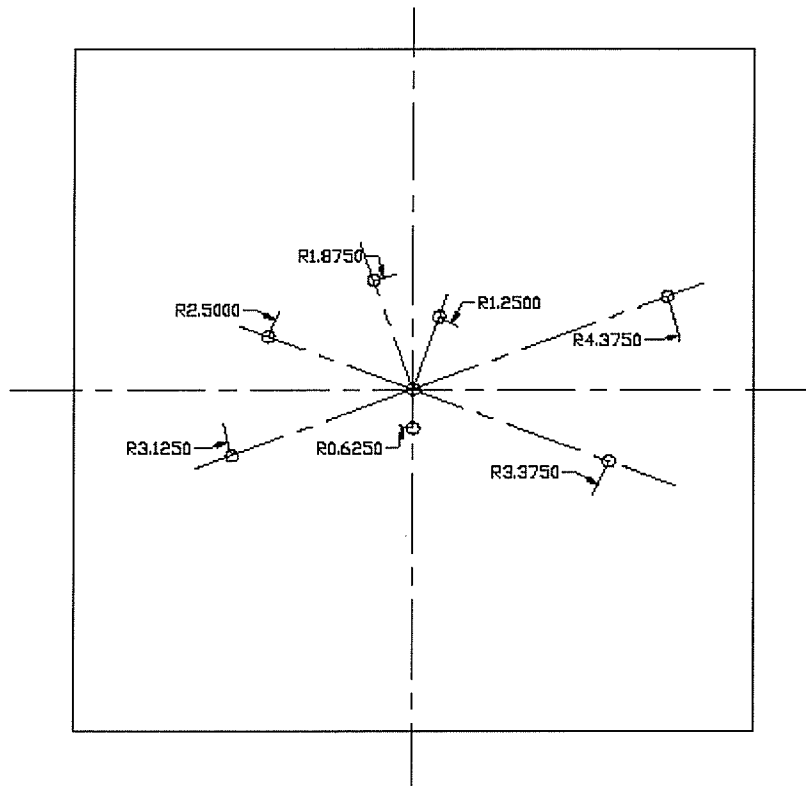


**Figure 3.3: Thermocouple layout at water temperatures up to 50°C**

For experiments consisting of water temperatures of 60°C to 95°C, the same radial increments were used with a slightly different layout, as shown in Figure 3.4. The ‘r’ values represent the radial distances in mm.

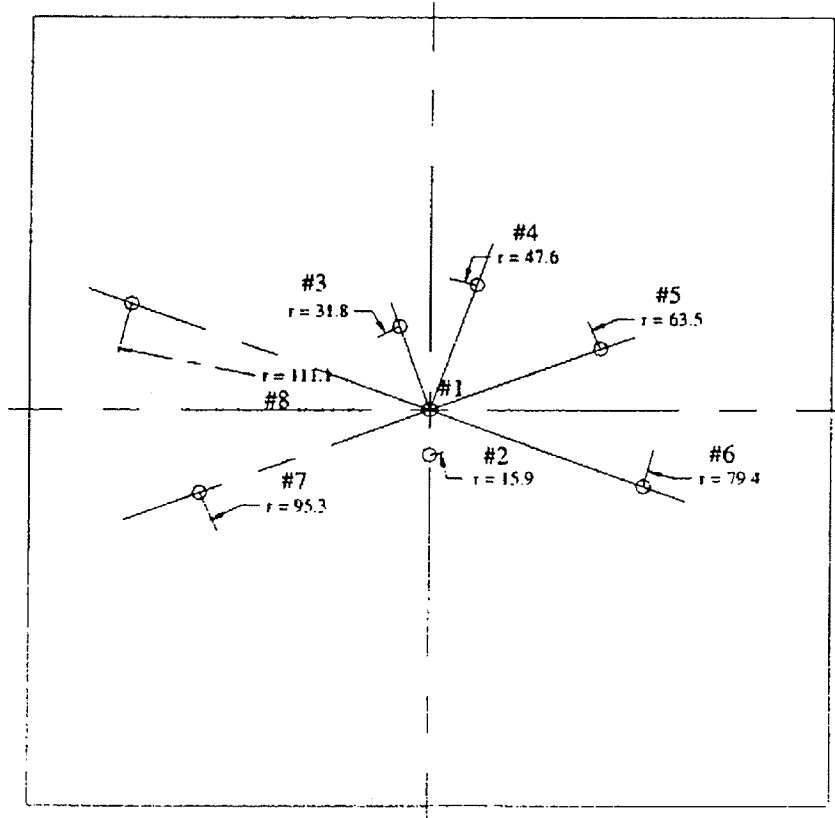


**Figure 3.4: Thermocouple layout at water temperatures of 60°C to 95°C**

The locations of the thermocouples in radial distance from the center of the plate are listed in Table 3.2.

**Table 3.2: Thermocouple Locations**

Location	r	r
1	0	0
2	5/8"	15.9 mm
3	1 1/4"	31.8 mm
4	1 7/8"	47.6 mm
5	2 1/2"	63.5 mm
6	3 1/8"	79.4 mm
7	3 3/4"	95.3 mm
8	4 3/8"	111.1 mm

The thermocouples were connected to a data acquisition system via a steel pipe attached to the bottom of the plate, converting the resistance between the wires to a

voltage that represents the temperature read. The pipe is also used as a handle allowing greater ease in moving the specimen to and from the furnace. Figure 3.5 shows a schematic view of the plate with the thermocouples.

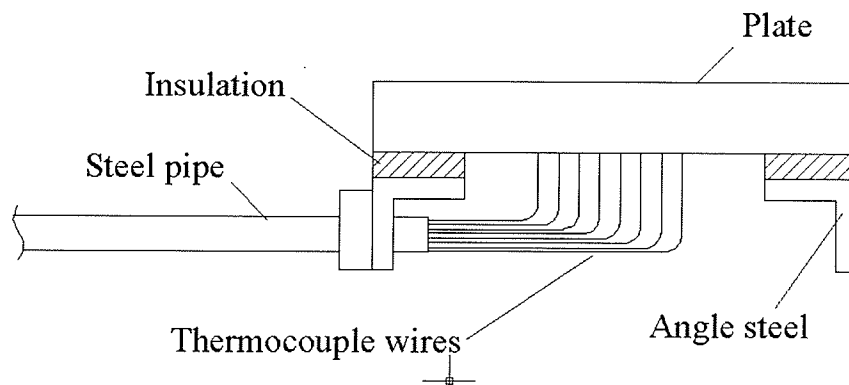


**Figure 3.5: Schematic view of test plate setup**

### 3.4 Experimental Procedure

One 19 mm diameter nozzle was used for cooling. After the apparatus and thermocouples were set up, the test was performed. It took approximately 3 hours to heat the steel plate up to 900°C in a nitrogen gas environment to prevent oxidation. The plate was heated to a temperature above the preferred test temperature because it cooled down while it was being positioned directly under the nozzle.

It took approximately 10-15 seconds to take the specimen out of the surface and position it correctly beneath the jet. Radiation and convection occurred during this process, cooling the plate slightly. However, this cooling was relatively slow when compared to the conductive heat transfer that would occur during the actual test. For that reason, it was unnecessary to consider heat losses before jet impingement.

Just before the water was turned on, the plate was cleaned with methanol to minimize the effects of surface impurities. Then the water flow valve was opened. At

first, the S shaped pipe diverted the water away from the plate until fully developed flow was initiated, where it was then removed. Data recordings, which began when the plate was removed from the furnace, were stopped when the plate cooled to the initial water temperature. A video camera was used to record the entire test.

#### 4. Test Conditions, Selection, and Observations

This section presents the experimental conditions of the experiments. As well, there is always the possibility of experimental error. All data from the tests was analyzed and it was determined which tests should be excluded from all the analyses due to experimental error. Additionally observations made of the experimental data will be presented. Other observations presented by Hauksson [3] and Meng [2], who performed the experiments, are contained in Appendix B.

##### 4.1 Experimental Conditions

Experiments were performed at the ROTC facility at water temperatures of 30°C, 40°C, 50°C, 60°C, 70°C, 80°C and 95°C. Flow rates of 15 l/min, 30 l/min, and 45 l/min, were tested at each of the water temperatures. This paper compares various correlations with this data within the stagnation region. Only those experiments for a DQSK steel plate will be considered. All tests were performed at an initial plate temperature of 900°C. Jet velocities, jet diameters, saturation temperature, and pressure depend upon the flow rate used.

Table 4.1 summarizes the tests performed and their corresponding conditions. Each test name is coded in a manner that indicates the researcher that performed the experiment, and the water temperature and flow rate used. The first letter signifies the researcher. An 'M' signifies Meng and an 'H' signifies Hauksson. The next two numbers signify the water temperature. The last two numbers signify the flow rate. For instance test 'H3015' indicates Hausson performed this experiment at a water temperature of 30°C and flow rate of 15 l/min. Or 'M6045' indicates that Meng

Table 4.1: Test Conditions

Test Name	Initial Water Temperature (°C)	Flow rate (l/min)	$v_{ji}$ (m/s)	$v_j$ (m/s)	$d_{ji}$ (mm)	$d_j$ (mm)	$T_{sat}$ (°C)	$P_{bar}$ (bar)	Researcher That Performed the Test
H3015	30	15	5.5	0.9	7.6	19	103.6	1.164	Hauksson [3]
H3030	30	30	5.7	1.8	10.6	19	103.9	1.173	Hauksson [3]
H3045	30	45	6	2.6	12.6	19	104.4	1.195	Hauksson [3]
H4015	40	15	5.5	0.9	7.6	19	103.6	1.164	Hauksson [3]
H4030	40	30	5.7	1.8	10.6	19	103.9	1.173	Hauksson [3]
H4045	40	45	6	2.6	12.6	19	104.4	1.195	Hauksson [3]
H5015	50	15	5.5	0.9	7.6	19	103.6	1.164	Hauksson [3]
H5030	50	30	5.7	1.8	10.6	19	103.9	1.173	Hauksson [3]
H5045	50	45	6	2.6	12.6	19	104.4	1.195	Hauksson [3]
M6015	60	15	5.5	0.9	7.6	19	103.6	1.164	Meng [2]
M6030	60	30	5.7	1.8	10.6	19	103.9	1.173	Meng [2]
M6045	60	45	6	2.6	12.6	19	104.4	1.195	Meng [2]
M7015	70	15	5.5	0.9	7.6	19	103.6	1.164	Meng [2]
M7030	70	30	5.7	1.8	10.6	19	103.9	1.173	Meng [2]
M7045	70	45	6	2.6	12.6	19	104.4	1.195	Meng [2]
M8015	80	15	5.5	0.9	7.6	19	103.6	1.164	Meng [2]
M8030	80	30	5.7	1.8	10.6	19	103.9	1.173	Meng [2]
M8045	80	45	6	2.6	12.6	19	104.4	1.195	Meng [2]
M9515	95	15	5.5	0.9	7.6	19	103.6	1.164	Meng [2]
M9530	95	30	5.7	1.8	10.6	19	103.9	1.173	Meng [2]
M9545	95	45	6	2.6	12.6	19	104.4	1.195	Meng [2]

performed the test at a water temperature of 60°C and a flow rate of 45 l/min and so forth.

#### 4.2 Calculating the Heat Flux

Temperature readings from each thermocouples pair (surface and internal), as described in Section 3.3.1, were used to calculate the temperature gradient through the plate. By knowing the temperatures at the surface and within the plate, Taylor's second order expansion was used to determine the temperature gradient ( $dT/dx$ ) as:

$$\frac{dT}{dx} \cong \frac{3 \cdot T_{surf} - 4 \cdot T_2 + T_3}{2 \cdot \Delta x} \quad (4.1)$$

Where  $T_2$  and  $T_3$  denote the calculated depths inside the plate at  $\Delta x$  and  $2\Delta x$  respectively.

$T_2$  and  $T_3$  were calculated using the Crank-Nicolson finite difference method:

$$T_n^{s+1} - T_n^s = \frac{\alpha \cdot \Delta t}{2 \cdot \Delta x^2} \cdot (T_{n+1}^s - 2 \cdot T_n^s + T_{n-1}^s) + \frac{\alpha \cdot \Delta t}{2 \cdot \Delta x^2} \cdot (T_{n+1}^{s+1} - 2 \cdot T_n^{s+1} + T_{n-1}^{s+1}) \quad (4.2)$$

Where  $s$  and  $s+1$  signify the successive timesteps,  $t$  is the time increment and  $n$  is the space index and:

$$\alpha = \frac{k_s}{\rho_s \cdot C_{ps}} \quad (4.3)$$

Once the gradient was known, then the heat flux was evaluated by:

$$q'' = k_s \cdot \frac{dT}{dx} \quad (4.4)$$

The thermal conductivity,  $k_s$  is a function of the plate surface temperature, as provided in Section 3.2.2. The data was then filtered to reduce the effects of temperature fluctuations that occurred during the experiments most likely due to water splashing on the plate.

### 4.3 Selecting the Tests to use for the Analyses

The heat flux data was graphed in different ways to help determine which tests should be excluded from the analyses due to experimental error. One cause of experimental error can be due to slight variations in the way the different tests were performed. This can be variation due to thermocouple setup, for instance. There could have been slight variations as to where the thermocouples were placed for each test. This can in turn affect the temperatures read and hence cause a variation in heat flux.

There could also have been variations between tests of the initial plate temperature. An initial plate temperature of 900°C was the goal. In reality, this temperature may not have been exactly the same between the tests. The plate cools when it leaves the furnace. It was purposely heated above 900°C to allow for the cooling that resulted until the plate was set into place and the experiment was started. However, this time frame may have been slightly different between the tests and therefore the initial plate temperature may have varied.

There could also have been fluctuations of the flow rates. Ideally, constant flow rates were desired. However, in a real world, precisely steady state conditions are hard to achieve and there can be fluctuations with time. This would in turn affect the jet velocity and jet diameter, which affects the heat flux (see Sections 2.4.3 and 2.4.4).

There was also the possibility of oxidation of the plate. The plate was heated in a nitrogen environment to help reduce this. However, there is still the possibility of oxides forming, which affect the heat transfer (see Section 2.4.7 and Appendix B.2.4). Some tests may have contained oxides on the plate while others did not. Furthermore, the

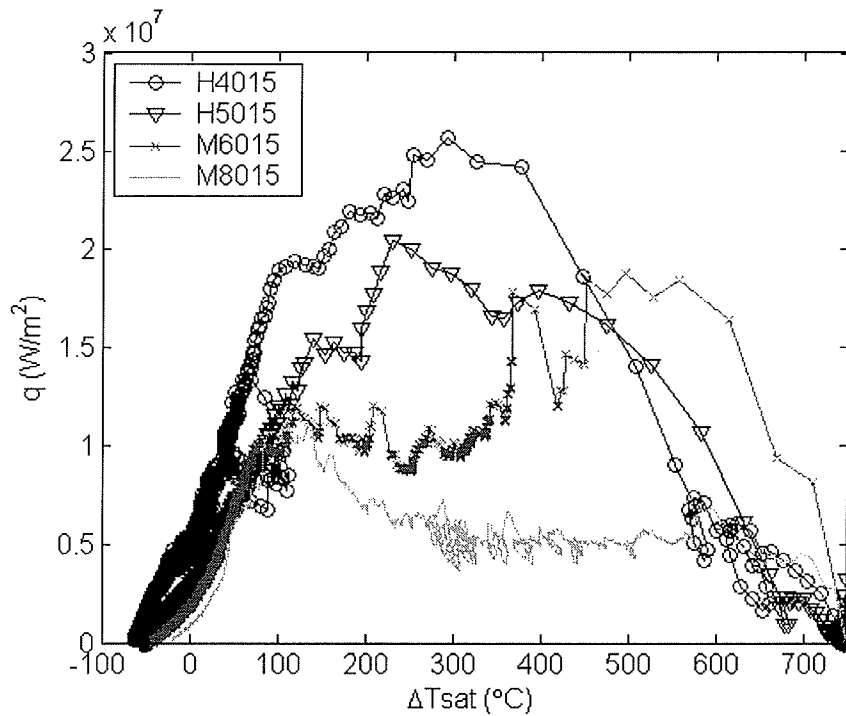
oxidation could occur on different parts of the plate. This can easily result in variations of heat flux across the tests.

There could also have been errors due to thermocouple failure. Thermocouples are sensitive devices and small diameters of around 1.5 mm were used. The forces from the flow of the water can damage thermocouples of this small size. The flow disturbance of the thermocouple can also cause heat transfer due to convection, which can lower the temperature of the thermocouple at the location it is to be read. This can result in lower temperature readings than what actually occurred, which directly affect the heat flux.

There is also the possibility of thermocouple conduction error. Intrinsic thermocouples were used in all test series, which protrude out of the plate (see Section 3.3). These wires can act as fins where conductive heat transfer can occur. Heat can conduct from the plate into the thermocouple wires. This can reduce the temperature of the thermocouple at its base, where the plate temperature is being read. Therefore, lower thermocouple readings can result, which in turn vary the heat flux. More information on thermocouples and this conduction error is contained in Appendix A.

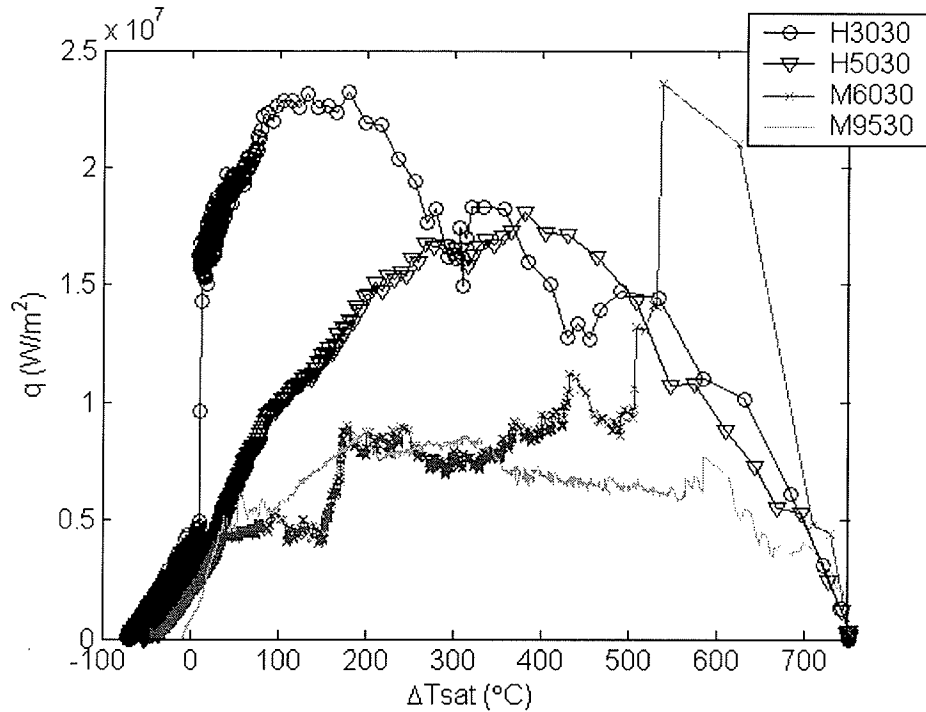
To find the tests that resulted in experimental error, the data for all the tests within the stagnation region was graphed. Any tests that contained results which deviated from the general trend of the data were excluded from the analyses. Figure 4.1 shows the stagnation region heat flux at 15 l/min at water temperatures of 40°C, 50°C, 60°C, and 80°C. It can be seen that the heat flux for test H4015 contained experimental errors at wall superheats ranging from 50°C to 110°C. The heat flux for test M6015 rose drastically at wall superheats greater than 400°C, which does not follow the generalized

trend of the other experiments. Therefore, tests H4015 and M6015 were excluded from the analyses.



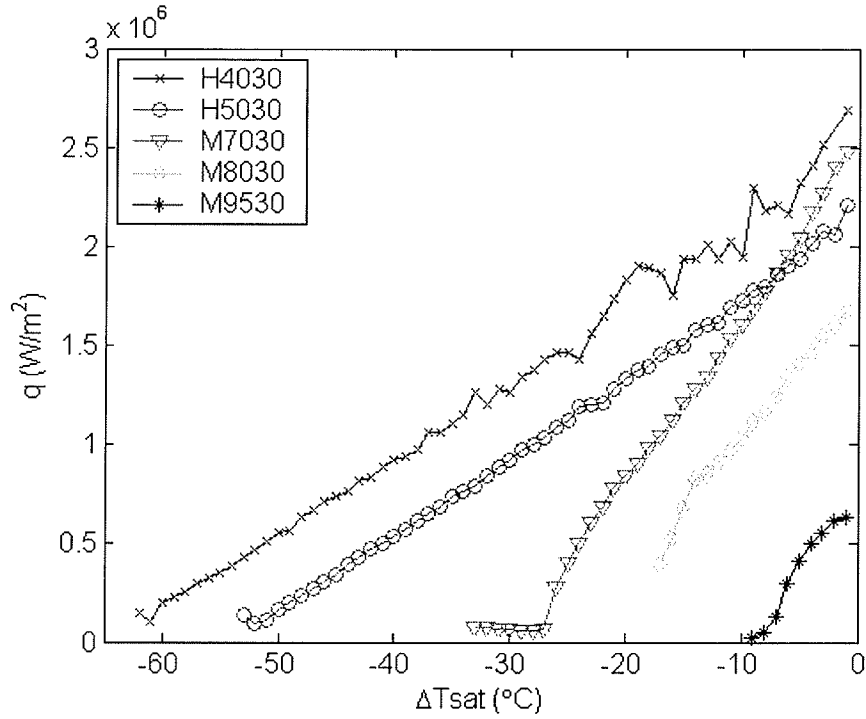
**Figure 4.1: Experimental heat flux at 15 l/min**

Figure 4.2 shows the stagnation region heat flux at 30 l/min at water temperatures of 30°C, 50°C, 60°C, and 95°C. Looking at the figure, it can be seen that the heat flux for test H3030 contained experimental error. At wall superheats below 100°C, there was a large spike in the heat flux. Additionally, the heat flux for test M6030 at a wall superheat of around 100°C was lower than those for the other water temperatures, most likely due to experimental error. Also for test M6030, the heat flux rose drastically just above a wall superheat of 520°C. Therefore, it was ascertained that test H3030 and M6030 be excluded from the analyses.



**Figure 4.2: Experimental heat flux at 30 l/min**

The heat flux was also graphed within the single-phase regime at 30 l/min to look for more experimental errors. Figure 4.3 shows the results. Looking at the graph, it can be seen that the heat flux for tests M7030 and M8030 did not follow the same trend as the other data did due to experimental error. Therefore, these tests were excluded from the analyses.



**Figure 4.3: Single-phase forced convection heat flux at 30 l/min**

Figure 4.4 shows the heat flux at different water temperatures at 45 l/min. For test M8045, the heat flux did not follow the same trend as the other experiments. It can be seen that at a wall superheat of 100°C, that the heat flux was lower than the other tests due to experimental error. Therefore, this particular test was excluded from the analyses.

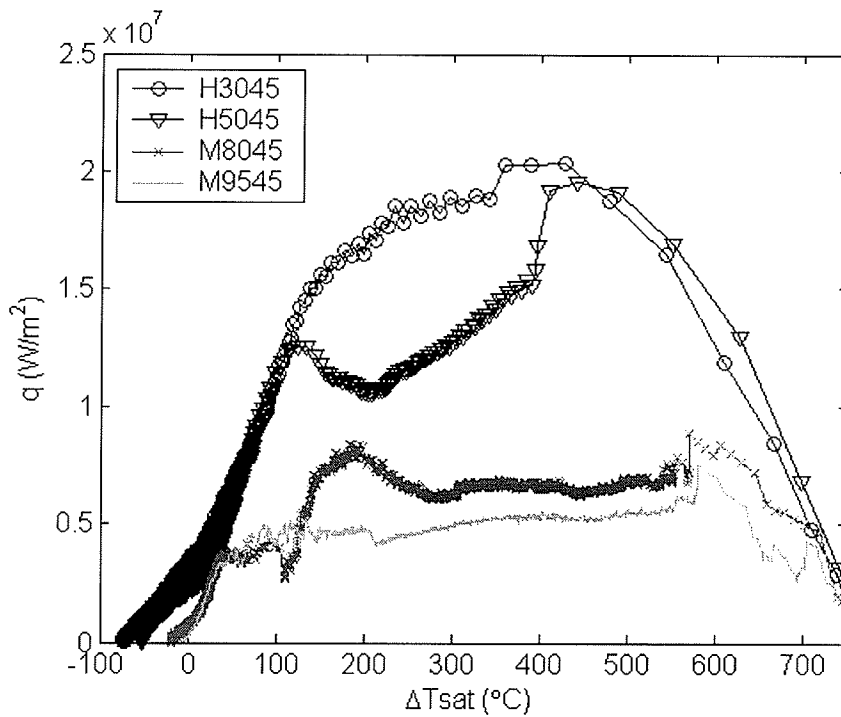


**Figure 4.4: Experimental heat flux at 45 l/min**

Figure 4.5 shows the single-phase forced convection heat flux at 45 l/min.

Looking at the graph, the heat flux for tests H5045 and M6045 did not follow the same trend as the other tests and thus were excluded from the analyses.

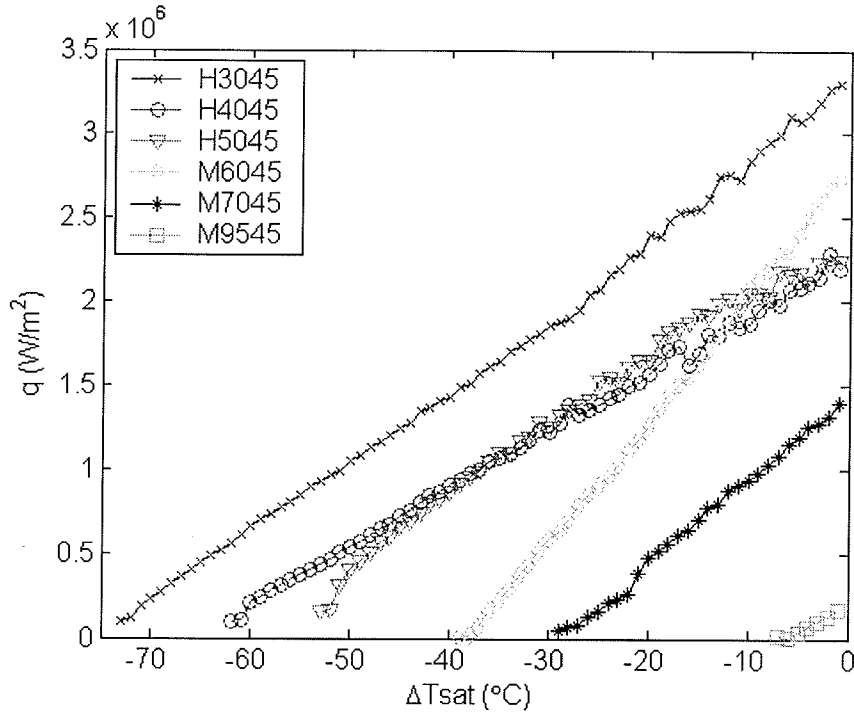


**Figure 4.5: Single-phase forced convection heat flux at 45 l/min**

Table 4.2 summarizes the tests selected to compare with all the correlations, which are indicated with a ‘yes’.

**Table 4.2: Summary of tests chosen to compare with the correlations**

Flow Rate	Water Temperature						
	30°C	40°C	50°C	60°C	70°C	80°C	95°C
15 l/min	yes		yes		yes	yes	yes
30 l/min		yes	yes				yes
45 l/min	yes	yes			yes		yes

#### 4.4 Experimental Data Observations

This section defines where the regimes are located. Observations made on the experimental data while performing the analyses within the single-phase forced convection and CHF regimes are also provided. Additionally, the duration of time that

each regime occurred for will be estimated. All observations apply to the stagnation region only.

#### 4.4.1 Boiling Regimes Defined

Figure 4.6 defines the boiling regimes for test H5030. Single-phase forced convection occurs when the wall superheat is less than zero. Nucleate boiling occurs between a wall superheat greater than zero up to the CHF. After this, transition boiling occurs. For all tests it was found that film boiling did not occur due to high enough cooling rates which would instantaneously cool the plate to surface temperatures below which film boiling would occur. These regimes were defined in a similar manner for all the other tests when performing the analyses.

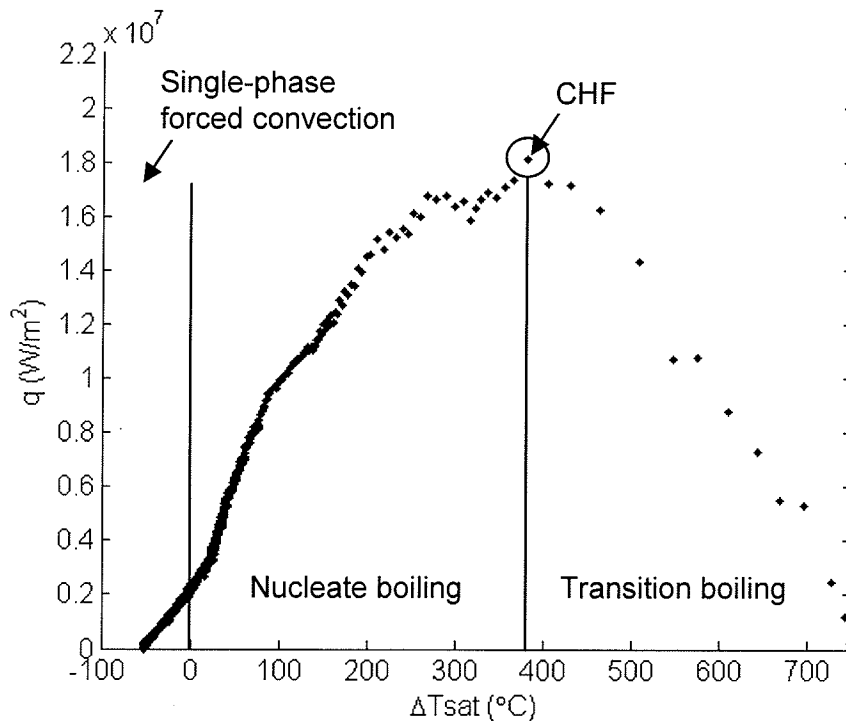
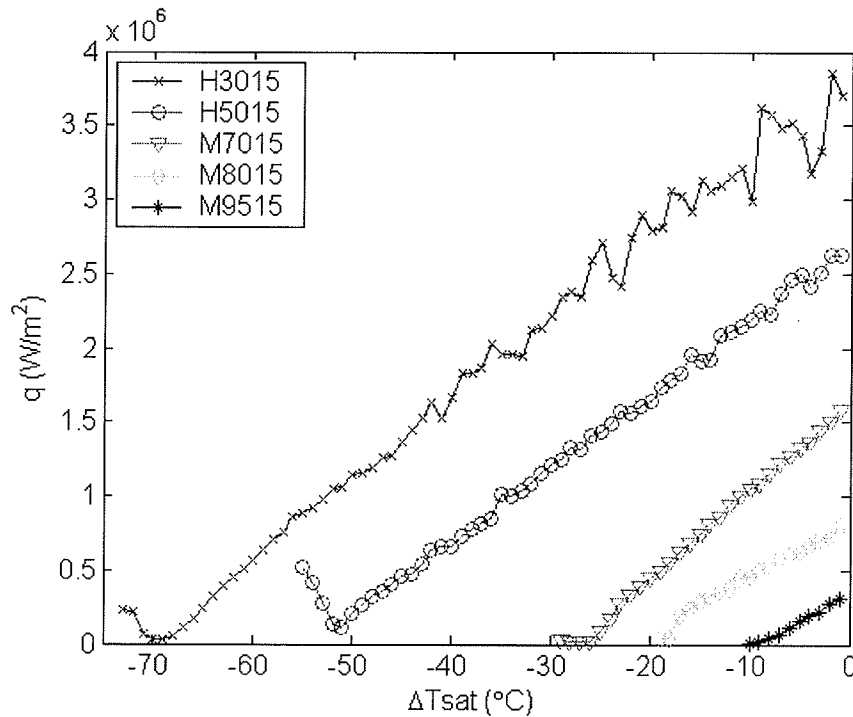


Figure 4.6: Boiling regimes for test H5030

#### 4.4.2 Single-phase Forced Convection Region

While comparing the experimental data with the correlations, there were observations made in the single-phase forced convection regime. Looking at Figure 4.7, it can be seen that the heat flux decreased with increasing water temperature in the stagnation region at a flow rate of 15 l/min.



**Figure 4.7: Single-phase forced convection heat flux at 15 l/min**

Similar trends were observed at the other flow rates. This makes sense, considering higher water temperatures permit less heat to be extracted from the plate during cooling.

#### 4.4.3 CHF Region

The CHF for the experimental data was determined by taking the maximum heat flux just after the nucleate boiling regime. Figure 4.8 shows the stagnation region heat flux for test H4030. The circled area shows the region where the CHF was taken as,

which is  $1.69 \times 10^7 \text{ W/m}^2$ . Matlab was used to determine the maximum heat flux within this region. A similar method was used in determining the CHF for all the other tests.

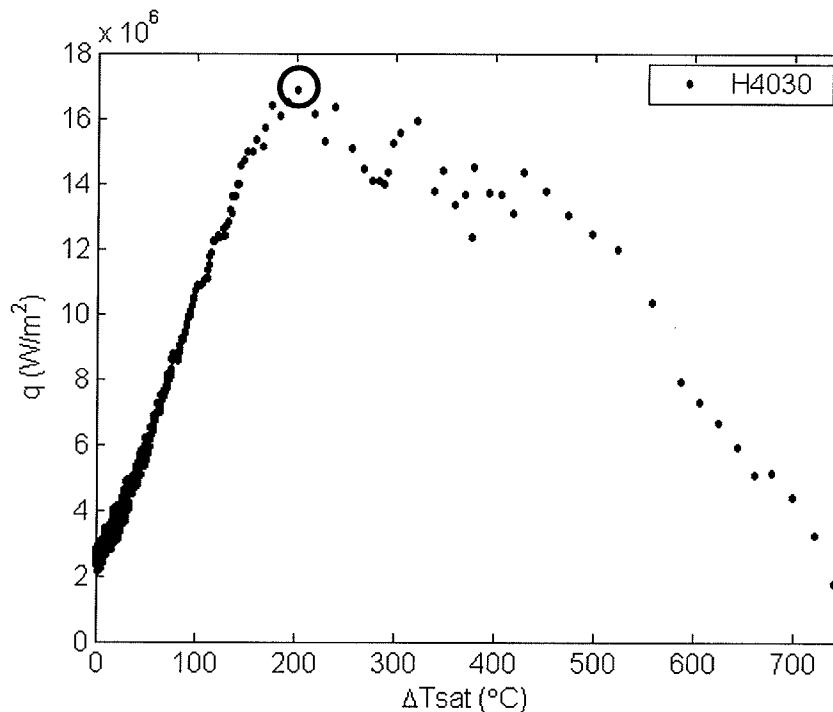


**Figure 4.8: Determining the CHF for test H4030**

Table 4.3 shows the experimental CHF determined. It can be seen that the CHF ranged from  $3.66 \times 10^6$  to  $2.14 \times 10^7 \text{ W/m}^2$ . Figure 4.9 shows the graphical results across the different water temperatures. It can be seen that the CHF decreases with increasing water temperature at all the flow rates evaluated. It can also be observed that the CHF did not vary significantly across the different flow rates. This most likely occurred because the variation in jet impingement velocity was 5 m/s to 6 m/s, which is not a significant difference.

**Table 4.3: Experimental data CHF**

Flow Rate	CHF (W/m <sup>2</sup> ) (at indicated water temperature)						
	30°C	40°C	50°C	60°C	70°C	80°C	95°C
15 l/min	2.14E+07	:	2.04E+07	:	1.11E+07	1.11E+07	3.66E+06
30 l/min	:	1.69E+07	1.81E+07	:	:	:	8.87E+06
45 l/min	2.04E+07	2.00E+07	:	:	1.10E+07	:	5.12E+06

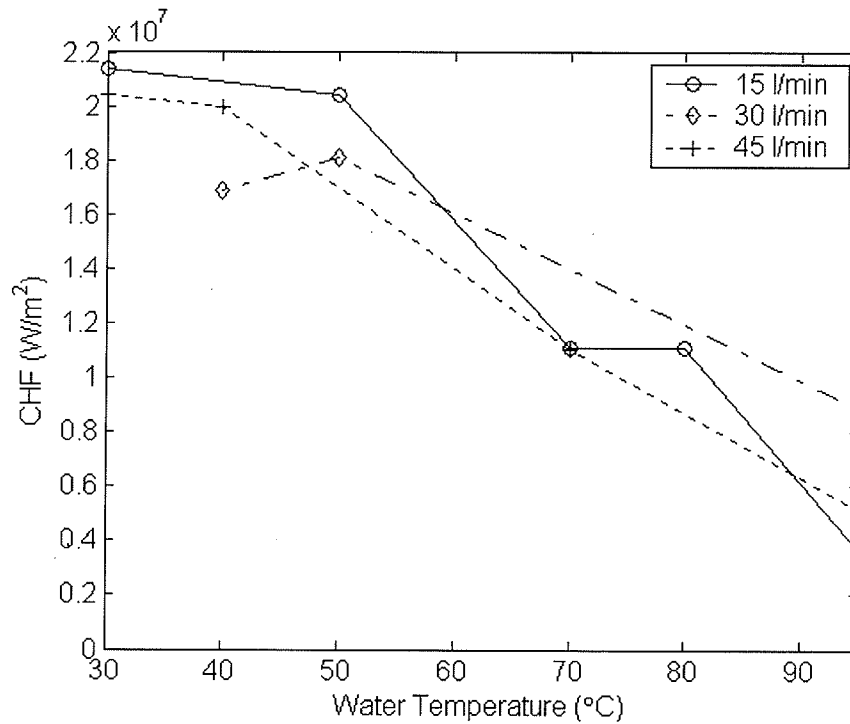


**Figure 4.9: Experimental data CHF**

Table 4.4 shows the wall superheat that the CHF occurred at for all the tests, with Figure 4.10 showing the graphical results. It can be seen that the wall superheat the CHF occurred at shifted to lower values as the water temperature increased.

**Table 4.4: Wall superheat CHF occurred at**

Flow Rate	Wall Superheat CHF Occurred at (°C) (at indicated water temperature)						
	30°C	40°C	50°C	60°C	70°C	80°C	95°C
15 l/min	296	:	229	:	149	108	71
30 l/min	:	202	381	:	:	:	197
45 l/min	428	451	:	:	282	:	116

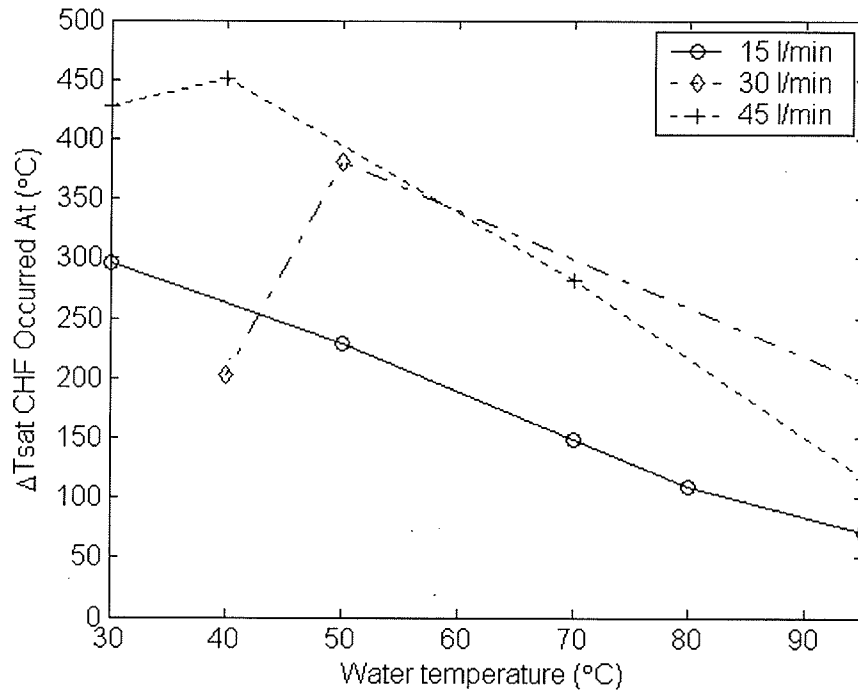


**Figure 4.10: Wall superheat CHF occurred at**

#### 4.4.4 Time Interval for the Boiling Regimes

The time interval for each boiling regime of the experimental data was calculated. Data was analyzed for tests H3015, H3045, M9515, and M9545. To do so, first each regime was defined by the wall superheats. Then the time plotted against the wall superheat allowed for the time interval of each regime to be calculated.

#### 4.4.4.1 Defining the Boiling Regimes

Each regime was defined by determining the wall superheat where each regime commenced and finished at. Figure 4.11 shows the different regimes defined for test H3045. Single-phase forced convection occurred at wall superheats less than  $0^{\circ}\text{C}$ . Nucleate boiling occurred between a wall superheat of  $0^{\circ}\text{C}$  up to  $428^{\circ}\text{C}$ . Transition boiling occurred at wall superheats greater than  $428^{\circ}\text{C}$ , where the CHF occurred (see Table 4.4). Film boiling did not occur. The regimes for test H3015 were determined using the same method as that for this test.

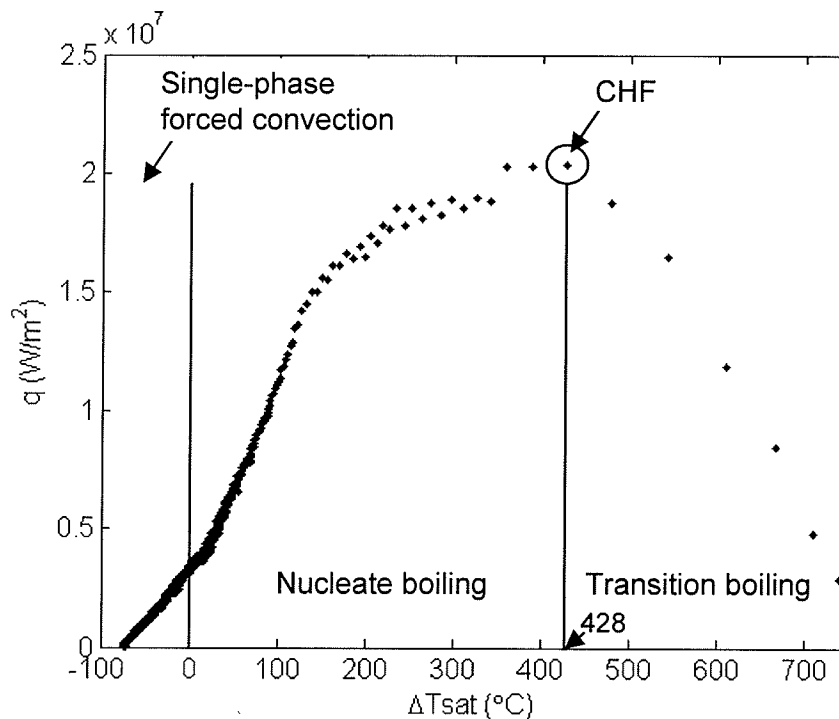


**Figure 4.11: Regimes defined for test H3045**

The boiling curve looked different at a water temperature of  $95^{\circ}\text{C}$ . The heat flux for test M9545 is shown in Figure 4.12. Single-phase forced convection occurred at wall superheats less than  $0^{\circ}\text{C}$ . From  $0^{\circ}\text{C}$  up to the CHF at a wall superheat of  $116^{\circ}\text{C}$  (see

Table 4.4), nucleate boiling occurred. Transition boiling occurred at wall superheats above which the CHF occurred. Like all the other tests, film boiling did not occur. The regimes for test M9515 were determined in the same manner as used this test.

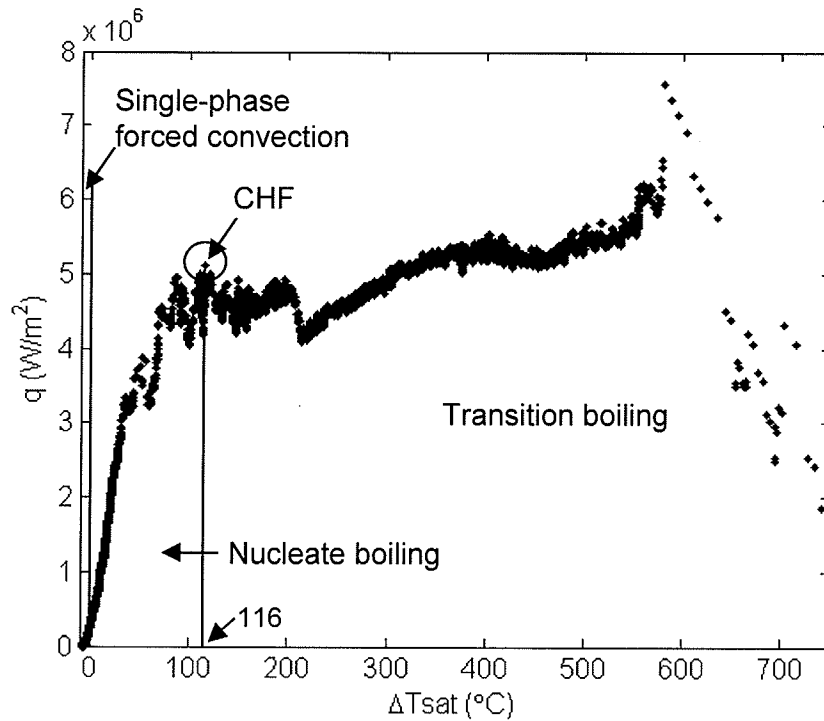


**Figure 4.12: Regimes defined for test M9545**

The wall superheat ranges for each boiling regime for the tests evaluated are summarized in Table 4.5.

**Table 4.5: Wall superheat ranges for the regimes**

Test	Wall Superheat Range			
	Single-Phase Forced Convection Regime	Nucleate Boiling Regime	Transition Boiling Regime	Film Boiling Regime
H3015	<0°C	0°C to 296°C	>296°C	N/a
H3045	<0°C	0°C to 428°C	>428°C	N/a
M9515	<0°C	0°C to 71°C	>71°C	N/a
M9545	<0°C	0°C to 116°C	>116°C	N/a

#### 4.4.4.2 Calculating the Regime Time Interval

In order to calculate the time interval of each boiling regime, the wall superheat was plotted against the time frame of the test. By knowing the range of wall superheats defined for each regime shown in Table 4.5, the time occurring for each boiling regime can be calculated. Looking at Figure 4.11 for test H3045, transition boiling occurs at the highest wall superheats. Therefore, thinking in terms of time, at the beginning of the test, transition boiling would occur first because it occurs at higher wall superheats or higher surface temperatures. Since the plate is being cooled, it would begin at higher surface temperatures.

Figure 4.13 shows the transition boiling regime time interval for test H3045. Looking at the figure and Table 4.5, transition boiling occurred at wall superheats greater than 428°C. Drawing a line across this wall superheat to the data, this occurred at a time of 0.08 seconds after the test began, shown in Figure 4.13.

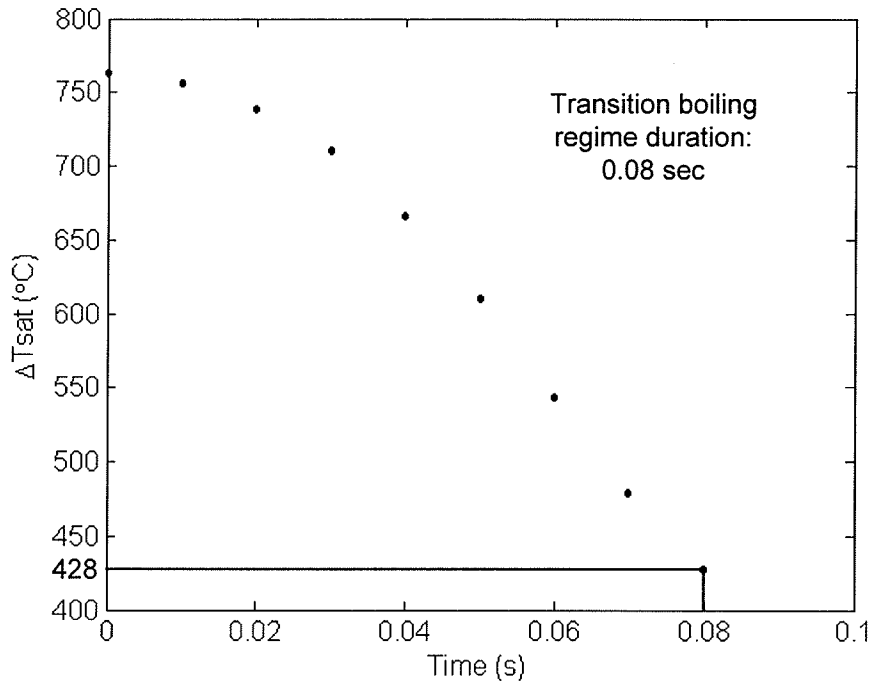


**Figure 4.13: Time interval for transition boiling regime for test H3045**

After transition boiling, nucleate boiling occurred between a wall superheat range of  $0^{\circ}\text{C}$  to  $428^{\circ}\text{C}$  (see Table 4.5). In Figure 4.14, nucleate boiling ends when the wall superheat equals  $0^{\circ}\text{C}$ . Drawing a line across to the data, this occurred 3.93 seconds after the test began. The time interval for nucleate boiling was calculated by subtracting the time where transition boiling ended from the time nucleate boiling ended ( $3.93 - 0.08$ ) to give 3.85 seconds.

Single-phase forced convection occurred last, beginning when the wall superheat is less than  $0^{\circ}\text{C}$ , or 3.93 seconds after the test began. It ended after 57 seconds from when the test began. The time interval was calculated by subtracting the time when single-phase forced convection began to the end of the test ( $57 - 3.03$ ) to give 53.07 seconds (see Figure 4.15).

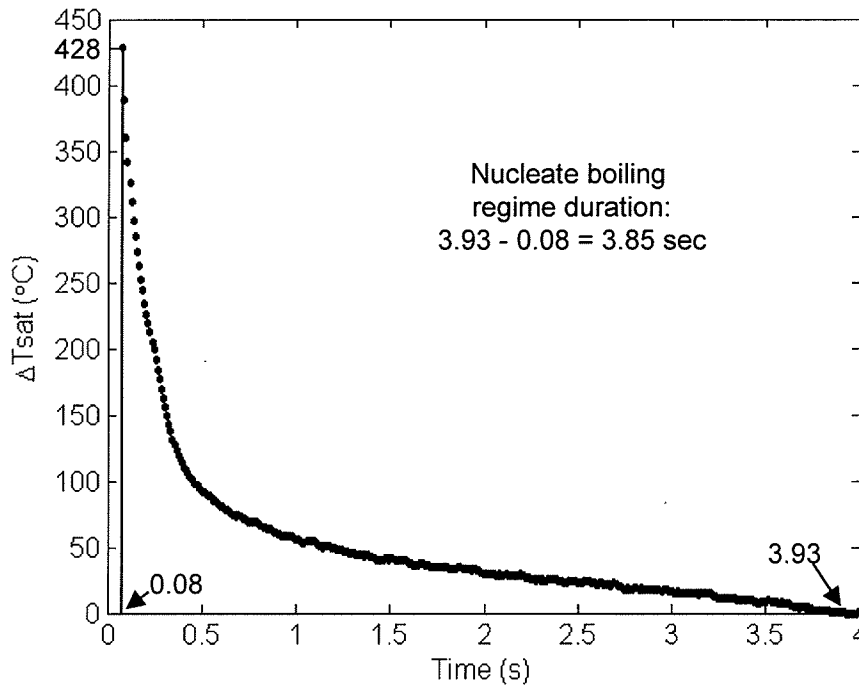


Figure 4.14: Time interval for nucleate boiling regime for test H3045

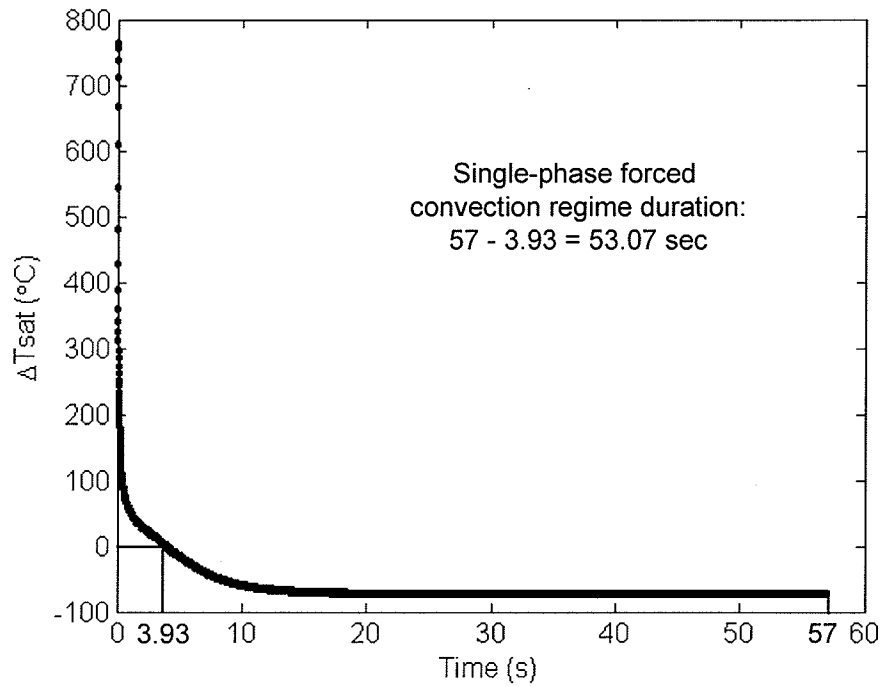


Figure 4.15: Time interval for single-phase forced convection regime for test H3045

The time intervals for the boiling regimes was calculated using the same technique for tests H3015, M9515, and M9545.

#### 4.4.4.3 Summary of Results

Table 4.6 summarizes the boiling regime time intervals and their percent of the total time for tests H3015, H3045, M9515, and M9545. At a water temperature of 30°C, the single-phase forced convection regime dominated for over 90% of the total time for the test, followed by approximately 7% for nucleate boiling and less than 1% for transition boiling.

At a water temperature of 95°C, the percent of the total time for the test for transition boiling increased considerably compared to those tests at a water temperature of 30°C. Single-phase forced convection occurred for the second longest, then transition boiling, and then nucleate boiling. At both water temperatures, the percent of the total time for nucleate boiling remained relatively consistent between 5-11%. This makes sense, considering earlier it was determined that nucleate boiling depends upon wall superheat and not the water temperature (see Section 2.4.2).

**Table 4.6: Time intervals for each boiling regime and percent of total cooling time**

Test	Total Time (s)	Single-phase forced convection		Nucleate boiling		Transition boiling		Film boiling	
		Time (s)	% of total time	Time (s)	% of total time	Time (s)	% of total time	Time (s)	% of total time
H3015	57	52.31	91.77%	4.27	7.49%	0.42	0.74%	N/a	N/a
H3045	57	53.07	93.11%	3.85	6.75%	0.08	0.14%	N/a	N/a
M9515	92.73	17.04	18.38%	9.85	10.62%	65.84	71%	N/a	N/a
M9545	183	93.85	51.28%	10.17	5.56%	78.98	43.16%	N/a	N/a

From Table 4.6, there was a considerable increase in percent duration from a water temperature of 30°C to 95°C for the transition boiling regime. At lower water temperatures the plate cools more quickly, which minimizes the amount of time the plate remains at higher temperatures, which is where transition boiling occurs at. On the contrary, at a higher water temperature of 95°C, the plate cools at a slower rate, which increases the amount of time the plate temperature can be in the transition boiling regime (at higher plate temperatures) when compared to a water temperature of 30°C.

This report thesis not examine correlations within the transition and film boiling regimes. After these observations, it can be concluded that film boiling does not occur for jet impingement boiling under all the test conditions. Therefore, it is not a high priority to evaluate heat transfer in this regime. However, after observing the percent duration increase for the transition boiling regime from lower to higher water temperatures, it is recommended that further research is required to investigate heat transfer within this regime.

## **5. Single-phase Forced Convection Analysis and Results**

This section presents the analysis and results for the single-phase forced convection equations. The single-phase forced convection regime occurs when wall superheats are less than or equal to  $0^{\circ}\text{C}$ . There are three goals for the single-phase forced convection analysis. The first two are to determine the effects of water temperature (or subcooling) and flow rate (or jet velocity) on the single-phase forced convection correlations. The effects of water temperature and jet velocity for the equations will be also be analyzed.

In addition, correlations provided by other researchers will be compared with the experimental data at the particular tests chosen, which were summarized in Table 4.2. The correlations provided earlier in Section 2.3.1 were inputted into Matlab and graphed against the experimental data to see how well they matched. The correlations used and descriptions on how well they fit with the data will be presented for the single-phase forced convection region. Their relationships with the variation in jet flow rate and water temperature will also be discussed.

### **5.1 Summary of Correlations Used**

The seven single-phase forced equations presented in Section 2.3.1.1 are summarized in Table 5.1. Each equation was calculated at varying jet flow rates and water temperatures selected as shown in Table 4.2 and compared with the experimental data.

**Table 5.1: Single-phase forced convection equations presented by other researchers**

Presented by	Correlation(s)	Applicable Conditions
Martin (1977) [11]	$\bar{Nu}_j = C_1 \cdot C_2 \cdot Re_j \cdot Pr^{0.42} \quad (2.8a)$ $C_1 = \frac{d_j}{r} \cdot \frac{1 - 1.1 \cdot \frac{d_j}{r}}{1 + 0.1 \cdot (Z/d_j - 6) \cdot d_j / r} \quad (2.8b)$ $C_2 = 2 \cdot Re_j^{0.5} \cdot (1 + 0.005 \cdot Re_j^{0.55})^{0.5} \quad (2.8c)$	$2,000 \leq Re_j \leq 400,000$ $2.5 \leq r/d_j \leq 7.5$ $2 \leq Z/d_j \leq 12$
Barsanti et. al (1989) [12]	$\bar{Nu}_{ji} = 0.0136 \cdot Re_{ji}^{0.837} \cdot Pr^{0.42} \quad (2.9)$	$3.26 < Pr < 6.04$ $53,025 < Re_{ji} < 210,709$ $10 \leq d_{ji} \leq 20 \text{ mm}$ $13^\circ\text{C} \leq T_{\text{water}} \leq 40^\circ\text{C}$
Faggiani and Grassi (1990) [13]	$\bar{Nu}_{ji} = 0.025 \cdot Re_{ji}^{0.8} \cdot Pr^{0.4} \quad (2.10)$	$Z/d_{ji} = 5$ $Re > 77,000$ $0.5 \leq Pr \leq 50$
Liu et al. (1991) [14]	$Nu_{ji} = 0.715 \cdot Re_{ji}^{0.5} \cdot Pr^{0.4} \quad (2.11a)$ $Nu_{ji} = 0.797 \cdot Re_{ji}^{0.5} \cdot Pr^{1/3} \quad (2.11b)$	- use (2.11a) when $0.15 \leq Pr \leq 3$ - use (2.11b) when $Pr > 3$
Wang (1989) [15]	$Nu_{ji} = 0.717 \cdot Re_{ji}^{0.5} \cdot Pr^{0.37} \quad (2.12)$	$0.5 \leq Pr \leq 50$
Stevens and Webb (1991) [15]	$Nu_j = 1.51 \cdot Re_j^{0.44} \cdot Pr^{0.4} \cdot \left(\frac{Z}{d_j}\right)^{-0.11} \quad (2.13)$	$2.2 \leq d_j \leq 8.9 \text{ mm}$ $0.56 \leq Z/d_j \leq 18.5$
Stevens and Webb (1991) [15]	$Nu_j = 2.67 \cdot Re_j^{0.567} \cdot Pr^{0.4} \cdot \left(\frac{Z}{d_j}\right)^{-0.0336} \cdot \left(\frac{v_j}{d_j}\right)^{-0.237} \quad (2.14)$	$2.2 \leq d_j \leq 8.9 \text{ mm}$ $0.56 \leq Z/d_j \leq 18.5$

## 5.2 Determining the Single-phase Forced Convection Heat Flux

The heat flux for each equation was determined by calculating the Nusselt number from the equations in Table 5.1. For correlations 2.9, 2.10, 2.11, and 2.12, the Reynold's number was calculated using Equation 2.7 at jet impingement. The heat transfer coefficient was then determined by rearranging Equation 2.6 at jet impingement:

$$h = \frac{Nu_{ji} \cdot k_f}{d_{ji}} \quad (5.1)$$

However, correlations 2.8, 2.13 and 2.14 were specified to be calculated at nozzle exit. It can be seen in Table 5.1 that each of these equations had specified nozzle height

to nozzle diameter ratios ( $Z/d_j$ ). On the contrary, the experiments were performed at a  $Z/d_j$  of 78.9, which is considerably higher than the ratios specified for each of these correlations. Therefore, a corrected nozzle height, nozzle jet velocity, and nozzle diameter had to be determined for these equations to allow the parameters to be within the specified conditions.

Martin [11] for Equation 2.8 specified a range for the nozzle height to diameter ratio of  $2 \leq Z/d_j \leq 12$ . For the analysis, a corrected nozzle height, jet diameter at nozzle exit, and nozzle diameter had to be determined in order for the ratio would be within the specified range. Martin also provided a specified a range of  $2.5 \leq r/d_j \leq 7.5$ . Therefore the ratio of the radial distance from the center to the corrected nozzle diameter also had to be within these values.

For convention, a  $Z_{cor}/d_{jcor}$  ratio of 4.31 was chosen. The corresponding corrected parameters were determined by trial and error by arbitrarily selecting a nozzle height and until the desired  $Z_{cor}/d_{jcor}$  ratio of 4.31 and range of  $2.5 \leq r/d_{jcor} \leq 7.5$  was accomplished. After selecting a nozzle height, the corrected jet velocity at the nozzle was calculated by rearranging Equation 2.1:

$$v_{jcor} = \sqrt{v_{ji}^2 - 2 \cdot g \cdot Z_{cor}} \quad (5.2)$$

The corresponding nozzle diameter was calculated by rearranging Equation 2.2:

$$d_{jcor} = d_{ji}^2 \cdot \frac{v_{ji}}{v_{jcor}} \quad (5.3)$$

Table 5.2 shows the corresponding corrected nozzle height, nozzle diameter, and nozzle jet velocity at this ratio for each of the different flow rates. The  $r/d_{jcor}$  ratio was also determined to ensure it was within the specified range. The radial distance at

thermocouple location 3 was chosen to achieve the desired  $r/d_{jcor}$  ratio. This means that Equation 2.8 was calculated at thermocouple 3 (31.8 mm from the center). As it can be seen, the differences between the corrected nozzle diameter and jet velocities and those at jet impingement are very small.

**Table 5.2: Corrected Parameters for Equation 2.8**

Flow rate	$Z_{cor}$ (m)	$v_{ji}$ (m/s)	$v_{jcor}$ (m/s)	$d_{ji}$ (m)	$d_{jcor}$ (m)	$Z_{cor}/d_{jcor}$	R (m)	$r/d_{jcor}$
15 l/min	0.0329	5.5	5.44	0.0076	0.0076	4.31	0.03175	4.16
30 l/min	0.0460	5.7	5.62	0.0106	0.0107	4.31	0.03175	2.97
45 l/min	0.0547	6.0	5.91	0.0126	0.0127	4.31	0.03175	2.50

Equations 2.13 and 2.14 specified a range of  $2.2 \leq d_j \leq 8.9$  mm and  $0.56 \leq Z/d_j \leq 18.5$  be used. For convection, a  $Z_{cor}/d_{jcor}$  value of 18 was chosen. Table 5.3 shows the corresponding parameters at the corrected nozzle height for Equations 2.13 and 2.14. These values were determined using the same technique as that used for Equation 2.8.

**Table 5.3: Corrected Parameters for Equations 2.13 and 2.14**

Flow rate	$Z_{cor}$ (m)	$v_{ji}$ (m/s)	$v_{jcor}$ (m/s)	$d_{ji}$ (m)	$d_{jcor}$ (m)	$Z_{cor}/d_{jcor}$
15 l/min	0.14	5.5	5.24	0.0076	0.0078	18
30 l/min	0.197	5.7	5.35	0.0106	0.0109	18
45 l/min	0.235	6	5.60	0.0126	0.0130	18

The heat transfer coefficients for Equations 2.8, 2.13, and 2.14 were calculated by:

$$h = \frac{Nu_j \cdot k_f}{d_{jcor}} \quad (5.4)$$

And the Reynold's numbers were calculated by:

$$\text{Re}_j = \frac{\rho_f \cdot v_{jcor} \cdot d_{jcor}}{\mu_f} \quad (5.5)$$

For all of the correlations, all water properties used were at the film temperature where:

$$T_{film} = \frac{(T_{surf} + T_{water})}{2} \quad (5.6)$$

The heat flux was then determined by:

$$q'' = \bar{h} \cdot (T_{surf} - T_{water}) \quad (5.7)$$

However, by looking at the equations in Table 5.1, Equations 2.9 and 2.10 were in terms of the average Nusselt number. The other equations were for the local Nusselt number. The heat flux calculation requires the average heat transfer coefficient be used. From Incropera and DeWitt [17], the average heat transfer coefficient can be calculated by:

$$\bar{h} = \frac{1}{A} \cdot \int_A h \cdot dA \quad (5.8)$$

Where:

$$A = \pi \cdot r^2 \quad (5.9)$$

And:

$$dA = 2 \cdot \pi \cdot r \cdot dr \quad (5.10)$$

Therefore the average heat transfer coefficient becomes:

$$\bar{h} = \frac{1}{\pi \cdot r^2} \cdot \int_r h \cdot 2 \cdot \pi \cdot r \cdot dr \quad (5.11)$$

However, it can be seen by looking at the equations involving the local Nusselt number in Table 5.1, that none of them depend upon the radial distance,  $r$ . Therefore, it

can be assumed that the local and average heat transfer coefficients for those equations are equivalent and Equation 5.7 can be used for all of the correlations as they are.

### 5.3 Effect of Water Flow rate

The equations were evaluated at a water temperature of 50°C at flow rates of 15 l/min, 30 l/min, and 45 l/min. The results for each equation will be discussed.

Figure 5.1 shows Equation 2.8 (see Table 5.1) at the different flow rates. The heat flux increased with increasing flow rate. However, different results were obtained for the other equations analyzed.

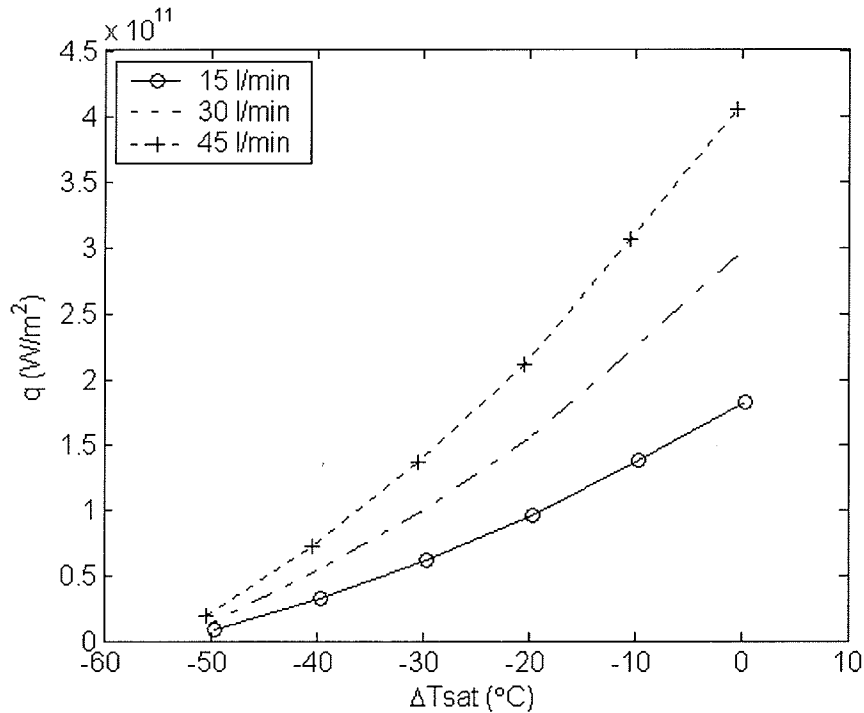


**Figure 5.1: Effect of flow rate for Equation 2.8**

Figure 5.2 shows Equation 2.12 at each of the different flow rates at a water temperature of 50°C. It can be seen that as the flow rate increased, the heat flux decreased. This can be explained by looking at the equation in Table 5.1. Since the water temperature is constant, the heat transfer coefficient varies by the change of jet

velocity and jet diameter, which vary with the flow rate. Essentially, as the flow rate increases, the jet velocity and jet diameter increase.

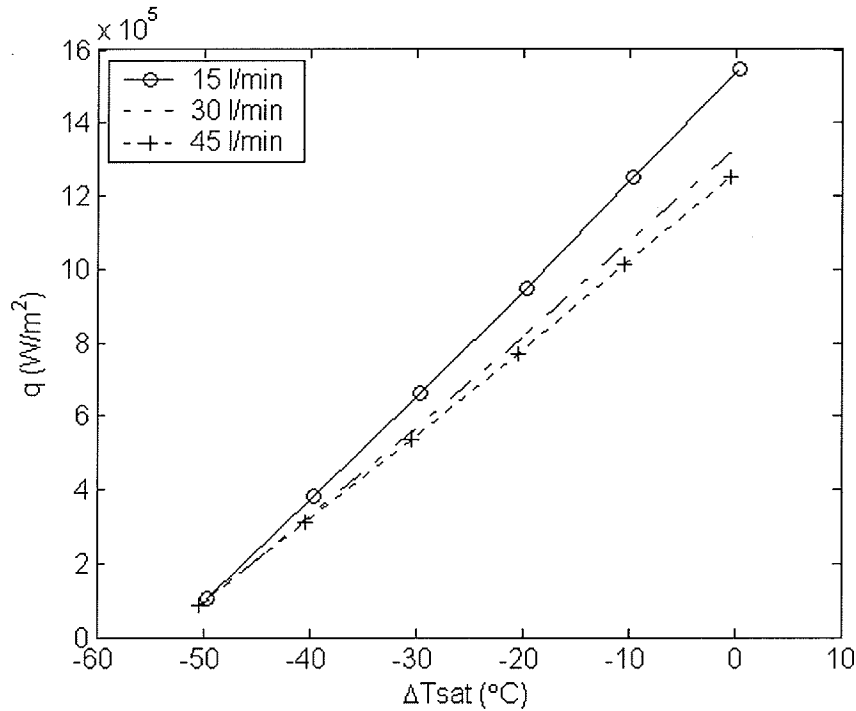


**Figure 5.2: Effect of flow rate for Equation 2.12**

Combining Equations 2.12, 5.1 (for the heat transfer coefficient), and 2.7 (for the Reynold's number), the heat transfer coefficient for Equation 2.12 becomes:

$$h_{2.12} = \frac{0.717 \cdot \rho_f^{0.5} \cdot v_{ji}^{0.5} \cdot d_{ji}^{0.5} \cdot \text{Pr}^{0.37}}{\mu_f^{0.5}} \cdot \frac{k_f}{d_{ji}} \quad (5.10)$$

When the water temperature is constant and the flow rate varies, the only variables that change are  $v_{ji}$  and  $d_{ji}$ . Isolating these variables and simplifying, the heat transfer coefficient becomes proportional to:

$$h_{2.12} \propto \frac{v_{ji}^{0.5}}{d_{ji}^{0.5}} \quad (5.11)$$

Incorporating the jet velocity and diameter into this proportional factor yields 26.9, 23.2, and 21.8 at 15 l/min, 30 l/min, and 45 l/min respectively. This factor decreases with increasing flow rate, which helps explain the results in Figure 5.2. This occurs because the heat transfer coefficient is inversely proportional to the jet diameter. Even though the jet velocity increases with increasing flow rate, the jet diameter parameter must increase at a greater rate than the velocity parameter did. Thus, this would reduce the heat transfer coefficient with increasing flow rate.

The proportional factors to the heat transfer coefficient for the other equations (excluding Equation 2.8) were determined and calculated at the different flow rates using the same method as that for Equation 2.12, as shown in Table 5.4. The graphical results are presented in Figure 5.3. The change in this factor is directly proportional to the change in heat flux. Therefore, if the factor decreases, then the heat flux for that equation decreases. It would be the other way around if it increased.

For Equations 2.11, 2.12, 2.13, and 2.14 from Figure 5.3, it can be ascertained that, the heat flux decreased with increasing flow rate. Equations 2.9, and 2.10 decrease slightly from 15 l/min to 30 l/min and increase slightly from 30 l/min to 45 l/min.

**Table 5.4: Proportional factors to h at each of the flow rates**

Equation	Proportional factor to h	Factor @ 15 l/min	Factor @ 30 l/min	Factor @ 45 l/min
2.9	$\frac{v_{ji}^{0.84}}{d_{ji}^{0.16}}$	9.1	8.9	9.1
2.10	$\frac{v_{ji}^{0.8}}{d_{ji}^{0.2}}$	10.4	10	10.1
2.11	$\frac{v_{ji}^{0.5}}{d_{ji}^{0.5}}$	26.9	23.2	21.8
2.12	$\frac{v_{ji}^{0.5}}{d_{ji}^{0.5}}$	26.9	23.2	21.8
2.13	$\frac{v_{jcor}^{0.44}}{d_{jcor}^{0.45} \cdot Z_{cor}^{0.11}}$	22.9	19.1	17.7
2.14	$\frac{v_{jcor}^{0.33}}{d_{jcor}^{0.7294} \cdot Z_{cor}^{0.0336}}$	4.1	3.82	3.75

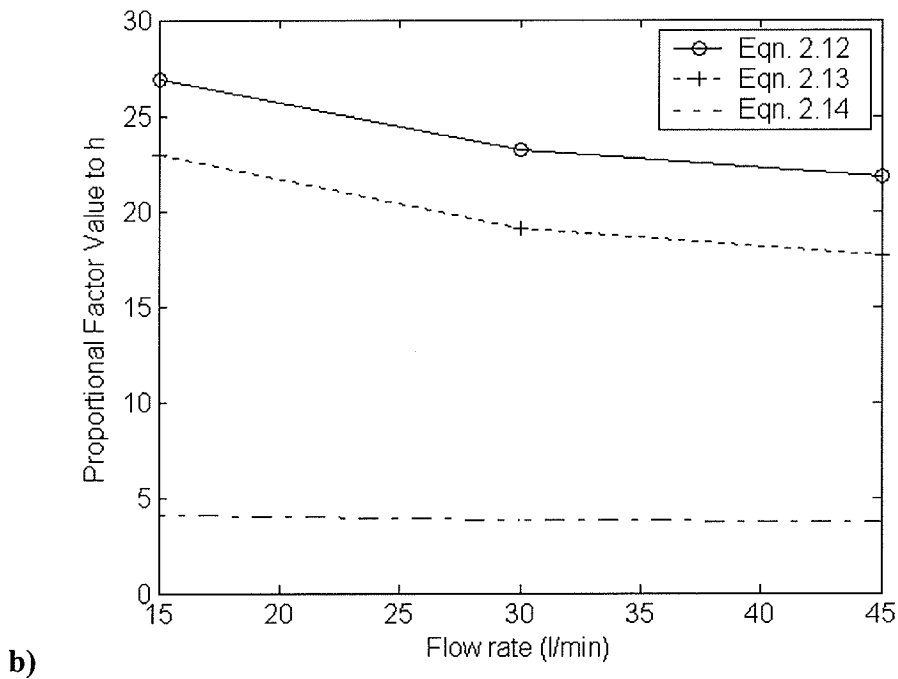
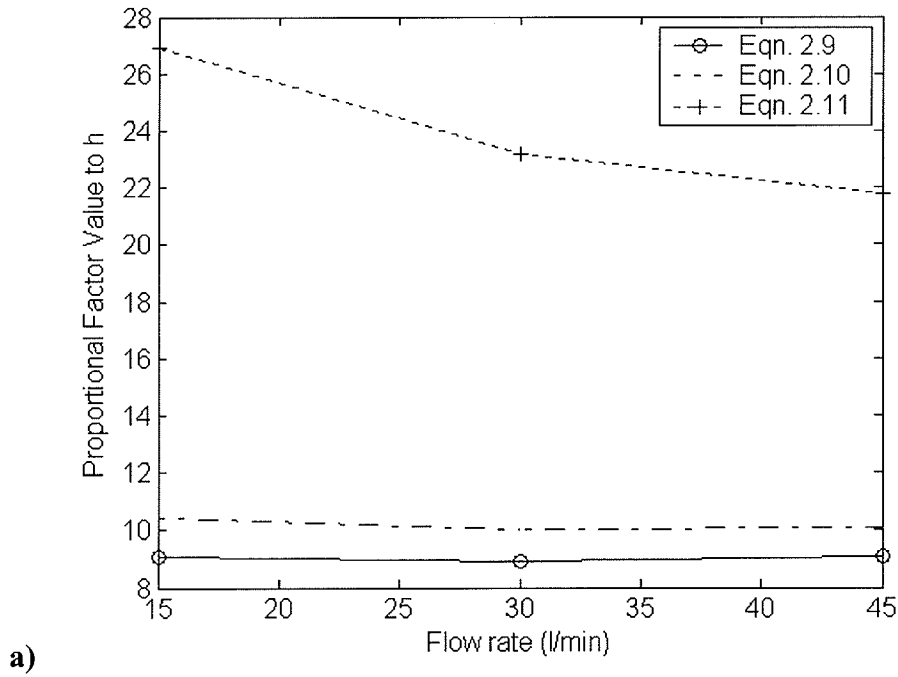


**Figure 5.3: Proportional Factors to h Values at Different Flow Rates for Equations a) 2.9, 2.10, 2.11 b) 2.12, 2.13, 2.14**

### 5.4 Effect of Water Temperature

As discussed in Section 4.2, the effect of water temperature on the heat transfer coefficient was examined at a flow rate of 45 l/min ( $v_{ji} = 6$  m/s). To observe the trends of the water temperature, the heat flux for each correlation was calculated at water temperatures of 30°C, 50°C, 70°C, and 95°C. Figure 5.4 shows the heat flux for Equation 2.14 (see Table 5.1) at these different water temperatures. As it can be seen, the heat flux decreased at a consistent rate with increasing water temperature. Similar results were obtained for all the other equations analyzed.

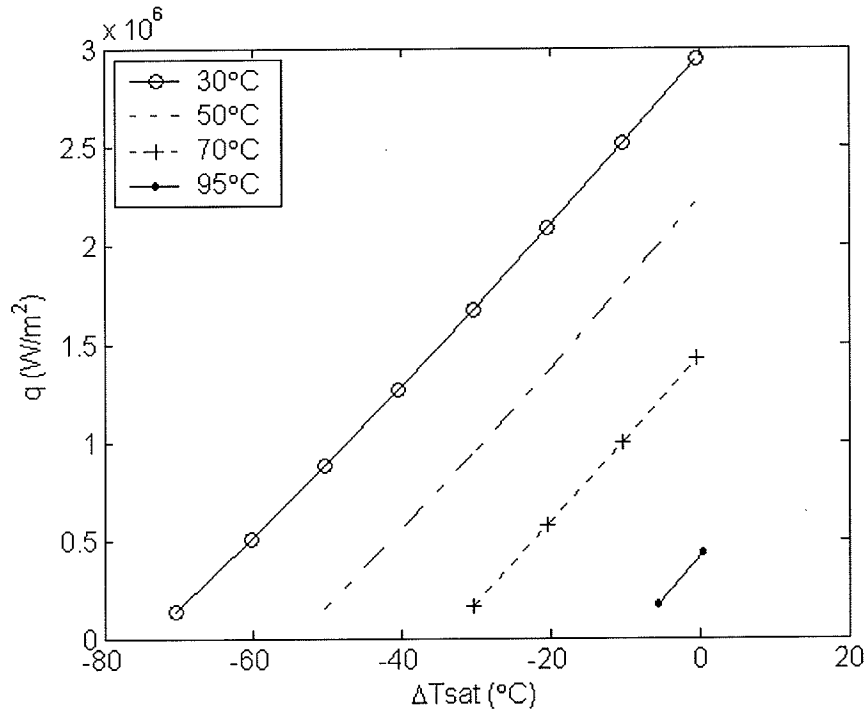


Figure 5.4: Heat flux for Equation 2.14 at different water temperatures

### 5.5 Comparison with the Experimental Data

Each correlation was compared graphically with the experimental data within the single-phase region at the tests summarized in Table 4.2. A graph was made for each of the water temperatures showing the correlation heat flux,  $\pm 30\%$  of the correlation heat

flux, and then the experimental heat flux. Then the percent of the experimental data that fell within the  $\pm 30\%$  region was determined graphically. All correlations (except Equation 2.8) were compared with the experimental data within the stagnation region at thermocouple 1 (center of the plate), which was located at the center of the plate.

### **5.5.1 Results for Equation 2.8**

Equation 2.8 (see Table 5.1) is applicable outside the stagnation region. As mentioned earlier, it was evaluated at thermocouple location 3, or a radial distance of 31.75 mm from the center. Figure 5.5 shows the results when compared to the data of test H5045. As it can be seen, the equation highly overestimated the heat flux, with none of the experimental data coming even close to the equation. The lowest value from the equation was  $1.8 \times 10^{10} \text{ W/m}^2\text{K}$  while the critical heat flux for the data was  $2 \times 10^7 \text{ W/m}^2\text{K}$ .

The most probable explanation for this difference is the equation was derived from data for a gas jet and is not applicable for a water jet. Similar results were obtained for the other tests, where the equation highly overestimated the heat flux.

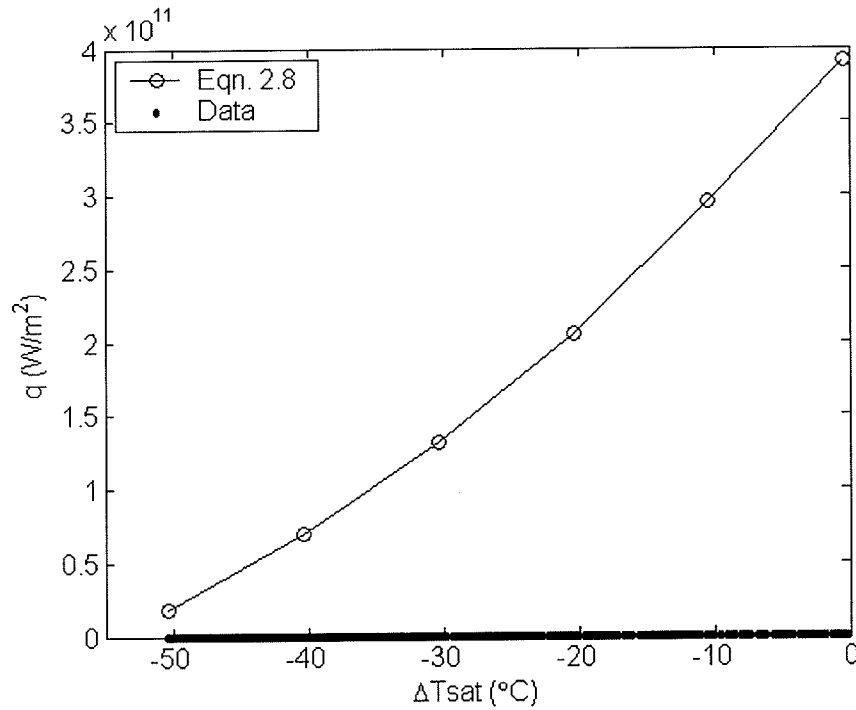


**Figure 5.5: Equation 2.8 compared with the data of test H5045**

### 5.5.2 Results for Equation 2.9

Figure 5.6 and Table 5.5 summarize the percent of the experimental data that fell within the  $\pm 30\%$  region of Equation 2.9 (see Table 5.1). In the table and figure, a positive sign indicates that the correlation was above the experimental heat flux and a negative sign means the correlation was below the heat flux.

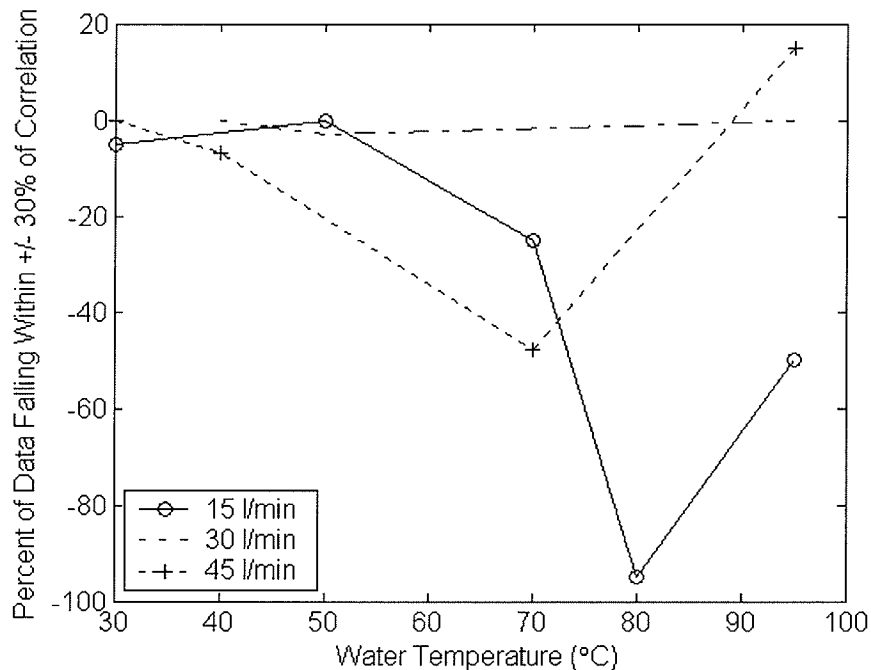


**Figure 5.6:** Percent of the experimental data that fell within  $\pm 30\%$  of Equation 2.9

**Table 5.5:** Percent of the experimental data that fell within  $\pm 30\%$  of Equation 2.9

Flow Rate	Water Temperature						
	30°C	40°C	50°C	60°C	70°C	80°C	95°C
15 l/min	-5%	:	-0.1%	:	-25%	-95%	-50%
30 l/min	:	-0.2%	-3%	:	:	:	0%
45 l/min	0%	-7%	:	:	-48%	:	15%

### 5.5.2.1 Results at 15 l/min

In all instances at 15 l/min, Equation 2.9 underestimated the heat flux. In Figure 5.7, compared with the data of test M7015, the percent of data matching was 25% (see Table 5.5). In Figure 5.8, compared with the data of M8015, the percent of the experimental data matching rose significantly to 95%. The experimental heat flux decreased at a greater rate than Equation 2.9 did from Figure 5.7 at a water temperature

of 70°C to Figure 5.8 at a water temperature of 80°C. This allowed the correlation to rise to match the data considerably better.

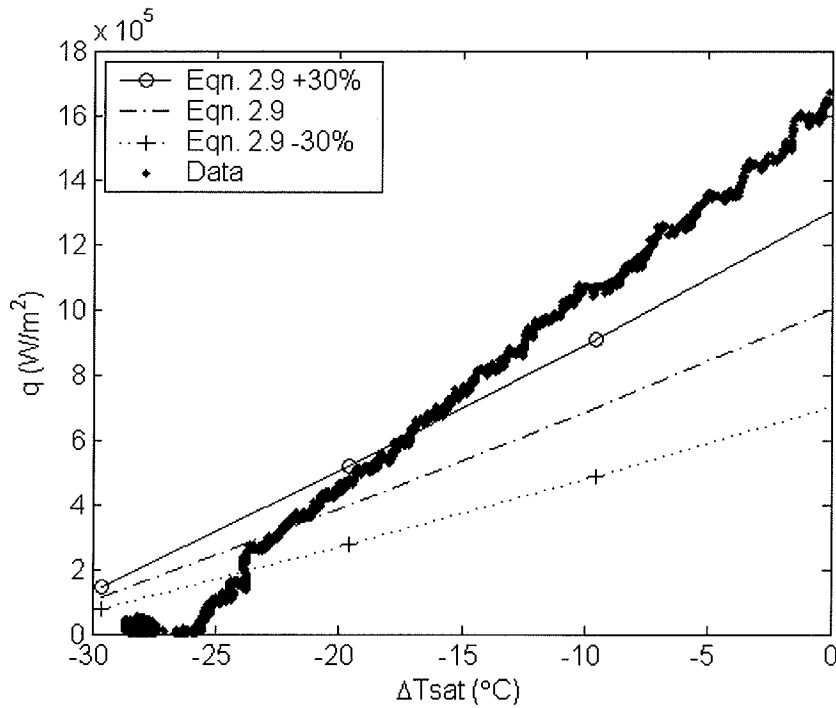


**Figure 5.7: Equation 2.9 compared with the data of test M7015**

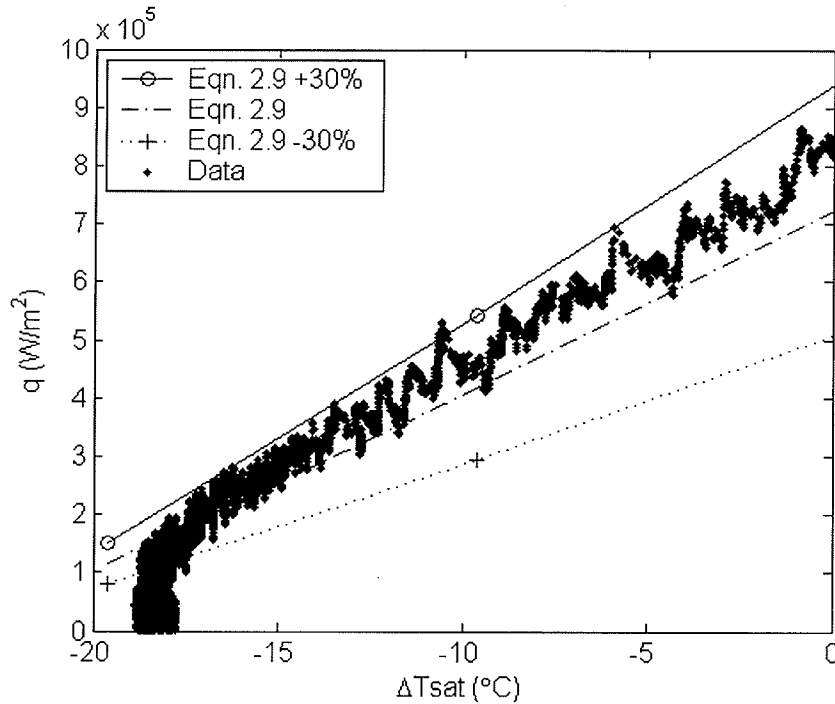


**Figure 5.8: Equation 2.9 compared with the data of test M8015**

#### 5.5.2.2 Results at 30 l/min

Equation 2.9 (see Table 5.1) underestimated the data at 30 l/min with a poor match. The best match occurred at a water temperature of 50°C, shown in Figure 5.9. Here, only 3% of the experimental data fell within the  $\pm 30\%$  range for the correlation (see Table 5.5), which is very little.

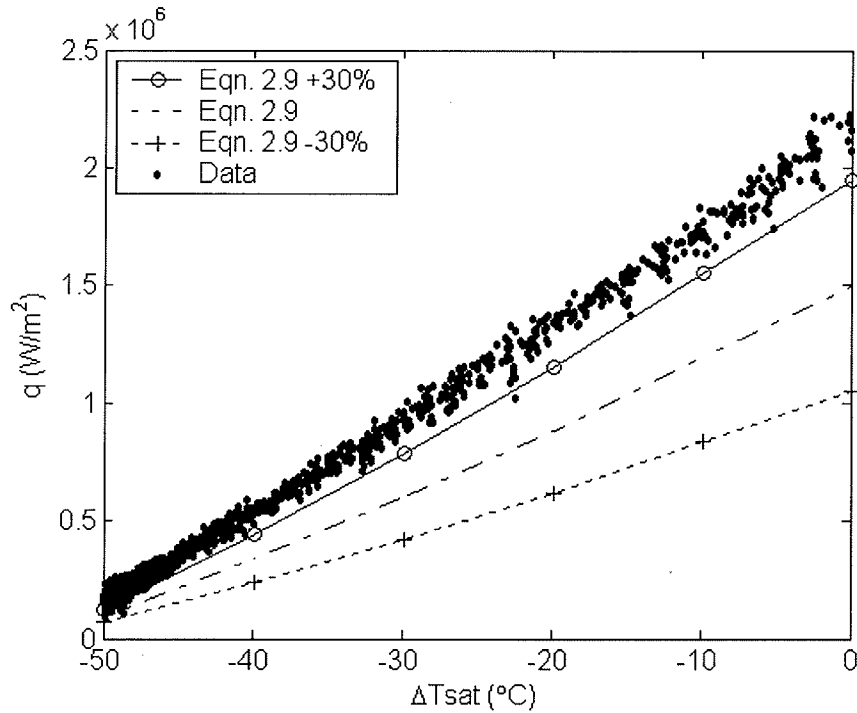


**Figure 5.9: Equation 2.9 compared with the data of test H5030**

### 5.5.2.3 Results at 45 l/min

In Table 5.5, the correlation underestimated the heat flux up to a water temperature of 70°C. Then the percent matching increased significantly from 48% compared with the data of test M7045 (Figure 5.10 and Table 5.5) to overestimating the heat flux of test M9545 (Figure 5.11 and Table 5.5), where 15% of the data matched. Once again, the data decreased at a higher rate with temperature than the correlation did. This allowed for the correlation to rise above the heat flux from a water temperature of 70°C to 95°C.

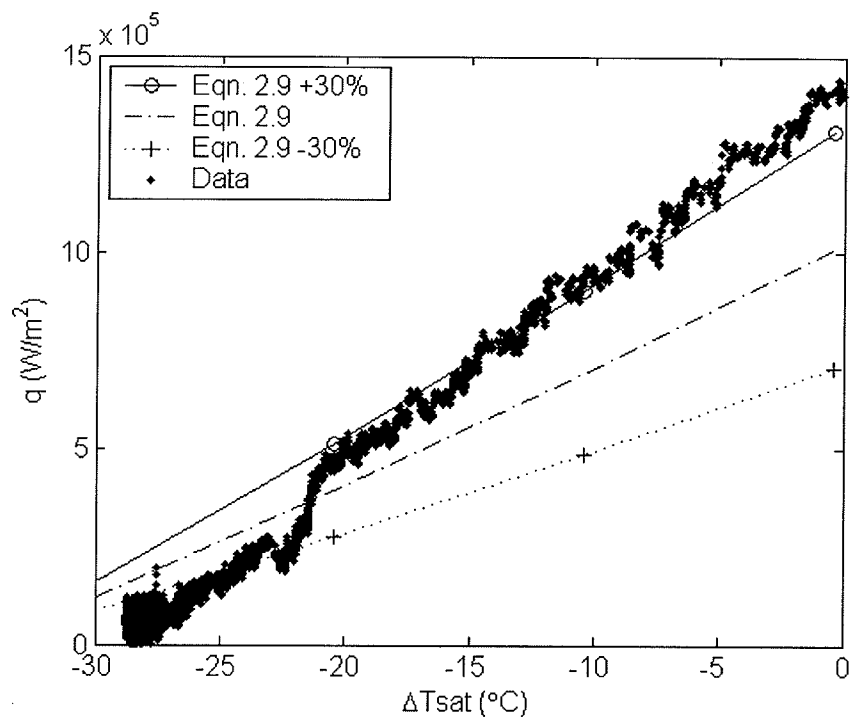


Figure 5.10: Equation 2.9 compared with the data of test M7045

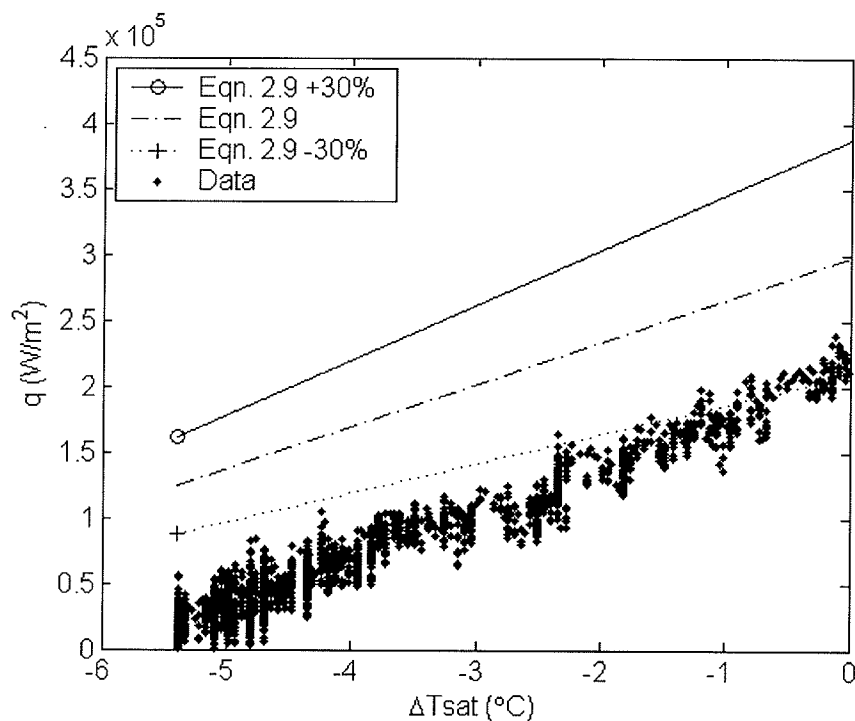


Figure 5.11: Equation 2.9 compared with the data of test M9545

#### 5.5.2.4 Summary

As it can be seen in Table 5.5, only 1 out of the 12 tests analyzed consisted of results with greater than a 70% match. Therefore, it is concluded that Equation 2.9 is not suitable for the experimental conditions of the tests.

These results are surprising, because Barsanti et. al [12] specified the ranges this equation is applicable for. These ranges are for  $0.26 < Pr < 6.04$ ,  $53,025 < Re_{ji} < 210,709$ ,  $10 \leq d_{ji} \leq 20$  mm, and  $13^{\circ}\text{C} \leq T_{\text{water}} \leq 40^{\circ}\text{C}$ . At 15 l/min, the  $d_{ji}$  was 7.6 mm, which is slightly below the lower limit of 10 mm. However, the  $d_{ji}$  for 30 l/min and 45 l/min, were within the range at 10.6 mm and 12.6 mm, respectively. For all the tests, the Prandtl and Reynold's numbers were in the specified range.

For the tests performed at lower water temperatures of  $30^{\circ}\text{C}$  and  $40^{\circ}\text{C}$ , the correlation highly underestimated the heat flux (see Table 5.5), even though they were within the specified temperature range. Since these temperatures are within the water temperature range, then Equation 2.9 must be applicable for experimental conditions that result in lower heat fluxes. Since the Reynold's numbers used are within the specified range, this rules out the possibility of a different flow rate.

However, the initial plate temperature was not specified. Lower plate temperatures result in lower heat fluxes. Consequently, Equation 2.9 must be applicable for initial plate temperatures lower than  $900^{\circ}\text{C}$ . More experimental tests need to be performed under the same flow rates at lower initial plate temperatures to see if this equation matches more accurately with the data.

### 5.5.3 Results for Equation 2.10

Figure 5.12 and Table 5.6 summarize the percent of the experimental data that matched within the  $\pm 30\%$  region of Equation 2.10 (see Table 5.1). In the table and figure, a positive sign indicates that the correlation was above the experimental heat flux and a negative sign means the correlation was below the heat flux.

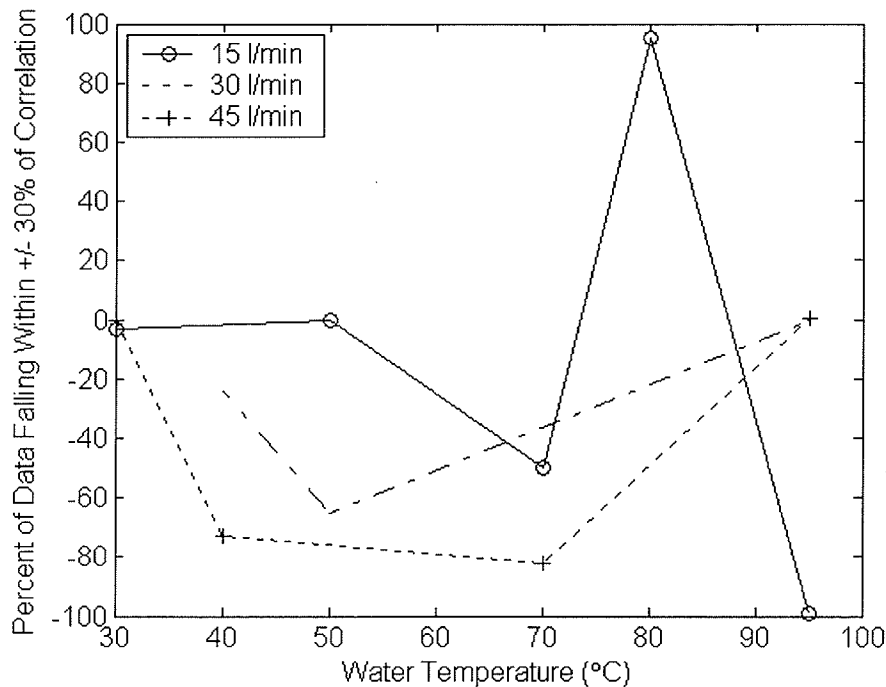


Figure 5.12: Percent of the experimental data that fell within  $\pm 30\%$  of Equation 2.10

Table 5.6: Percent of the experimental data that fell within  $\pm 30\%$  of Equation 2.10

Flow Rate	Water Temperature						
	30°C	40°C	50°C	60°C	70°C	80°C	95°C
15 l/min	-3%	:	-0.2%	:	-50%	95%	-99%
30 l/min	:	-24%	-65%	:	:	:	0%
45 l/min	0%	-73%	:	:	-82%	:	0.1%

### 5.5.3.1 Results for 15 l/min

Looking at Table 5.6, the Equation 2.10 matched well with the data at 15 l/min at water temperatures above 70°C. Figure 5.13, shows the correlation compared with the experimental heat flux of test M9515, with a which 99% match (see Table 5.6).

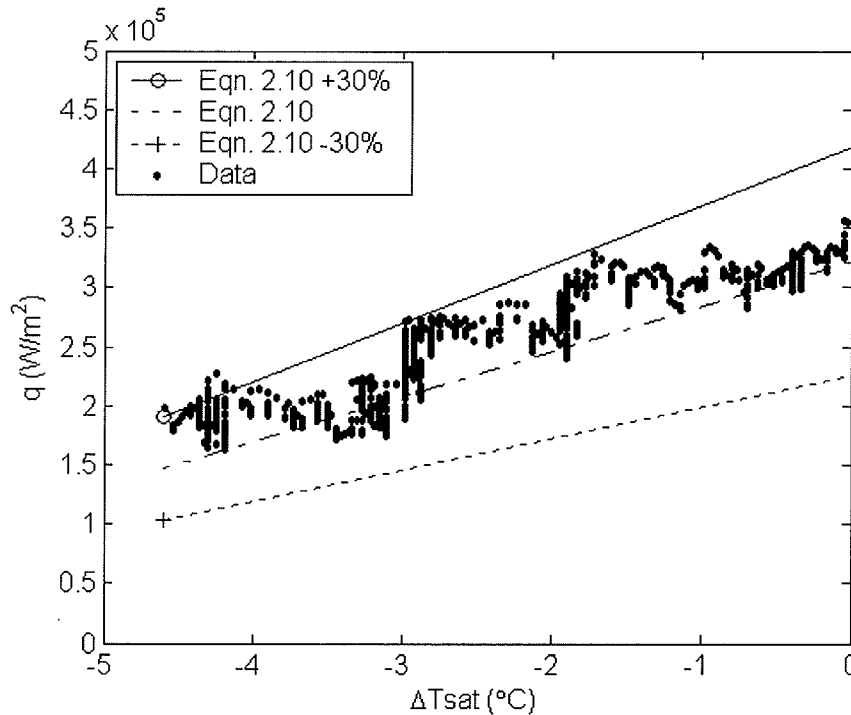
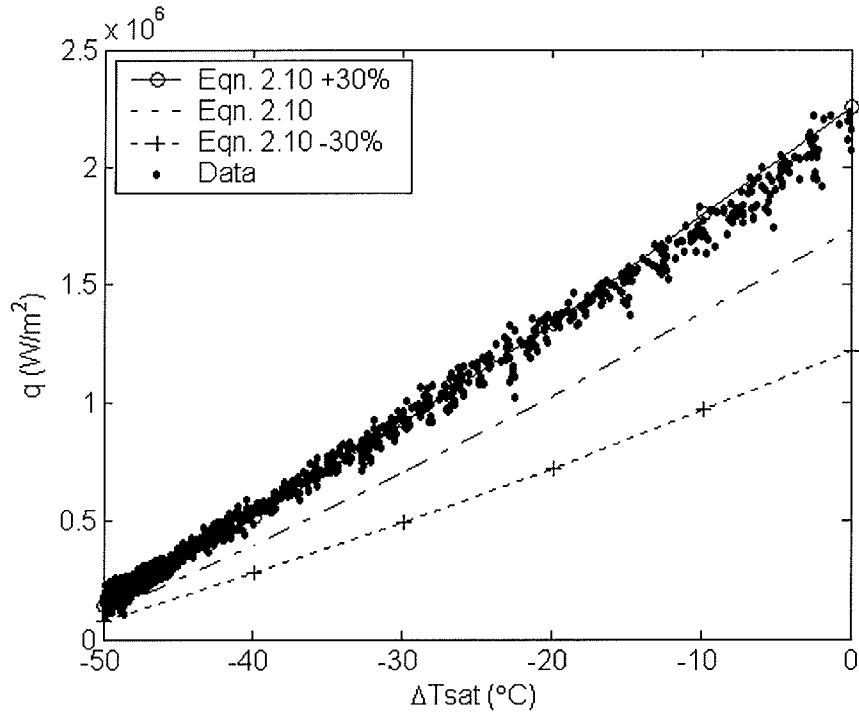


Figure 5.13: Equation 2.10 compared with the data of test M9515

### 5.5.3.2 Results for 30 l/min

Referring to Table 5.6, the experimental data was underestimated by Equation 2.10 at all the temperatures at 30 l/min. The best matched occurred at a water temperature of 50°C (Figure 5.14), with 65% matching. In Figure 5.15, at a water temperature of 95°C, no data matched within the  $\pm 30\%$  region.



**Figure 5.14: Equation 2.10 compared with the data of test H5030**

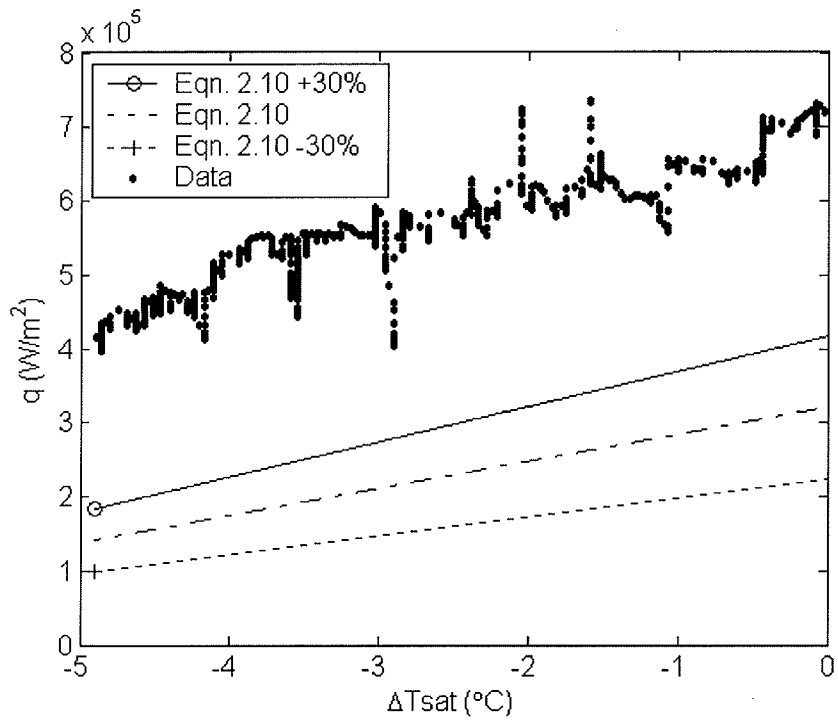


**Figure 5.15: Equation 2.10 compared with the data of test M9530**

### 5.5.3.3 Results for 45 l/min

At a water temperature of 30°C, the data was underestimated by the equation at 45 l/min, as shown in Figure 5.16. However with increasing water temperature, the correlation gradually rose higher to match with the heat flux well at a water temperature of 40°C with a 73% match (see Figure 5.17 and Table 5.6). Equation 2.10 continued to rise above the heat flux until was overestimated at 95°C with only 0.1% of the data matching within the +30% region of the correlation (see Figure 5.18 and Table 5.6).

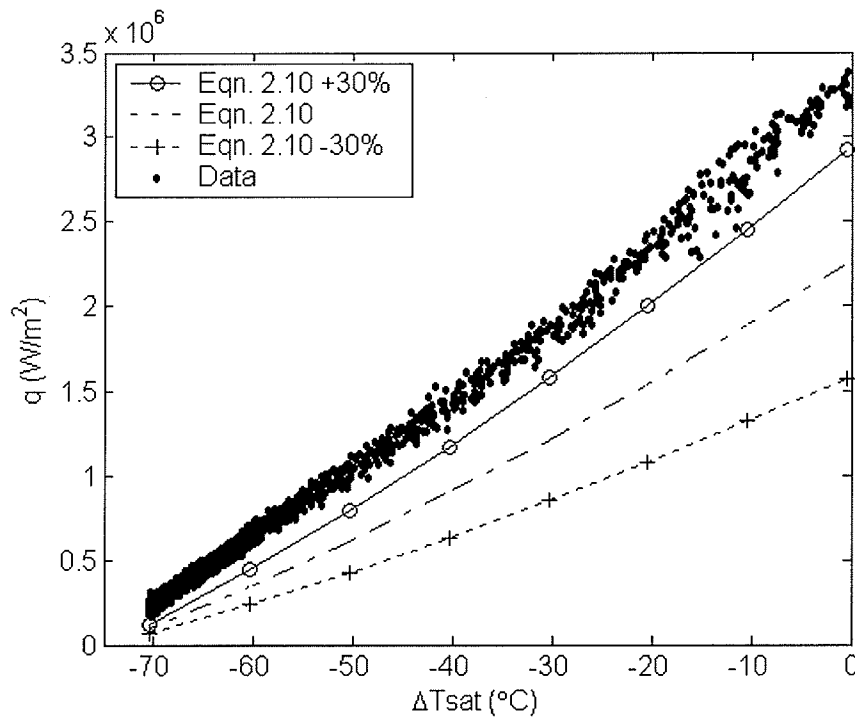
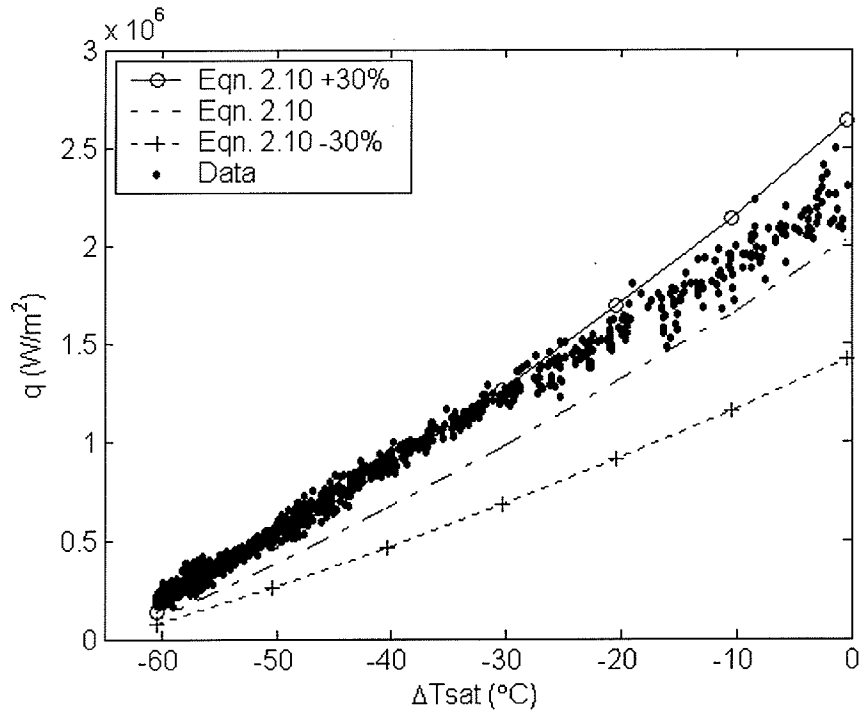
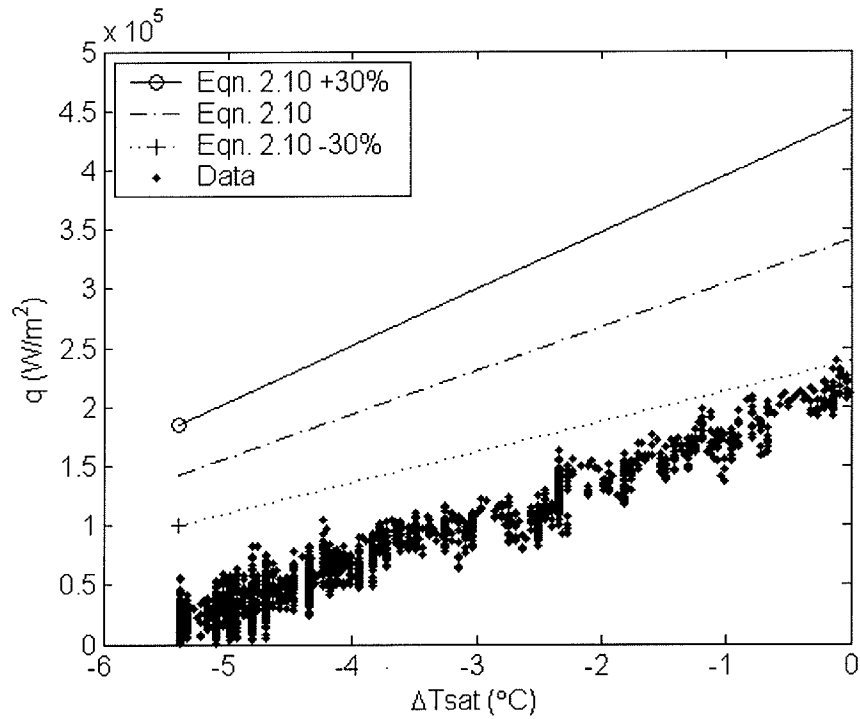


Figure 5.16: Equation 2.10 compared with the data of test H3045



**Figure 5.17: Equation 2.10 compared with the data of test H4045**



**Figure 5.18: Equation 2.10 compared with the data of test M9545**

#### 5.5.3.4 Summary

The ranges specified by Faggiani and Grassi [13] were  $Z/d_{ji}=5$ ,  $Re>77,000$ , and  $0.5 \leq Pr \leq 50$ . For the analysis, the Reynold's numbers and Prandtl numbers were used were within the range. However, the  $Z/d_{ji}$  used for the experimental data ranged from 119 to 197 at 15 l/min to 45 l/min, respectively, which was considerably higher than the specified parameter of  $Z/d_{ji}=5$ . However, as determined earlier in Section 2.4.6, there are contradictory results as to the effects of nozzle-to-surface spacing on the heat flux. Therefore, it is difficult to say what the trend is for heat transfer at the high ratios used for the experiments. Therefore, Equation 2.10 may not be applicable to high nozzle height to jet diameter ratios. Furthermore, the applicable water temperature range and initial plate temperature was not specified.

Looking at Table 5.6, only 3 out of the 12 tests examined consisted of results where at least 70% of the experimental data fell within the region of  $\pm 30\%$  of Equation 2.10. At 15 l/min, this occurred at water temperatures of 80°C and 95°C. It is assumed that if the experimental results were sound, that it most likely would have matched as well with the data as at water temperatures of 80°C and 95°C. At 45 l/min, this occurred at a water temperature of 70°C. This suggests that this equation is applicable at conditions which result in lower heat fluxes. This can be due to higher water temperatures and/or lower jet velocities, and/or lower initial plate temperatures. As to which is the correct answer, more experiments need to be performed at lower initial plate temperatures ( $<900^\circ\text{C}$ ), lower jet velocities ( $<5\text{ m/s}$ ) and higher water temperatures ( $>70^\circ\text{C}$ ) to see whether the correlation provides a better fit of the data.

### 5.5.4 Results for Equation 2.11

Figure 5.19 and Table 5.7 summarize the percent of the experimental data that fell within the  $\pm 30\%$  region of Equation 2.11 (see Table 5.1). In the table and figure, a positive sign indicates that the correlation was above the experimental heat flux and a negative sign means the correlation was below the heat flux.

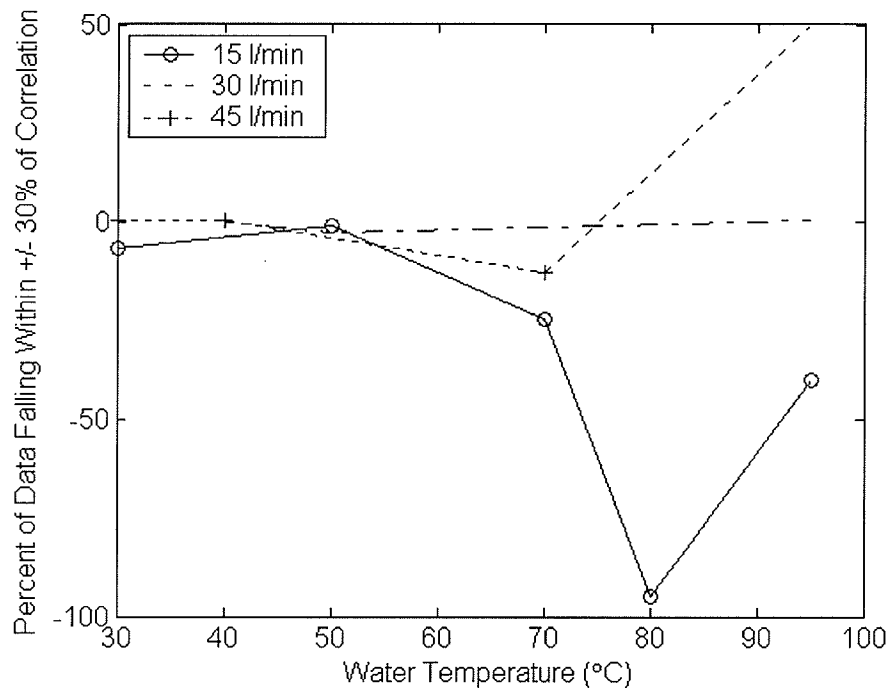


**Figure 5.19: Percent of the experimental data that fell within  $\pm 30\%$  of Equation 2.11**

**Table 5.7: Percent of the experimental data that fell within  $\pm 30\%$  of Equation 2.11**

Flow Rate	Water Temperature						
	30°C	40°C	50°C	60°C	70°C	80°C	95°C
15 l/min	-7%	:	-1.0%	:	-25%	-95%	-40%
30 l/min	:	0%	-3%	:	:	:	0%
45 l/min	0%	0%	:	:	-13%	:	50%

#### 5.5.4.1 Results at 15 l/min

In all instances, Equation 2.11 underestimated the heat flux at 15 l/min. In Figure 5.19, it can be seen that there was no particular trend for how the equation matched with the data. Compared with the data of test H3015 in Figure 5.20, Equation 2.11 underestimated the heat flux. It also underestimated the heat flux of test H5015 (see Table 5.7). Compared with test M7015, in Figure 5.21, the correlation underestimated the heat flux to a lesser degree. Looking at the graph shows this occurred because the experimental heat flux decreased at a greater rate than the correlation did, resulting in a poorer match.

However at a water temperature of 80°C, (Figure 5.22) the equation matched the best at this flow rate with 95% of the experimental data matching (see Table 5.7). Then it dropped further below the data at a water temperature of 95°C, as shown in Figure 5.23. It is difficult to say why there was no pattern. It is most likely due to experimental variations between the different water temperatures because it was determined earlier that Equation 2.11 dropped at a constant rate as the water temperature increased.

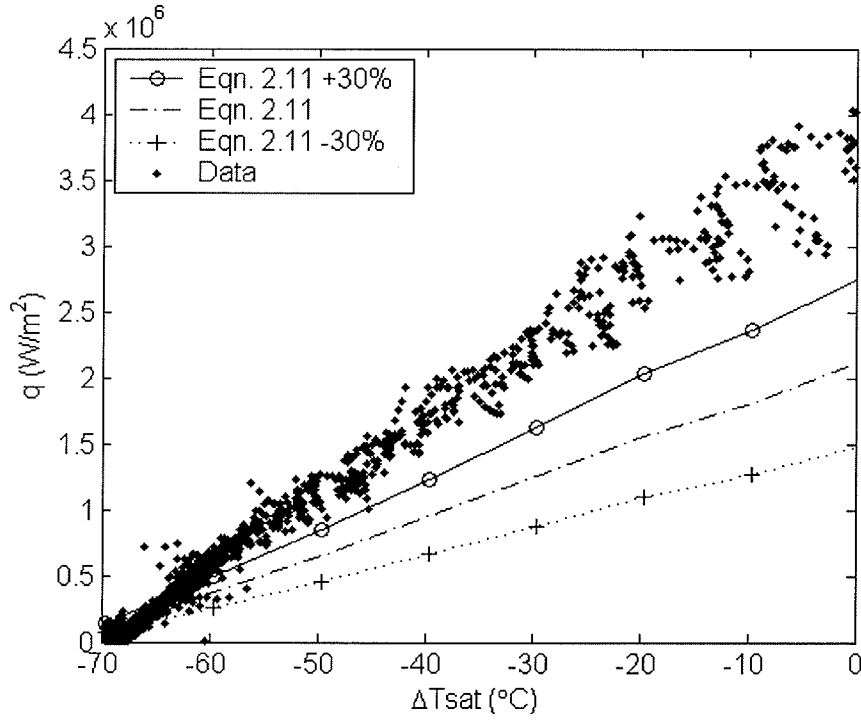


**Figure 5.20: Equation 2.11 compared with the data of test H3015**

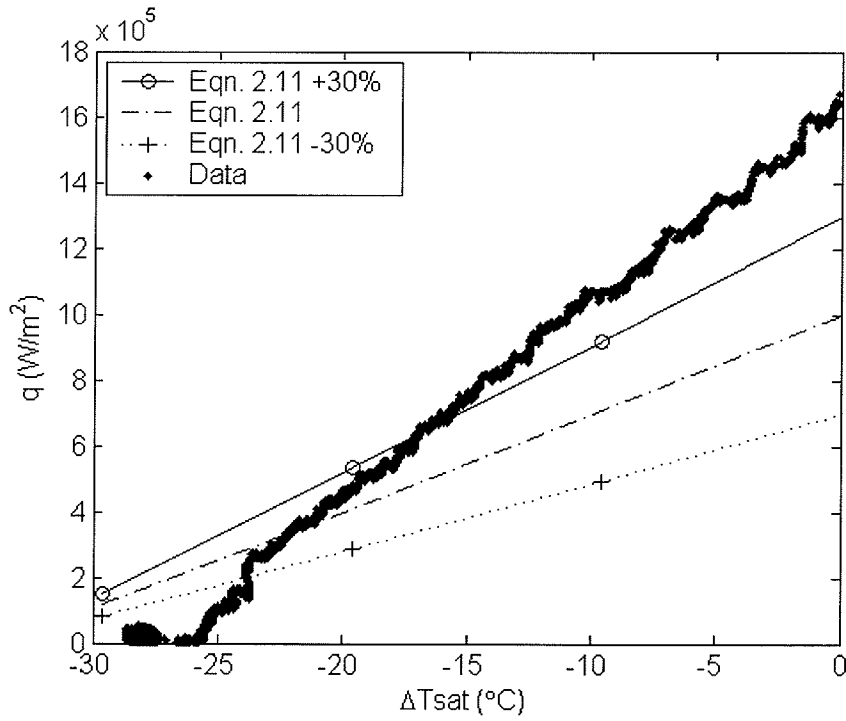


**Figure 5.21: Equation 2.11 compared with the data of test M7015**

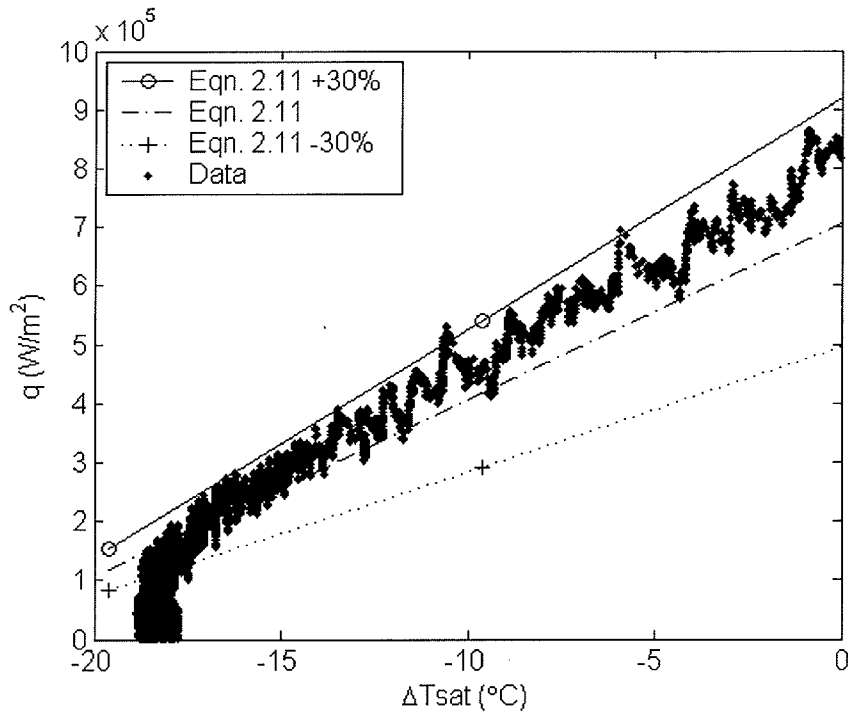


Figure 5.22: Equation 2.11 compared with the data of test M8015

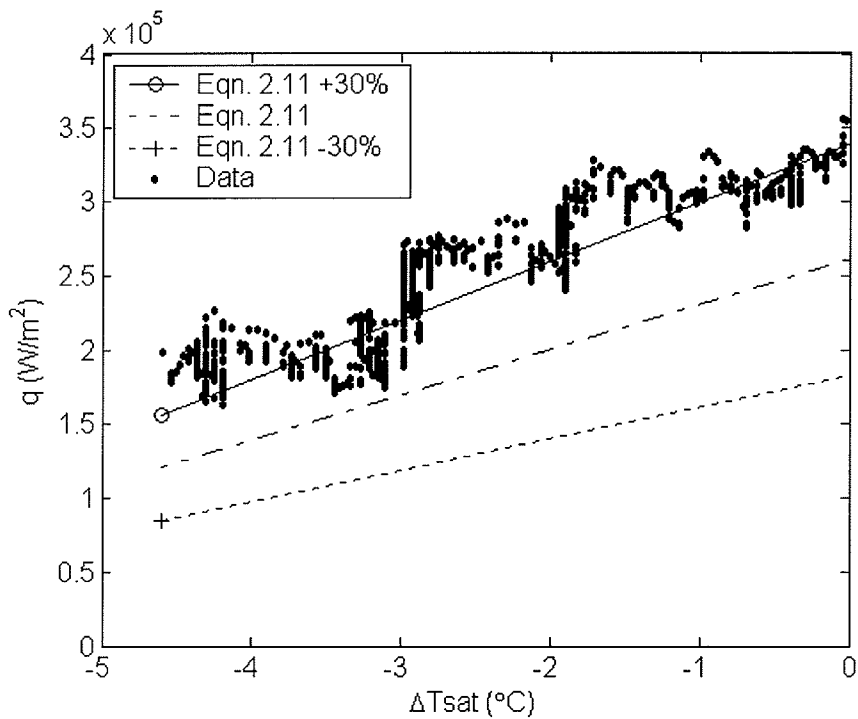
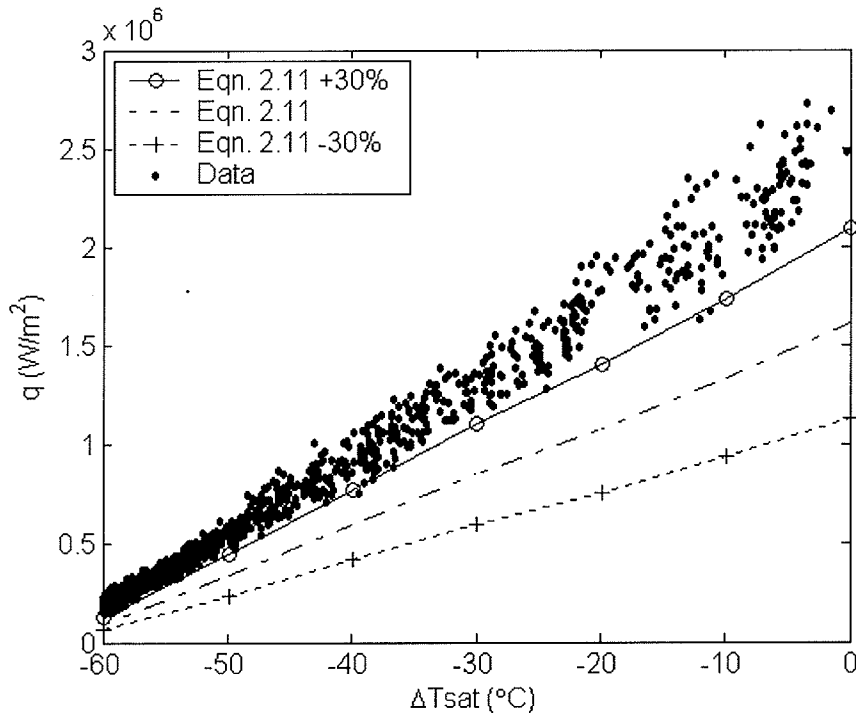


Figure 5.23: Equation 2.11 compared with the data of test M9515

### 5.5.4.2 Results at 30 l/min

The data did not match well at 30 l/min. As can be seen compared with test H4030 in Figure 5.24, Equation 2.11 underestimated the heat flux. It also underestimated the heat flux at all the other water temperatures (see Table 5.7).



**Figure 5.24: Equation 2.11 compared with the data of test H4030**

### 5.5.4.3 Results at 45 l/min

Compared with test M7045, Equation 2.11 underestimated the heat flux, as shown in Table 5.7. It can be seen that the percent matching made a jump from 13% matching at a water temperature of 70°C to 50% matching at a water temperature of 95°C (see Figure 5.25, Figure 5.26, and Table 5.7). As occurred at the same temperature at 15 l/min, the experimental heat flux increased at a greater rate than the correlation did. This explains why the heat flux of test M7045 was underestimated shown in Figure 5.25, and rose to overestimate the heat flux of test M9545 in Figure 5.26.

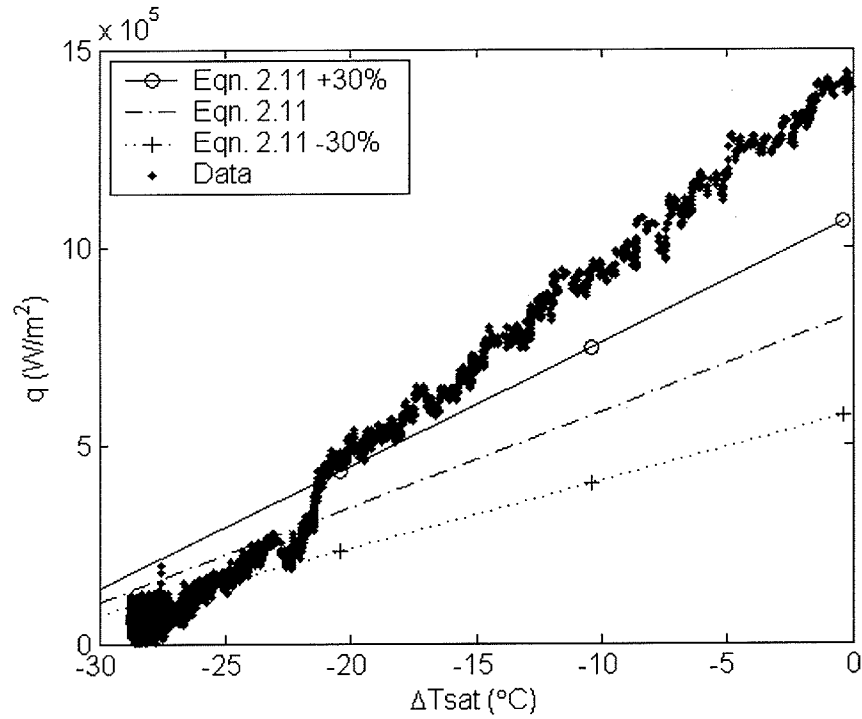


**Figure 5.25: Equation 2.11 compared with the data of test M7045**

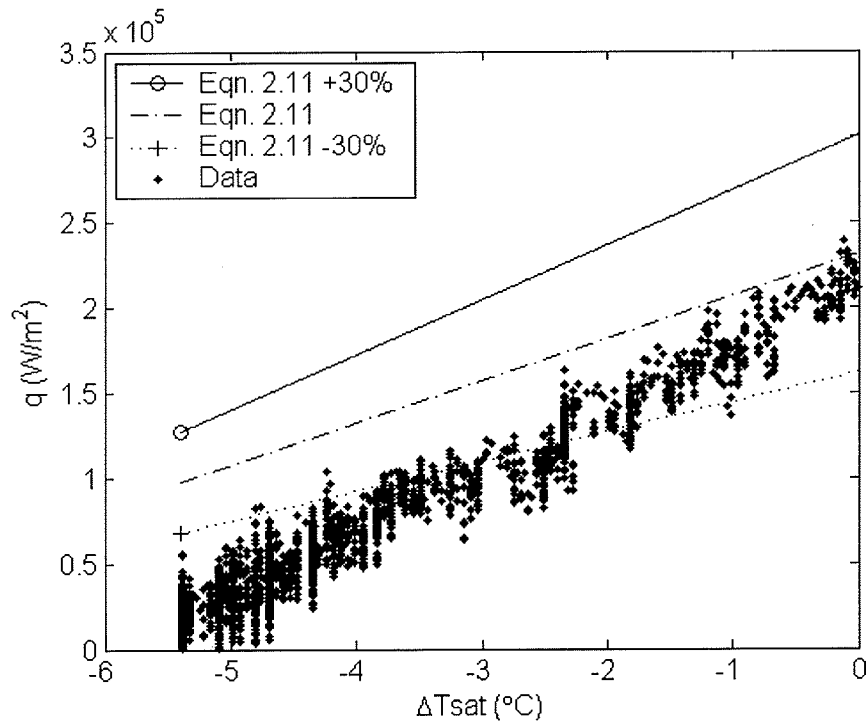


**Figure 5.26: Equation 2.11 compared with the data of test M9545**

#### 5.5.4.4 Summary

Looking at Table 5.7, only 1 out of the 12 tests analyzed contained results where at least 70% of the data fell within the  $\pm 30\%$  region of Equation 2.11. Therefore, it is concluded that Equation 2.11 should not be used to represent the data.

In Table 5.1, only the Prandtl number range was specified. Since the heat flux was underestimated for 11 out of 12 of the tests, then this equation is applicable for experimental conditions that produce lower heat flux. Two parameters that can be changed to cause this is at reduced the flow rates and/or reduced initial plate temperature. More experiments at flow rates below 15 l/min and initial plate temperatures below 900°C to test this hypothesis.

#### 5.5.5 Results for Equation 2.12

Figure 5.27 and Table 5.8 summarize the percent of the experimental data that fell within the  $\pm 30\%$  region of Equation 2.12 (see Table 5.1). In the table and figure, a positive sign indicates that the correlation was above the experimental heat flux and a negative sign means the correlation was below the heat flux.

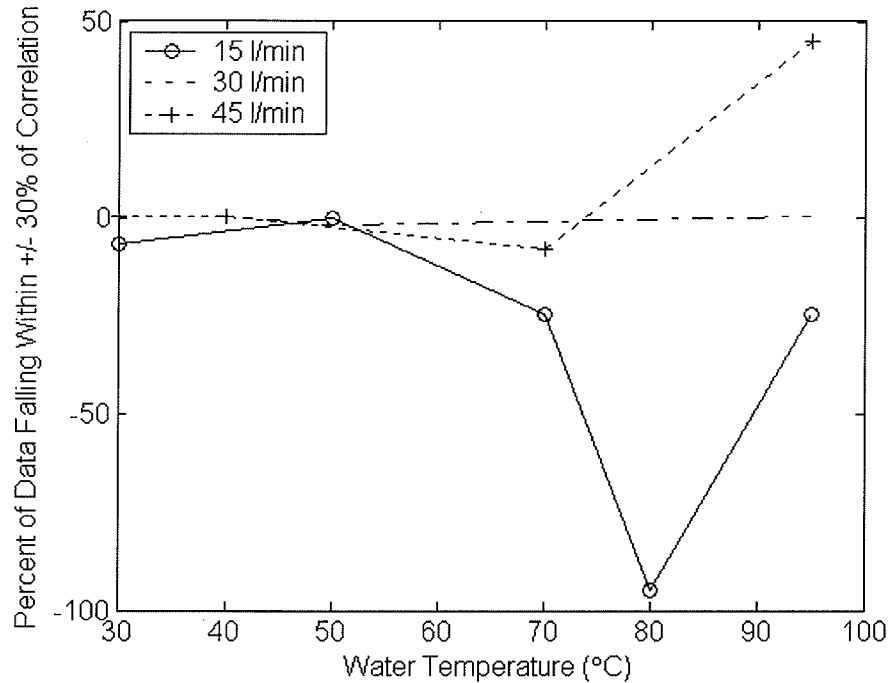


**Figure 5.27: Percent of the experimental data that fell within  $\pm 30\%$  of Equation 2.12**

**Table 5.8: Percent of the experimental data that fell within  $\pm 30\%$  of Equation 2.12**

Flow Rate	Water Temperature						
	30°C	40°C	50°C	60°C	70°C	80°C	95°C
15 l/min	-7%	:	-0.1%	:	-25%	-95%	-25%
30 l/min	:	0%	-2%	:	:	:	0%
45 l/min	0%	0%	:	:	-8%	:	45%

Figure 5.28 compares Equation 2.11 with Equation 2.12 at 15 l/min and a water temperature of 30°C. As it can be seen, their heat flux is almost exactly the same. The same trend occurred for all the other tests. This explains why Equation 2.12 had very similar results as Equation 2.11, when comparing the results in Table 5.8 for Equation 2.12 and Table 5.7 for Equation 2.11. Therefore, Equation 2.12 had the same trends as Equation 2.11 did.

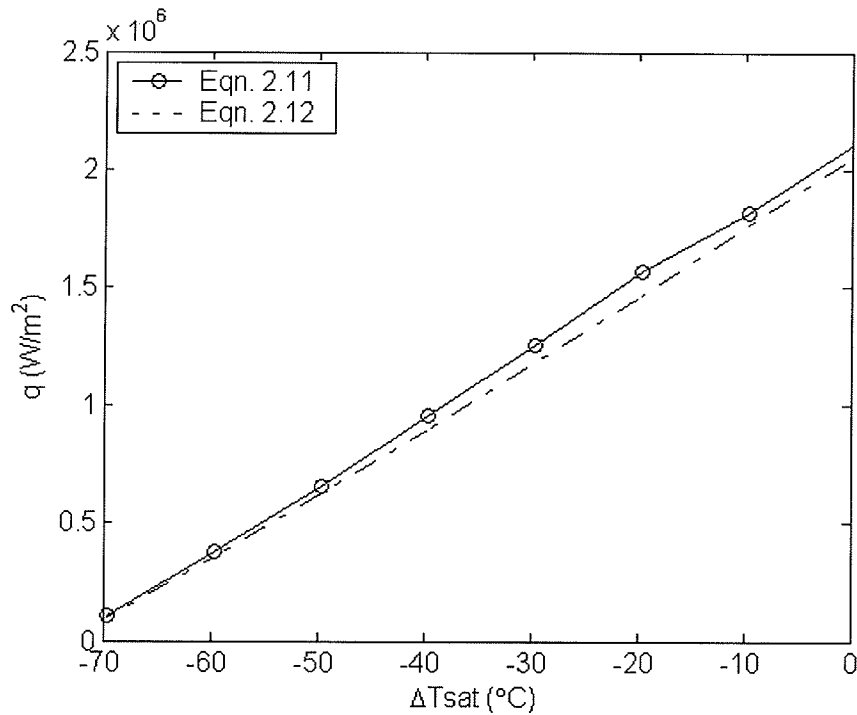


**Figure 5.28: Equation 2.11 compared with 2.12 at 15 l/min and  $T_{\text{water}} = 30\text{°C}$**

#### 5.5.5.1 Summary

Looking at Table 5.8, only 1 out of the 12 tests evaluated consisted of results where greater than 70% of the experimental data matched within  $\pm 30\%$  of Equation 2.12. Furthermore, there was no particular pattern in how the percent matching varied between the different water temperatures. Therefore, it can be concluded this equation is not a good representation of the data.

Looking at the equation in Table 5.1, only a Prandtl number range was provided. Since the data matched poorly, then it can be hypothesized that the experimental conditions Equation 2.12 best apply to is not within the range of those experiments performed.

The majority the time this equation underestimated the heat flux (see Table 5.8). Therefore, it must be applicable for lower heat fluxes. Lower heat fluxes occur at higher

water temperatures. However, high water temperatures were evaluated. Lower heat fluxes can also occur at lower flow rates. Therefore, it is possible that this equation is applicable for flow rates less than 15 l/min (or jet impingement velocity of 5.5 m/s). Also, a lower initial plate temperature would also yield lower heat fluxes. In addition, perhaps this equation is meant to be used for jet impingement experiments performed at plate temperatures lower than 900°C. To test these theories, experiments should be performed at lower flow rates and lower initial plate temperatures to see how well Equation 2.12 matches with the data.

### **5.5.6 Results for Equation 2.13**

Figure 5.29 and Table 5.9 present the percent of the experimental data that matched within  $\pm 30\%$  of Equation 2.13. In the table and figure, a positive sign indicates that the correlation was above the experimental heat flux and a negative sign means the correlation was below the heat flux. Equation 2.13 poorly matched with the experimental data and underestimated the heat flux in all instances.

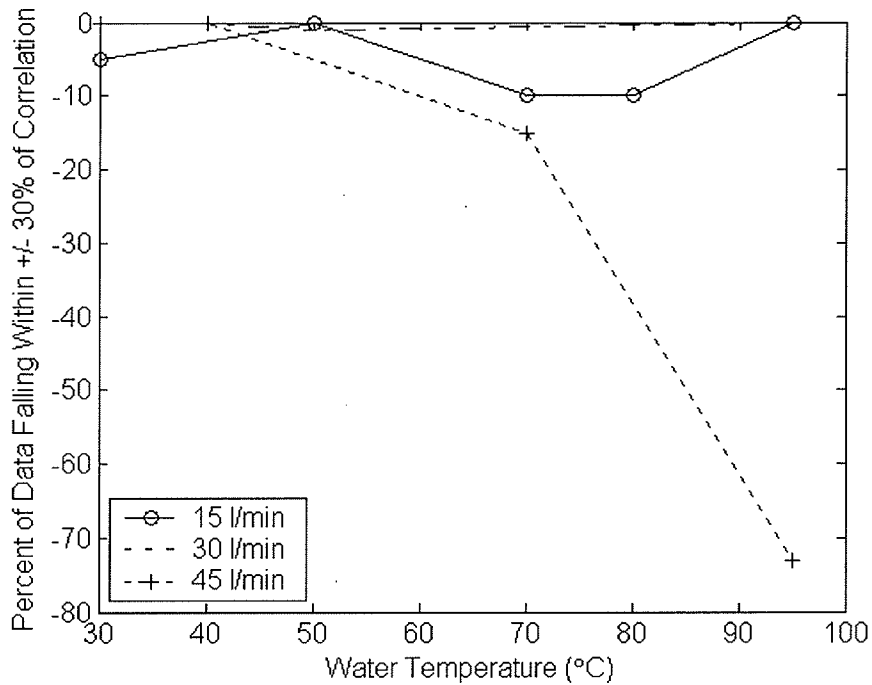


**Figure 5.29: Percent of the experimental data that fell within  $\pm 30\%$  of Equation 2.13**

**Table 5.9: Percent of the experimental data that fell within  $\pm 30\%$  of Equation 2.13**

Flow Rate	Water Temperature						
	30°C	40°C	50°C	60°C	70°C	80°C	95°C
15 l/min	-5%	:	-0.2%	:	-10%	-10%	0%
30 l/min	:	0%	-1%	:	:	:	0%
45 l/min	0%	0%	:	:	-15%	:	-73%

In Table 5.9, at 45 l/min, at a water temperature of 80°C to 95°C, the percent of matching data jumped from 12% to 73%. At this flow rate, as the water temperature increased, the correlation seemed to “rise” upwards to match closer with the heat flux, when comparing results between tests H3045 (see Figure 5.30), M7045 (see Figure 5.31), and M9545 (see Figure 5.32).

From earlier, it was determined that as the water temperature increased, the heat flux decreased for Equation 2.13. It was also determined that the experimental heat flux decreased with increasing water temperature. Therefore, the experimental heat flux must

have decreased at a greater rate than Equation 2.13 did, which explains why it matched closer and closer with the heat flux at higher water temperatures at 45 l/min.

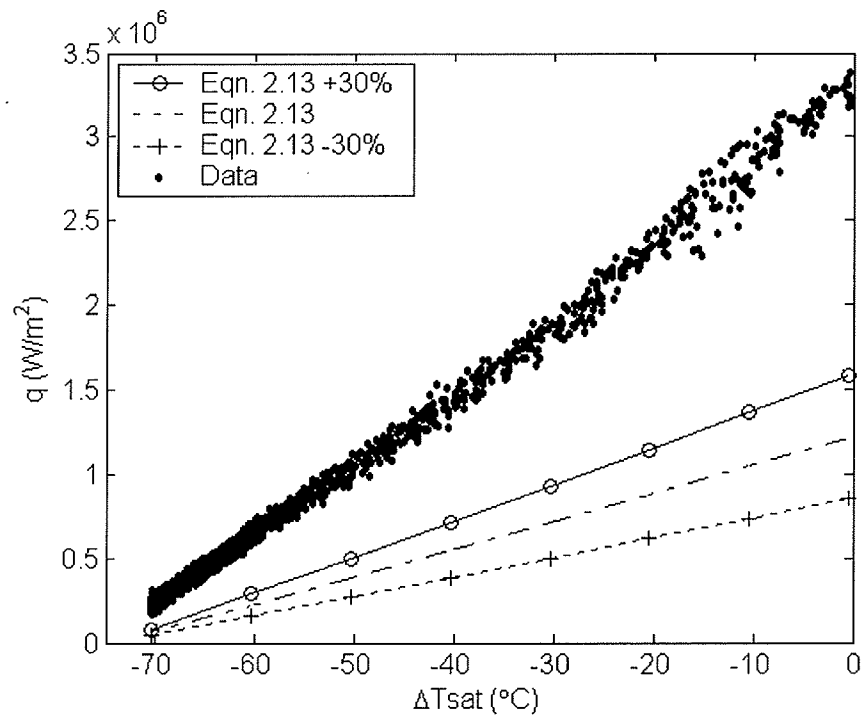


**Figure 5.30: Equation 2.13 compared with the data of test H3045**

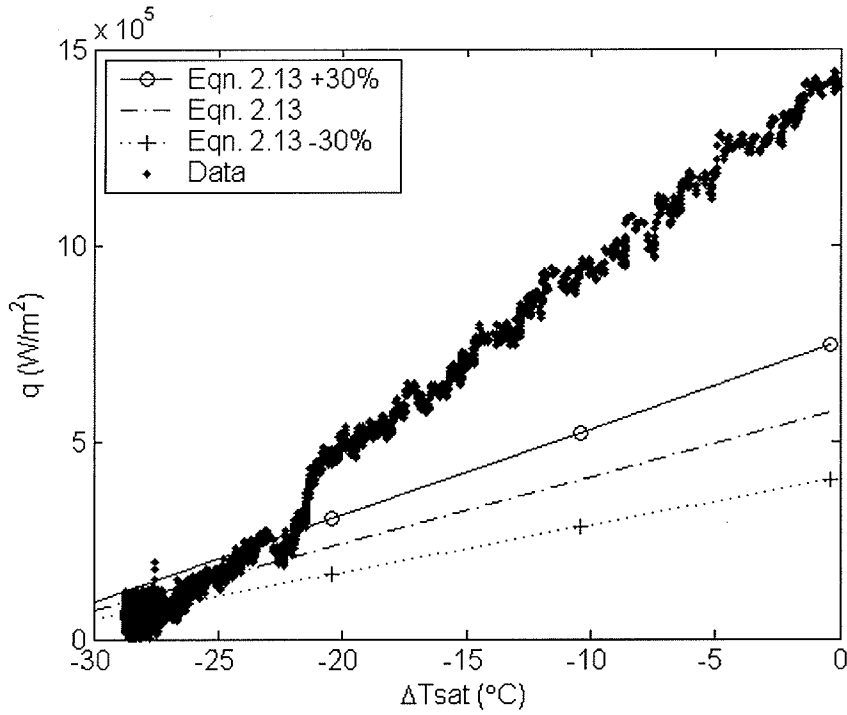


**Figure 5.31: Equation 2.13 compared with the data of test M7045**

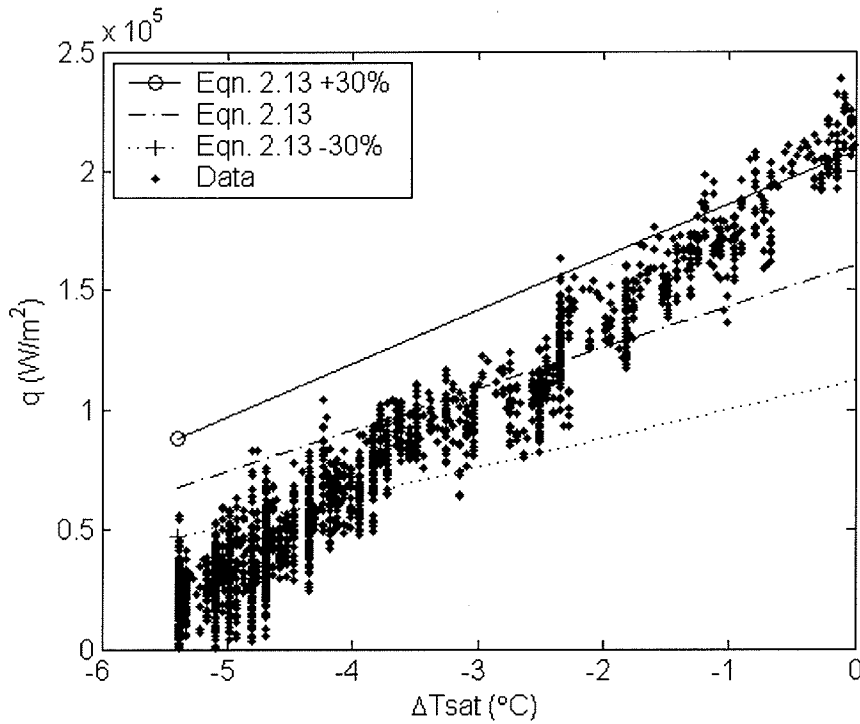


**Figure 5.32: Equation 2.13 compared with the data of test M9545**

In summary, Equation 2.13 underestimated the heat flux at all the flow rates. Looking at Table 5.9, only 1 test out of 12 contained results where at least 70% of the experimental data fell with the  $\pm 30\%$  range of Equation 2.13. Therefore, it is concluded that this equation is not a good match for the experimental. Stevens and Webb [15] determined Equation 2.13 and Equation 2.14 under the same experimental conditions. Therefore, the results for Equation 2.14 will be discussed next.

### **5.5.7 Results for Equation 2.14**

Figure 5.33 and Table 5.10 summarize the percent of the experimental data that fell within  $\pm 30\%$  of Equation 2.14 (see Table 5.1). In the table and figure, a positive sign indicates that the correlation was above the experimental heat flux and a negative sign means the correlation was below the heat flux. Results at each of the different flow rates will be provided. Then a general conclusion will be drawn out from this as to the experimental conditions this equation applies to. Since this equation was performed under the same conditions as Equation 2.13, these two equations will be compared.

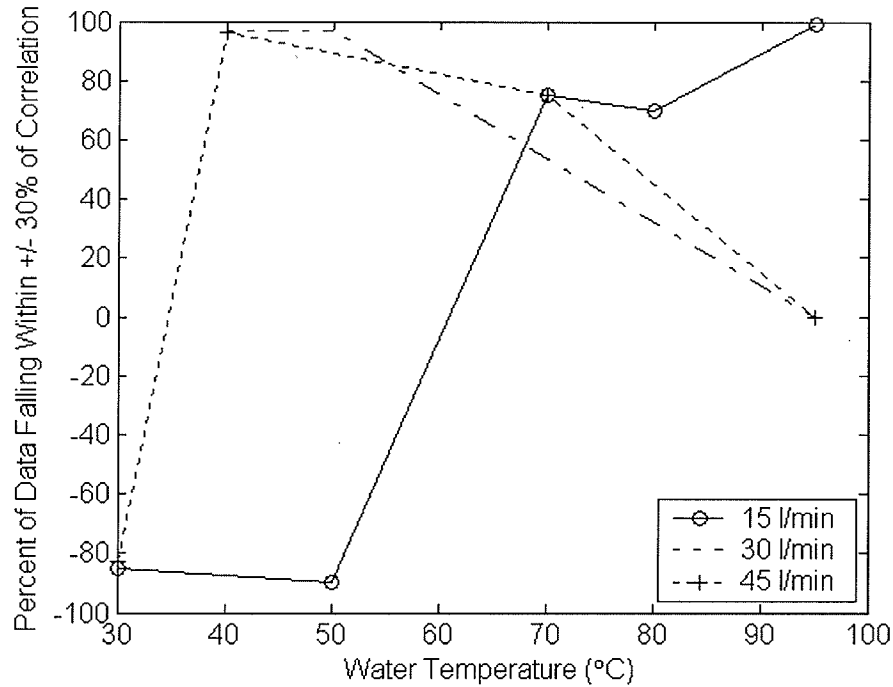


**Figure 5.33: Percent of the experimental data that fell within  $\pm 30\%$  of Equation 2.14**

**Table 5.10: Percent of the experimental data that fell within  $\pm 30\%$  of Equation 2.14**

Flow Rate	Water Temperature						
	30°C	40°C	50°C	60°C	70°C	80°C	95°C
15 l/min	-85%	:	-90.0%	:	75%	70%	99%
30 l/min	:	97%	97%	:	:	:	0%
45 l/min	-83%	96%	:	:	75%	:	0%

### 5.5.7.1 Results at 15 l/min

At all of the different water temperatures, at least 70% of the data matched within  $\pm 30\%$  of Equation 2.14 at a flow rate of 15 l/min (Table 5.10). Compared with tests H3015 and H5015, Equation 2.14 slightly underestimated the heat flux. For test M8015 in Figure 5.34, the correlation slightly overestimated the heat flux. The same pattern occurred at water temperatures of 70°C and 95°C (see Table 5.10), where the correlation slightly overestimated the heat flux.

Both the correlation and experimental heat flux decreased with increasing water temperature. Therefore, at this instance, the experimental heat flux must have decreased at a greater rate than Equation 2.14 did, allowing correlation to be above the heat flux.

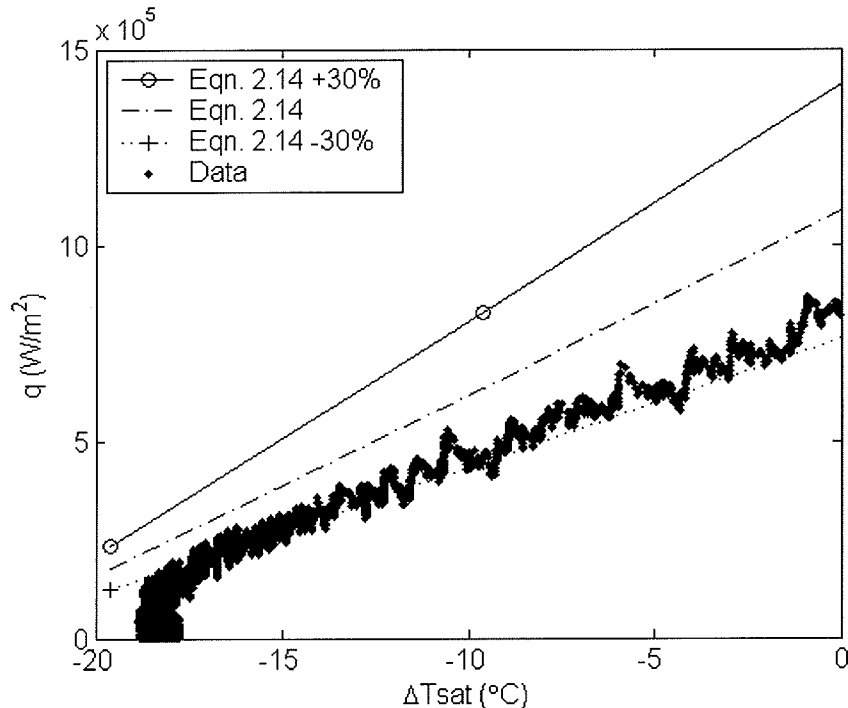


**Figure 5.34: Equation 2.14 compared with the data of test M8015**

### 5.5.7.2 Results at 30 l/min

At water temperatures of 40°C and 50°C, the data was correlated well at 97% falling within the  $\pm 30\%$ , where the correlation was slightly above the heat flux (see Table 5.10). Figure 5.35 shows Equation 2.14 compared with the data of test H4030. The pattern took a twist for test M9530, where the correlation highly underestimated the experimental heat flux, as can be seen in Figure 5.36. It is difficult to determine why this occurred considering there was no comparison made at water temperatures of 60°C, 70°C, and 80°C due to experimental error.

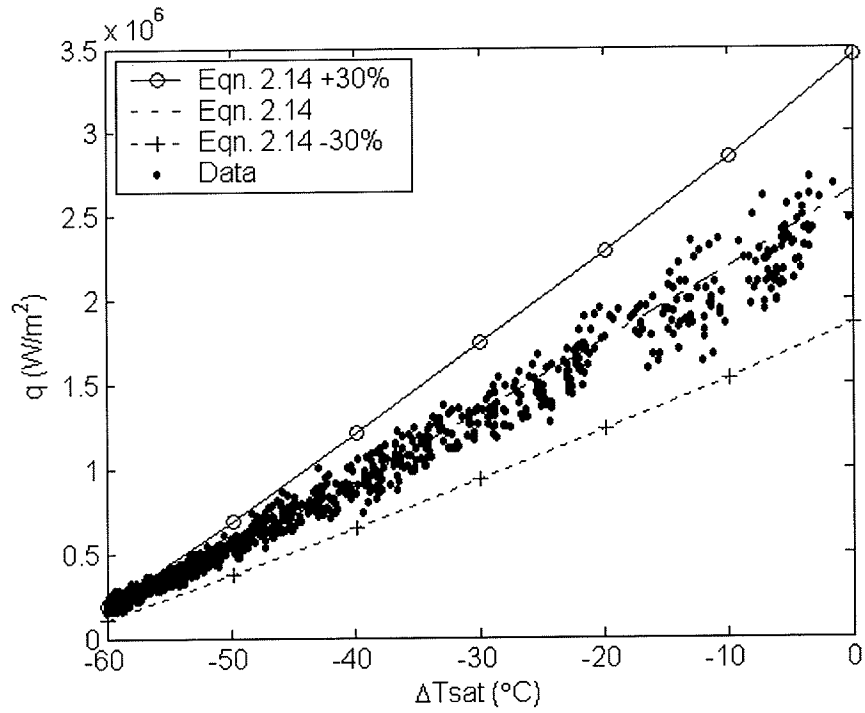


Figure 5.35: Equation 2.14 compared with the data of test H4030

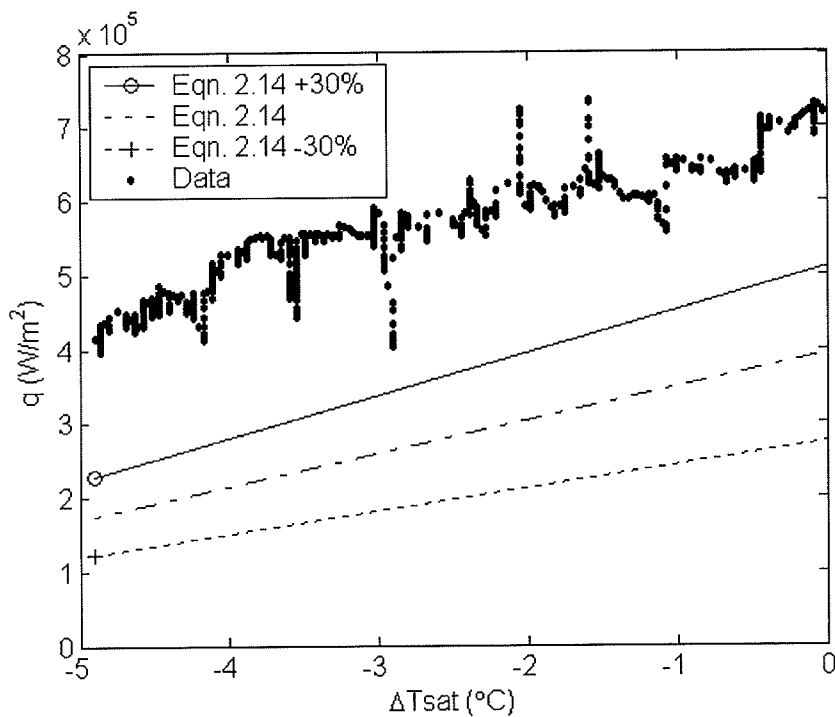
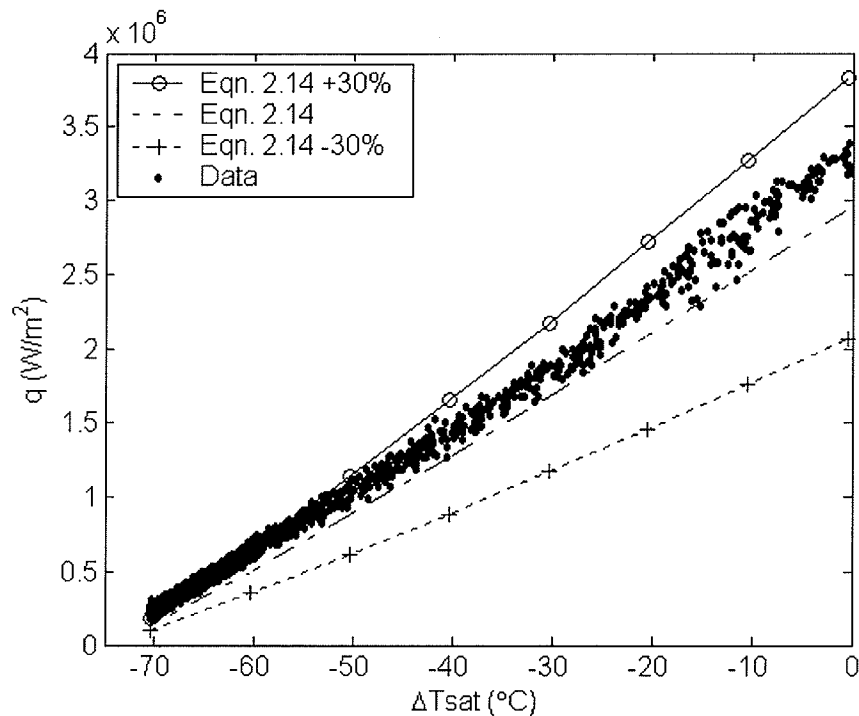


Figure 5.36: Equation 2.14 compared with the data of test M9530

### 5.5.7.3 Results at 45 l/min

Figure 5.37 shows Equation 2.14 compared with the experimental data of test H3045. It is revealed that approximately 83% of the experimental heat flux fell within the range of  $\pm 30\%$  of the correlation, as shown in Table 5.10. Also, the correlation underestimated the heat flux.



**Figure 5.37: Equation 2.14 compared with the data of test H3045**

However, for test H4045, the correlation rose above the heat flux, as can be seen in Figure 5.38. The correlation continue to rise above the experimental heat flux with increasing water temperature until it was no longer within the  $\pm 30\%$  range at a water temperature of  $95^{\circ}\text{C}$ , in Figure 5.39. From earlier, it was determined that Equation 2.14 decreased with increasing water temperature. The experimental heat flux also decreased with increasing water temperature. Therefore, at 45 l/min, the experimental heat flux must have decreased at a greater rate than the correlation did.

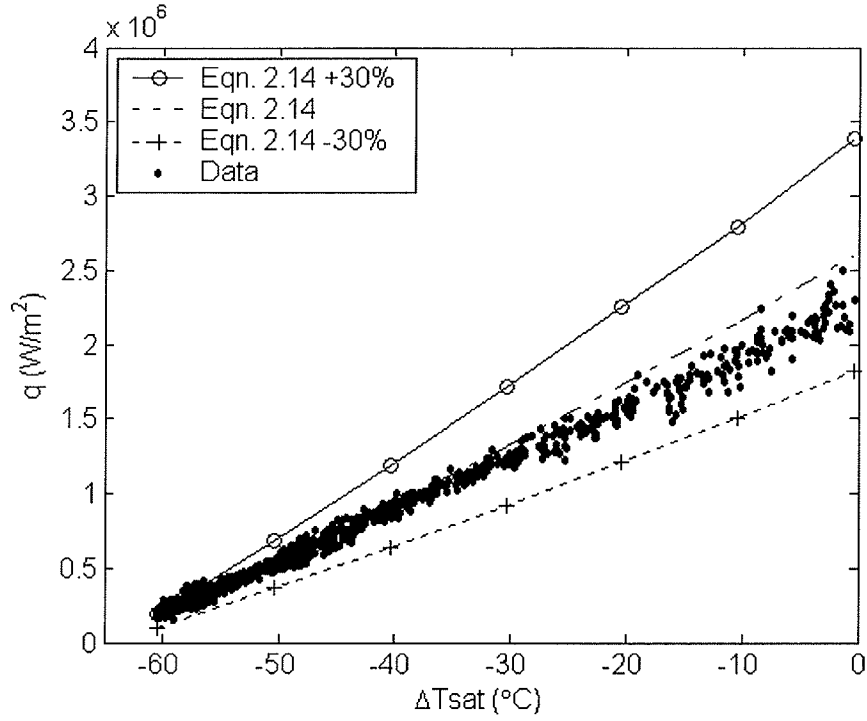


Figure 5.38: Equation 2.14 compared with the data of test H4045

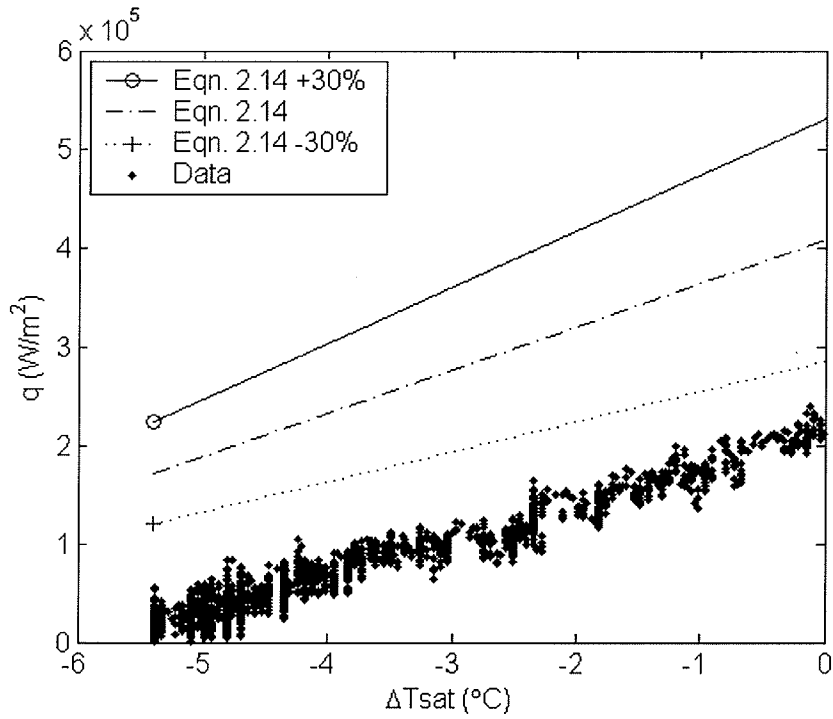


Figure 5.39: Equation 2.14 compared with the data of test M9545

#### **5.5.7.4 Summary**

The patterns for the way which the correlation matched with the data varied between the different flow rates. At 15 l/min, the correlation matched well consistently through all the water temperatures. At 30 l/min, the correlation matched well at water temperatures of 40°C and 50°C. However at a water temperature of 95°C, the correlation underestimated the experimental heat flux with a 0% match (see Table 5.10).

At 45 l/min, the correlation gradually rose above the experimental heat flux with increasing water temperature. The variation in trends between each of the flow rates is most likely due to experimental error between the flow rates at the different water temperatures.

However, what can be determined from the results is that Equation 2.14 provides a good representation of the experimental data. Of the 12 tests reviewed, 10 of the tests contained results of at least 70% of the experimental data falling within the region of  $\pm 30\%$  of Equation 2.14 (see Table 5.10). This occurred at all the water temperatures tested at 15 l/min, and water temperatures up to 80°C at 30 l/min and 45 l/min. Therefore, it is concluded that Equation 2.14 can be used to represent the data from 15 l/min to 45 l/min at water temperatures up to 80°C. It can also be said that it is applicable for an initial plate temperature of 900°C.

#### **5.5.8 Comparison Between Equations 2.13 and 2.14**

It was determined earlier that Equation 2.13 poorly represented the experimental data. Yet Equation 2.14 coincided with the data well. Both equations were presented by Stevens and Webb [15] under the same experimental conditions.

In their paper, Stevens and Webb [15], reported that Equation 2.14 matched with their data better than Equation 2.13 did. The same trend occurred when comparing these two equations with the data. Therefore, it is recommended that Equation 2.14 be used instead of 2.13 to predict the experimental data.

The main difference between the two equations is Equation 2.14 incorporates a  $v_j/d_j$  parameter, as seen in Table 5.1. This helps provide a better relation that takes into account the change in velocity and jet diameter (and hence the flow rate which these two variables depend upon).

### 5.5.9 Summary of Results

Table 5.11 shows the number and percentage of tests where at least 70% of the experimental data matched with  $\pm 30\%$  of each correlation analyzed. It can be seen that Equation 2.14 proved to best represent the data with 83.3% of the tests evaluated containing results with at least a 70% of the experimental data falling with the  $\pm 30\%$  region.

**Table 5.11: Number and percentage of tests with  $\geq 70\%$  of the experimental data falling with  $\pm 30\%$  of the correlation**

Equation	Number of test(s) with at least a 70% match	Percentage of tests with at least a 70% match
2.14	10 out of 12	83.3%
2.10	3 out of 12	25%
2.9	1 out of 12	8.3%
2.11	1 out of 12	8.3%
2.12	1 out of 12	8.3%
2.13	1 out of 12	8.3%
2.8	0 out of 12	0%

However, for all of the correlations excluding Equation 2.8 (which was for a gas jet), the researchers did not provide enough adequate conditions they are best applicable to. Therefore, it is difficult to ascertain the applicability of these correlations.

In order to determine this, all the experimental conditions such as the water temperature, initial plate temperature, plate material, jet diameter, nozzle to plate distance, jet velocity need to be presented.

Looking at Table 5.1, Wang [15] for Equation 2.12 only provided an applicable Prandtl number range. Stevens and Webb [15] for Equations 2.13 and 2.14 provided the nozzle diameter and nozzle height to diameter ratio. Faggiani and Grassi [13] for Equation 2.10 provided the range for nozzle height to jet diameter ratio, Reynold's number, and Prandtl number. Liu et. al [14] for Equation 2.11 only provided the acceptable Prandtl range. Barsanti et. al for Equation 2.9 [12] provided the most amount of experimental conditions, however, they did not provide the initial plate temperature.

Therefore, one can only speculate under what conditions these equations can best be used to represent jet impingement cooling data in the single-phase forced convection region. Table 5.12 summarizes the conditions specified by the researchers. It also provides additional suspected applicable conditions determined from analyzing the data earlier. Equations 2.9, 2.11, and 2.12 are theorized to be applicable for initial plate temperatures less than 900°C. As to a specific temperature, this needs to be determined experimentally. Equations 2.10, 2.11, and 2.12 may also be applicable for flow rates below 15 l/min. Like the initial plate temperatures, this needs to be determined through further experiments.

**Table 5.12: Given and Theorized Applicable Conditions for Each Correlation**

Equation	Given Applicable Conditions	Theorized Additional Conditions
2.8 Martin (1977)	$2,000 \leq Re_j \leq 400,000$ $2.5 \leq r/d_j \leq 7.5$ $2 \leq Z/d_j \leq 12$ gas jet	N/a
2.9 Barsanti et. al (1989)	$3.26 < Pr < 6.04$ $53,025 < Re_{ji} < 210,709$ $10 \leq d_{ji} \leq 20$ mm $13^\circ\text{C} \leq T_{\text{water}} \leq 40^\circ\text{C}$	Initial plate temperature $< 900^\circ\text{C}$
2.10 Faggiani and Grassi (1990)	$Z/d_{ji} = 5$ $Re > 77,000$ $0.5 \leq Pr \leq 50$	Initial plate temperature $< 900^\circ\text{C}$ and/or flow rates $< 15$ l/min and/or higher water temperatures ( $> 70^\circ\text{C}$ )
2.11 Liu et al. (1991)	$Pr \leq 3$	$< 15$ l/min and/or initial plate temperature $< 900^\circ\text{C}$
2.12 Wang (1989)	$0.5 \leq Pr \leq 50$	$< 15$ l/min and/or initial plate temperature $< 900^\circ\text{C}$
2.13 Stevens and Webb (1991)	$2.2 \leq d_j \leq 8.9$ mm $0.56 \leq Z/d_j \leq 18.5$	N/a
2.14 Stevens and Webb (1991)	$2.2 \leq d_j \leq 8.9$ mm $0.56 \leq Z/d_j \leq 18.5$	15-45 l/min flow rate at water temperatures up to $80^\circ\text{C}$ and initial plate temperature of $900^\circ\text{C}$

In conclusion, Equation 2.14 seems to best represent the data at water temperatures up to  $80^\circ\text{C}$  at flow rates from 15 l/min to 45 l/min. It is also recommended that Equations 2.8 and 2.13 not be used at all to predict experimental data. Further experiments need to be performed to determine which conditions Equations 2.9, 2.10, 2.11, and 2.12 can best be used at or whether they should be used at all to represent the data.

## 6. Nucleate Boiling Analysis and Results

This section compares impinging jet nucleate boiling correlations presented in Section 2.3.2.1 with the experimental data. All correlations were compared with the data within the stagnation region at thermocouple 1, which was located at the center of the plate. The nucleate boiling regime is taken from a wall superheat of 0°C to the CHF.

The following table summarizes these correlations and the conditions they are applicable for. As it can be seen, the nucleate boiling heat flux depends upon the wall superheat ( $\Delta T_{sat}$ ).

**Table 6.1: Summary of nucleate boiling correlations analyzed**

Presented by	Correlation	Applicable Conditions
Monde and Katto's results (1978) [6 and 19]	$q_{FNB}'' = 450 \cdot (\Delta T_{sat})^{2.7} \quad (2.16)$	11 mm $\leq$ D $\leq$ 21 mm d of 2 and 2.5 mm 3.9 m/s $\leq$ v <sub>j</sub> $\leq$ 26 m/s Circular saturated water jet on a copper plate
Katsuta and Kurose (1981) [6]	$q_{FNB}'' = 2.93 \times 10^{-6} \cdot (\Delta T_{sat})^{7.4} \quad (2.17)$	R-113 saturated circular jet

### 6.1 Results

Figure 6.1 shows the nucleate boiling heat flux correlations compared with test M9545. It can be seen that both correlations highly overestimated the heat flux at the majority of the superheats within the nucleate boiling region. The correlations seemed to match better with the heat flux at wall superheats below 40°C. However, this is only a small region of the nucleate boiling region and does not fully represent the whole nucleate boiling region.

Similar results were obtained when the heat flux was calculated and compared with test H3045, shown in Figure 6.2, where the heat flux was highly overestimated by the correlations. Comparable results were also obtained for all the other tests. Therefore,

the correlations are a poor representation of the data. Perhaps these equations are only applicable for the researchers' particular experimental conditions. Consequently, a new correlation needs to be developed to better represent this regime.

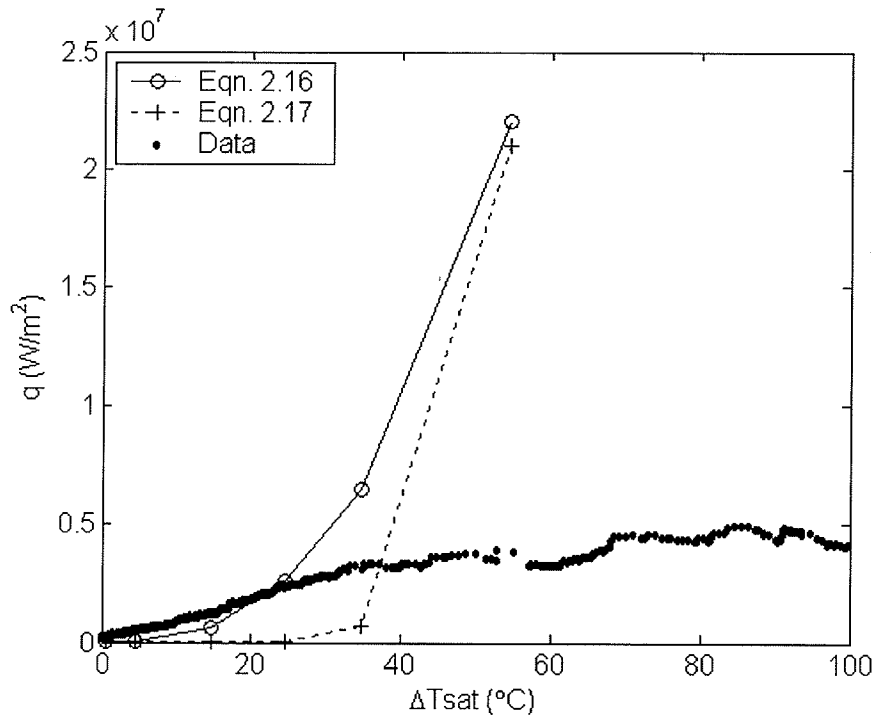


**Figure 6.1: Nucleate boiling correlations compared with the data of test M9545**

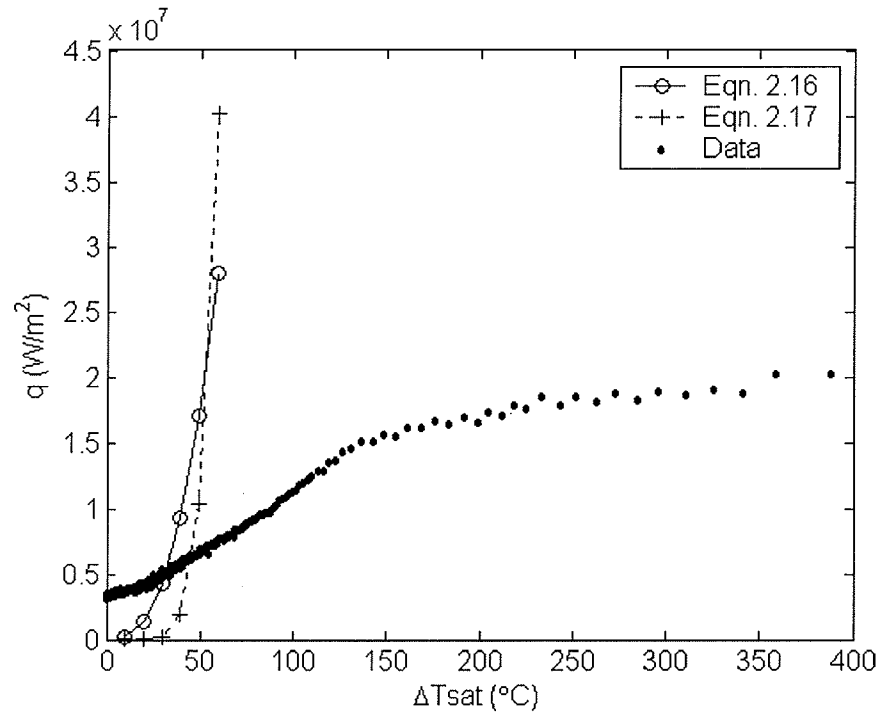


Figure 6.2: Nucleate boiling correlations compared with the data of test H3045

## 7. Two-phase Analysis and Results

The nucleate boiling analysis presented earlier concluded that the nucleate boiling correlations were a poor representation of the data. Therefore, another correlation needs to be developed for this region. This is where two-phase forced convection comes in where the subcooled Chen correlation can be used to correlate the data.

### 7.1 Modification of the Chen Correlation

As presented in Section 2.3.3, the Chen correlation was originally developed for flow within a vertical tube. The equation needs to be modified to represent boiling of a circular jet. Collier and Thome [20] suggested the following modification of the Chen Correlation for subcooled flow boiling within a vertical tube:

$$q_{SUB}'' = h_{mic} \cdot \Delta T_{sat} + h_{mac} \cdot (T_{surf} - T_{water}) \quad (2.40)$$

#### 7.1.1 Macroconvective Heat Transfer Coefficient

Mentioned earlier in Section 2.3.3, Chen suggested the macroconvective heat transfer coefficient be represented by the Dittus-Boelter equation multiplied by an enhancement factor [21]. However, this is applicable for flow within a tube and thus can not be used to represent a circular jet.

Since this is the single-phase forced convective component, a circular jet correlation for this region can be used. It was determined in Section 5 that the single-phase forced convection Equation 2.14 recommended by Stevens and Webb (1991) correlated well with the experimental data. Therefore, this equation was used for this component. For subcooled boiling, Collier and Thome suggested the enhancement factor be set to unity [20]. Therefore, this component for a circular jet becomes:

$$h_{mac} = 2.67 \cdot \text{Re}_j^{0.567} \cdot \text{Pr}^{0.4} \cdot \left( \frac{Z}{d_j} \right)^{-0.0336} \cdot \left( \frac{v_j}{d_j} \right)^{-0.237} \cdot \frac{k_f}{d_j} \quad (7.1)$$

All water variables were calculated at the film temperature. The Reynold's number and diameter and velocity were calculated at the corrected variables provided in Table 5.3.

### 7.1.2 Microconvective Heat Transfer Coefficient

As mentioned in Section 2.3.3, Chen suggested the microconvective heat transfer coefficient be represented by the Forster and Zuber correlation for nucleate pool boiling, which is then multiplied by a suppression factor to account for the reduction in heat transfer due to flow boiling:

$$h_{mic} = 0.00122 \cdot \left( \frac{k_f^{0.79} \cdot C_{pf}^{0.45} \cdot \rho_f^{0.49} \cdot g^{0.25}}{\sigma^{0.25} \mu_f^{0.29} \cdot h_{fg}^{0.24} \cdot \rho_g^{0.24}} \right) \cdot \Delta T_{sat}^{0.24} \cdot \Delta p_{sat}^{0.75} \cdot S \quad (2.37)$$

For a circular jet, it was decided to also use the Forster and Zuber correlation. However, Chen empirically derived the suppression factor from data for flow within a tube. A new suppression factor needed to be developed to represent that for a circular jet.

For all the tests chosen for the analysis at various wall superheats, a suppression factor was calculated in a manner for  $q_{SUB}''$  in Equation 2.40 to be equal to the average value of the experimental data.  $S$  was calculated at each wall superheat by substituting Equations 7.1 (macroconvective component) and 2.37 (microconvective component) into Equation 2.40 (subcooled two-phase correlation) and solving for this value to get:

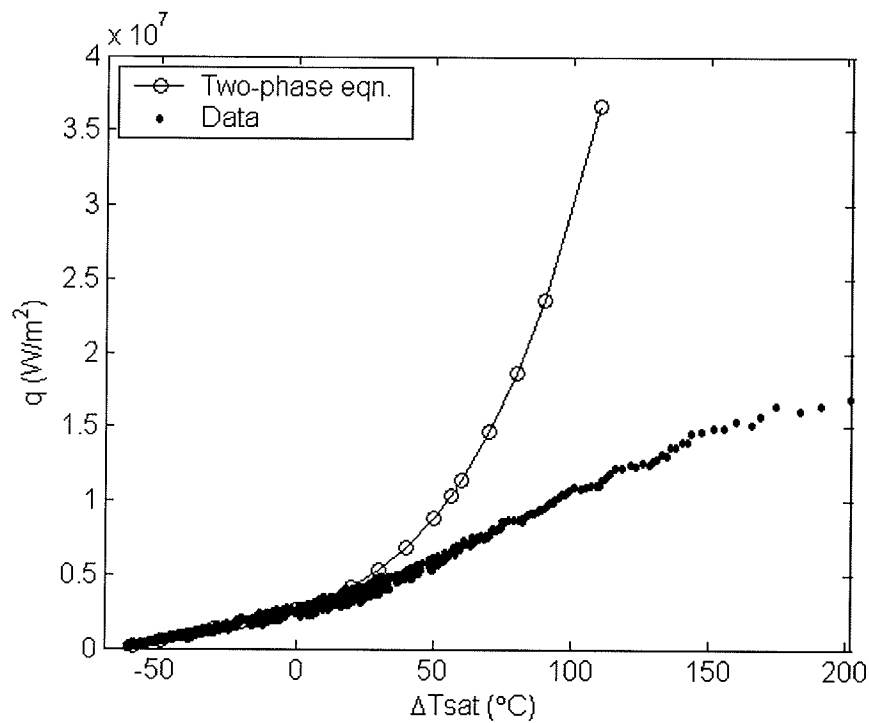
$$S = \frac{q_{data}'' - h_{mac} \cdot (T_{surf} - T_{water})}{0.00122 \cdot \left( \frac{k_f^{0.79} \cdot C_{pf}^{0.45} \cdot \rho_f^{0.49} \cdot g^{0.25}}{\sigma^{0.25} \mu_f^{0.29} \cdot h_{fg}^{0.24} \cdot \rho_g^{0.24}} \right) \cdot \Delta T_{sat}^{0.24} \cdot \Delta p_{sat}^{0.75} \cdot \Delta T_{sat}} \quad (7.2)$$

Where the difference in saturation pressure was determined by taking the value of pressure corresponding the surface temperature subtracted by the saturation pressure:

$$\Delta p_{sat} = P_{surf} - P_{sat} \quad (7.3)$$

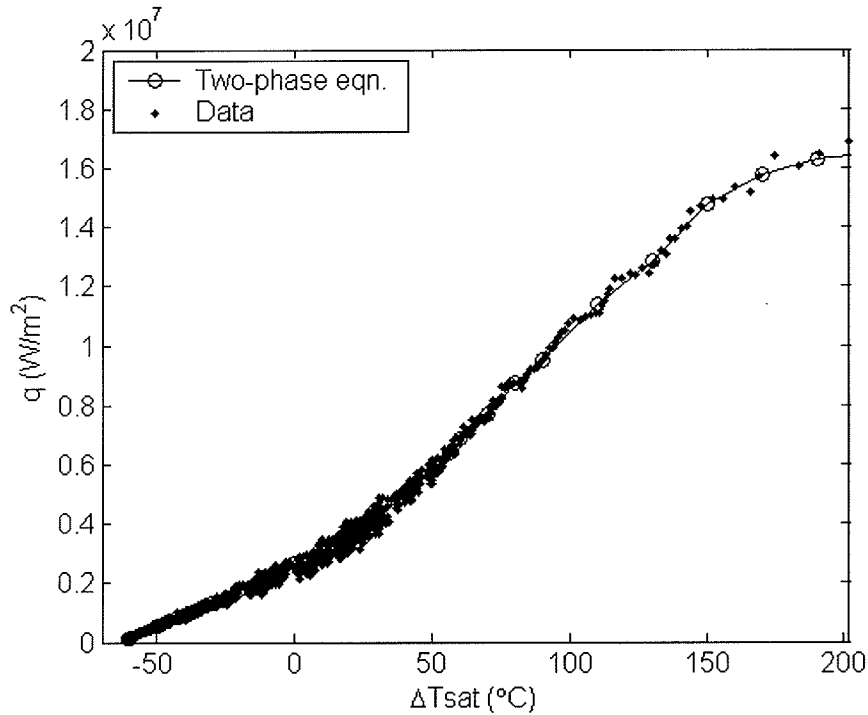
All other water properties were taken at the film temperature. To get the suppression factor, for each test, the subcooled Chen correlation (Equation 2.40) was calculated with the suggested macroconvective component (Equation 7.1) and microconvective components (Equation 2.37 with the suppression factor set to unity).

Figure 7.1 shows this modified subcooled chen correlation compared with the results of test H4030. As it can be seen, the heat flux is highly overestimated at higher superheats. This is where the suppression factor comes in.



**Figure 7.1: Subcooled correlation with S=1 compared with the data of test H4030**

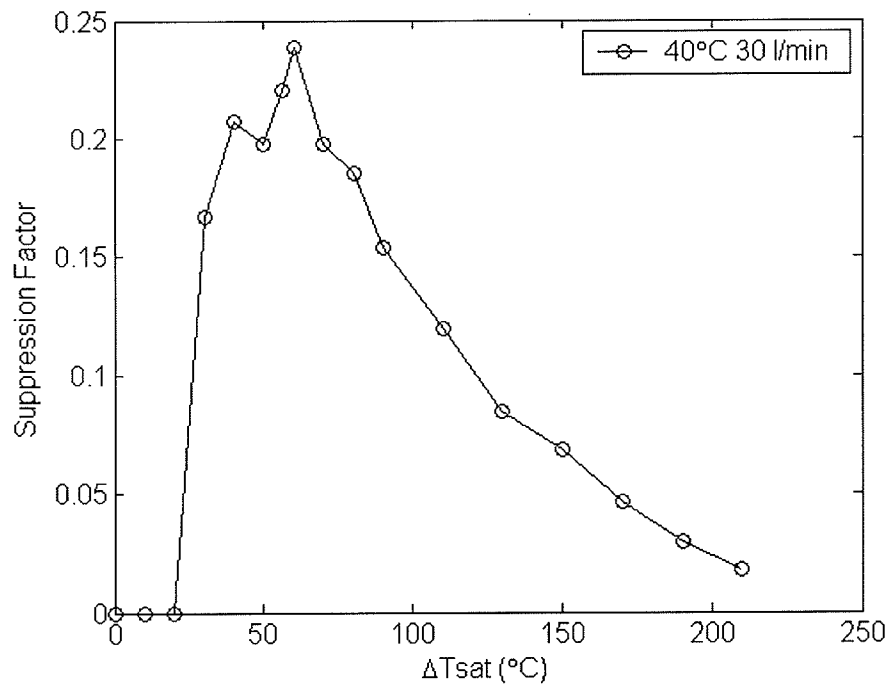
Using Equation 7.2, a suppression factor was calculated in order to allow for the correlation to match with the experimental data. Figure 7.2 shows the correlation with the calculated suppression factor compared with the data of test H4030. Having a suppression factor allows the correlation to match with the data. Table 7.1 shows the calculated suppression factors required for the correlation to match with the data at various wall superheats at a water temperature of 40°C and 30 l/min. The associated plot is shown in Figure 7.3, which resembles an exponential curve.



**Figure 7.2: Subcooled correlation with calculated  $S$  compared with the data of test H4030**

**Table 7.1: Calculated suppression factor at  $T_{\text{water}} = 40^\circ\text{C}$  and 30 l/min**

$\Delta T_{\text{sat}} (^\circ\text{C})$	S
0	0.000
10	0.000
20	0.000
30	0.167
40	0.207
50	0.198
56	0.221
60	0.239
70	0.198
80	0.185
90	0.154
110	0.120
130	0.084
150	0.068
170	0.047
190	0.030
210	0.018

**Figure 7.3: Calculated suppression factor for test H4030**

All the calculated values for the suppression factors for each test were plotted against the wall superheat, as shown in Figure 7.4. An exponential least squares fit was performed at a water temperature of 50°C and 30 l/min to get a curve which approximates an average representation of all the data.

When the wall superheat is greater than zero the suppression factor resulting from this is correlated by the following equation as determined from the exponential least squares fit. It should be noted that when the wall superheat is zero the suppression factor should be set to unity. When the wall superheat is less than zero, the suppression factor should be equal to zero, as nucleate boiling does not occur here.

$$S = 1.218 \cdot e^{-0.023 \cdot \Delta T_{sat}} \quad (7.4)$$

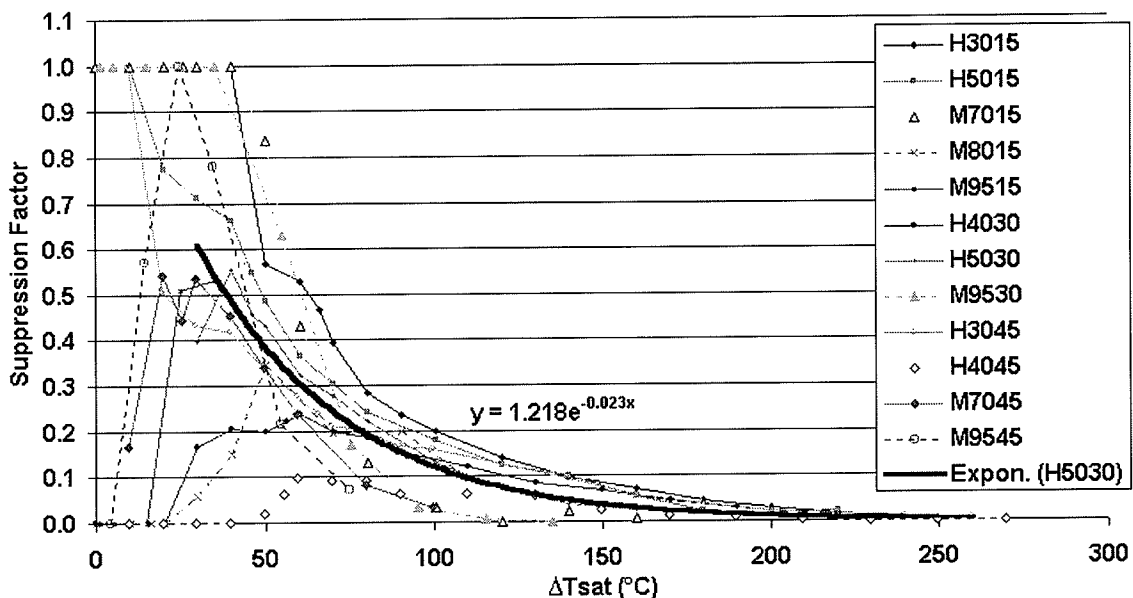


Figure 7.4: Calculated suppression factors for all the tests

### 7.1.3 The New Correlation

The new correlation derived to represent the experimental data is summarized in the following table. This correlation can be used to represent both the single-phase

forced convection and nucleate boiling regimes for an impinging circular jet on a hot steel plate.

**Table 7.2: New two-phase forced convection correlation**

$$q''_{SUB} = h_{mic} \cdot \Delta T_{sat} + h_{mac} \cdot (T_{surf} - T_{water}) \quad (2.40)$$

where:

$$h_{mac} = 2.67 \cdot \text{Re}_j^{0.567} \cdot \text{Pr}^{0.4} \cdot \left(\frac{Z}{d_j}\right)^{-0.0336} \cdot \left(\frac{v_j}{d_j}\right)^{-0.237} \cdot \frac{k_f}{d_j} \quad (7.1)$$

$$h_{mic} = 0.00122 \cdot \left(\frac{k_f^{0.79} \cdot C_{pf}^{0.45} \cdot \rho_f^{0.49} \cdot g^{0.25}}{\sigma^{0.25} \mu_f^{0.29} \cdot h_{fg}^{0.24} \cdot \rho_g^{0.24}}\right) \cdot \Delta T_{sat}^{0.24} \cdot \Delta p_{sat}^{0.75} \cdot S \quad (2.37)$$

$$S = 1.218 \cdot e^{-0.023 \cdot \Delta T_{sat}} \quad \text{when } \Delta T_{sat} > 0 \quad (7.4)$$

$$S = 1 \quad \text{when } \Delta T_{sat} = 0$$

$$S = 0 \quad \text{when } \Delta T_{sat} < 0$$

## 7.2 Comparison with Experimental Data

The new two-phase forced convection correlation shown in Table 7.2 was compared with the experimental data. All correlations were compared with the experimental data within the stagnation region at thermocouple 1, which was located at the center of the plate.

The percent of the experimental data that fell within  $\pm 30\%$  of the correlation was determined graphically through the single-phase and nucleate boiling regions up to the CHF. Table 7.3 and Figure 7.5 summarize the results. As it can be seen, all of the 12 tests were represented well by the correlation, where all tests contained greater than or 70% of the experimental data fell within the  $\pm 30\%$  region of the correlation.

**Table 7.3: Percent of the experimental data that fell within  $\pm 30\%$  of the correlation**

Flow Rate	Water Temperature						
	30°C	40°C	50°C	60°C	70°C	80°C	95°C
15 l/min	94%	:	98%	:	75%	91%	86%
30 l/min	:	99%	99%	:	:	:	75%
45 l/min	96%	98%	:	:	71%	:	76%

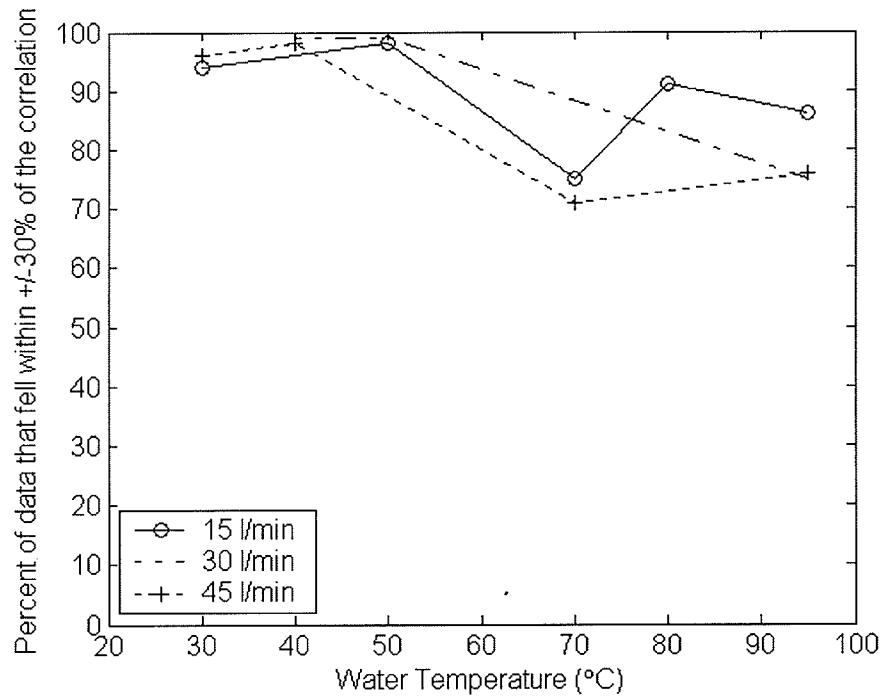
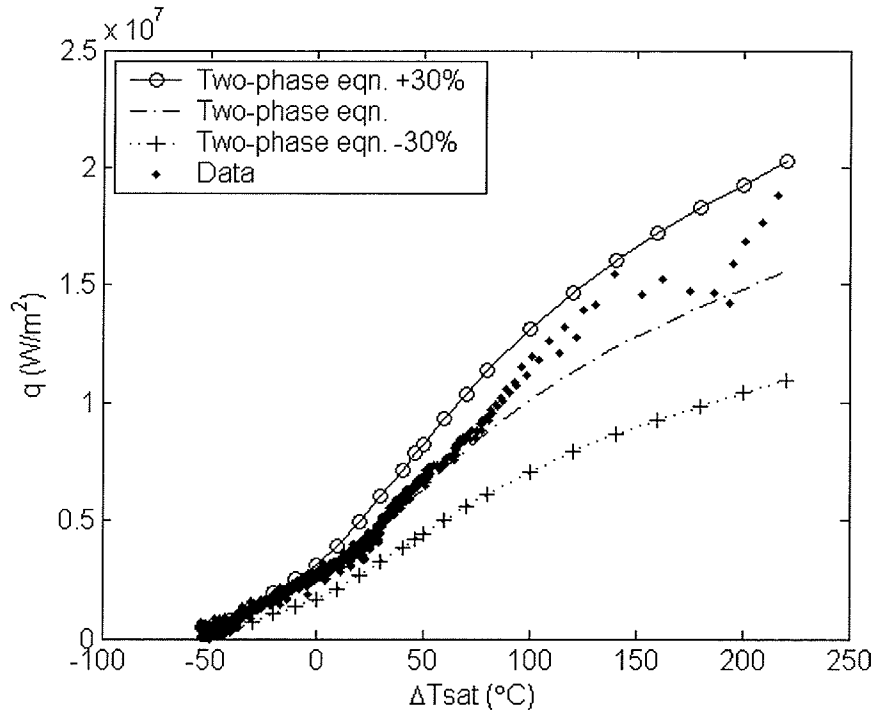
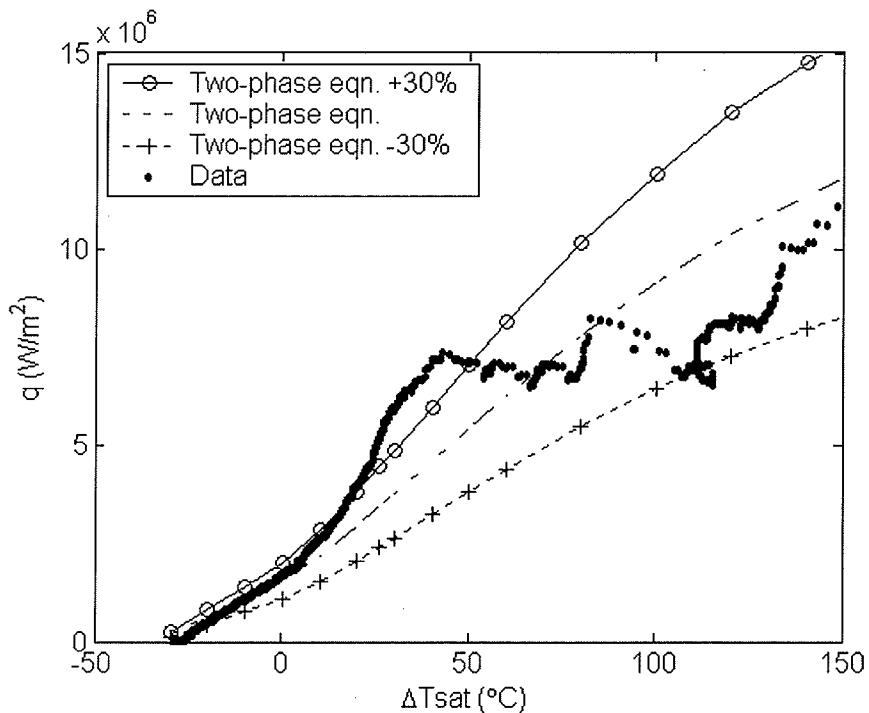
**Figure 7.5: Percent of the experimental data that fell within  $\pm 30\%$  of the correlation**

Figure 7.6 shows the two-phase forced convection correlation compared with the results of test H5015. As summarized in Table 7.3, approximately 98% of the data fell within  $\pm 30\%$  of the correlation. Similar graphs were obtained at all the flow rates at water temperatures below and including 50°C, and at 80°C at 15 l/min.



**Figure 7.6: Two-phase correlation compared with the results of test H5015**

However, at a water temperature of 70°C and 15 l/min, the percent of data fell within 75% range (Table 7.3). Figure 7.7 shows the two-phase correlation compared with the data of test M7015. In the figure at wall superheats ranging from 20°C to 50°C, it can be seen that the correlation slightly underestimated the experimental data. Looking at Figure 7.8, the suppression factor required for the data to best match was around unity within this wall superheat range. It can be seen that the average suppression factor curve used for the correlation calculation ( $S = 1.218 \cdot e^{-0.023 \cdot \Delta T_{sat}}$ ) consisted of factors less than unity at this wall superheat range. Therefore, when the two-phase correlation is calculated with the average suppression curve, it will underestimate the data in this region for this test because the factor used is less than the one required.



**Figure 7.7: Two-phase correlation compared with the data of test M7015**

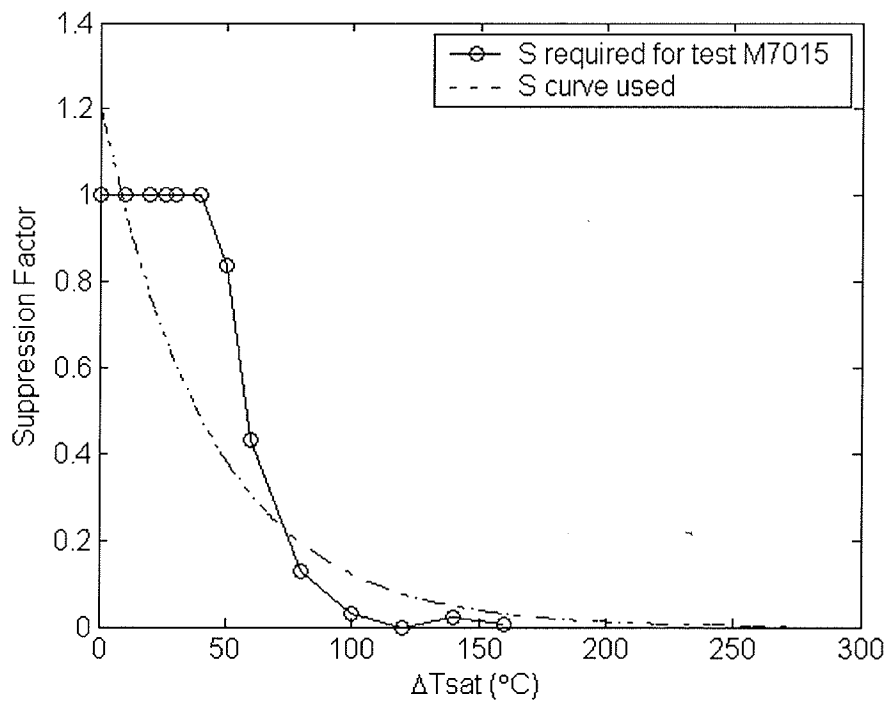


**Figure 7.8: Suppression factor comparison at  $T_{water} = 70^{\circ}C$  and 15 l/min**

The opposite occurred for test M7045, shown in Figure 7.9. At wall superheats greater than 60°C, the correlation overestimated the data. Looking at Figure 7.10, the suppression factors required for the correlation to best match with the data at this wall superheat range was lower than the factor provided by the average suppression curve used for the calculation. Higher suppression factors increase the heat flux for the correlation, allowing it to overestimate the data. The same trend occurred for test M9545, where the heat flux was overestimated the data at wall superheats greater than 50°C (see Figure 7.11 and Figure 7.12).

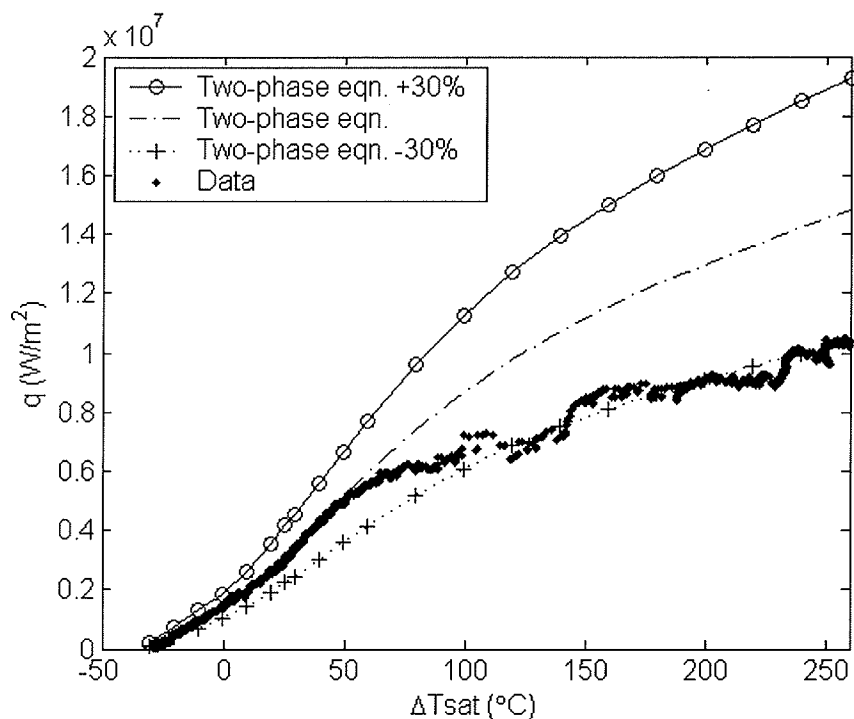


**Figure 7.9: Two-phase correlation compared with the data of test M7045**

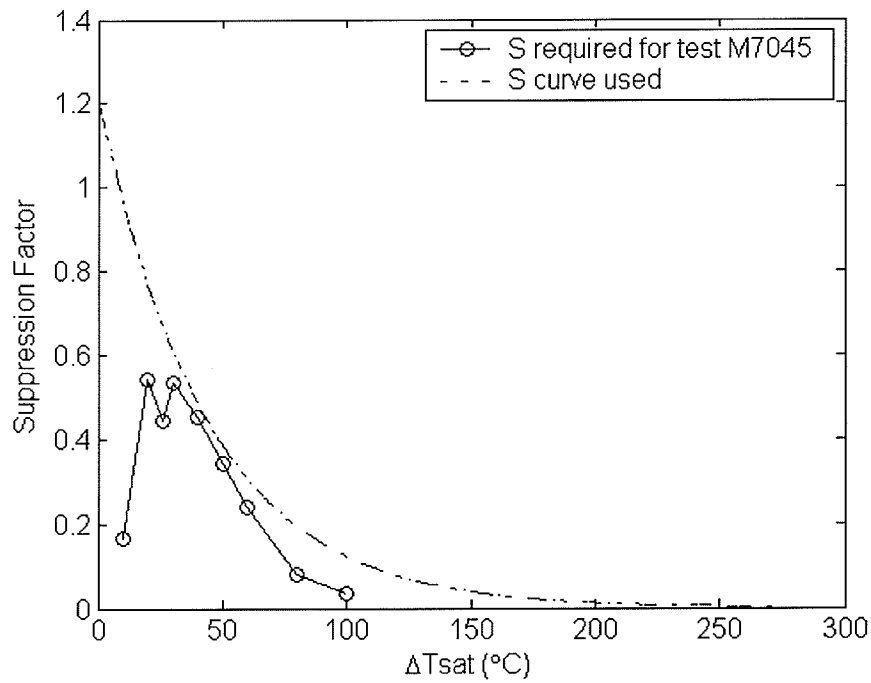


**Figure 7.10: Suppression factor comparison at  $T_{\text{water}} = 70^\circ\text{C}$  and 45 l/min**

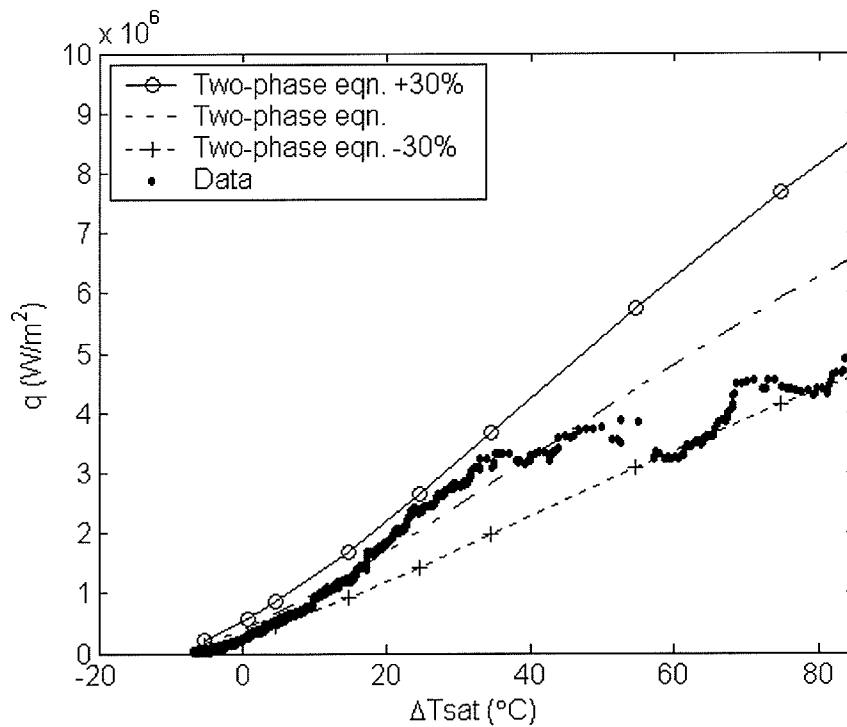


**Figure 7.11: Two-phase correlation compared with the data of test M9545**

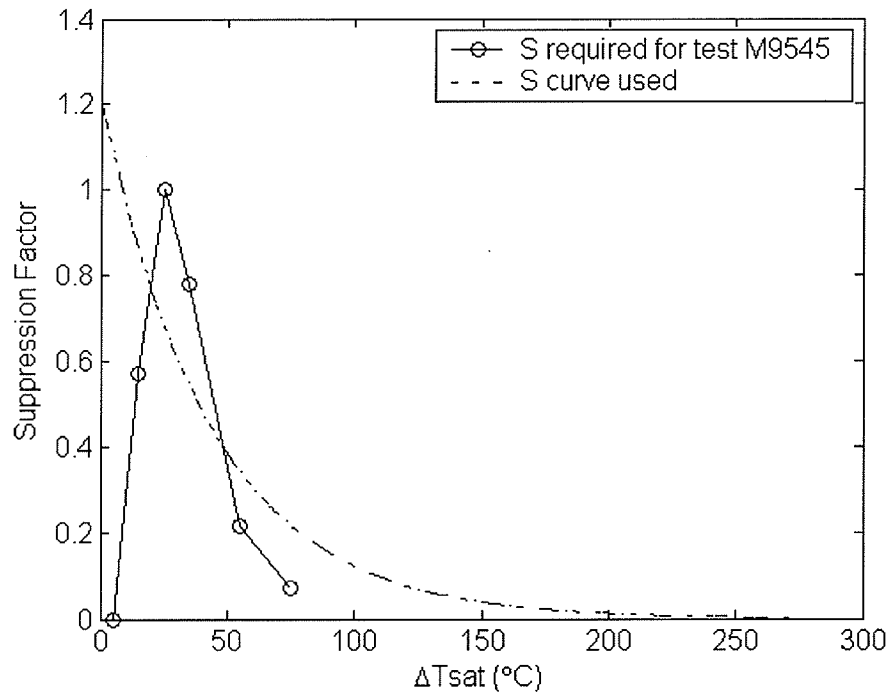


**Figure 7.12: Suppression factor comparison at  $T_{\text{water}} = 95^{\circ}\text{C}$  and 45 l/min**

At a water temperature of  $95^{\circ}\text{C}$  and 30 l/min in Figure 7.13, the correlation underestimated the heat flux at lower wall superheats ranging from  $20^{\circ}\text{C}$  to  $50^{\circ}\text{C}$ . However, higher superheats above  $50^{\circ}\text{C}$ , the heat flux was overestimated. This can be explained by looking at Figure 7.14. At the lower superheats, a higher suppression factor was required to match the correlation with the data that that provided by the exponential curve used for the calculations. At higher superheats, smaller factors were required than the curve used. Therefore, at lower superheats where higher suppression factors are required, the correlation will be below the heat flux. At higher superheats, the correlation would overestimate the flux because lower suppression factors are required.

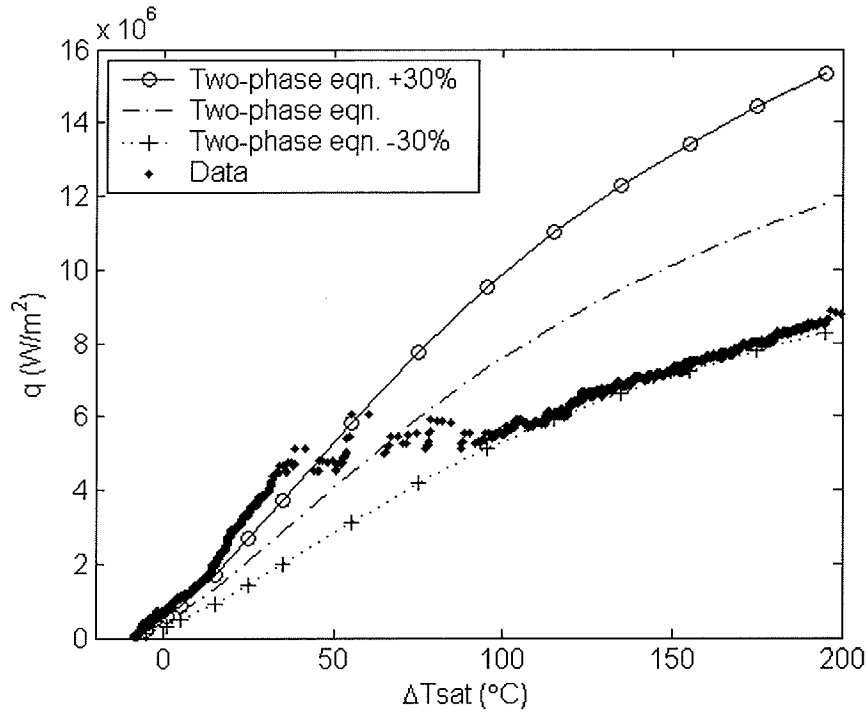


Figure 7.13: Two-phase correlation compared with the data of test M9530

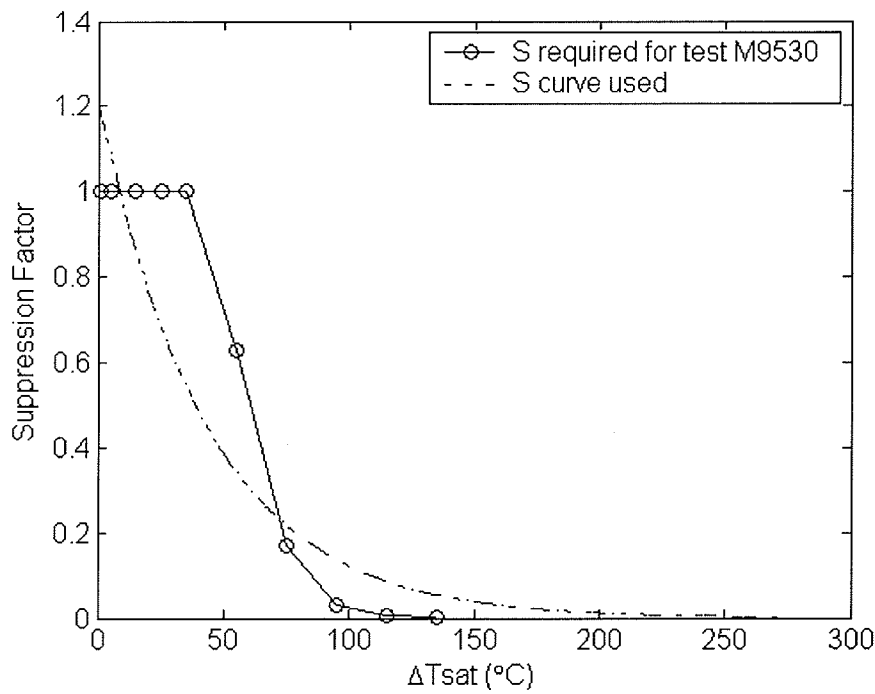


Figure 7.14: Suppression factor comparison at  $T_{water} = 95^{\circ}C$  and 30 l/min

In the instances described earlier where the percent matching was below 80%, this occurred because the suppression curve derived earlier provides an average factor. This may be above or below the required factor for the data to match perfectly, which explains why not all the tests matched greater than 95%. However, since greater than 70% of the data fell within  $\pm 30\%$  of the correlation (refer to Table 7.3) can be concluded that the new two-phase correlation can be used to represent all of the data.

### **7.3 Comparison with Other Researcher's Data**

The derived two-phase correlation was compared with experimental data gathered by Hall et. al [64]. It should be noted that other papers contained heat flux results. However, not all the parameters required to use the correlation were provided, such as the nozzle-to-plate distance. Therefore, the these data were not used.

The parameters used for the tests and by Hall et. al [64] are shown in Table 7.4. The actual values from Hall et. al are provided. However, this provides and nozzle-to-plate distance over jet diameter ratio of 19.6, which is outside the specified range of the equation of 18. Therefore, the nozzle-to-plate distance was corrected to 18 in the same manner as was done for Equation 2.14 described in Section 5.2 (see Table 5.3). These corrected values were used to calculate the correlation when comparing to Hall et. al's data. Take note that the corrected parameters versus the actual values are almost exactly the same and thus would not make a significant difference in the calculation if the actual values were used.

**Table 7.4: Parameters for the two-phase equation**

Parameters	Experimental Data	Actual Values from Hall et. al [64]	Corrected Values from Hall et. al [64]
Initial plate temperature	900°C	650°C	650°C
Water temperature	30°C – 95°C	25°C	25°C
Jet velocity, $v_j$	5.24 m/s – 5.6 m/s	3 m/s	3.03 m/s
Jet diameter $d_j$	7.8 mm – 13 mm	5.1 mm	5.08 mm
Nozzle-to-plate distance, $Z$	0.14 m – 0.235 m	0.1 mm	0.0915 m
$Z/d_j$	18	19.6	18

Figure 7.15 shows the correlation compared with Hall et. al's data. It can be seen that the correlation overestimated the heat flux at wall superheats below 50°C and underestimated the heat flux at higher wall superheats. Shown in Table 7.4, Hall et. al used a lower initial plate temperature than was used for the tests. The jet velocities were also lower. A lower jet velocity and lower plate temperature will provide lower heat fluxes. This explains why the heat flux was overestimated at lower wall superheats because the equation was design for a plate temperature of 900°C and higher jet velocities.

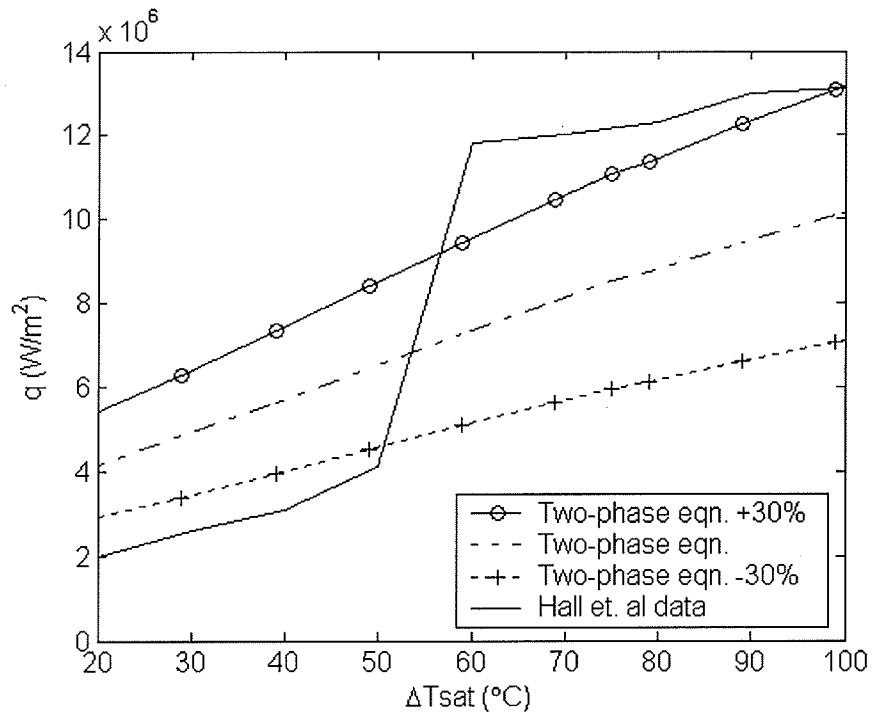


**Figure 7.15: The two-phase correlation compared with data from Hall et. al [64]**

However, at higher wall superheats, the correlation overestimated the heat flux. It is difficult to ascertain why this occurred. Either way, this proves that the new two-phase correlation developed has its limitations and most likely is best applicable within the parameters used for the experiments. This correlation should be compared with experimental data from other researchers to ascertain its limitations of use.

## 8. CHF Analysis and Results

This section compares the CHF correlations presented in Section 2.3.4 with the experimental data. Only those for an upward circular jet were used. These correlations are summarized in Table 8.1. All refer to a circular jet within the V-regime unless otherwise noted.

In the table, it can be seen that the CHF depends upon various water properties, the heater diameter ( $D$ ), jet velocity ( $v_j$ ) and jet diameter ( $d_j$ ). Along with comparison with the experimental data, the variation of CHF with heater diameter, and flow rate, hence the jet velocity (which the jet diameter depends upon), and water temperature will be presented.

Table 8.1: CHF equations presented by other researchers

Presented by	Correlation(s)	Applicable Conditions
Ishigai and Mizuno (1974) [2]	$q_{CHF}'' = 1.42 \times 10^4 \cdot \left( \frac{v_j}{d_j} \right)^{0.34} \cdot \Delta T_{sub}^{1.15} \quad (2.41)$	$45^\circ\text{C} \leq \Delta T_{sub} \leq 80^\circ\text{C}$
Monde and Katto (1978) [19]	$\frac{q_{CHF}''}{\rho_g \cdot h_{fg} \cdot v_j} = 0.0745 \cdot \left( \frac{\rho_f}{\rho_g} \right)^{0.725} \cdot \left[ \frac{2 \cdot \sigma}{\rho_f \cdot v_j^2 \cdot D} \right]^{1/3} \quad (2.42)$	$11 \text{ mm} \leq D \leq 21 \text{ mm}$ d of 2 and 2.5 mm $3.9 \text{ m/s} \leq v_j \leq 26 \text{ m/s}$ saturated jet on a copper plate
Monde and Katto (1978) [19]	$\frac{q_{CHF}''}{\rho_g \cdot h_{fg} \cdot v_j} = 0.0745 \cdot \left( \frac{\rho_f}{\rho_g} \right)^{0.725} \cdot \left[ \frac{2 \cdot \sigma}{\rho_f \cdot v_j^2 \cdot D} \right]^{1/3} \cdot (1 + \varepsilon_{sub}) \quad (2.43a)$ $\varepsilon_{sub} = 2.7 \cdot \left( \frac{\rho_f}{\rho_g} \right)^{0.5} \cdot \left( \frac{C_{pf} \cdot \Delta T_{sub}}{h_{fg}} \right) \quad (2.43b)$	$30^\circ\text{C} \leq T_{water} \leq 80^\circ\text{C}$ $11 \text{ mm} \leq D \leq 21 \text{ mm}$ copper plate
Lienhard and Eichhorn (1979) [24]	$q_{CHF}'' = f(\rho_f / \rho_g) \cdot \left( \frac{(D/d_j)^3}{We} \right)^{A(\rho_f / \rho_g)} \cdot \frac{1}{D/d_j} \quad (2.44a)$ $We = \frac{\rho_f \cdot v_j^2 D}{\sigma} \quad (2.44b)$	Generalized equation for a saturated jet

Table 8.1: CHF equations presented by other researchers (cont.)

Presented by	Correlation(s)	Applicable Conditions
Lienhard and Hasan (1979) [25]	$\frac{q_{CHF}''}{\rho_g \cdot h_{fg} \cdot v_j} = f(\rho_f / \rho_g) \cdot \left[ \frac{\sigma}{\rho_f \cdot v_j^2 \cdot D} \right]^{A(\rho_f / \rho_g)} \cdot \left( \frac{D}{d_j} \right)^{3 \cdot A(\rho_f / \rho_g) - 1} \quad (2.45a)$ $f = \left( 0.744 + 0.0084 \cdot \frac{\rho_f}{\rho_g} \right) \quad (2.45b)$ $A = 0.4346 + 0.1027 \cdot \ln\left(\frac{\rho_f}{\rho_g}\right) - 0.0474 \cdot \left( \ln\left(\frac{\rho_f}{\rho_g}\right) \right)^2 + 0.00426 \cdot \left( \ln\left(\frac{\rho_f}{\rho_g}\right) \right)^3 \quad (2.45c)$	$11 \text{ mm} \leq D \leq 21 \text{ mm}$ $v_j \leq 60 \text{ m/s}$ $6 \leq p_{\text{bar}} \leq 27.9 \text{ bar}$ saturated jet
Monde (1980) [28]	$\frac{q_{CHF}''}{\rho_g \cdot h_{fg} \cdot v_j} = \frac{0.0601 \cdot \left( \frac{\rho_f}{\rho_g} \right)^{0.725} \cdot \left[ \frac{2 \cdot \sigma}{\rho_f \cdot v_j^2 \cdot D} \right]^{1/3}}{1 + 0.00113 \cdot (D/d_j)^2} \quad (2.46)$	$0.3 \text{ m/s} \leq v_j \leq 15 \text{ m/s}$ $5 \leq D/d_j \leq 36.4$ saturated jet on a copper plate
Monde et. al (1982) [6]	$\frac{q_{CHF}''}{\rho_g \cdot h_{fg} \cdot v_j} = 0.068 \cdot \left( \frac{\rho_f}{\rho_g} \right)^{0.725} \cdot \left[ \frac{2 \cdot \sigma}{\rho_f \cdot v_j^2 \cdot D} \right]^{1/3} \cdot \left( 1 + 7 \cdot \left( \frac{\rho_f}{\rho_g} \right)^{-1} \right) \quad (2.47)$	$1 \leq p_{\text{bar}} \leq 6 \text{ bars}$ $0.7 \text{ m/s} \leq v_j \leq 20 \text{ m/s}$ saturated jet
Monde et. al (1982) [6]	$\frac{q_{CHF}''}{\rho_g \cdot h_{fg} \cdot v_j} = 2.02 \cdot \left( \frac{\rho_f}{\rho_g} \right)^{1/3} \cdot \left[ \frac{\sigma}{\rho_f \cdot v_j^2 \cdot D} \right]^{1/2} \quad (2.48)$	$1 \leq p_{\text{bar}} \leq 6 \text{ bars}$ $0.7 \text{ m/s} \leq v_j \leq 20 \text{ m/s}$ I-regime, saturated jet

Table 8.1: CHF equations presented by other researchers (cont.)

Presented by	Correlation(s)	Applicable Conditions
Monde (1985) [23]	$\frac{q_{CHF}''}{\rho_g \cdot h_{fg} \cdot v_j} = 0.221 \cdot \left(\frac{\rho_f}{\rho_g}\right)^{0.645} \cdot \left[\frac{2 \cdot \sigma}{\rho_f \cdot v_j^2 \cdot (D - d_{ji})}\right]^{-0.343} \cdot \left(1 + \frac{D}{d_{ji}}\right)^{-0.364} \quad (2.49)$	$292 \leq p_f/p_g \leq 1603$ $0.36 \leq v_j \leq 60 \text{ m/s}$ $5 \leq D/d_{ji} \leq 57.1$ saturated jet
Sharan and Lienhard (1985) [29]	$\frac{q_{CHF}''}{\rho_g \cdot h_{fg} \cdot v_j} = f(\rho_f / \rho_g) \cdot \left[\frac{1000 \cdot \sigma}{\rho_f \cdot v_j^2 \cdot D}\right]^{A(\rho_f / \rho_g)} \cdot \left(\frac{D}{d_j}\right)^{-1/3} \quad (2.50a)$ $f = \left(0.21 + 0.00171 \cdot \frac{\rho_f}{\rho_g}\right) \quad (2.50b)$ $A = 0.486 + 0.06052 \cdot \ln\left(\frac{\rho_f}{\rho_g}\right) - 0.0378 \cdot \left(\ln\left(\frac{\rho_f}{\rho_g}\right)\right)^2 + 0.00362 \cdot \left(\ln\left(\frac{\rho_f}{\rho_g}\right)\right)^3 \quad (2.50c)$	$11 \text{ mm} \leq D \leq 21 \text{ mm}$ $0.3 \leq v_j \leq 60 \text{ m/s}$ $5 \leq D/d_j \leq 36.4$ $6 \leq p_{bar} \leq 27.9 \text{ bar}$ saturated jet
Katto and Yokoya (1988) [30]	$\frac{q_{CHF}''}{\rho_g \cdot h_{fg} \cdot v_j} = \left(\frac{\rho_f}{\rho_g}\right) \cdot \left[0.0166 + 7 \cdot \left(\frac{\rho_f}{\rho_g}\right)^{-1.12}\right] \cdot \left[\frac{\sigma}{\rho_f \cdot v_j^2 \cdot (D - d_j)}\right]^m \cdot \left(1 + \frac{D}{d_j}\right)^{-m} \quad (2.51a)$ $m = 0.532 \cdot \left(\frac{\rho_f}{\rho_g}\right)^{-0.0794} \quad \text{for } \frac{\rho_f}{\rho_g} \leq 248 \quad (2.51b)$ $m = 0.374 \cdot \left(\frac{\rho_f}{\rho_g}\right)^{-0.0155} \quad \text{for } \frac{\rho_f}{\rho_g} \geq 248 \quad (2.51c)$	$5.3 \leq p_f/p_g \leq 1603$ $0.7 \leq d_j \leq 4.1 \text{ mm}$ $0.3 \leq v_j \leq 60 \text{ m/s}$ $10 \leq D \leq 60.1 \text{ mm}$ $3.9 \leq D/d_j \leq 53.9$ saturated jet

## 8.1 Determining the Correlation CHF

It can be seen in Table 8.1 that the researchers specify the jet velocity and diameter at the nozzle exit be used. For the analysis, however, it was decided to evaluate the equations at the jet impingement velocity and diameter. The reason being is the velocity and diameter at the nozzle exit are different than at impingement. Since the analysis is looking within the impingement region, it makes better sense to use the jet impingement diameter and velocity.

The researchers also specify a heater diameter parameter,  $D$ . It was decided to take the heater diameter as the size of the impingement zone, which is the size of the jet diameter. However, looking at Table 8.1, Equations 2.49 and 2.51 have a “ $D-d_{ji}$ ” term. Therefore, if a heater diameter equivalent to  $d_{ji}$  were used, the CHF calculated would be zero. To prevent this from occurring, it was decided to calculate the CHF at a heater diameter slightly larger than the jet impingement diameter. For convention, a value of  $1.1*d_{ji}$  was used.

The CHF was calculated at  $d_{ji}$  and  $1.1*d_{ji}$  for the other correlations not containing the “ $D-d_{ji}$ ” term to verify that using a heater diameter slightly larger than the jet diameter would not greatly effect the CHF calculated. Figure 8.1 shows the results at a water temperature of  $30^{\circ}\text{C}$ , flow rate of 15 l/min, and wall superheat of  $200^{\circ}\text{C}$ . As it can be seen, the CHF decreased minutely with the increased heater diameter. Due to this small variation, it can be ascertained that using a slightly larger heater diameter has little effect on the CHF calculated and thus a heater diameter of  $1.1*d_{ji}$  can be used.

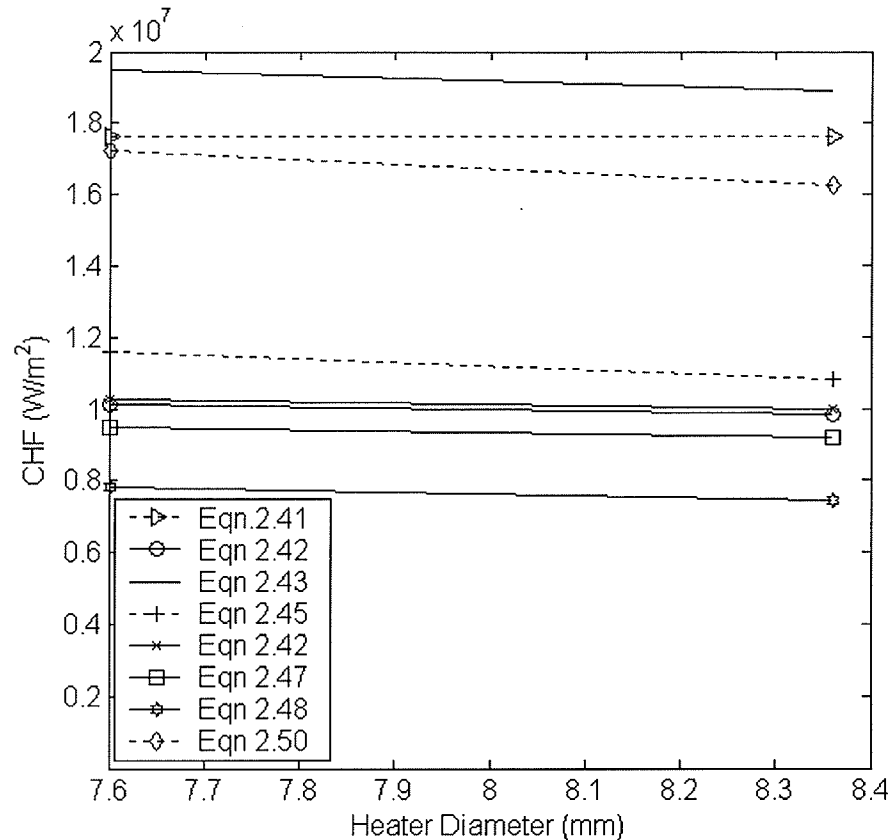


**Figure 8.1: CHF calculated at  $D=d_{ji}$  and  $D=1.1*d_{ji}$  at  $T_{water} = 30^{\circ}C$ , flow rate of 15 l/min, and wall superheat of  $200^{\circ}C$**

The heater diameters used for each of the flow rates are presented in Table 8.2.

The CHF for each equation was evaluated at the same wall superheat that the CHF for the experimental data occurred at, as described in Table 4.4. All water properties were evaluated at the film temperature. The tests the CHF was evaluated at are summarized in Table 4.2.

**Table 8.2: Heater diameters used for the analysis**

Flow Rate	$d_{ji}$ (mm)	D (mm)
15 l/min	7.6	8.36
30 l/min	10.6	11.66
45 l/min	12.6	13.86

## 8.2 Effect of Heater Diameter

As mentioned earlier, all the correlations, except for Equation 2.41, depend upon a heater diameter,  $D$ . The effect of heater diameter was determined by calculating the CHF at five different heater diameters at a constant water temperature, flow rate, and wall superheat. The heater diameters the CHF was evaluated at were at  $1.1 \cdot d_{ji}$ , thermocouple location 2, thermocouple location 5, and thermocouple location 8. The last diameter evaluated was at the equivalent diameter of the plate surface. A plate of 280 mm X 280 mm was used. Therefore, an equivalent diameter required to achieve the same area is at 316 mm. Table 8.3 summarizes the five different heater diameters used at each of the flow rates.

**Table 8.3: D used to examine effect of heater diameter**

Flow Rate	$d_{ji}$ (mm)	D (mm)
15 l/min	7.6	8.36, 15.9, 63.5, 111.1, 316
30 l/min	10.6	11.66, 15.9, 63.5, 111.1, 316
45 l/min	12.6	13.86, 15.9, 63.5, 111.1, 316

Figure 8.2 shows the CHF evaluated at a water temperature of 30°C, flow rate of 15 l/min, and a wall superheat of 200°C was used. As it can be seen, for all the equations, the CHF decreased with increasing heater diameter. This excludes Equation 2.41, which does not incorporate the heater diameter.

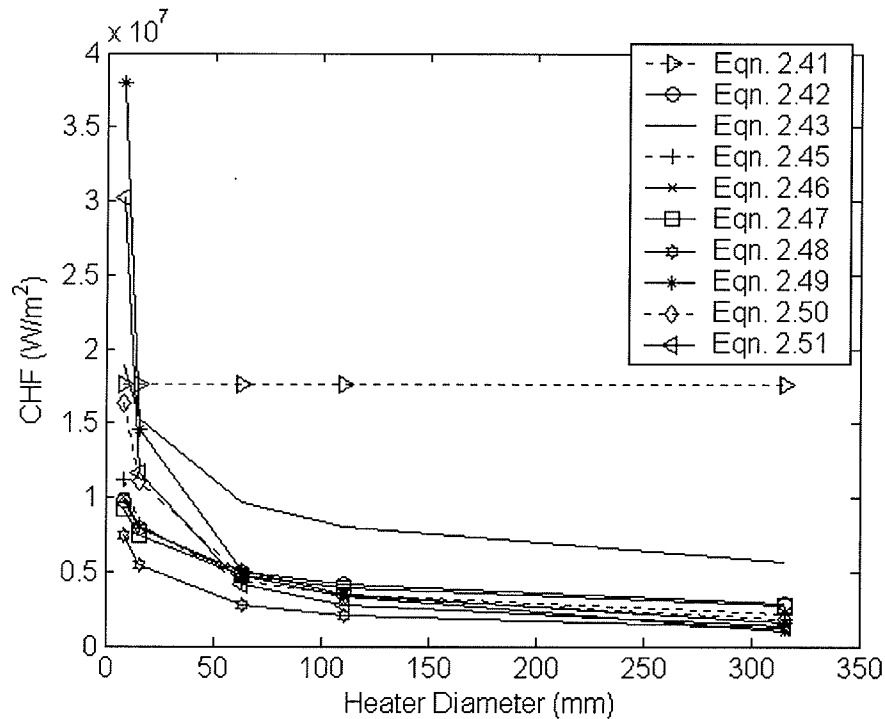
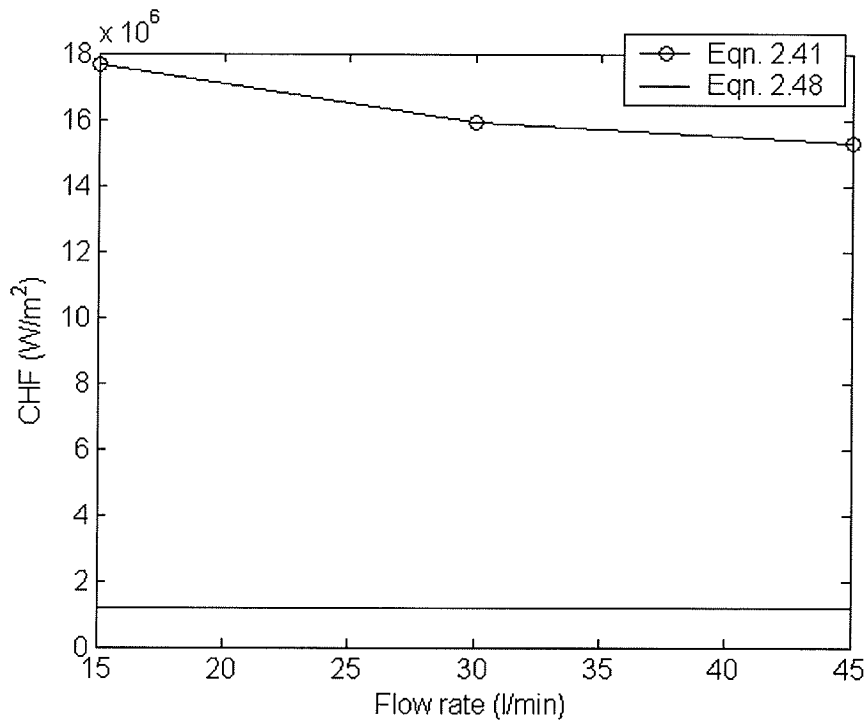


Figure 8.2: CHF at  $T_{\text{water}} = 30^{\circ}\text{C}$ , 15 l/min, and  $\Delta T_{\text{sat}}$  of  $200^{\circ}\text{C}$

### 8.3 Effect of Water Flow Rate

The effect of varying the water flow rate was also evaluated. The jet velocity and jet diameter increase with increasing flow rate. Figure 8.3 shows Equations 2.41 and 2.48 at flow rates ranging from 15 l/min to 45 l/min, a water temperature of  $30^{\circ}\text{C}$ , and a wall superheat of  $200^{\circ}\text{C}$ . At a constant water temperature and wall superheat, it was observed that the CHF decreased with increasing flow rate for Equation 2.41. Equation 2.48, however, does not vary with jet flow rate. The reason being is this equation is for the I-regime (see Table 8.1), which does not normally depend upon jet velocity.



**Figure 8.3: CHF for Equations 2.41 and 2.48 at  $T_{\text{water}} = 30^{\circ}\text{C}$  and  $\Delta T_{\text{sat}}$  of  $200^{\circ}\text{C}$  at different flow rates**

Figure 8.4 shows all the other equations at flow rates ranging from 15 l/min to 45 l/min, a water temperature of  $30^{\circ}\text{C}$ , and a wall superheat of  $200^{\circ}\text{C}$ . Unlike Equation 2.41, the CHF increased with increasing flow rate for all the equations evaluated.

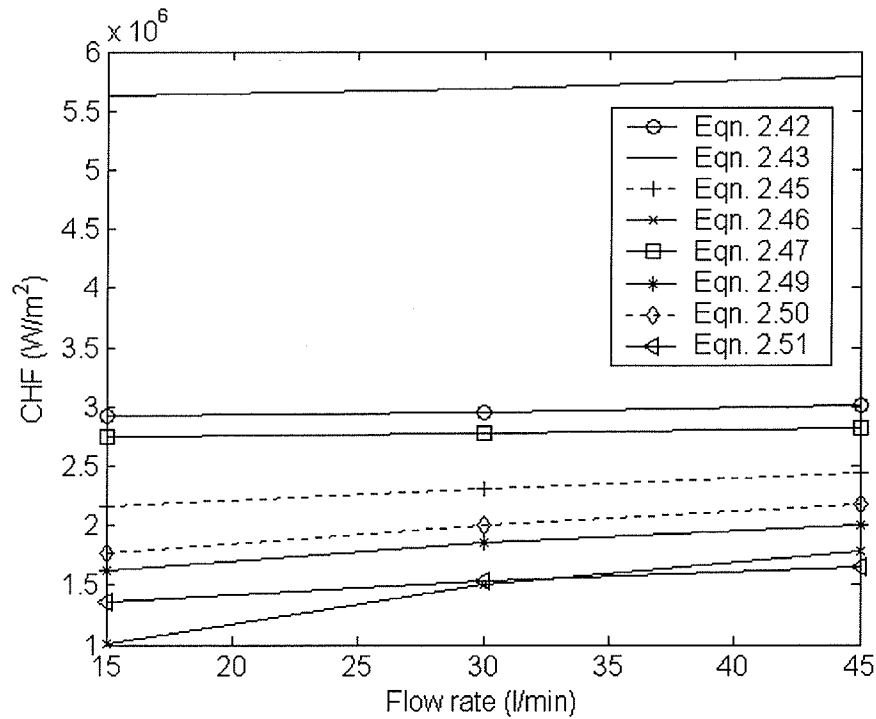


**Figure 8.4: CHF for all other equations at  $T_{\text{water}} = 30^{\circ}\text{C}$  and  $\Delta T_{\text{sat}}$  of  $200^{\circ}\text{C}$  at different flow rates**

#### 8.4 Effect of Water Temperature

The CHF was evaluated at all the tests described in Table 4.2. From these results, the effects of varying the water temperature can be determined. Figure 8.5 and Figure 8.6 show the CHF evaluated for all the equations at 15 l/min. In general, it can be seen that the CHF decreased with increasing water temperature. This excludes Equation 2.45 as shown in Figure 8.6, where the CHF increased with increasing water temperature. Similar trends were observed at the other flow rates.

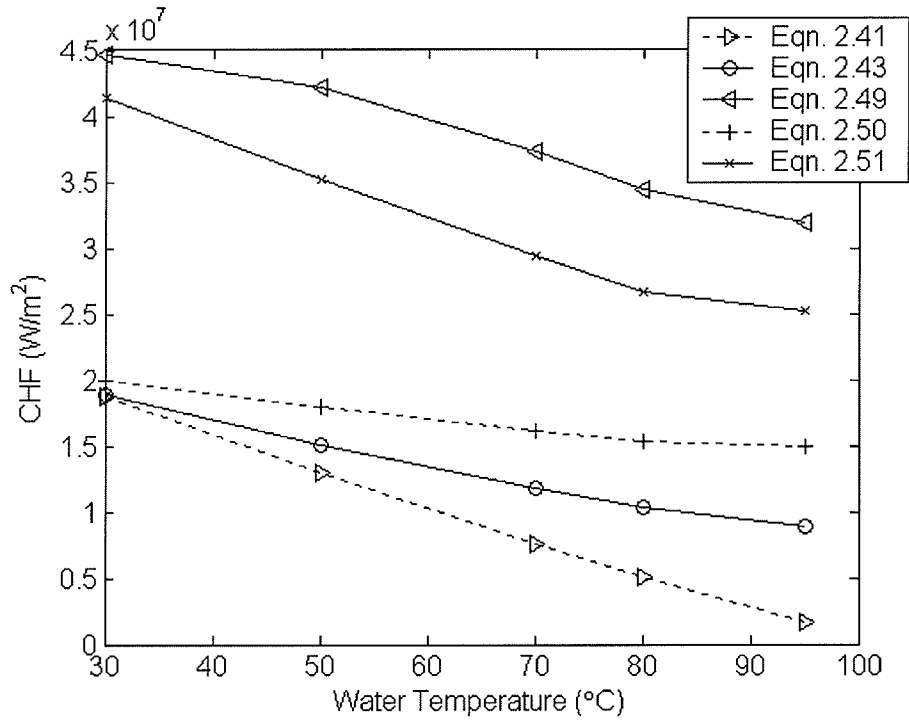


**Figure 8.5: CHF for Equations 2.41, 2.43, 2.49, 2.50, and 2.51 at 15 l/min at different water temperatures**

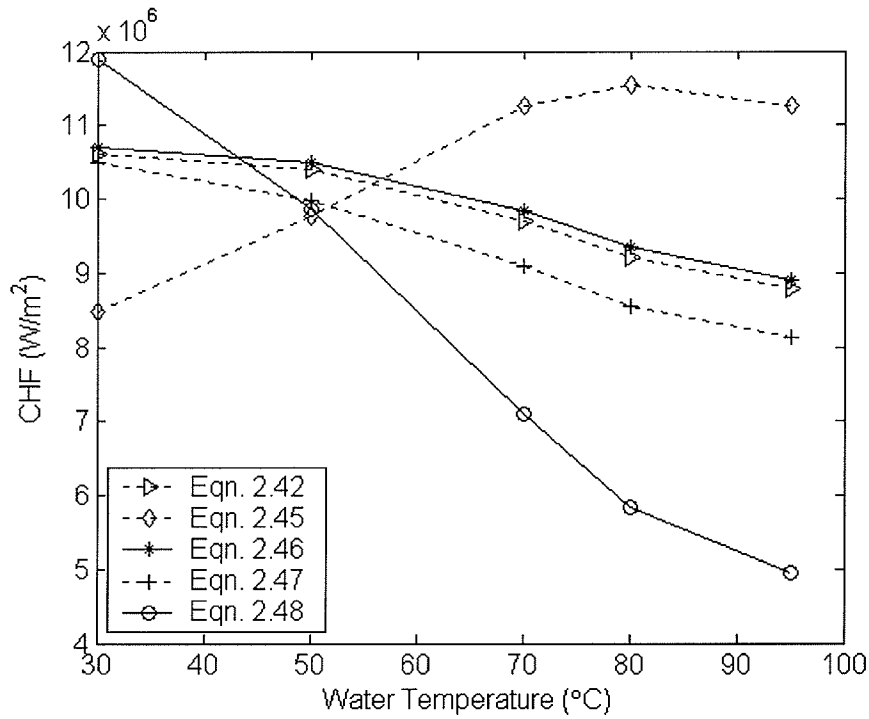


**Figure 8.6: CHF for Equations 2.42, 2.45, 2.46, 2.47, and 2.48 at 15 l/min at different water temperatures**

## 8.5 Comparison with the Experimental Data

The CHF calculated for all the equations were compared with the experimental data. The data CHF was determined as the highest heat flux directly after nucleate boiling, which is summarized in Table 4.3. The results for each equation will be presented with the equations calculated at a heater diameter of  $1.1 \cdot d_{ji}$ , as mentioned in Section 8.1. The percent error was calculated by calculating the difference between the CHF calculated and the experimental CHF and dividing this by the CHF determined from the experimental data:

$$\text{percent error} = \frac{CHF_{\text{equation}} - CHF_{\text{data}}}{CHF_{\text{data}}} \quad (8.1)$$

It can be seen in Equation 8.1 that a negative percent error signifies that the CHF calculated from the correlation is lower than that obtained from the experimental data. A positive percent error indicates that the calculated CHF was greater than the experimental CHF.

### 8.5.1 Results for Equation 2.41

Figure 8.7 and Table 8.4 summarize the percent error for Equation 2.41. In all instances, the equation underestimated the CHF. The percent error also increased with increasing water temperature. Also, the equation best represented the data at water temperatures below 40°C.

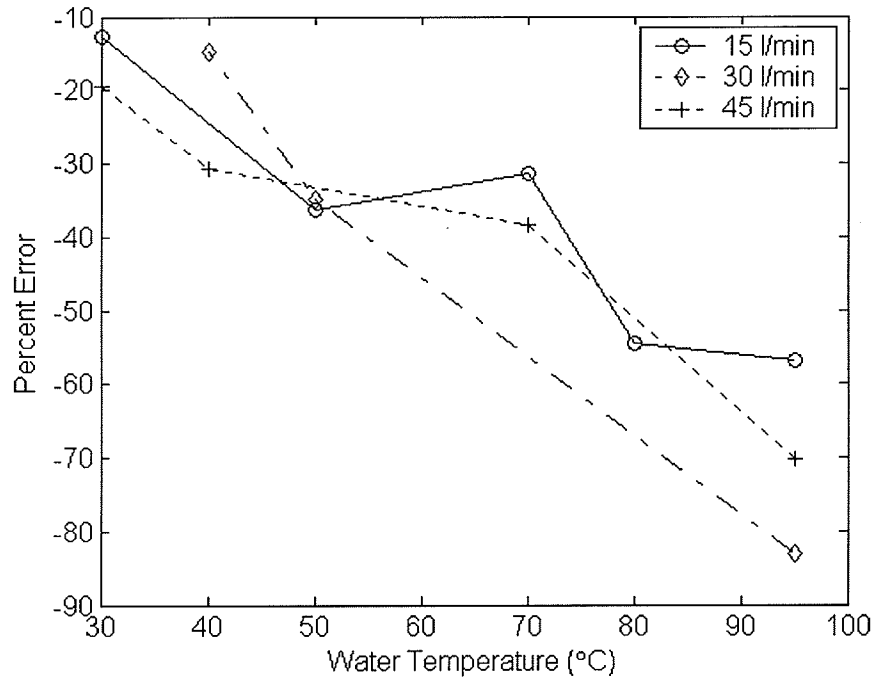


**Figure 8.7: Percent error for Equation 2.41**

**Table 8.4: Percent error for Equation 2.41**

Flow Rate	Water Temperature						
	30°C	40°C	50°C	60°C	70°C	80°C	95°C
15 l/min	-12.7%	:	-36.3%	:	-31.5%	-54.5%	-56.8%
30 l/min	:	-14.9%	-34.8%	:	:	:	-83.2%
45 l/min	-19.5%	-30.6%	:	:	-38.5%	:	-70.3%

Figure 8.8, Figure 8.9, and Figure 8.10 show Equation 2.41 compared with the experimental data at 15 l/min, 30 l/min, and 45 l/min, respectively. In Figure 8.8 at 15 l/min, it can be seen that the difference between the correlation and data is relatively the same at water temperatures of 30°C and 95°C. However, the percent error in Table 8.4 is higher at a water temperature of 95°C. The reason being is the percent error in Equation 8.1 is determined by dividing the difference by the experimental CHF. Since the experimental CHF at 95°C is lower, the percent error will be higher. The same explanation can be provided for the other flow rates.

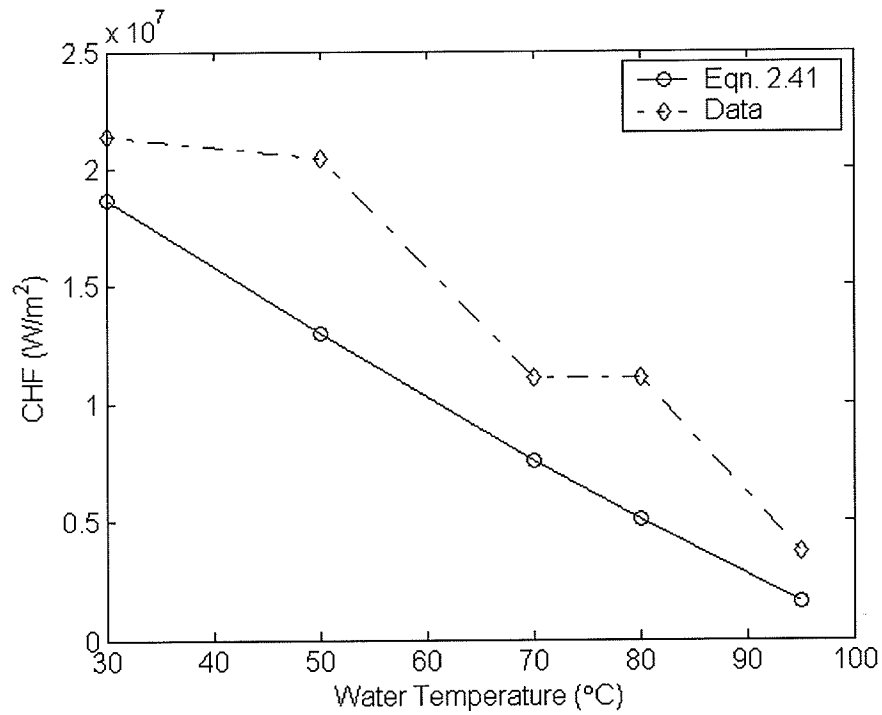


Figure 8.8: Equation 2.41 compared with the experimental data at 15 l/min

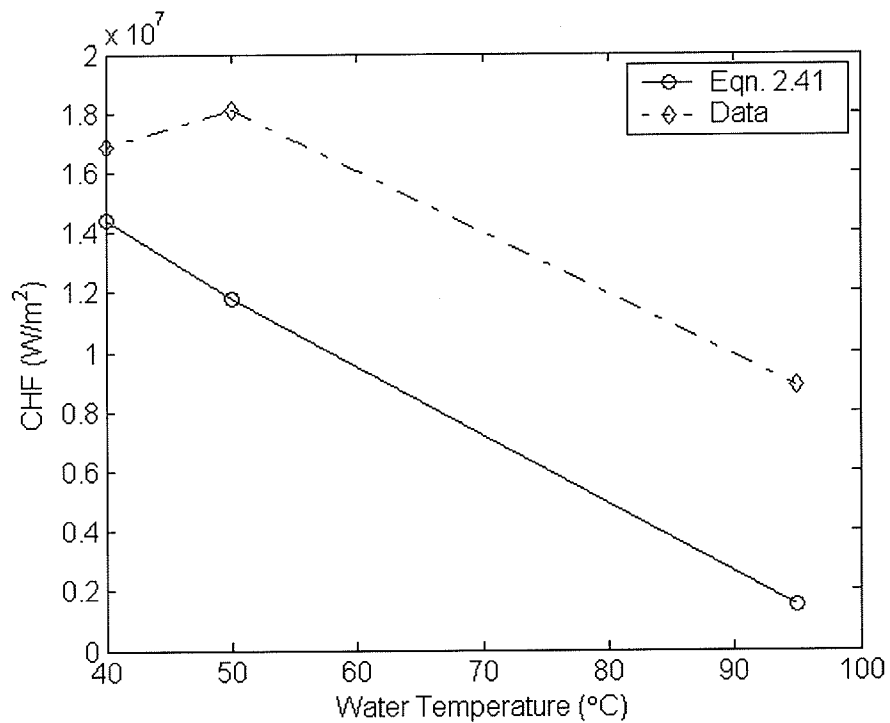
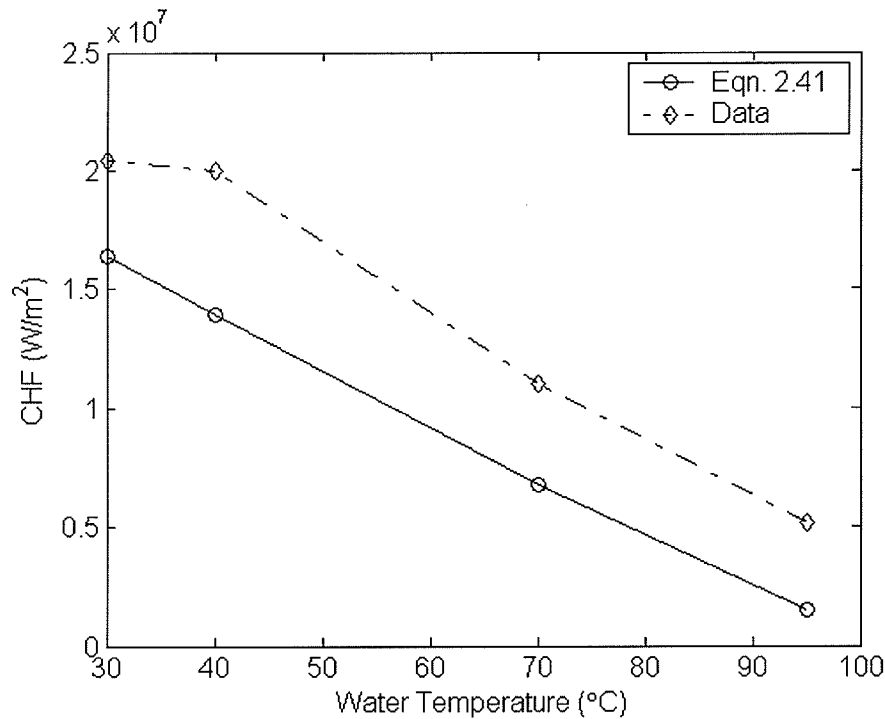


Figure 8.9: Equation 2.41 compared with the experimental data at 30 l/min



**Figure 8.10: Equation 2.41 compared with the experimental data at 45 l/min**

It can also be seen in Figure 8.8, Figure 8.9, and Figure 8.10 that at all of the flow rates, Equation 2.41 and the data CHF seemed to both decrease at the same rate with increasing water temperature.

In general, it can be summarized that Equation 2.41 adequately represents the data at water temperatures below and including 40°C. Looking at Table 8.1, the applicable conditions for the equation are at subcoolings ranging from 45°C to 80°C, or water temperatures ranging from 20°C to 55°C. Therefore, the equation seems to adequately represent the majority of its water temperature range. Considering only the tests within this range up to a water temperature of 55°C, 66.7% (4 out of 6) of the tests contained percent error less than 30%, which is a reasonably good fit.

### 8.5.2 Results for Equation 2.42

Figure 8.11 and Table 8.5 summarize the percent error for Equation 2.42. It can be seen that at water temperatures below and including 50°C, the equation matched poorly with the data. However, at water temperatures of 70°C and 80°C, the percent error was less than 20%. Then at a water temperature of 95°C at 15 and 45 l/min, the equation highly overestimated the heat flux. However, at 30 l/min, the equation matched well.

This can be explained by looking at the CHF compared with the data in Figure 8.12, Figure 8.13, and Figure 8.14 at 15 l/min, 30 l/min, and 45 l/min, respectively. At all the flow rates, Equation 2.42 seemed to remain relatively consistent across the different water temperatures. However, the experimental CHF decreased with increasing water temperature. Therefore, this led to a point where the correlation matched the CHF well at a particular water temperature. At 15 l/min, 30 l/min, and 45 l/min, the best match was at water temperatures of 84°C, 92°C, and 79°C, respectively (see Figure 8.12, Figure 8.13, and Figure 8.14).

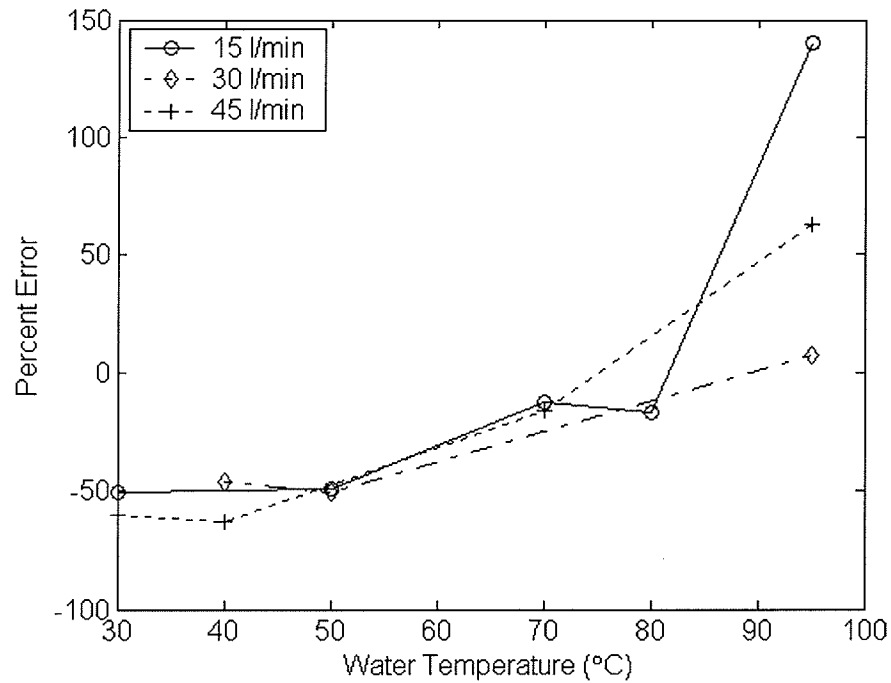


**Figure 8.11: Percent error for Equation 2.42**

**Table 8.5: Percent error for Equation 2.42**

Flow Rate	Water Temperature						
	30°C	40°C	50°C	60°C	70°C	80°C	95°C
15 l/min	-50.6%	:	-49.0%	:	-12.4%	-17.0%	139.9%
30 l/min	:	-46.3%	-50.9%	:	:	:	6.8%
45 l/min	-60.3%	-63.3%	:	:	-16.5%	:	62.8%

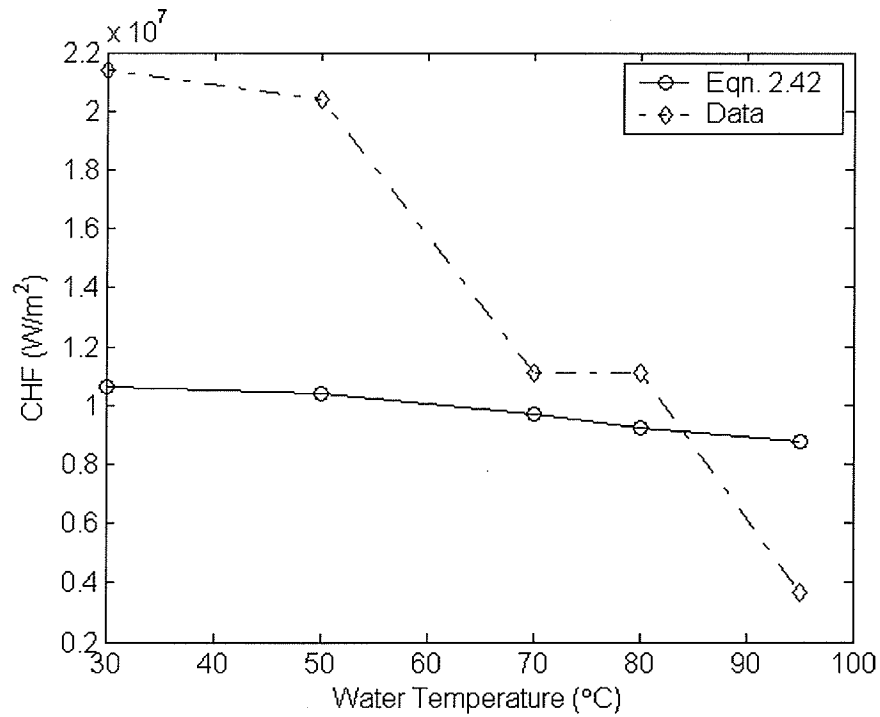


**Figure 8.12: Equation 2.42 compared with the experimental data at 15 l/min**

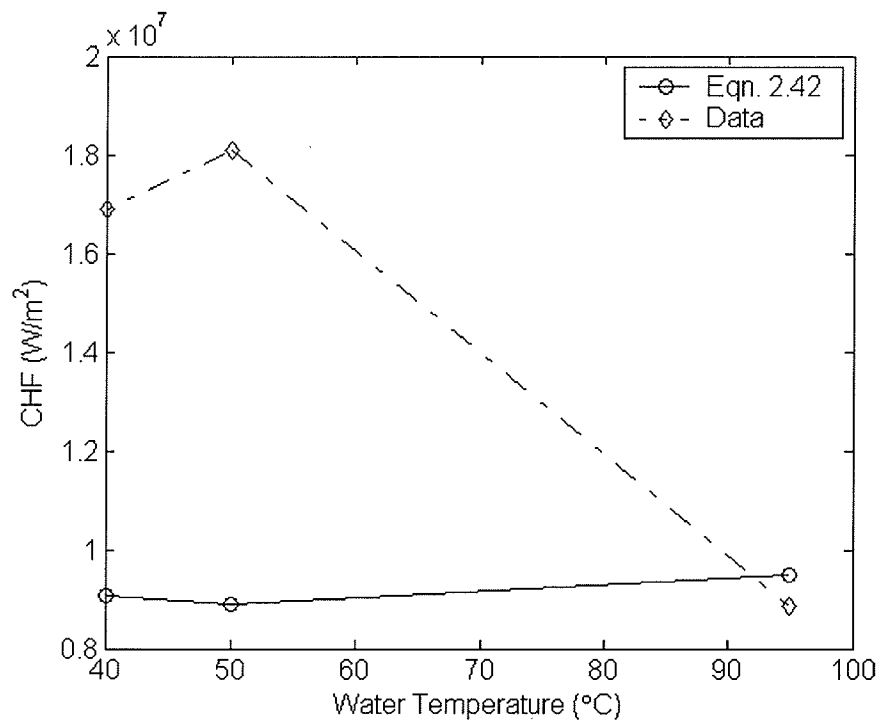


**Figure 8.13: Equation 2.42 compared with the experimental data at 30 l/min**

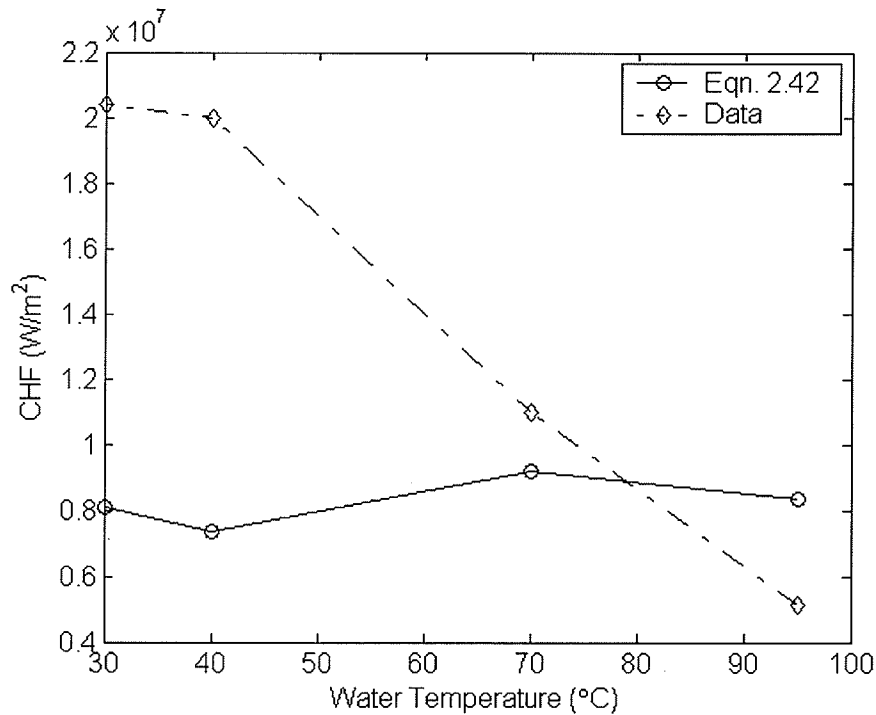


**Figure 8.14: Equation 2.42 compared with the experimental data at 45 l/min**

In general, however, Equation 2.42 poorly represented the data. Referring to Table 8.1, this equation is applicable for a saturated water jet. At a water temperature of 95°C in Table 8.5, the equation highly overestimated the CHF at 15 l/min and 45 l/min. However, it matched well at 30 l/min. Since it didn't match well at 15 l/min and 45 l/min, this shows that it can not be used to represent data at a water temperature of 95°C.

Furthermore, looking at Table 8.5, only 33.3% of the tests contained results with a percent error of less than 30%. Three out of these four tests occurred at water temperatures below 95°C. Since this occurred at water temperatures reasonably below the saturation temperature, this supports that Equation 2.42 should not be used to represent the data.

### 8.5.3 Results for Equation 2.43

Equation 2.43 is a modified version of Equation 2.42 provided by Monde and Katto (1978) [19] that incorporates the water subcooling. Figure 8.15 and Table 8.6 summarize the percent error. It can be seen that Equation 2.43 better represents the data than 2.42 did. Figure 8.16, Figure 8.17, and Figure 8.18 show the CHF compared with the data at 15 l/min, 30 l/min, and 45 l/min, respectively.

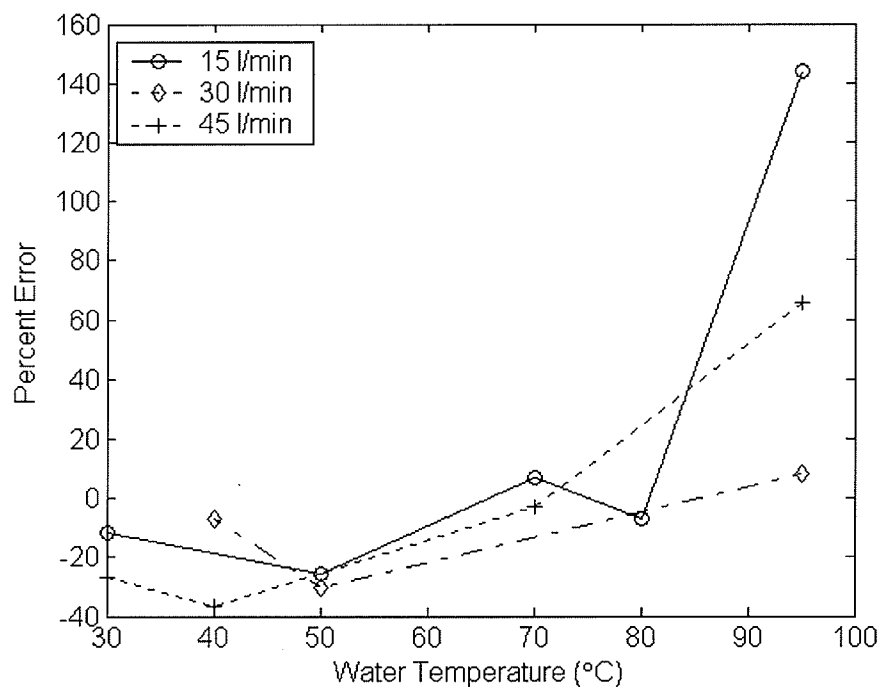


Figure 8.15: Percent error for Equation 2.43

Table 8.6: Percent error for Equation 2.43

Flow Rate	Water Temperature						
	30°C	40°C	50°C	60°C	70°C	80°C	95°C
15 l/min	-11.9%	:	-25.7%	:	6.8%	-6.8%	144.3%
30 l/min	:	-7.1%	-30.5%	:	:	:	8.1%
45 l/min	-26.9%	-36.8%	:	:	-2.7%	:	65.7%

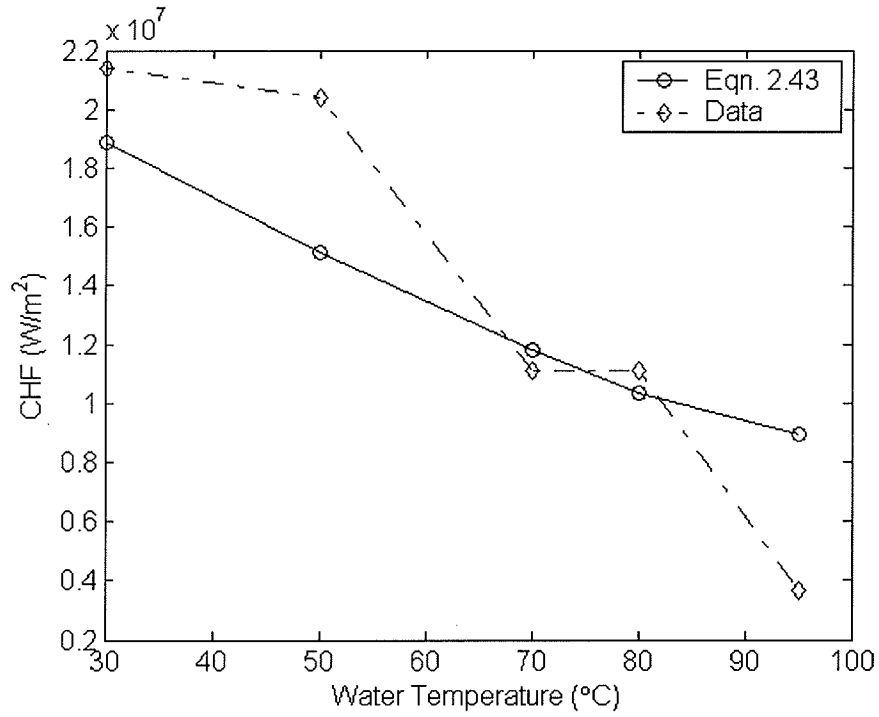


Figure 8.16: Equation 2.43 compared with the experimental data at 15 l/min

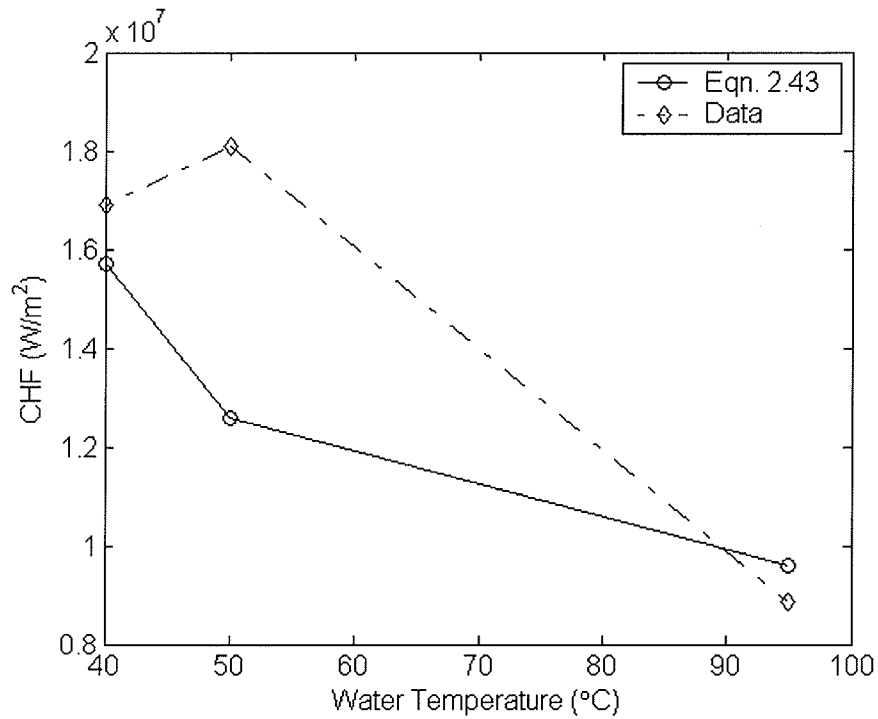
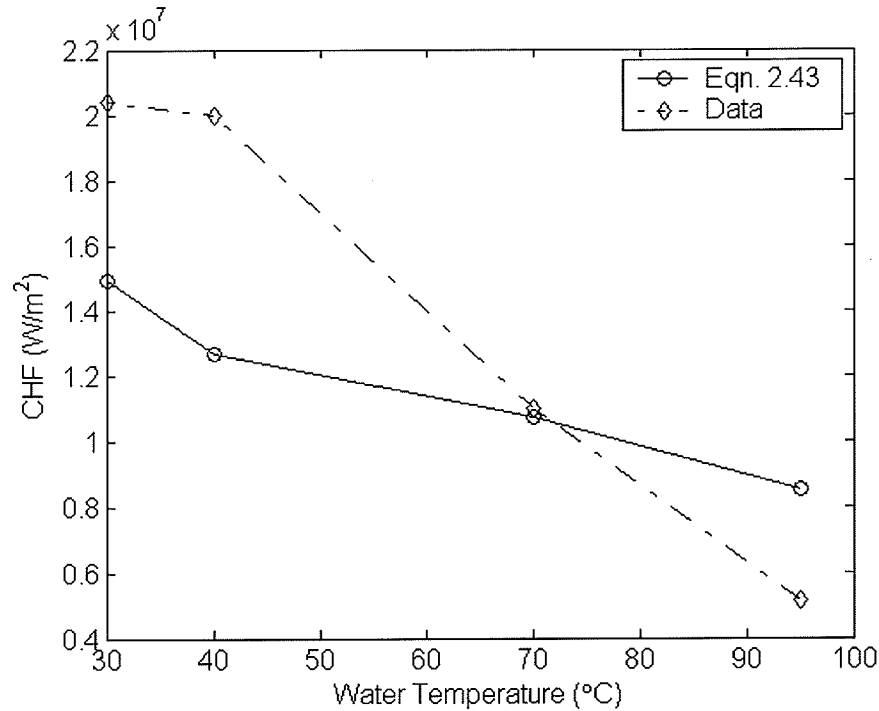


Figure 8.17: Equation 2.43 compared with the experimental data at 30 l/min



**Figure 8.18: Equation 2.43 compared with the experimental data at 45 l/min**

In Table 8.1, Equation 2.43 is applicable for water temperatures ranging from 30°C to 80°C. In Table 8.6, at water temperatures up to 80°C, 77.7% (7 out of 9) of these tests contained results with the percent error less than 30%. The best matches occurred at water temperatures of 70°C and 80°C. Therefore, it can be concluded that Equation 2.43 can be used to represent the data at all flow rates for water temperatures up to 80°C.

#### 8.5.4 Results for Equation 2.45

Figure 8.19 and Table 8.7 summarize the percent error for Equation 2.45. Figure 8.20, Figure 8.21, and Figure 8.22 show the equation compared with the experimental CHF at 15 l/min, 30 l/min, and 45 l/min, respectively. As determined in Section 8.4, Equation 2.45 increased with increasing water temperature. The experimental CHF decreased with increasing water temperature. Therefore, there should be a point where the CHF would be the closest. Looking at Figure 8.20, Figure 8.21, and Figure 8.22, this

occurred at water temperatures of 70°C, 95°C, and 81°C, for 15 l/min, 30 l/min, and 45 l/min, respectively.

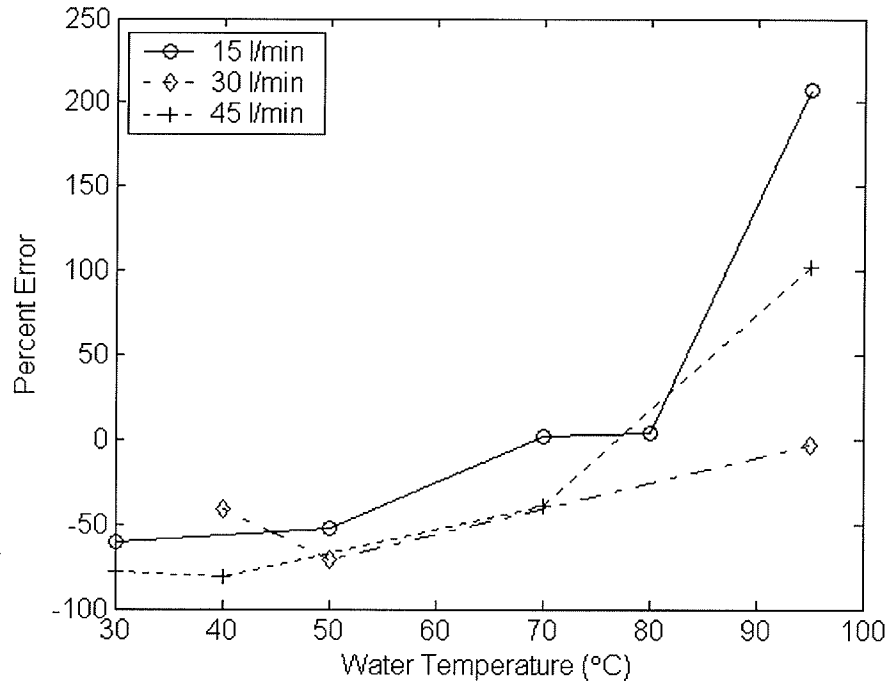


**Figure 8.19: Percent error for Equation 2.45**

**Table 8.7: Percent error for Equation 2.45**

Flow Rate	Water Temperature						
	30°C	40°C	50°C	60°C	70°C	80°C	95°C
15 l/min	-60.4%	:	-52.0%	:	1.7%	4.0%	207.8%
30 l/min	:	-41.0%	-70.9%	:	:	:	-3.0%
45 l/min	-78.1%	-80.7%	:	:	-39.3%	:	101.8%

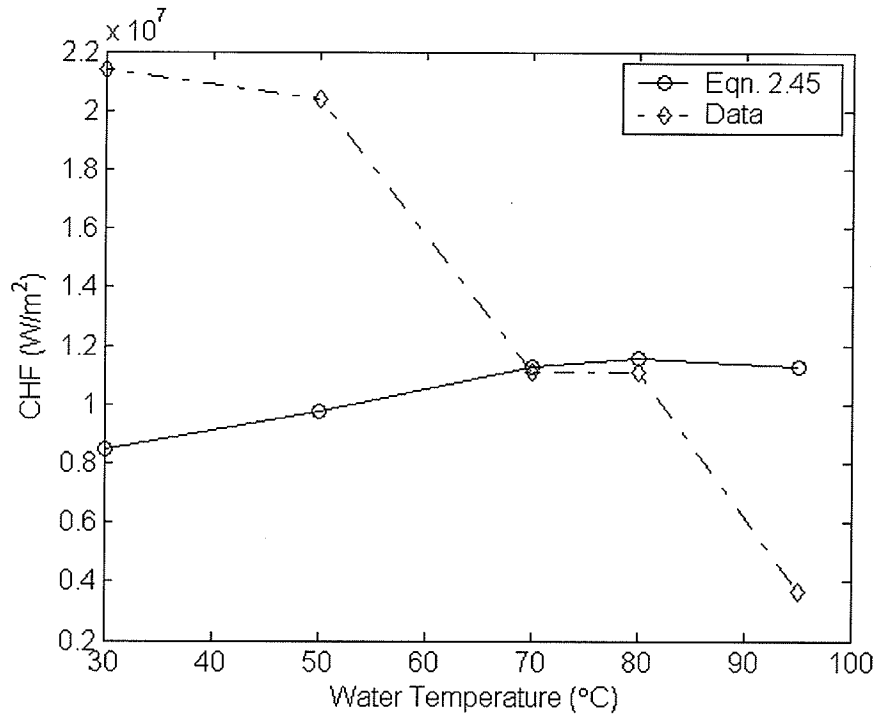


Figure 8.20: Equation 2.45 compared with the experimental data at 15 l/min

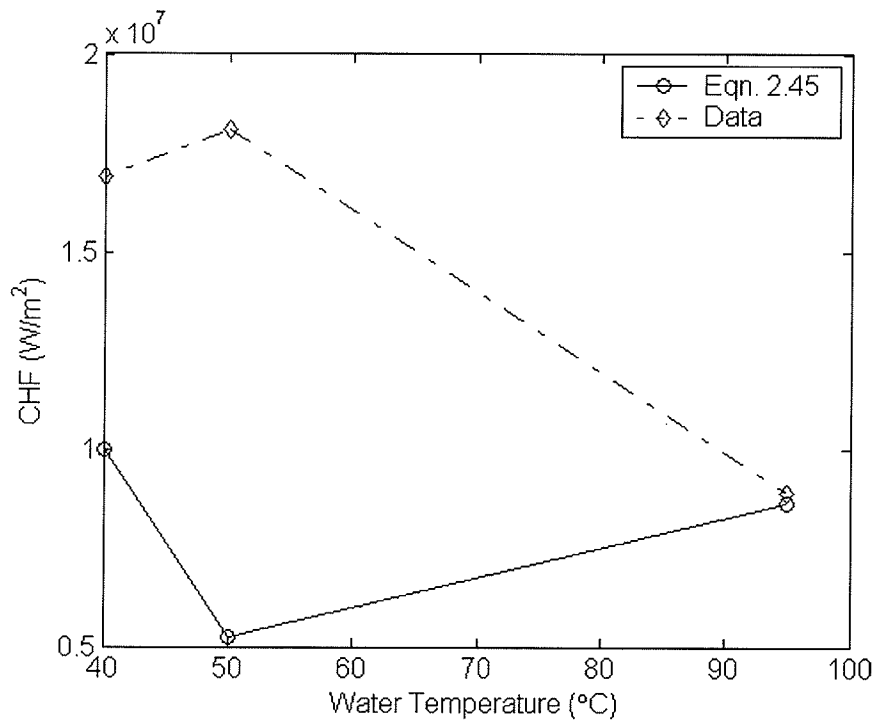
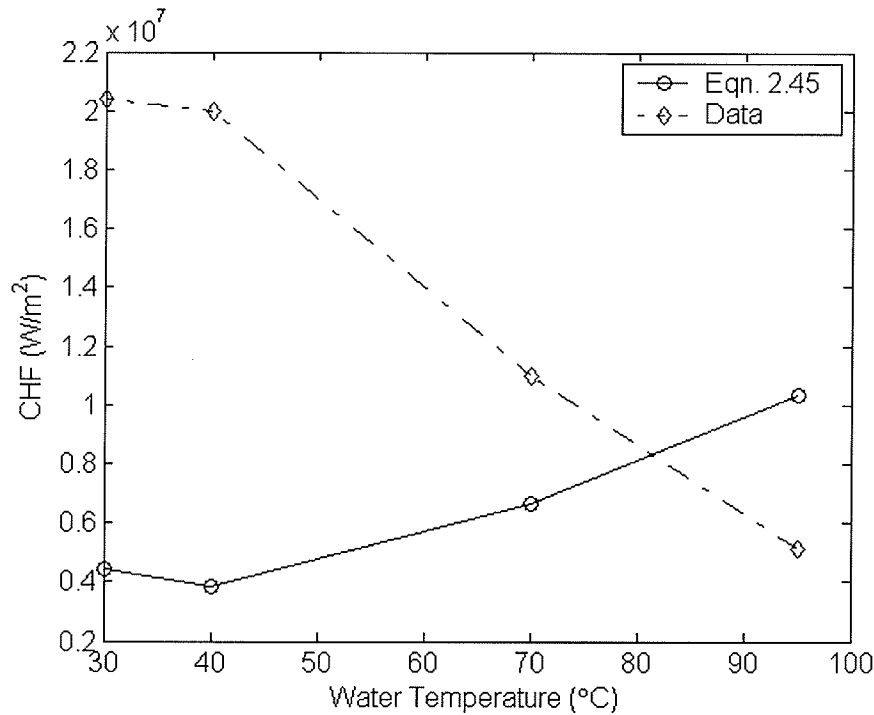


Figure 8.21: Equation 2.45 compared with the experimental data at 30 l/min



**Figure 8.22: Equation 2.45 compared with the experimental data at 45 l/min**

Looking at Table 8.1, this equation is applicable for a saturated jet. However, at 95°C, only 33.3% of the three tests at this temperature closest to saturation contained good results (see Table 8.7). Therefore, it can be concluded that Equation 2.45 is not a good representation of the data.

#### 8.5.5 Results for Equation 2.46

Figure 8.23 and Table 8.8 show the percent error for Equation 2.46. It can be seen in Figure 8.6 that Equations 2.42 and 2.46 contained almost exactly the same results. Looking at Table 8.1 and Section 2.3.4.1, Equation 2.46 was a modification of Equation 2.42. Therefore, Equation 2.46 will contain the same trends as Equation 2.42. Therefore, like Equation 2.42, Equation 2.46 is a poor representation of the data.

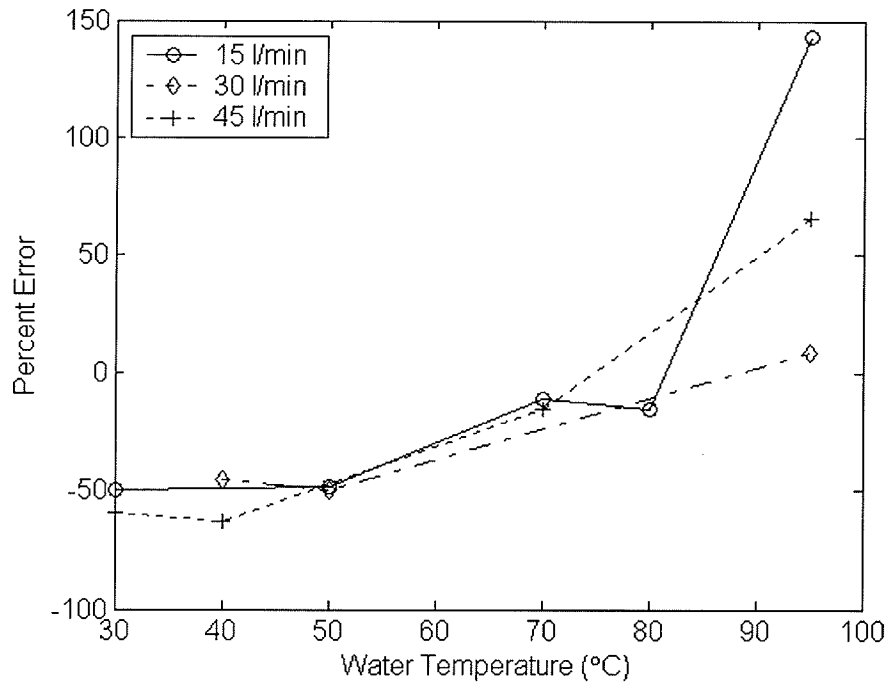


**Figure 8.23: Percent error for Equation 2.46**

**Table 8.8: Percent error for Equation 2.46**

Flow Rate	Water Temperature						
	30°C	40°C	50°C	60°C	70°C	80°C	95°C
15 l/min	-49.8%	:	-48.3%	:	-11.1%	-15.8%	143.5%
30 l/min	:	-45.4%	-50.1%	:	:	:	8.4%
45 l/min	-59.7%	-62.8%	:	:	-15.3%	:	65.3%

### 8.5.6 Results for Equation 2.47

Figure 8.24 and Table 8.9 show the percent error for Equation 2.47. Figure 8.25, Figure 8.26, and Figure 8.27 show the equation compared with the experimental CHF at 15 l/min, 30 l/min, and 45 l/min, respectively. It can be seen in Figure 8.6, that Equation 2.47 contained results close to that of Equations 2.42 and 2.46. This is because these equations were developed by one of the same researchers (Monde in [5, 18, and 27]).

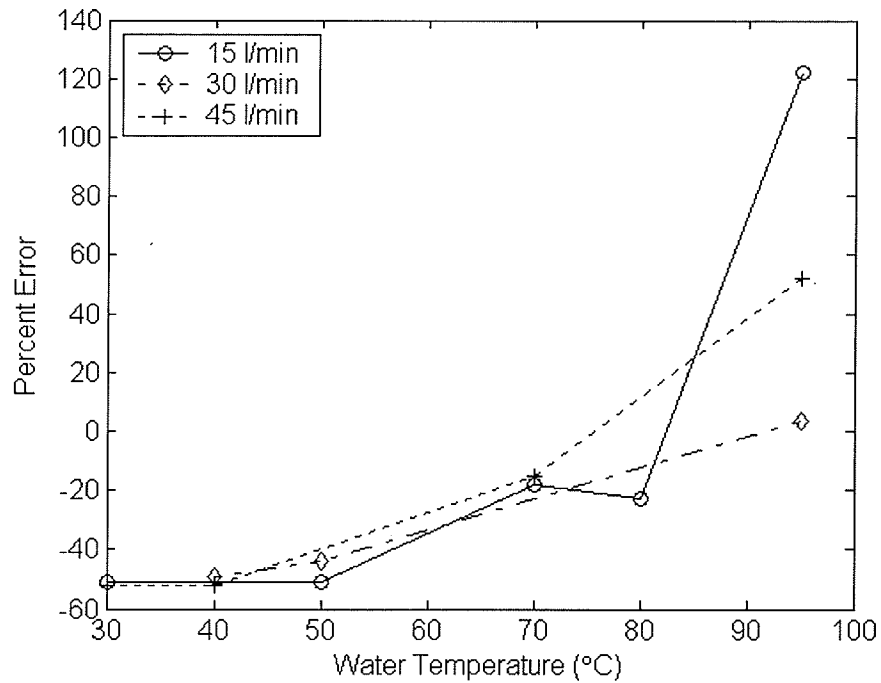


**Figure 8.24: Percent error for Equation 2.47**

**Table 8.9: Percent error for Equation 2.47**

Flow Rate	Water Temperature						
	30°C	40°C	50°C	60°C	70°C	80°C	95°C
15 l/min	-51.0%	:	-51.0%	:	-18.0%	-22.9%	121.8%
30 l/min	:	-49.2%	-44.2%	:	:	:	3.4%
45 l/min	-52.3%	-52.0%	:	:	-15.2%	:	52.1%

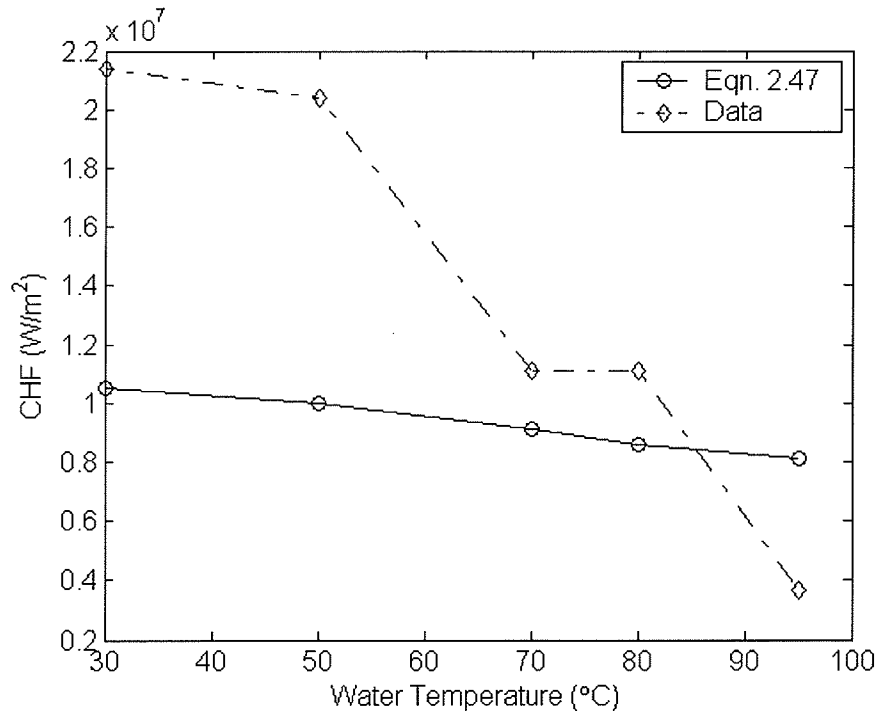


**Figure 8.25: Equation 2.47 compared with the experimental data at 15 l/min**

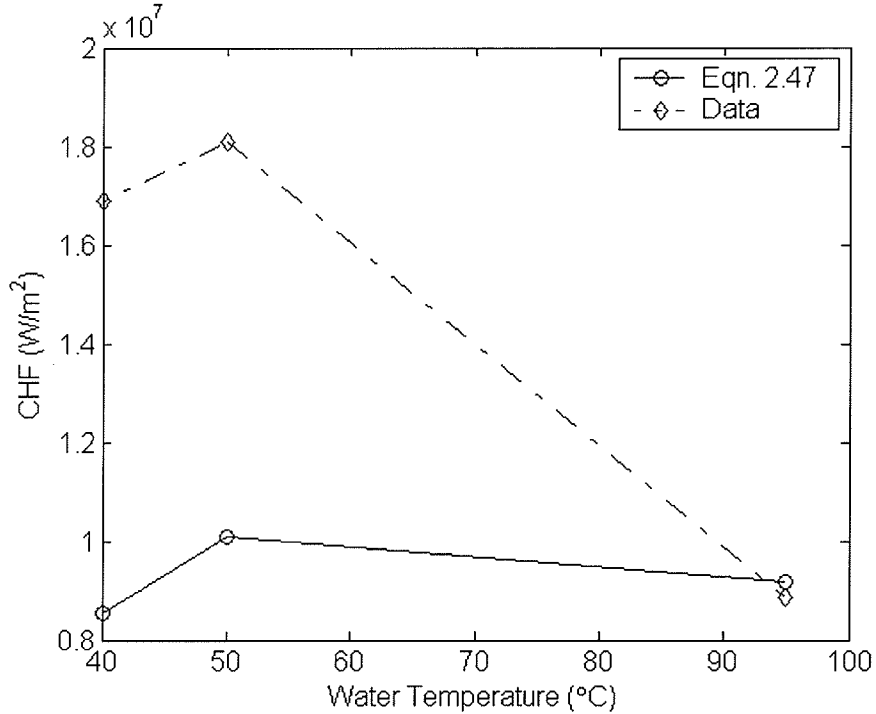


**Figure 8.26: Equation 2.47 compared with the experimental data at 30 l/min**

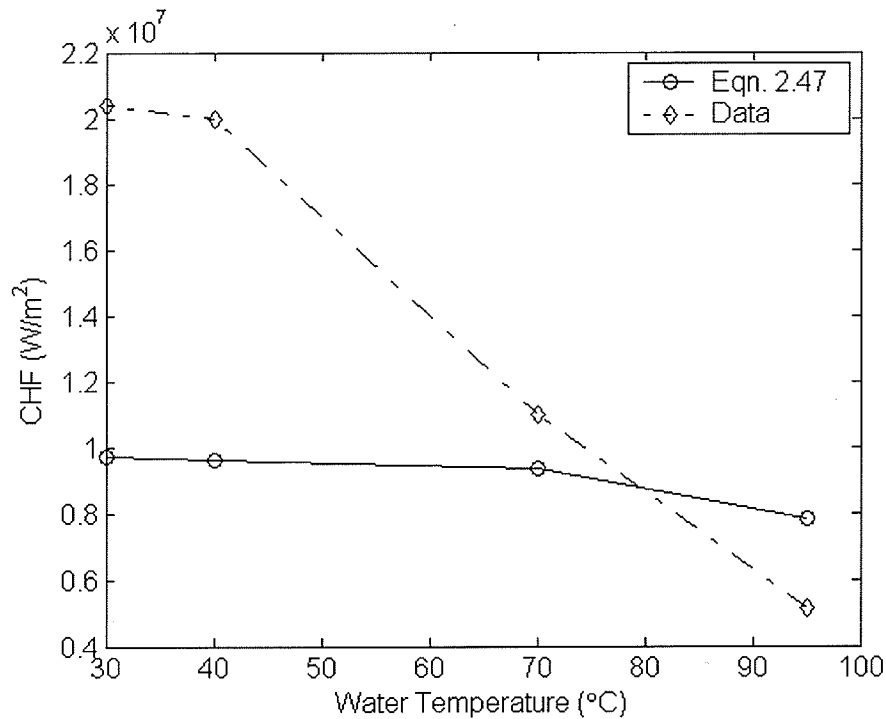


**Figure 8.27: Equation 2.47 compared with the experimental data at 45 l/min**

Looking at Figure 8.25, Figure 8.26, and Figure 8.27, Equation 2.47 decreased slightly with water temperature, but at a lesser rate than the experimental heat flux did. Looking at these figures, the temperature that the correlation CHF matched the best with the experimental CHF occurred at water temperatures of 85°C, 95°C, and 80°C, at 15 l/min, 30 l/min, and 45 l/min, respectively.

Looking at Table 8.1, Equation 2.47 is applicable for a saturated jet. However, looking at Table 8.9, only one of the three tests evaluated at 95°C contained a percent error of less than 30%. Furthermore, at 15 l/min and 45 l/min, the heat flux was highly overestimated at a water temperature of 95°C and the best match at these flow rates occurred at lower water temperatures. Therefore, it can be ascertained that Equation 2.47 should not be used to adequately represent the data.

### 8.5.7 Results for Equation 2.48

Figure 8.28 and Table 8.10 show the percent error for Equation 2.48. Figure 8.29, Figure 8.30, and Figure 8.31 show the correlation compared with the experimental CHF at 15 l/min, 30 l/min, and 45 l/min, respectively. It should be noted that Equation 2.48 was developed by the same researchers that devised Equation 2.47. However, Equation 2.48 is for the I-regime while Equation 2.47 is for the V-regime.

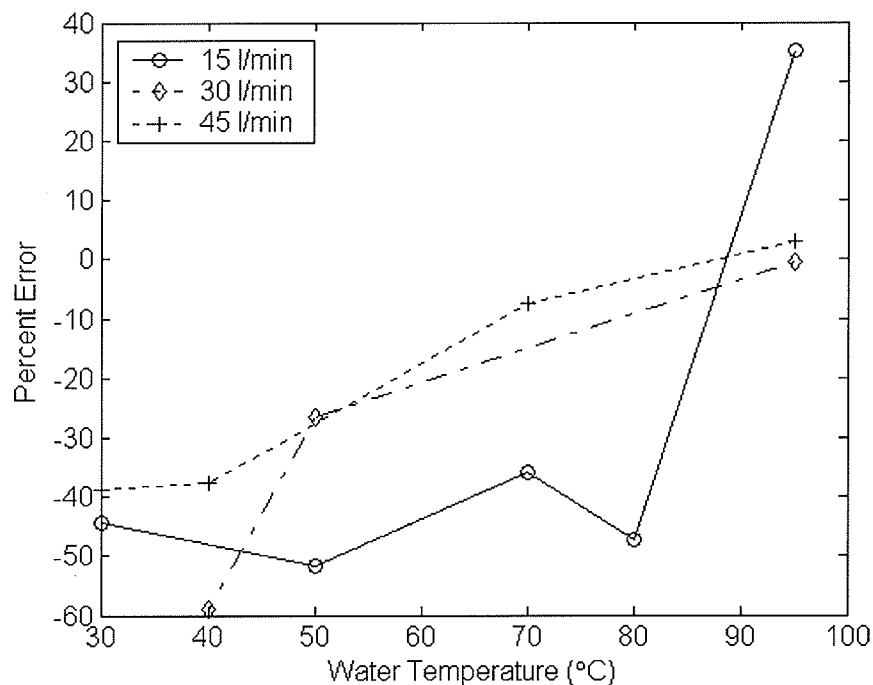


Figure 8.28: Percent error for Equation 2.48

Table 8.10: Percent error for Equation 2.48

Flow Rate	Water Temperature						
	30°C	40°C	50°C	60°C	70°C	80°C	95°C
15 l/min	-44.3%	:	-51.6%	:	-35.8%	-47.4%	35.3%
30 l/min	:	-59.1%	-26.4%	:	:	:	-0.6%
45 l/min	-38.7%	-37.8%	:	:	-7.5%	:	3.0%

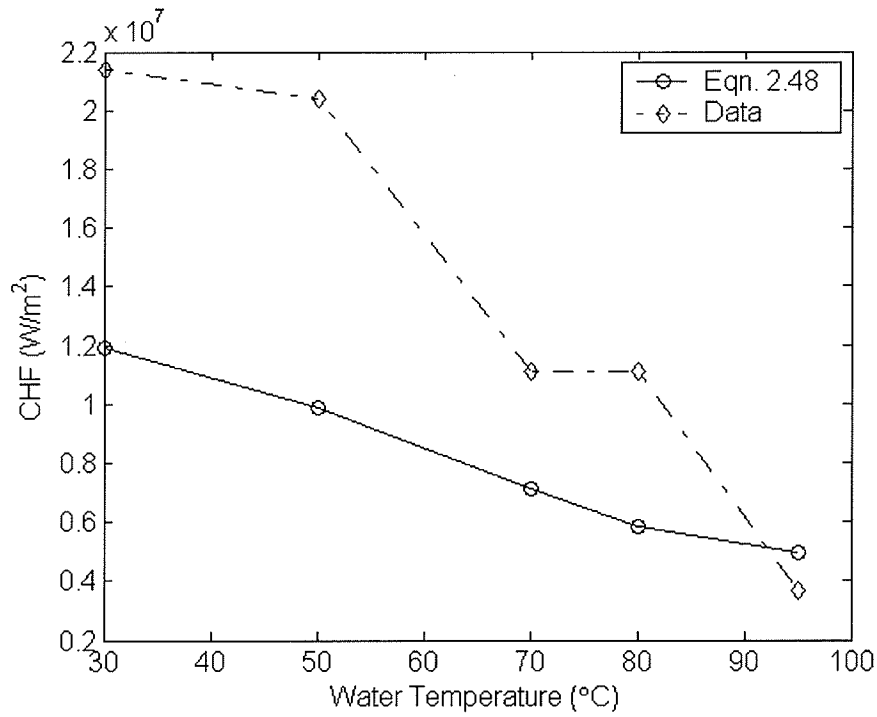


Figure 8.29: Equation 2.48 compared with the experimental data at 15 l/min

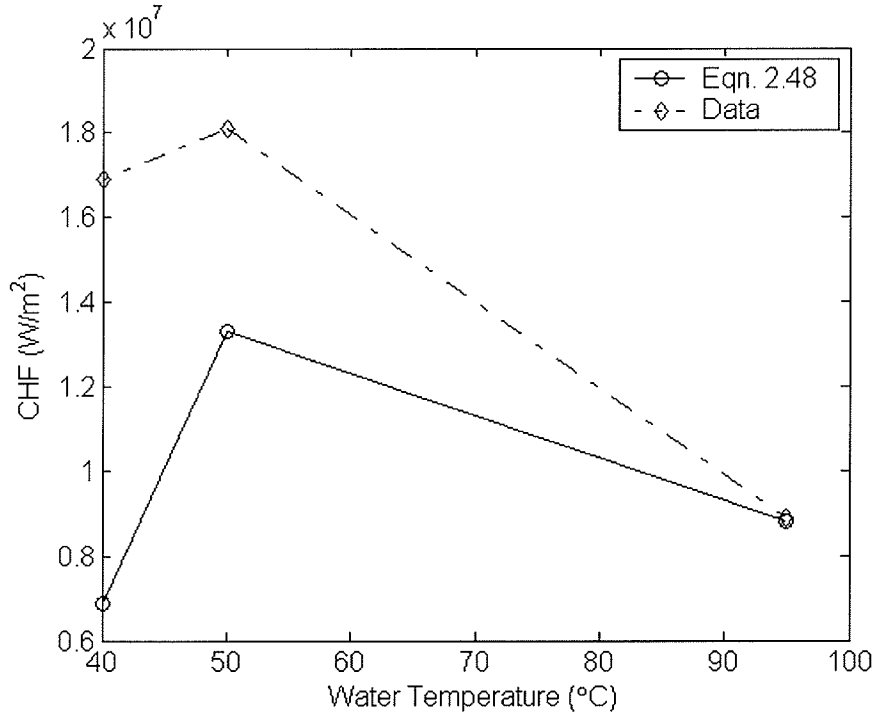
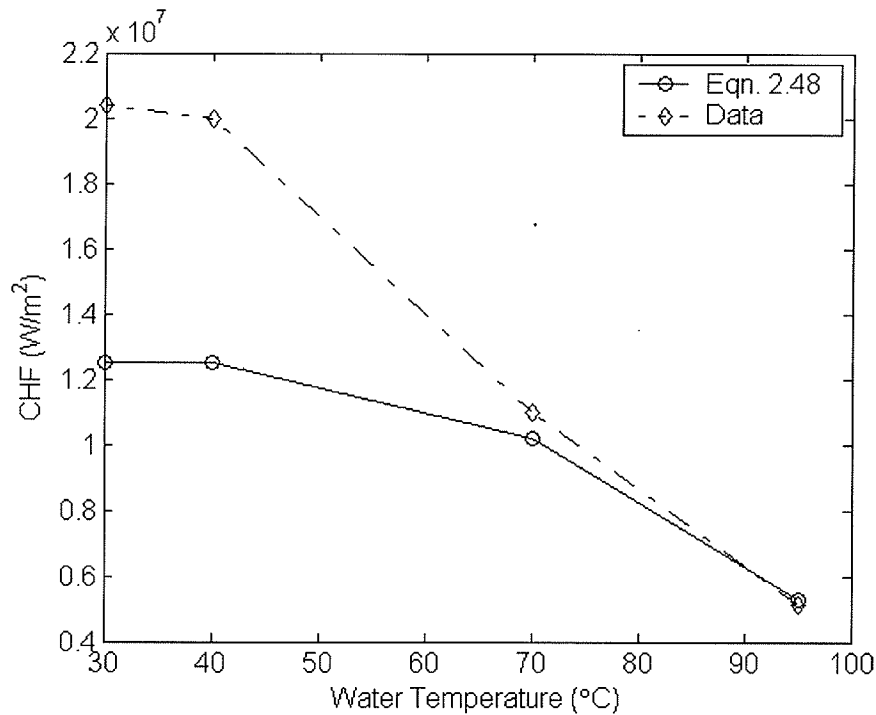


Figure 8.30: Equation 2.48 compared with the experimental data at 30 l/min



**Figure 8.31: Equation 2.48 compared with the experimental data at 45 l/min**

It can be seen in Figure 8.29, Figure 8.30, and Figure 8.31 that the best match occurred at water temperatures of 92°C, 95°C, and 95°C at 15 l/min, 30 l/min, and 45 l/min, respectively. In addition, at 30 l/min and 45 l/min, the percent match was only -0.6% and 3% in Table 8.10, which is extremely close. In Table 8.1, this equation is applicable for a saturated jet. Therefore, since the best matches occurred at water temperatures relatively close to the saturation temperature, then it can be concluded that Equation 2.48 can be used to represent the data at a water temperature of 95°C.

### 8.5.8 Results for Equation 2.49

Figure 8.32 and Table 8.11 show the percent error for Equation 2.49. As it can be seen, in all tests, the equation highly overestimated the data. In Table 8.1, Equation 2.49 is for a saturated jet. However, at a water temperature of 95°C, the equation contained

the greatest error with errors greater than 300% (see Table 8.11). Therefore, this equation should not be used to represent the data.

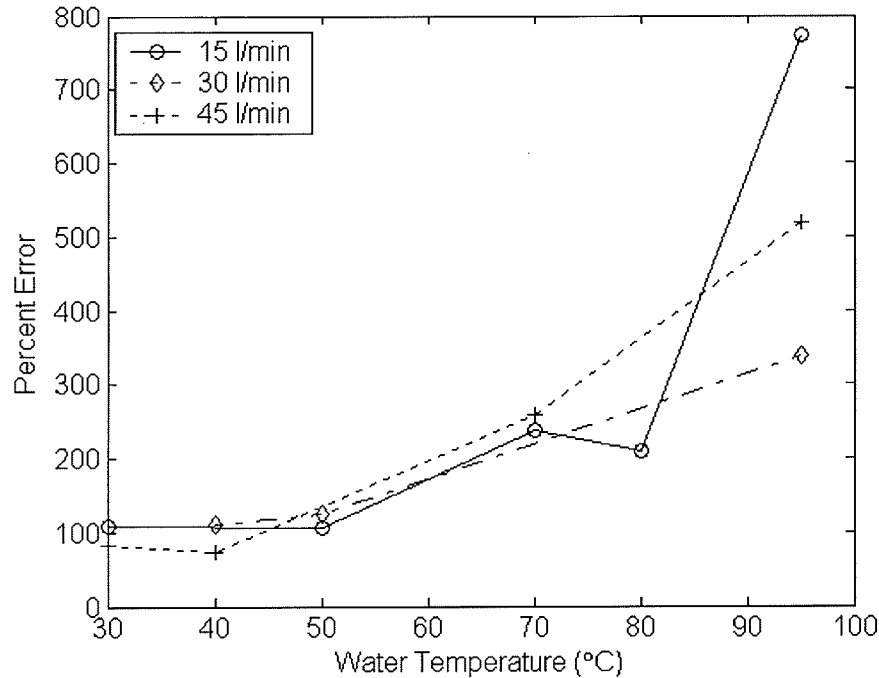


**Figure 8.32: Percent error for Equation 2.49**

**Table 8.11: Percent error for Equation 2.49**

Flow Rate	Water Temperature						
	30°C	40°C	50°C	60°C	70°C	80°C	95°C
15 l/min	108.8%	:	107.4%	:	237.0%	209.5%	772.8%
30 l/min	:	110.6%	124.1%	:	:	:	337.4%
45 l/min	83.9%	74.1%	:	:	257.9%	:	517.8%

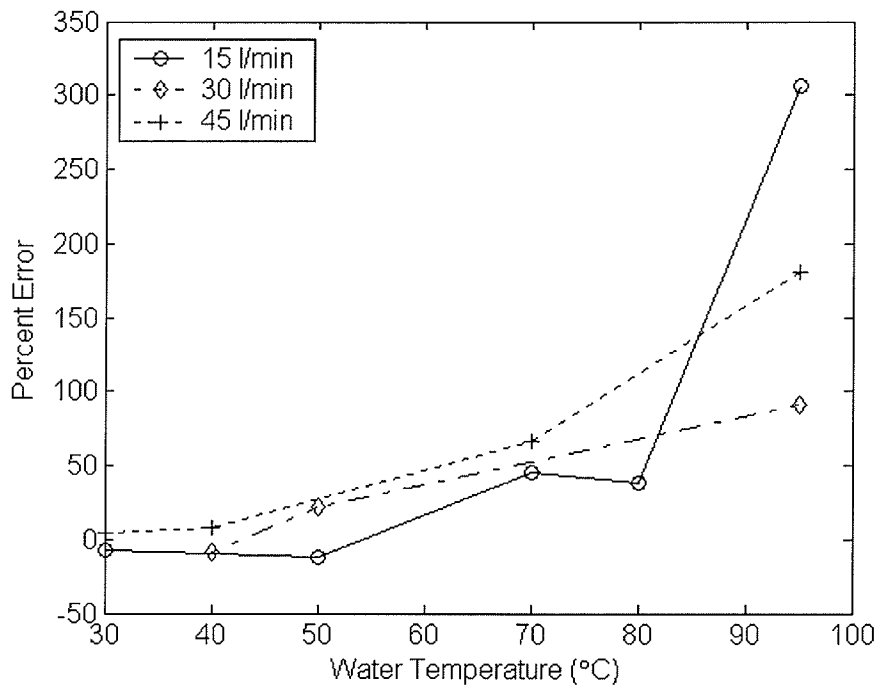
### 8.5.9 Results for Equation 2.50

Figure 8.33 and Table 8.12 show the percent error for Equation 2.50. Figure 8.34, Figure 8.35, and Figure 8.36 show Equation 2.50 compared with the experimental CHF at 15 l/min, 30 l/min, and 45 l/min, respectively. It can be seen that the best matches occurred at water temperatures less than 60°C, which is well below saturated conditions. Also, in Table 8.12, the equation represented the data well at water temperatures less than

50°C. On the contrary, in Table 8.1, this equation is applicable for a saturated jet.

However, the percent error was the highest at a water temperature of 95°C.

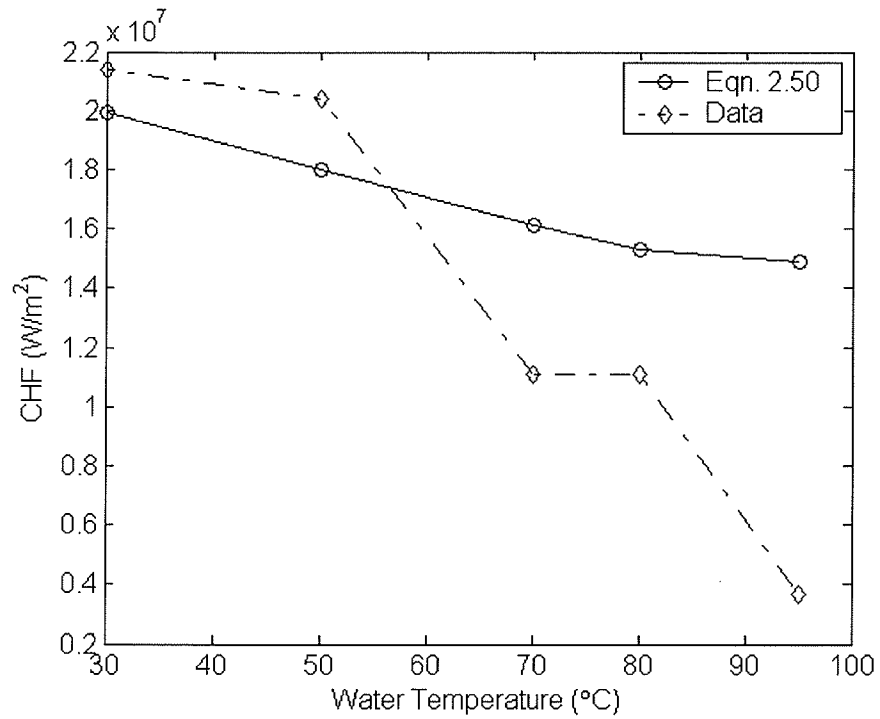
This equation was derived from the experimental data from Monde and Katto [19], and Monde [28], which both provided CHF equations presented earlier (Equations 2.42, 2.43, and 2.46). Equation 2.43 (Section 8.5.3) was applicable for lower water temperatures. Yet Equations 2.42 (Section 8.5.2) and 2.46 (Section 8.5.5) did not match well with the data. Since there was a discrepancy between these equations, it is difficult to say why Equation 2.50 was higher at lower water temperatures. However, it can be determined that Equation 2.50 poorly represents the data.



**Figure 8.33: Percent error for Equation 2.50**

**Table 8.12: Percent error for Equation 2.50**

Flow Rate	Water Temperature						
	30°C	40°C	50°C	60°C	70°C	80°C	95°C
15 l/min	-6.8%	:	-11.5%	:	45.1%	38.2%	305.8%
30 l/min	:	-8.3%	22.2%	:	:	:	90.7%
45 l/min	4.8%	7.5%	:	:	66.5%	:	180.6%

**Figure 8.34: Equation 2.50 compared with the experimental data at 15 l/min**

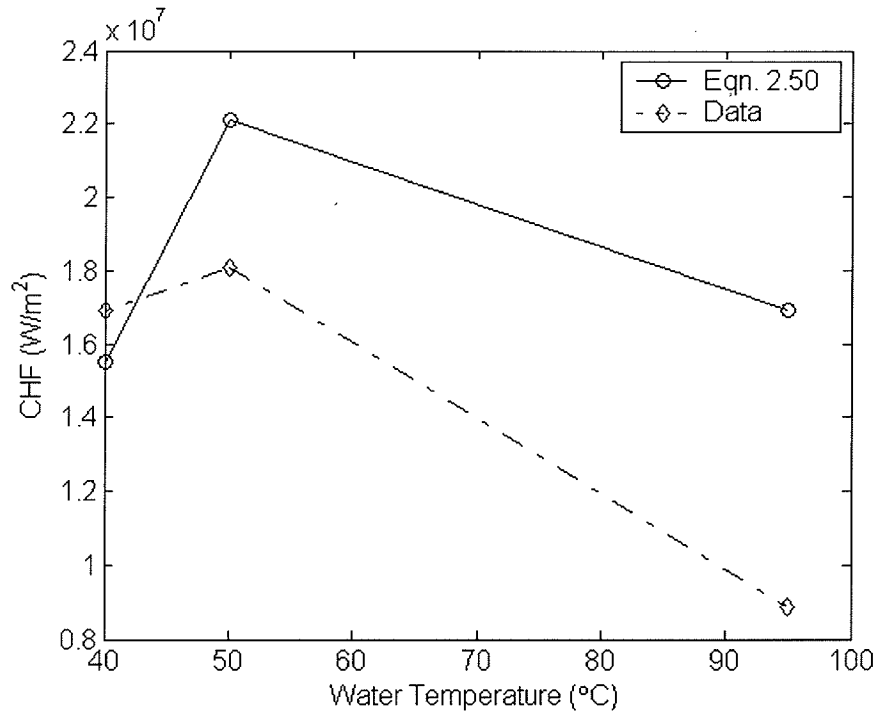


Figure 8.35: Equation 2.50 compared with the experimental data at 30 l/min

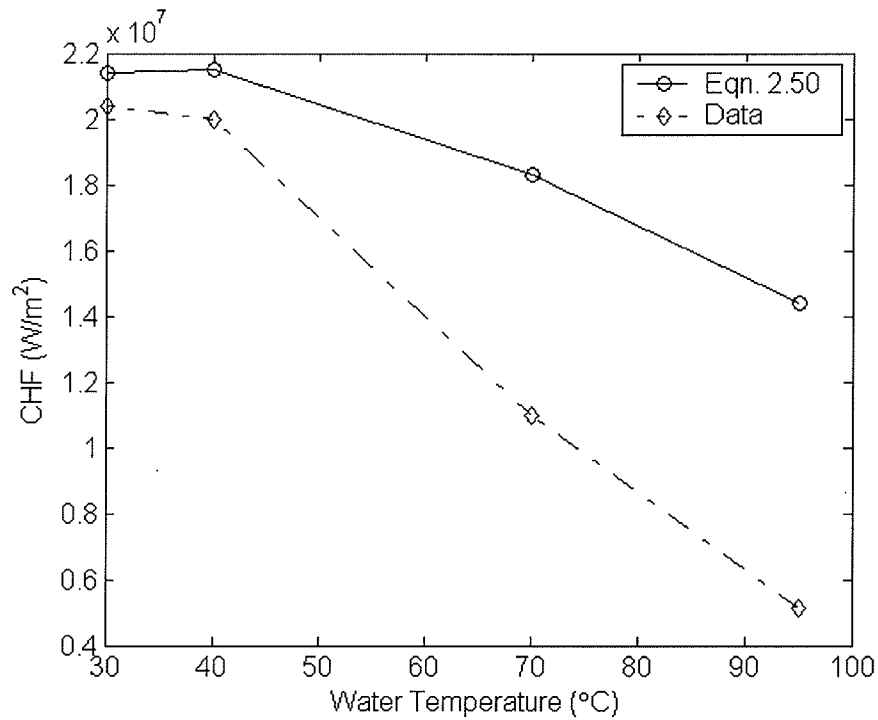


Figure 8.36: Equation 2.50 compared with the experimental data at 45 l/min

### 8.5.10 Results for Equation 2.51

Figure 8.37 and Table 8.13 show the percent error for Equation 2.51. Like Equation 2.49, this equation highly overestimated the CHF. Furthermore, this equation is applicable for a saturated jet. Yet at a water temperature of 95°C in Table 8.13, the percent error was the greatest with errors greater than 270%. Therefore, it can be concluded that Equation 2.51 is a poor representation of the experimental data.

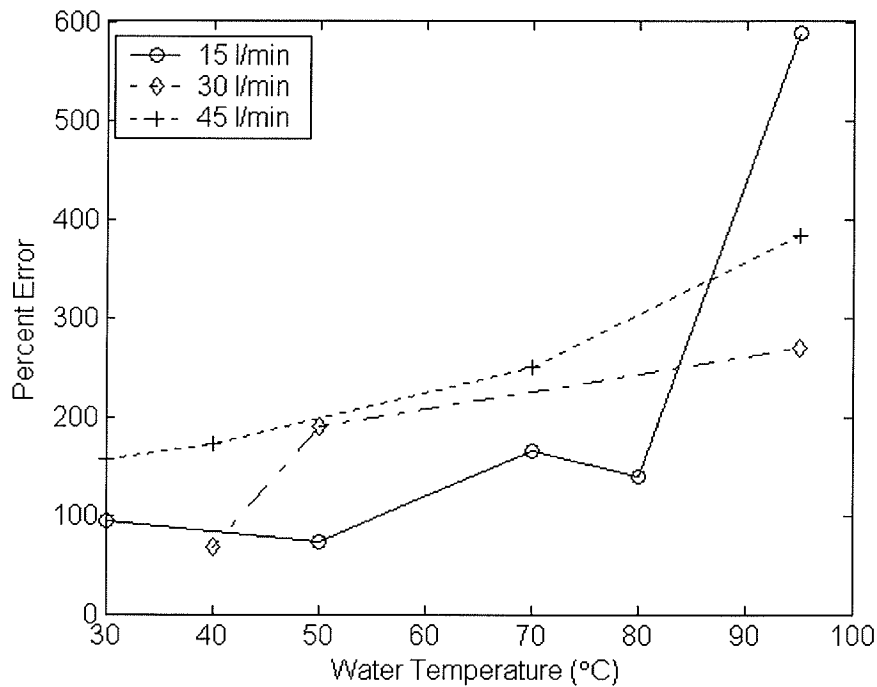


Figure 8.37: Percent error for Equation 2.51

Table 8.13: Percent error for Equation 2.51

Flow Rate	Water Temperature						
	30°C	40°C	50°C	60°C	70°C	80°C	95°C
15 l/min	93.4%	:	73.1%	:	165.7%	140.1%	589.2%
30 l/min	:	68.2%	189.9%	:	:	:	270.0%
45 l/min	156.9%	173.6%	:	:	249.8%	:	383.8%

### 8.5.11 Summary of Results

The majority of the CHF equations presented by other researchers should not be used to represent the data. The conditions where these equations can represent the data are summarized in Table 8.14. The three equations that can be used to represent the data are Equations 2.41, 2.43, and 2.48. Equations 2.41 and 2.43 incorporate the water subcooling and thus are applicable at particular water temperatures.

Equation 2.41 can be used for water temperatures less than or equal to 40°C at all the flow rates evaluated. Equation 2.43 is applicable for water temperatures at and below 80°C for flow rates from 15 l/min to 45 l/min. Equation 2.48 is for the I-regime and can be used at a water temperature of 95°C since it is for a saturated jet.

**Table 8.14: Conditions when the CHF equations can represent the data**

Equation	Conditions When can Represent the Data
2.41	Water temperatures $\leq 40^\circ\text{C}$ Flow rate of 15–45 l/min
2.42	N/a
2.43	Water temperatures $\leq 80^\circ\text{C}$ Flow rate of 15–45 l/min
2.45	N/a
2.46	N/a
2.47	N/a
2.48	Water temperature of $95^\circ\text{C}$ Flow rate of 15–45 l/min
2.49	N/a
2.50	N/a
2.51	N/a

## 9. Conclusion

The cooling process in a hot steel mill has a great effect on determining the metallurgical properties of the steel. Researchers have examined jet impingement heat transfer to better understand this cooling process. This report reviewed the effects of various parameters on jet impingement heat transfer for a stationary jet. A summary of these most important effects are:

- Increasing the jet velocity increases heat transfer within the CHF, transition boiling and film boiling regimes. Doing so also increases the advancement of the rewetting front.
- Decreasing the water temperature increases the CHF and minimum heat flux and increases heat transfer within the single-phase forced convection regime.
- Increasing the jet diameter increases the size of the stagnation region, which thereby enhances heat transfer.
- Increasing the wall superheat increases heat transfer within the nucleate boiling region.
- There is conflicting evidence on the effect of nozzle-to-surface spacing.
- Surface oxidation increases the heat flux within the transition and film boiling regions.
- The effect of a moving plate increases heat transfer downstream from the stagnation point and decreases heat transfer upstream.

This thesis also compared correlations presented by other researchers with the experimental data from the ROTC facility within the single-phase forced convection, nucleate boiling, two-phase, and CHF regimes. Only correlations within the stagnation region for a circular stationary jet were examined. Using these equations will help provide an estimate as to the amount of cooling that occurs in a steel mill depending upon various conditions such as jet velocity and diameter. This can help control the metallurgical properties of the steel desired. An outline of the results is presented below.

- In the single-phase forced convection the following equation presented by Stevens and Webb (1991) [15] best represented the data at water temperatures up to 80°C:

$$Nu_j = 2.67 \cdot Re_j^{0.567} \cdot Pr^{0.4} \cdot \left(\frac{Z}{d_j}\right)^{-0.0336} \cdot \left(\frac{v_j}{d_j}\right)^{-0.237} \quad (2.14)$$

- All of the nucleate boiling correlations evaluated highly overestimated the experimental data.
- A new correlation was developed, which can be used to represent heat transfer within the single-phase forced convection and nucleate boiling regimes at water temperatures from 30°C to 95°C, and flow rates from 15 l/min to 45 l/min:

$$q''_{SUB} = h_{mic} \cdot \Delta T_{sat} + h_{mac} \cdot (T_{surf} - T_{water}) \quad (2.40)$$

where:

$$h_{mac} = 2.67 \cdot Re_j^{0.567} \cdot Pr^{0.4} \cdot \left(\frac{Z}{d_j}\right)^{-0.0336} \cdot \left(\frac{v_j}{d_j}\right)^{-0.237} \cdot \frac{k_f}{d_j} \quad (7.1)$$

$$h_{mic} = 0.00122 \cdot \left(\frac{k_f^{0.79} \cdot C_{pf}^{0.45} \cdot \rho_f^{0.49} \cdot g^{0.25}}{\sigma^{0.25} \mu_f^{0.29} \cdot h_{fg}^{0.24} \cdot \rho_g^{0.24}}\right) \cdot \Delta T_{sat}^{0.24} \cdot \Delta p_{sat}^{0.75} \cdot S \quad (2.37)$$

$$S = 1.218 \cdot e^{-0.023 \cdot \Delta T_{sat}} \text{ when } \Delta T_{sat} > 0 \quad (7.4)$$

$$S = 1 \text{ when } \Delta T_{sat} = 0$$

$$S = 0 \text{ when } \Delta T_{sat} < 0$$

- Three CHF correlations were found to well represent the data. The first two incorporate the water temperature and the last one is applicable for a saturated jet. These correlations apply for flow rates ranging from 15 l/min to 45 l/min. The applicable conditions for these equations when compared with the data are:

$$1. \quad \dot{q}_{CHF}'' = 1.42 \times 10^4 \cdot \left( \frac{v_j}{d_j} \right)^{0.34} \cdot \Delta T_{sub}^{1.15} \text{ at water temperatures } \leq 40^\circ\text{C} \quad (2.41)$$

$$2. \quad \frac{\dot{q}_{CHF}''}{\rho_g \cdot h_{fg} \cdot v_j} = 0.0745 \cdot \left( \frac{\rho_f}{\rho_g} \right)^{0.725} \cdot \left[ \frac{2 \cdot \sigma}{\rho_f \cdot v_j^2 \cdot D} \right]^{1/3} \cdot (1 + \varepsilon_{sub}) \quad (2.43)$$

Where:

$$\varepsilon_{sub} = 2.7 \cdot \left( \frac{\rho_f}{\rho_g} \right)^{0.5} \cdot \left( \frac{C_{pf} \cdot \Delta T_{sub}}{h_{fg}} \right) \text{ at water temperatures } \leq 80^\circ\text{C}$$

$$3. \quad \frac{\dot{q}_{CHF}''}{\rho_g \cdot h_{fg} \cdot v_j} = 2.02 \cdot \left( \frac{\rho_f}{\rho_g} \right)^{1/3} \cdot \left[ \frac{\sigma}{\rho_f \cdot v_j^2 \cdot D} \right]^{1/2} \text{ at a water temperature of } 95^\circ\text{C} \quad (2.48)$$

When calculating the heat flux, it is recommended to use the new two-phase correlation for the single-phase forced convection and nucleate boiling regions. At water temperatures less than or equal to 80°C, Equation 2.43 can be used to calculate the CHF. At a water temperature of 95°C to the saturation temperature, Equation 2.48 can be used.

## 10. Recommendations for Future Work

Jet impingement heat transfer has been widely researched for the past few decades. However, further research needs to be performed in order to really understand the cooling process that occurs in a hot steel mill. Some recommendations for future work are:

- Jet impingement heat transfer has been widely researched for planar and circular jets on a stationary plate. However, in a mill, the steel sheet is moving. Therefore, considerable research needs to be performed for a moving plate. The ROTC facility is currently being modified to incorporate this. When completed, jet impingement tests will be performed with plate speeds ranging up to 5 m/s. Then more experiments need to be performed. Furthermore, correlations for a moving plate need to be developed.
- The ROTC facility only uses downward facing jets. To better simulate actual conditions on the hot rolling table, the facility should be modified to facilitate both upward and downward facing jets.
- The majority of the research only incorporates a single jet. In a steel mill, large arrays of water jets are used. Therefore, more experiments need to be performed incorporating an array of jets as the heat transfer is different. The ROTC facility has three circular nozzles. More experiments should be performed there using three jets and compared to the single jet experiments.
- Correlations presented by other researchers for the transition boiling regime need to be compared with the experimental data gathered previously at the ROTC facility. As found earlier in Section 4.4.4.3, film boiling does not occur at all the water

temperatures evaluated. Therefore, it is not necessary to compare film boiling correlations with the experimental data.

- The mechanism of what the suppression factor is for the microconvective heat transfer component for two-phase forced convection is not fully understood. More research needs to be performed to examine how the bubble formation changes with two-phase flow when compared to nucleate pool boiling heat transfer to better comprehend how adding a suppression factor affects the microconvective component.
- More research needs to be performed to accurately determine the effects of nozzle-to-surface spacing. It is recommended that large spacings up to 1.5 m be examined to simulate conditions in a steel mill.
- The difference between planar and circular jets needs to be determined. This is especially so if one is more effective than the other when the same cooling area is considered. Knowing this difference may help reduce the amount of water required to cool the steel sheet.
- The thermocouple conduction error needs to be determined so when experiments are performed, more accurate temperature readings can be achieved.

---

## 11. References

1. "2002 World Steel Production Breaks Previous Records". Association of Iron and Steel Engineers. 2003. <http://www.steelnews.com/news/jan03/jan82.htm>
2. Meng Q. "Experimental Study of Transient Cooling of a Hot Steel Plate by an Impinging Circular Jet". M.Sc. Thesis. University of British Columbia. Oct. 2002.
3. Hauksson A. "Experimental Study of Boiling Heat Transfer During Water Jet Impingement on a Hot Steel Plate". M.Sc. Thesis. University of British Columbia. Nov. 2001.
4. Filipovic J., Viskanta R., Incropera F.P., Veslocki T. "Thermal Behaviour of a Moving Steel Strip Cooled by an Array of Planar Water Jets". *Steel Research*. Vol. 63, No 10. pp. 438-446. 1992.
5. Chen S.J., Tseng A.A. "Spray and Jet Cooling in Steel Rolling". *International Journal of Heat and Fluid Flow*. Vol. 13, No. 4, pp. 358-369. 1992.
6. Wolf D.H., Incropera F.P., Viskanta R. "Jet Impingement Boiling". *Advances in Heat Transfer*. Vol. 23, pp. 1-132. 1993.
7. Zumbrennen D.A., Incropera F.P., Viskanta R. "Method and Apparatus for Measuring Heat Transfer Distributions on Moving and Stationary Plates Cooled by a Planar Liquid Jet". *Experimental Thermal and Fluid Science*. Vol. 3, pp. 202-213. 1990.
8. Filipovic J., Incropera F.P., Viskanta R. "Quenching Phenomena Associated with a Water Wall Jet: II Comparison of Experimental and Theoretical Results for the Film Boiling Region". *Experimental Heat Transfer*. Vol. 8, pp. 119-130. 1995.
9. Zumbrennen D.A., Incropera F.P., Viskanta R. "Convective Heat Transfer Distribution on a Plate Cooled by Planar Water Jets". *Journal of Heat Transfer*. Vol. 111, No 4. pp. 889-896. 1989.
10. Blazevic D.T. "Comparison of Cooling Methods: Sprays, Water Curtains, Laminar Tubes, and Aspirated Sprays". *35th MWSP Conference Proceedings*. Vol. 31, pp. 297-310. 1994.
11. Martin H. "Heat and Mass Transfer Between Impinging Gas Jets and Solid Surfaces". *Advances in Heat Transfer*. Vol. 13, pp.1-60. 1977.
12. Barsanti G., Faggiani S., Grassi W. "Single-Phase Forced Convection Cooling of Heating Surfaces by Liquid Jet Impingement". *International Journal of Heat and Technology*. Vol. 7 pp.1-11. 1989.
13. Faggiani S., Grassi W. "Impinging liquid jets on heated surfaces". 9th *International Heat Transfer Conference*. Vol. 1, pp. 275-285. 1990.
14. Liu X., Gabour L.A., Lienhard J.H. "Convective Heat Transfer by Impingement of Circular Liquid Jets". *Journal of Heat Transfer*. Vol. 113, No. 3., pp. 571-582. 1991.
15. Stevens J., Webb B.W. "Local Heat Transfer Coefficients Under an Axisymmetric, Single-phase Liquid Jet". *Journal of Heat Transfer*. Vol. 113, pp. 71-78. 1991.

16. Tong L.S. Boiling Heat Transfer and Two-Phase Flow. John Wiley and Sons, New York. 1965.
17. Incropera F.P., DeWitt D.P. "Fundamentals of Heat and Mass Transfer". Fundamentals of Heat and Mass Transfer. John Wiley & Sons, Toronto, Canada. 1994.
18. Stralen S.V., Cole R. Boiling Phenomena Volume 1. Hemisphere Publishing Corporation, New York. 1979.
19. Monde M., Katto Y. "Burnout in a High Heat Flux Boiling system With an Impinging Jet". International Journal of Heat and Mass Transfer. Vol. 21, pp. 295-305. 1978.
20. Collier J.G., Thome J.R. Convective Boiling and Condensation. Oxford University Press, New York. 1994.
21. Chen J.C. "Correlation for Boiling Heat Transfer to Saturated Fluids in Convective Flow". I&CE Process Design and Development. Vol. 5, pp. 322-329. 1966.
22. Naterer G.F. Heat Transfer in Single and Multiphase Systems. CRC Press, New York. 2003.
23. Monde M. "Critical Heat Flux in Saturated Forced Convective Boiling on a Heated Disk With an Impinging Jet". Wärme- und Stoffübertragung. Vol. 19, pp. 205-209. 1985.
24. Lienhard J.H., Eichhorn R. "On Predicting Boiling Burnout for Heaters Cooled by Liquid Jets". International Journal of Heat and Mass Transfer. Vol. 22, pp. 774-776. 1979.
25. Lienhard J.H., Hasan M.Z. "Correlation of Burnout Data for Disk Heaters Cooled by Liquid Jets". Journal of Heat Transfer. Vol. 101, pp. 383-384. 1979.
26. Katto Y, Shimizu M. "Upper Limit of CHF in the Saturated Forced Convection Boiling on a Heated Disk with a Small Impinging Jet". Journal of Heat Transfer. Vol. 101 pp. 265-269. 1979.
27. Katto Y., Monde M. "Study of Mechanism of Burnout in a High Heat Flux Boiling System with and Impinging Jet". 5th International Heat Transfer Conference, Tokyo, Japan. Pp. 245-249. 1974.
28. Monde M. "Burnout Heat Flux in Saturated Forced Convection Boiling With an Impinging Jet". Heat Transfer Japanese Research. Vol. 9, pp. 31-41. 1980.
29. Sharan A. Lienhard J.H. "On Predicting Burnout in the Jet-Disk Configuration". Journal of Heat Transfer. Vol. 107, pp. 398-401. 1985.
30. Katto Y., Yokoya S. "Critical Heat Flux on a Disk Heater Cooled by a Circular Jet of Saturated Liquid Impinging at the Center". International Journal of Heat and Mass Transfer. Vol. 31, pp. 219-227. 1988.
31. Monde M., Okuma Y. "Critical Heat Flux in Saturated Forced Convective Boiling on a Heated Disk With and Impinging Jet - CHF in L-Regime". International Journal of Heat and Mass Transfer. Vol. 28, pp. 547-552. 1985.
32. Walker J. "Boiling and the Leidenfrost Effect". Cleveland State University. 2003.

33. Guo R.M.. "Heat Transfer of Laminar Flow Cooling During Strip Acceleration on Hot Strip Mill Runout Tables". *Trans ISS*. pp. 49-59. Aug.1993.
34. Zumbrunnen D.A., Viskanta R., Incropera F.P. "The Effect of Surface Motion on Forced Convection Film Boiling Heat Transfer". *Journal of Heat Transfer*. Vol. 111 pp. 760-766. Aug. 1989.
35. Kumagai S., Suzuki S., Sano Y., Kawazoe M. "Transient Cooling of a Hot Metal Slab by an Impinging Jet With Boiling Heat Transfer". *ASME/JSME Thermal Engineering Conference Proceedings*. Vol. 2, 347-352. 1995.
36. Ochi T., Nakanishi S., Kaji M., Ishigai S. "Cooling of a Hot Plate With an Impinging Circular Water Jet". *Multiphase Flow and Heat Transfer III Part A, Fundamentals*. pp. 671-680. 1984.
37. Wolf D.H., Incropera F.P., Viskanta R. "Local Jet Impingement Boiling Heat Transfer". *International Journal of Heat and Mass Transfer*. Vol. 39, No. 7. pp. 1395-1406. 1996.
38. Liu L., Fraser D. Samarasekera I. "Experimental Study of Boiling Heat Transfer of Steel Plates During Runout table Operation in a Hot Strip Mill". *Proceedings of NHTC'01 35th National Heat Transfer Conference*. Anaheim, California. June 10-12, 2001.
39. Liu Z.D., Fraser D. Samarasekera I.V., Lockhart G. "Experimental Observations and Modelling of Thermal History Within a Steel Plate During Water Jet Impingement". *Canadian Metallurgical Quarterly*. Vol. 41, pp. 75-85. Jan. 2002.
40. Kokado J., Hatta N., Takuda H., Harada J., Yasuhira N. "An Analysis of Film Boiling Phenomena of Subcooled Water Spreading Radially on a Hot Steel Plate". *Arch. Eisenhüttenwes.* Vol. 55, No 3. pp. 113-118. 1984.
41. Filipovic J., Incropera F.P., Viskanta R. "Rewetting Temperatures and Velocity in a Quenching Experiment". *Experimental Heat Transfer*. Vol. 8, pp. 257-270. 1995.
42. Lee J., Lee S.J. "The Effect of Nozzle Configuration on Stagnation Region Heat Transfer Enhancement of Axisymmetric Jet Impingement". *International Journal of Heat and Mass Transfer*. Vol. 43, Issue 18, pp. 3497-3509. Sept. 2000.
43. Miyasaka Y., Inada S., Owase Y. "Critical Heat Flux and Subcooled Nucleate Boiling in Transient Region Between a Two-dimensional Water Jet and a Heated Surface". *Journal of Chemical Engineering of Japan*. Vol. 13, No 1. pp. 29-35. 1980.
44. Robidou H., Auracher H., Gardin P., Lebushe M. "Controlled Cooling of a Hot Plate With a Water Jet". *Experimental Thermal and Fluid Science*. Vol. 26, pp. 123-129. 2002.
45. Mitsutake Y., Monde M. "Heat Transfer During Transient Cooling of High Temperature Surface with an Impinging Jet". *Heat and Mass Transfer*. Vol. 37, pp. 321-328. 2001.
46. Liu Z.H., Wang J. "Study on Film Boiling Heat Transfer for Water Jet Impinging on High temperature Flat Plate". *International Journal of Heat and Mass Transfer*. Vol. 44, pp. 2475-2481. 2001.

47. Ishigai S., Nakanishi S., Ochi T. "Boiling Heat Transfer for a Plane Water Jet Impinging on a Hot Surface". 6<sup>th</sup> International Heat Transfer Conference Proceedings. FB-30. 1978.
48. Monde M., Kitajima K., Inoue T., Mitsutake Y. "Critical Heat Flux in a Forced Convective Subcooled Boiling With an Impinging Jet". Department of Mechanical Engineering, Saga University. 1994.
49. Womac D.J., Ramadhyani S., Incropera F.P. "Correlating Equations for Impingement Cooling of Small Heat Sources With Single Circular Liquid Jets". Journal of Heat Transfer. Vol. 115, pp. 107-115. 1993.
50. Chowdhury S.K.R., Winterton R.H.S. "Surface Effects in Pool Boiling". International Journal of Heat and Mass Transfer. Vol. 28, No 10. pp. 1881-1889. 1985.
51. Gabour L.A., Lienhard J.H.V. "Wall Roughness Effects on a Stagnation Point Heat Transfer Beneath an Impinging Liquid Jet". ASME HTD Heat transfer Measurements and Analysis. Vol. 249, pp. 35-43. 1993.
52. Pan C., Hwang J.Y., Lin T.L. "The Mechanism of Heat Transfer in Transition Boiling". International Journal of Heat and Mass Transfer. Vol. 32, No 7. pp. 1337-1349. 1989.
53. Tong A.Y. "On the Impingement Heat Transfer of an Oblique Free Surface Plane Jet". International Journal of Heat and Mass Transfer. Vol. 46, Issue 11 pp. 2077-2085. May 2003.
54. Zumbrunnen D.A., Aziz M. "Convective Heat Transfer Enhancement Due to Intermittency in an Impinging Jet". Journal of Heat Transfer. Vol. 115, pp. 91-98. Feb. 1993.
55. Hall D.E., Incropera F.P., Viskanta R. "Jet Impingement Boiling from a Circular Free-surface Jet During Quenching: Part 2 - Two-phase Jet". Journal of Heat Transfer. Vol. 123, pp. 911-917. 2001.
56. Zumbrunnen D.A., Incropera F.P., Viskanta R. "A Laminar Boundary Layer Model of Heat Transfer Due to a Nonuniform Planar Jet Impinging on a Moving Plate". Wärme und Stoffübertragung. Vol. 27, pp. 311-319. 1992.
57. Bierbrauer F., Soh W.K., Yuen W.Y.D. "Application of the Eulerian-Lagrangian Method to Water Jet Cooling of a Hot Moving Strip". Faculty of Engineering, Univeristy of Wollongong, Australia. 2000.
58. Filipovic J., Viskanta R., Incropera F.P., Veslocki T. "Cooling of a Moving Steel Strip by an Array of Round Jets". Steel Research. Vol. 65, No 12. pp. 541-547. 1994.
59. Filipovic J., Viskanta R., Incropera F.P. "A Parametric Study of the Accelerated Cooling of Steel Strip". Steel Research. Vol. 63, No. 11, pp. 496-499. 1992.
60. Hatta N., Osakabe H. "Numerical Modeling for Cooling Process of a Moving Hot Plate by a Laminar Water Curtain". ISIJ International. Vol. 29, No. 11, pp. 919-925. 1989.

61. Zumbrennen D.A. "Convective Heat and Mass Transfer in the Stagnation Region of a Laminar Planar Jet Impinging on a Moving Surface". *Journal of Heat Transfer*. Vol.113, No. 3., pp. 563-570. 1991.
62. Soh W.K., Yuen W.Y.D. "Flow Visualization of the Boiling Heat Transfer at the Runout Table". 41st MWSP Conference Proceedings. 1999.
63. Taga M., Ochi T., Akagawa K. "Cooling of a Hot Moving Plate by an Impinging Water Jet". *Proceedings of ASME-JSME thermal Engineering Joint Conference*. pp.183-189. 1983.
64. Hall D.E., Incropera F.P., Viskanta R. "Jet impingement boiling from a circular free-surface jet during quenching: Part 1 - Single-phase jet". *Journal of Heat Transfer*. Vol. 123, pp. 901-910. 2001.

## Appendix A: Thermocouple Conduction Error Literature Review

A thermocouple is a temperature measurement device highly used in industrial applications. They are used to measure temperatures within internal combustion engines, space vehicles, and industrial heating and structural applications, too name a few.

### A.1 The Seebeck Effect

The main theory behind thermocouples is based upon the Seebeck effect, as discovered by Thomas Seebeck in 1821. When two dissimilar wires form a circuit and the junctions are at different temperatures, the thermal energy is converted to electrical energy, resulting in a current. In open circuit conditions, a net thermal emf is produced, otherwise known as the Seebeck voltage. The thermocouple is attached to a data acquisition system that reads the corresponding voltage, which is then converted to a temperature value.

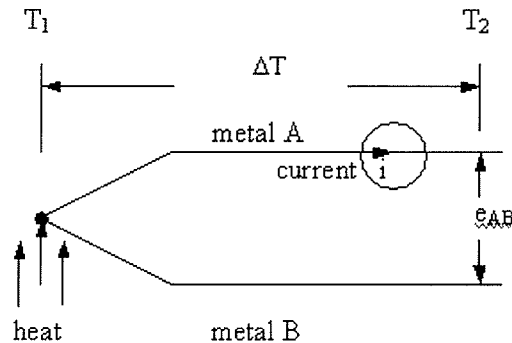


**Figure A.1: The Seebeck Voltage**

The following equation provided by Benedict [A1] can be used to calculate the Seebeck voltage based on the circuit shown in Figure A.1.

$$e_{AB} = \alpha_{AB} \cdot \Delta T \quad (\text{A.1})$$

where

$e_{AB}$  = net open circuit voltage

$\alpha_{AB} = \alpha_A - \alpha_B$  = relative Seebeck coefficient of materials A and B

$\Delta T$  = temperature difference between the 2 junctions

The connection between the temperature and the Seebeck voltage has a the following polynomial relationship defined as in [A2] [A3]:

$$T = a_0 + a_1 \cdot x + a_2 \cdot x^2 + a_3 \cdot x^3 + a_4 \cdot x^4 + \dots + a_n \cdot x^n \quad (\text{A.2})$$

where

T = temperature in degrees Celsius

x = thermocouple voltage in Volts

$a_n$  = polynomial coefficients

Generally, the higher the order of the polynomial, the better the accuracy of the temperature conversion. The polynomial coefficients,  $a_n$ , depend on the thermocouple type and are different for each order. The coefficients can be read off a table provided by a thermocouple manufacturer, such as the Omega Engineering temperature measurement book [A2].

## **A.2 Beaded and Intrinsic Thermocouples**

There are beaded thermocouples and intrinsic thermocouples. A beaded thermocouple is formed by joining together the two wires usually by spot welding or brazing (see Figure A.2). The bead is usually around three times the wire diameter. An intrinsic thermocouple is formed by attaching each wire separately, but very close together (1 to 2 diameters apart), at the surface to be measured [A4]. The measured output is the weighted mean of the two different junction temperatures [A1]:

$$e_o = e_m + (\alpha_A - \alpha_B) \cdot (T_A - T_B) \quad (\text{A.3})$$

where:

$T_A, T_B$  = junction temperatures of metals A and B, respectively

$e_o$  = measured output voltage

$e_m$  = output measured if both junctions were at the mean temperature

$\alpha_A, \alpha_B$  = Seebeck coefficients of metals A and B, respectively

Figure A.2 shows a basic beaded thermocouple. The end of the thermocouple measures the temperature. Each wire has to be insulated to prevent them from touching. If the wires touch, then the thermocouple voltage changes and gives an improper temperature. To protect the wires from the surrounding environment, the thermocouples are enclosed in a sheath. Aside from the way the wires are joined at the end, the make-up of an intrinsic thermocouple is essentially the same as that for a beaded one.

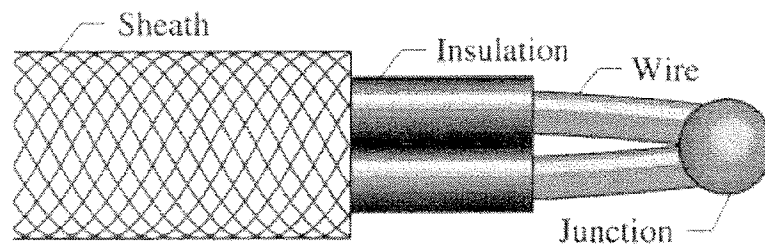


**Figure A.2: Basic Thermocouple [A3]**

Intrinsic thermocouples are more accurate at measuring temperatures in transient conditions than beaded ones. With a beaded thermocouple, the mass of the junction bead causes a difference in surface temperature at the bead, which takes more time to heat up

to surrounding conditions. To reduce this error, the bead should be as small as possible and the leads should be attached as close to the plate as possible.

With an intrinsic thermocouple, there is essentially no mass, reducing the response time. The response time is the time it takes for a temperature change of the material being measured to affect the temperature of the thermocouple (which is the temperature recorded). This is highly desirable for time-dependent measurements, as performed in the experiments presented in this report. Also, compare to the bead junction, the effects of heat conduction are reduced [A4].

### **A.3 Thermocouple Calibration**

Before the thermocouple can be used, it has to be calibrated. The thermocouple circuit is set up as shown in Figure A.3. “A” and “B” represents the two different metals. The thermocouple tip measures the temperature of the target surface. A gage measures the voltage and this is then converted to a temperature value.

When calibrating a thermocouple, both junctions are exposed to two different known temperatures. The most common method is to expose the measurement junction to boiling water, which is at 100°C. The other junction is exposed to an ice bath, which is at 0°C [A5].

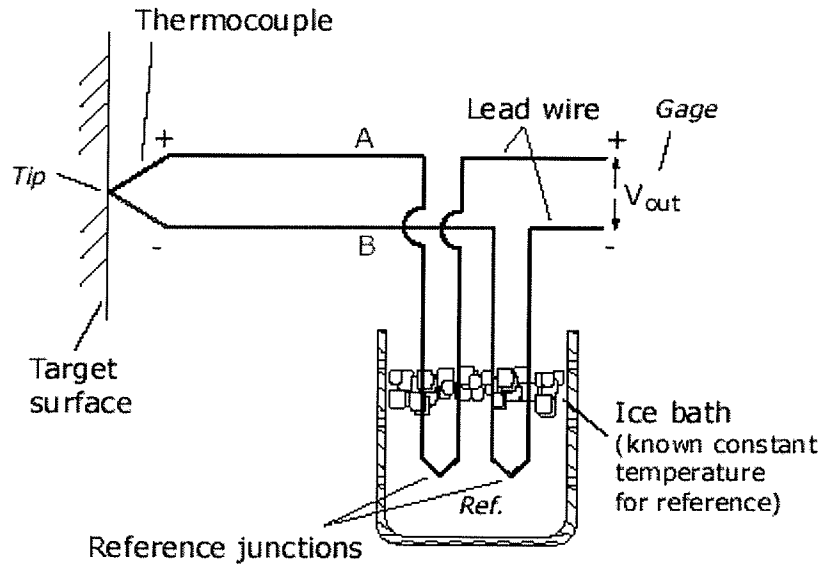


**Figure A.3: Thermocouple Circuit [A5]**

The voltage between the two junctions is measured and Equation A.1 is used to get the Seebeck voltage and Equation A.2 to calculate the temperature. If the temperature calculated is at  $100^{\circ}\text{C}$ , then the thermocouple is working properly.

#### **A.4 Advantages and Disadvantages**

There are four main advantages thermocouples have over other temperature measuring devices, which explains their common use. They are relatively inexpensive and can operate in a broad temperature range of around  $-270^{\circ}\text{C}$  to  $2100^{\circ}\text{C}$ . They are small, achieving sizes down to 0.25 mm diameter. Figure A.4 demonstrates the small size of a thermocouple compared to the end of a needle. Finally, they are relatively easy to integrate into automated data systems which can be used to acquire large amounts of data with time [A6].

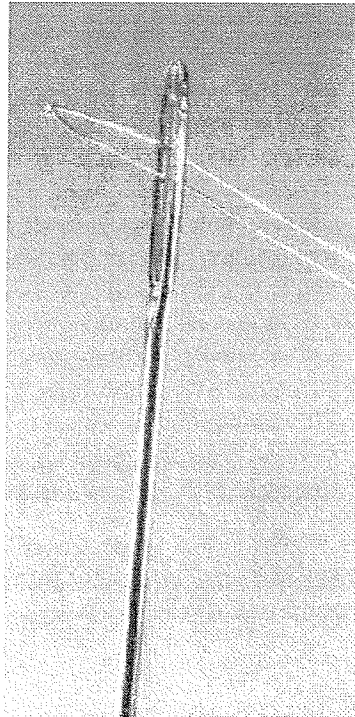


**Figure A.4: Beaded Thermocouple Compared to the End of a Needle [A2]**

However, thermocouples have disadvantages. Thermocouples operate at a low voltage in the micro-volt range if it is required to measure temperatures differing by about  $0.1^{\circ}\text{C}$  [A2]. This requires a sensitive voltage measurement device. Recalibration of certain types of thermocouples can be very difficult. Some thermocouples may change chemically and physically under high temperatures and corrosive environments, resulting in measurement error [A6].

### **A.5 Thermocouple Types**

To help accommodate for some of their disadvantages, it is important to choose the type of thermocouple that best suits the conditions it will be exposed to. There are 11 main types of thermocouples to choose from as shown in Table A.1. The most common types used are E, J, K, R, S, and T [A3].

As it can be seen, the thermocouples are each composed of different metals and are designated by a letter. Each different type of thermocouple has its own characteristics. The type of thermocouple chosen will depend upon the operating conditions and the characteristics required for the thermocouple to work properly.

**Table A.1: Thermocouple Types [A4]**

<b>Thermocouple Type</b>	<b>Metal 1</b>	<b>Metal 2</b>	<b>Optimum Temperature Operating Range</b>
J	Iron	Constantan Copper-Nickel	0°C to 750°C
K	Chromega Nickel-Chromium	Alomega Nickel-Alomega	-200°C to 1250°C
T	Copper	Constantan Copper-Nickel	-200°C to 350°C
E	Chromega Nickel-Chromium	Constantan Copper-Nickel	-200°C to 900°C
N	Omega-P Nicrosil	Omega-N Nisil	-270°C to 1300°C
R	Platinum- 13% Rhodium	Platinum	0°C to 1450°C
S	Platinum- 10% Rhodium	Platinum	0°C to 1450°C
B	Platinum- 30% Rhodium	Platinum- 6% Rhodium	0°C to 1700°C
G	Tungsten	Tungsten- 26% Rhenium	0°C to 2320°C
C	Tungsten- 5% Rhenium	Tungsten- 26% Rhenium	0°C to 2320°C
D	Tungsten- 3% Rhenium	Tungsten- 25% Rhenium	0°C to 2320°C

## **A.6 Choosing a Thermocouple**

Three main things need to be considered when choosing the type of thermocouple to be used. The first is the operating temperature range. If the temperature is higher or lower than the specified range, incorrect readings will result. As it can be seen in Table A.1, each type of thermocouple has a specific temperature range it operates best in.

The second thing to take into account is what the thermocouple is measuring the temperature of. That is, choosing the correct thermocouple type depends upon the chemical composition of the material and whether a liquid, solid, or gas is being measured. Some thermocouples are more suitable for measuring gases versus solids, for instance. Or other thermocouples negatively react with certain materials.

Finally, the third thing to be contemplated is the measurement environment the thermocouple will be exposed to. It has to be determined whether the thermocouple needs to be chemical resistant, abrasion resistant, and/or vibration resistant [A2].

Aside from choosing the type of thermocouple to be used, it is also important to determine the diameter of the thermocouple required. This depends upon the response time desired. Essentially, the smaller the diameter, the faster the response time. Having a relatively fast response time is especially important where rapid cooling or heating occurs and the temperature is to be measured under transient conditions. However, it should be noted that the diameter of the thermocouple can not be so small that great strain is imposed on the wire which can break the thermocouple.

## A.7 Thermocouple Error

There are many causes that can contribute to error of temperature measurement with a thermocouple. This could be due to electronic noise, improper calibration and improper conversion of recorded voltages into temperatures [A4].

Another source of error that can occur is when the wires are attached to the surface being measured, they may represent pin fins where heat can flow mainly due to conduction. In the case where the wires are at a lesser temperature than the substrate, heat flows into the wires. This reduces the temperature at the junction compared to the actual plate temperature.

### A.7.1 Thermocouple Conduction Error

Several researchers have focused on heat conduction error in thermocouples [A2, A4, A7, A8, A9, and A10]. They have looked at heat conduction through the leads above and/or below the substrate and how it changes the temperature of the junction compared to the actual surface temperature. How some of them approached the problem and their findings will be discussed.

In their thermocouple manual, the American Society for Testing and Materials [A11] described the installation factor which can be found experimentally or calculated by:

$$Z = \frac{T_a - T_j}{T_a - T_\infty} \quad (\text{A.4})$$

where:

$Z$  = installation factor

$T_a$  = actual surface temperature

$T_j$  = thermocouple junction temperature

$T_\infty$  = Temperature of the surroundings

However, they did not fully explain what type of measurement error(s) nor configuration(s) this is valid for.

Attia and Kops [A7] studied the temperature variation at the surface due to conduction through the leads. They analyzed both the embedded and ambient segment of the thermocouple. They modeled the leads as a cylindrical fin of radius  $r_f = \sqrt{2} \cdot r_w$  where  $r_w$  is the radius of the thermocouple wires. The thermal conductivity is the average of the conductivities of the thermocouple wires 1 and 2:

$$k_f = \frac{(k_1 + k_2)}{2} \tag{A.5}$$

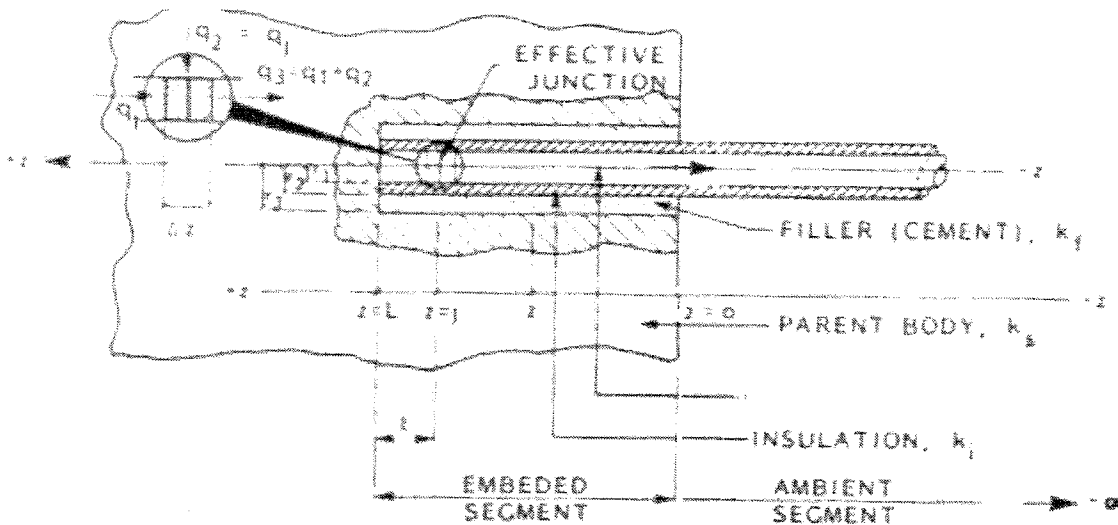


**Figure A.5: Diagram for Analytical Model from [A7]**

Figure A.5 shows the diagram they used to help set up their analytical model.

They neglected that the flow rate at the base of the fin in the embedded region at  $Z = L$ .

i.e.:

$$\left(\frac{\partial t}{\partial z}\right)_{z=L} = 0 \quad (\text{A.6})$$

They calculated the heat flow rate out of the thermocouple to the ambient section, which went through the embedded part as:

$$q = \sqrt{h \cdot P \cdot k_i \cdot A} \cdot (t_o - t_a) \quad (\text{A.7})$$

where:

$h$  = heat transfer coefficient

$P$  = wire perimeter

$A$  = area of the fin

$t_o$  = temperature of the base of the fin

$t_a$  = ambient temperature

Essentially, it was found that increasing the wire diameter increased heat conduction through the wires. Also, heat transfer was augmented with increasing the mean thermal conductivity of the wires.

Behrmann [A8] studied heat conduction through the thermowell or sheath of a thermocouple. They modeled the thermocouple as a fin. A general rule of thumb they provided is to immerse the thermocouple to a depth of 10 sheath diameters to reduce conduction error through the sheath. They also determined that bent thermocouples give better readings than straight ones. Just like Attia and Kops [A7], they concluded that reducing the diameter of the thermocouple minimizes conduction.

Park et. al [A4] analytically determined the temperature error of a type K intrinsic thermocouple due to conduction of a nickel piece using finite difference methods. The

plate was initially set at 500°C. From this, they saw that the difference between the measured and actual surface temperature error could be up to 40°C.

Keltner [A9] looked at steady state conduction error through the leads of an intrinsic thermocouple attached to a surface. They approximated the thermocouple temperature by:

$$T_{TC} = \frac{T_{surface} \cdot e^{-2 \cdot x \cdot \sqrt{Bi}}}{1 + 2 \cdot K + \sqrt{Bi} \cdot \left(\frac{1}{B} + \frac{\pi}{4}\right)} \quad (A.8)$$

Where  $x$  is the ratio of the thermocouple base over the wire radius. In the case where there is no thermocouple bead,  $x = 1$

$$x = \frac{\text{beadthickness}}{r_{wire}} \quad (A.9)$$

The lateral surface Biot modulus is:

$$Bi = \frac{h \cdot r_{wire}}{k_{wire}} \quad (A.10)$$

The contact surface Biot Modulus is:

$$B = \frac{h_{contact} \cdot r_{wire}}{k_{surface}} \quad (A.11)$$

The thermal conductivity ratio is:

$$K = \frac{k_{wire}}{k_{surface}} \quad (A.12)$$

where:

$T_{TC}$  = measured thermocouple temperature

$T_{surface}$  = surface temperature

$B_i$  = lateral surface Biot Modulus

$B$  = contact surface Biot Modulus

$K$  = thermal conductivity ratio

$r_{\text{wire}}$  = the radius of the thermocouple

beadthickness = thickness of the bead

$k_{\text{wire}}$  = thermal conductivity of the wire

$h_{\text{contact}}$  = contact heat transfer coefficient

$h$  = heat transfer coefficient

$k_{\text{surface}}$  = thermal conductivity of the surface being measured

However, they did not state whether the wire thermal conductivity,  $k_{\text{wire}}$ , is the average of the two wires, or the greater of the two. Equation A.8 only applies if the wall thickness is at least 10X the wire diameter.

Henning and Parker [A10] analytically and experimentally determined the transient lead conduction error for an intrinsic thermocouple. To simplify their analysis, they assumed the region between  $x = 0$  and  $r = R$  in Figure A.6 to have no thermal capacity. They analyzed the conduction through the wire and substrate separately using the general heat conduction equation. Each wire was modeled as an infinitely long cylinder attached perpendicular to the surface of a semi-infinite body as shown in the figure.

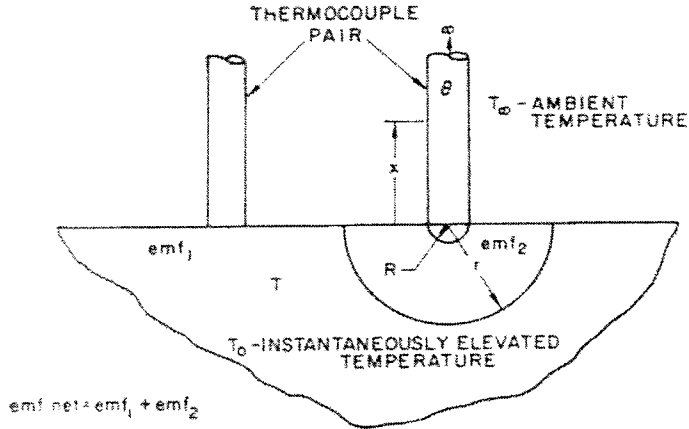


**Figure A.6: Analytical Model Setup used by Henning and Parker [A10]**

They assumed perfect contact between the thermocouple and substrate and that all properties were temperature independent. Convection and radiation heat transfer were neglected. By assuming a product solution and using separation of variables, they determined the transient temperature response at the thermocouple junction as:

$$\theta(t^*, 0) = 1 - (1 - a) \cdot \exp(a^2 \cdot t^*) \cdot \text{Erfc}(a\sqrt{t^*}) \quad (\text{A.13})$$

$\theta(t^*, 0)$  is the dimensionless temperature in the thermocouple junction defined as:

$$\theta(t^*, 0) = \frac{T_{TC} - T_\infty}{T_{substrate} - T_\infty} \quad (\text{A.14})$$

The dimensionless time is defined as:

$$t^* = \alpha_{substrate} \cdot t / R^2 \quad (\text{A.15})$$

The constant  $a$  is defined as:

$$a = \frac{1}{a + 1/G \cdot \sqrt{\frac{k_{TC} \cdot \rho_{TC} \cdot C_{pTC}}{k_{substrate} \cdot \rho_{substrate} \cdot C_{psubstrate}}}}} \quad (\text{A.16})$$

where:

$T_{TC}$  = thermocouple temperature

$T_{\text{substrate}}$  = surface temperature

$T_{\infty}$  = the ambient temperature

$R$  = radius thermocouple wire

$\alpha_{\text{substrate}}$  = thermal diffusivity of the surface

$k_{\text{substrate}}$  = thermal conductivity of the surface

$k_{TC}$  = thermal conductivity of the thermocouple

$\rho_{TC}$  = density of the thermocouple

$\rho_{\text{substrate}}$  = density of the surface

$C_{pTC}$  = specific heat of the thermocouple

$C_{p\text{substrate}}$  = specific heat of the surface

The geometrical factor  $G$  was experimentally determined to be around 1.5. At 95% steady state, the time can be approximated by:

$$t \Big|_{95\%} = \frac{25}{\pi} \cdot \frac{D^2}{\alpha_{\text{substrate}}} \cdot \frac{k_{TC}}{k_{\text{substrate}}} \quad (\text{A.17})$$

where:

$D$  = diameter of the thermocouple wire

Similar to Attia and Kops [A7], Henning and Parker [A10] determined that a thermocouple wire with a small diameter and relatively low thermal conductivity reduces conduction error and produces a faster response than that with a larger diameter and high thermal conductivity.

Keltner and Beck [A12] analytically determined the steady state result for an intrinsic thermocouple temperature at the junction as:

$$T_{TC} = \frac{1}{1 + \pi \cdot K \cdot \sqrt{Bi} / 2} \quad (\text{A.18})$$

Where they assumed a different lateral surface Biot modulus,  $Bi$ , than Keltner [A9] did in Equation A.10:

$$Bi = \frac{h_{\text{contact}} \cdot r_{\text{wire}}}{2 \cdot k_{\text{wire}}} \quad (\text{A.19})$$

The thermal conductivity ratio,  $K$ , is defined by Equation A.12 and  $h_{\text{contact}}$  is the contact heat transfer coefficient.

Hagen [A3] provided the following relation between the true surface, fluid, and thermocouple temperatures for a thermocouple attached to the surface. They took the wire insulation into account. They also modeled the two wires as one wire. However, they did not state whether it was a beaded or intrinsic thermocouple. On the contrary, since they modeled the thermocouple wires as one wire, then it most likely would not make a difference in calculations between an intrinsic or beaded thermocouple.

$$\frac{T_{\text{substrate}} - T_{TC}}{T_{\text{substrate}} - T_{\infty}} = \frac{X - Bi}{X + 1.27 + 1.08 \cdot Bi - 0.5 \cdot Bi^2} \quad (\text{A.20})$$

where:

$$X = \frac{\sqrt{k_{\text{wire}} \cdot A_{\text{wire}} / R}}{\pi \cdot r_{\text{eff}} \cdot k_{\text{substrate}}} \cdot \tanh\left(\frac{L_{\text{wire}}}{\sqrt{k_{\text{wire}} \cdot A_{\text{wire}} / R}}\right) \quad (\text{A.21})$$

The total radial thermal resistance is:

$$R = \frac{1}{2 \cdot \pi \cdot r_o \cdot h_{wire}} + \frac{\ln(r_o / r_i)}{2 \cdot \pi \cdot k_{ins}} \quad (\text{A.22})$$

The effective wire radius of the two wires is:

$$r_{eff} = \sqrt{2} \cdot r_o \quad (\text{A.23})$$

Therefore, the effective area is:

$$A_{wire} = \pi \cdot r_{eff} \quad (\text{A.24})$$

The Biot modulus is provided as:

$$Bi = \frac{h_{substrate} \cdot r_{eff}}{k_{substrate}} \quad (\text{A.25})$$

where:

$r_o$  = outside insulation radius

$r_i$  = inside insulation radius

$k_{ins}$  = thermal conductivity of the wire insulation

$L_{wire}$  = length of the thermocouple wires

Hagen [A3] concluded that installing the thermocouples in a way where they lay flat on the surface rather than have them sticking out like a fin would reduce the conduction error.

Boelter et. al [A13] analytically calculated the thermocouple error where the flat plate is surrounding above and below by fluids of differing temperature to simulate an airfoil. They considered the thermocouple leads as sources of heat where heat can flow. They assumed steady state conditions, uniform convection coefficients, and that the

section is at uniform temperature. There is also no temperature gradient normal to the plate surface anywhere.

Figure A.7 depicts the setup they use to calculate the thermocouple error.  $f_{p1}$  and  $f_{p2}$  denote the convective coefficients of the fluid above and below the plate, respectively. They performed a heat balance on the differential annulus of radius  $r$  and width  $dr$ , which is concentric with the source (thermocouple) center.

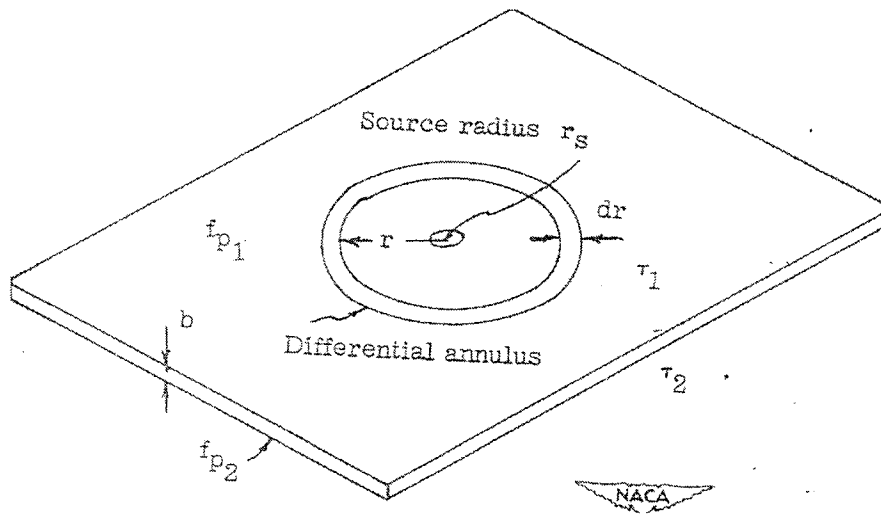


**Figure A.7: Setup used by Boelter et. al [A13]**

They determined that:

$$\frac{T_{Tc} - T_{\infty}}{T_{surface} - T_{\infty}} \cong \frac{r_{wire} \cdot \sqrt{2 \cdot h_1 \cdot k_e \cdot r_{wire}}}{k_{surface} \cdot b_{plate}} \cdot (\log_e(\sqrt{\beta/2 \cdot r_{wire}}) - 0.577) \quad (A.26)$$

The equivalent wire conductance is defined as:

$$k_e = \left( \frac{\sqrt{k_1} + \sqrt{k_2}}{2} \right)^2 \quad (A.27)$$

The constant  $\beta$  is defined as:

$$\beta = \frac{h_1 + h_2}{b_{plate} \cdot k_{surface}} \quad (A.28)$$

where:

$h_1$  = convective conductance of the surrounding hot fluid above the plate

$h_2$  = convective conductance of the surrounding cold fluid below the plate

$k_1$  = thermal conductivity of thermocouple wire material 1

$k_2$  = thermal conductivity of thermocouple wire material 2

$k_{surface}$  = thermal conductivity of the surface

$b_{plate}$  = thickness of the plate

They determined that the thermocouple conduction error would increase with decreasing plate thickness and decreasing plate thermal conductivity. The error would also decrease with decreasing heat transfer coefficients. Finally, the error would increase if the conductance of the thermocouple leads increases.

To reduce the thermocouple error, they suggested the same as Attia and Kops [A7] and Henning and Parker [A10] to reduce the diameters of the thermocouple wires and use thermocouple metals having low conductivities. They also recommended that the thermocouple leads be embedded in the substrate, which is similar to what Hagen [A3] concluded.

## Appendix A References

- A1. Benedict R.P. Fundamentals of Temperature, Pressure and Flow Measurements. John Wiley & Sons, Toronto, Canada. 1984.
- A2. The Temperature Handbook. Omega Engineering, USA. Vol. 28. 1992.
- A3. Hagen R.D. Heat Transfer With Applications. Prentice-Hall, Columbus, Ohio. 1999.
- A4. Park J.E., Childs K.W., Ludtka G.M. "Correction of Errors in Intrinsic Thermocouple Signals Recorded During Quenching". 27th National Heat Transfer Conference. Minneapolis, Minnesota. Vol. 87, Issue 283, pp. 309-318. July 1991.
- A5. "Thermocouple Circuit". eFunda (Engineering Fundamentals). 2003.  
[http://www.efunda.com/designstandards/sensors/thermocouples/thmcpole\\_theory.cfm](http://www.efunda.com/designstandards/sensors/thermocouples/thmcpole_theory.cfm)
- A6. Chan T.L., Leung C. W., Jambunathan K., Ashforth-Frost S., Zhou Y. , Liu M.H. "Heat Transfer Characteristics of a Slot Jet Impinging on Semi-circular Convex Surface". International Journal of Heat and Mass Transfer. Vol. 45, pp. 993-1006. Feb. 2002.
- A7. Attia M.H., Kops L. "Distortion in Thermal Field Around Inserted Thermocouples in Experimental Interfacial Studies - Part II: Effect of the Heat Flow Through the Thermocouple". Journal of Engineering for Industry. Vol. 110, pp. 7-14. Feb. 1988.
- A8. Behrmann W.C. "Thermocouple Errors due the Sheath Conduction". Intech. Vol. 37 pp. 36-39. Aug. 1990.
- A9. Keltner N.R. "Heat Transfer Measurements in Electronics Cooling Applications". Electronics Cooling Magazine. Vol 4, No. 3. Sept. 1998. [http://www.electronics-cooling.com/Resources/EC\\_Articles/sep98/article3.htm](http://www.electronics-cooling.com/Resources/EC_Articles/sep98/article3.htm)
- A10. Henning C.D., Parker R. "Transient Response of an Intrinsic Thermocouple". Journal of Heat Transfer. pp. 146-154. May 1967.
- A11. Manual on the User of Thermocouples in Temperature Measurement. American Society for Testing and Materials, Philadelphia, Pa. 1974.
- A12. Keltner N.R., Beck J.V. "Surface Temperature Measurement Errors". Journal of Heat Transfer. Vol. 105, pp. 312-318. May 1983.
- A13. Boelter B.M.K., Romie F.E., Guibert A.G., Miller M.A. "An Investigation of aircraft Heaters XXVIII - Equations for Steady-State Temperature Distribution Caused by Thermal Sources in Flat Plates Applied to Calculation of Thermocouple Errors, Heat-Meter Corrections, and Heat Transfer by Pin-Fin Plates". National Advisory Committee for Aeronautics, Washington, D.C. Aug. 1948.

## **Appendix B: Hauksson's and Meng's Observations**

Hauksson [3] and Meng [2] performed a considerable amount of experiments on circular jet impingement heat transfer at the ROTC facility. Their observations will be summarized.

### **B.1 Hauksson's Results**

Hauksson performed experiments at jet subcoolings of 30°C, 40°C, and 50°C. Jet impingement velocities of 5.5 m/s, 5.7 m/s, and 6 m/s (flow rates of 15 l/min, 30 l/min, and 45 l/min, respectively) were also tested at each of the different subcoolings. His findings for visual observations, cooling and boiling curves, and the effects of subcooling and jet velocity will be presented.

#### **B.1.1 Cooling Curve**

By graphing the temperature variations of the surface and internal thermocouples during cooling, it was discovered that the temperature profile in the plate was highly nonlinear. Figure B.1 shows the results. As it can be seen, initially the surface temperature dropped very rapidly but the internal temperature dropped at a slower rate. Furthermore, as the temperature difference increased, the heat flux increased.

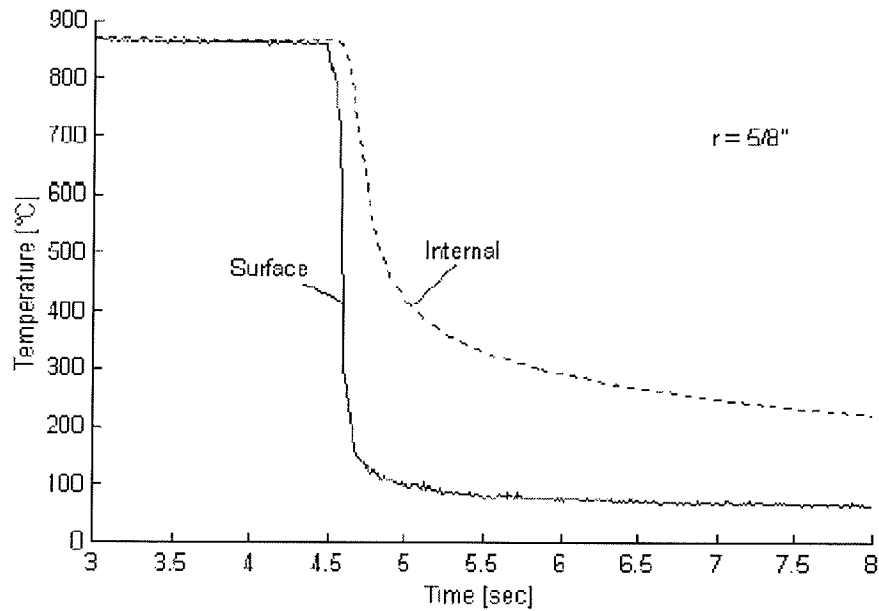
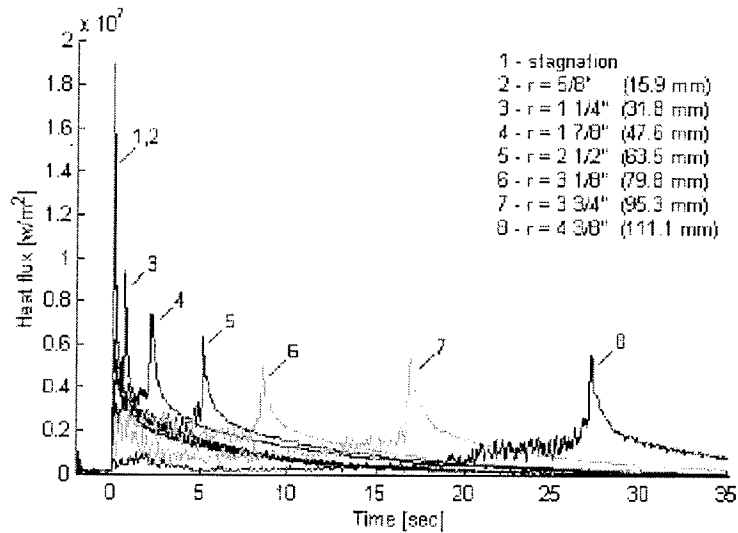


**Figure B.1: Cooling of internal and surface thermocouples [3]**

### B.1.2 Boiling Curves

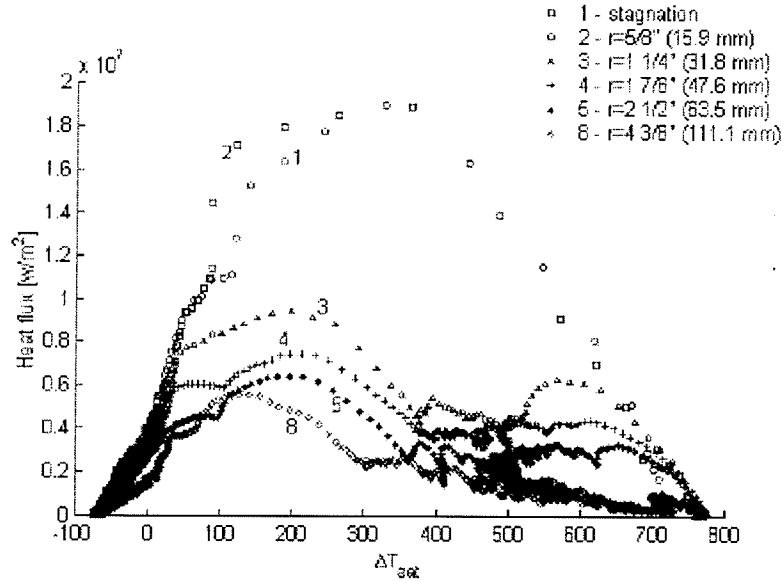
The heat flux with respect to time and saturation temperature was studied.

Figure B.2 shows the heat flux with respect to time for a water temperature of 30°C and jet impingement velocity of 5.7 m/s. At locations 1 and 2, the critical heat flux (CHF) was virtually the same. The CHF decreased with increasing distance from the stagnation point.



**Figure B.2: Heat flux versus time at a water temperature of 30°C and jet impingement velocity of 5.7 m/s [3]**

Figure B.3 shows the heat flux versus wall superheat for a water temperature of 30°C and jet impingement velocity of 5.7 m/s. From this, it was found that the CHF shifted to a lower value of wall superheat at locations further away from the stagnation region. It can also be seen that the CHF was relatively constant at regions further away from the stagnation point.



**Figure B.3: Heat flux versus wall superheat at a water temperature of 30°C and jet impingement velocity of 5.7 m/s [3]**

### B.1.3 Visual Observations

Hauksson saw that when the jet hit the plate it instantaneously darkened (i.e. turned grey) in the stagnation region. It was surmised that this colour showed the presence of vapour bubbles on the surface. Violent boiling was observed in the grey zone. Outside this region, the plate was red hot. A picture of the jet during cooling is shown in Figure B.4. The points in green indicate the thermocouple locations.

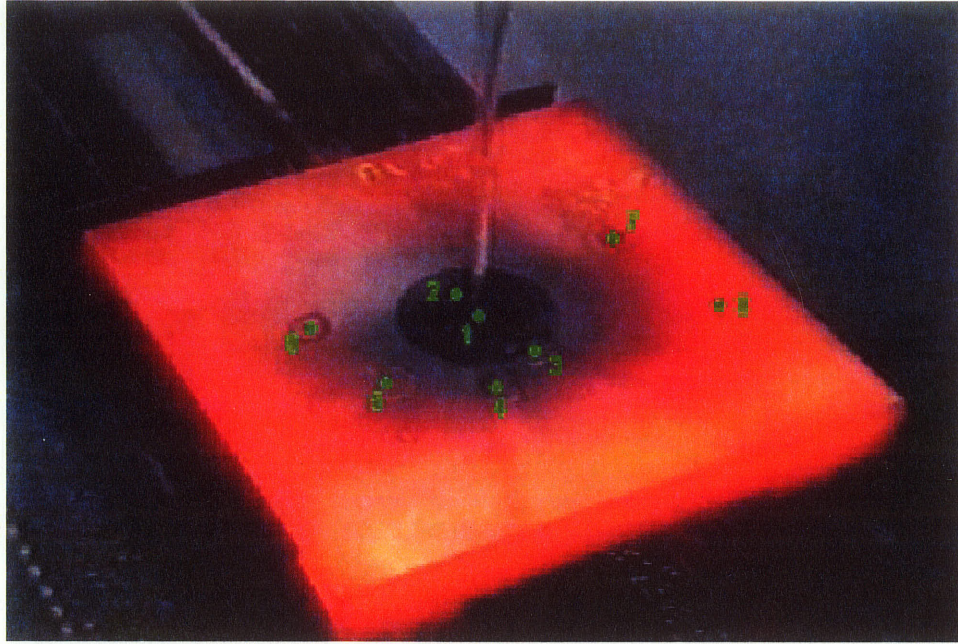


**Figure B.1: Cooling of a hot steel plate [3]**

Slightly after cooling commenced the grey region around the impingement zone turned black and progressed radially outwards. Alongside, the grey zone grew at a slower rate. When the black zone size reached the size of the grey zone, they both grew at approximately the same rate.

#### **B.1.4 Effect of Subcooling and Water Flow rate**

At a constant jet velocity, it was determined that increasing the subcooling increased the CHF as expected. This occurred for water temperatures varying from 30°C to 50°C (subcoolings from 50° to 70°C).

At constant subcoolings and flow rates ranging from 15 l/min to 45 l/min (5.5 to 5.8 m/s), it was found that the CHF increased with increasing flow rate. Additionally, the flow rate had little effect for nucleate and transition boiling.

## **B.2 Meng's Results**

Meng [2] performed experiments at water temperatures of 60°C, 70°C, 80°C, and 95°C. Water flow rates of 15 l/min, 30 l/min, and 45 l/min were also tested at each of the different subcoolings. Visual observations were provided and the effects of subcooling, water flow rate, and surface oxidation were discussed. These results will be summarized.

### **B.2.1 Visual Observations**

Meng had similar visual observations as Hauksson did. Meng referred to the black zone as the rewetting front. It was added that single-phase forced convection was most the prominent heat transfer mode in the blackened region. The CHF occurred in the grey zone just before the black zone was formed. Nucleate boiling occurred after that.

### **B.2.2 Effect of Subcooling**

It was found that for tests with lower subcoolings, that the grey zone was lighter and almost white. This occurred for a while before the stagnation region was rewetted. During this period, it was suspected that a vapour film was present, which insulated the water film from the plate surface. Also, as the subcooling decreased or water temperature increased, the rewetting front velocity decreased.

Meng compared her results at different subcoolings with Hauksson's results. Figure B.5 shows the boiling curves at the stagnation region (location 2) at different subcoolings ranging from 5°C to 70°C and a constant flow rate of 45 l/min. It was discovered that no film boiling occurs in the impingement zone when the subcooling was higher than 30°C. The film boiling duration was longer for lower subcoolings.

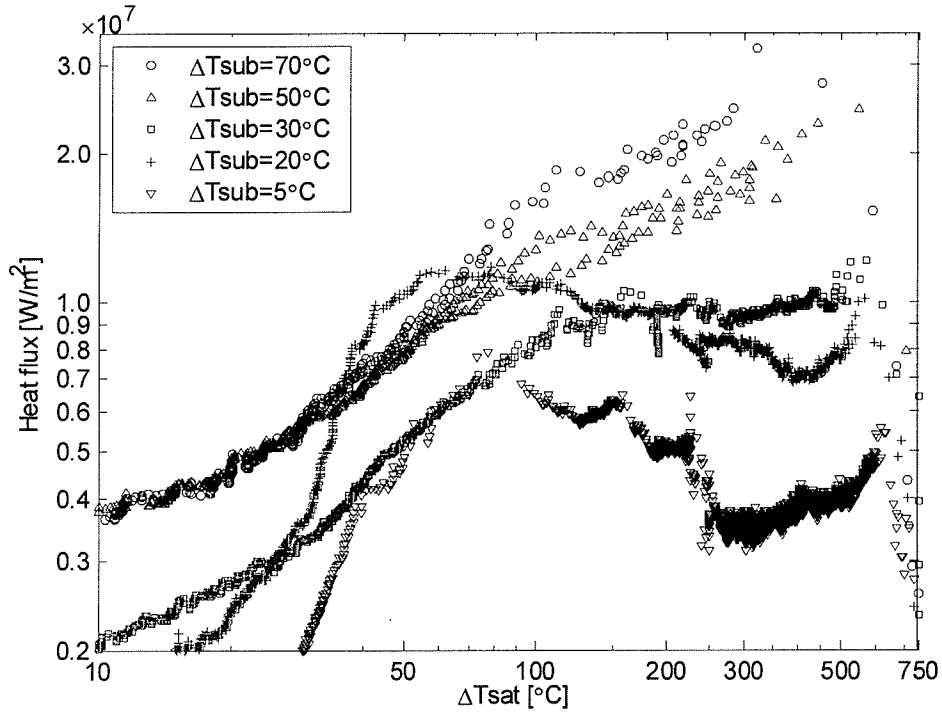


**Figure B.5: Boiling curves at location 2 for different subcoolings at a flow rate of 45 l/min [2]**

The CHF at subcoolings ranging from 5°C to 40°C was compared. Figure B.6 shows that increasing the subcooling increases the CHF. The minimum heat flux (MHF) at different subcoolings was also compared. Figure B.7 shows that the MHF increases with increasing subcooling temperature. Both figures represent a flow rate of 45 l/min.

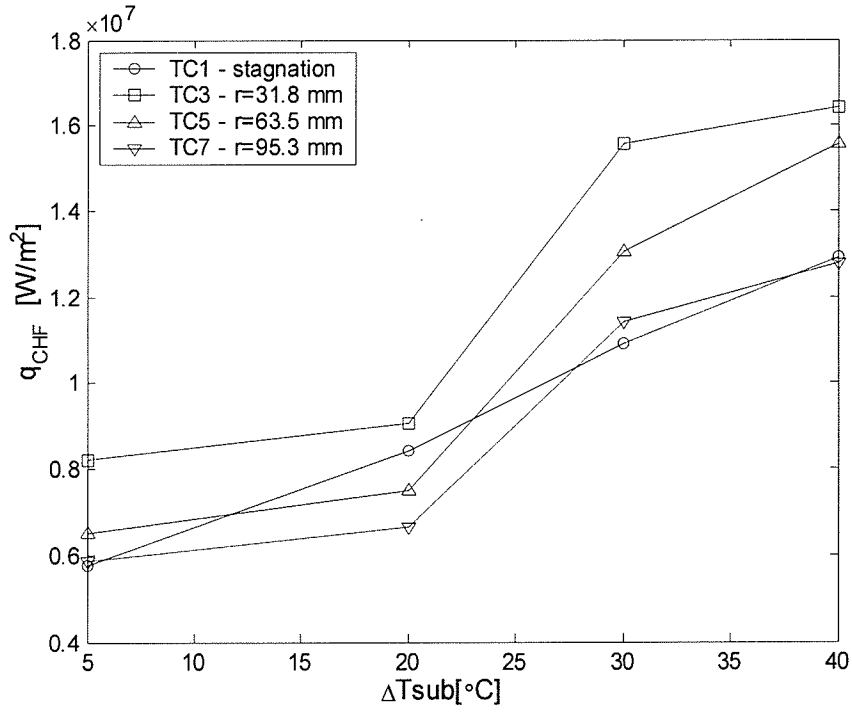


Figure B.6: CHF at different subcoolings [2]

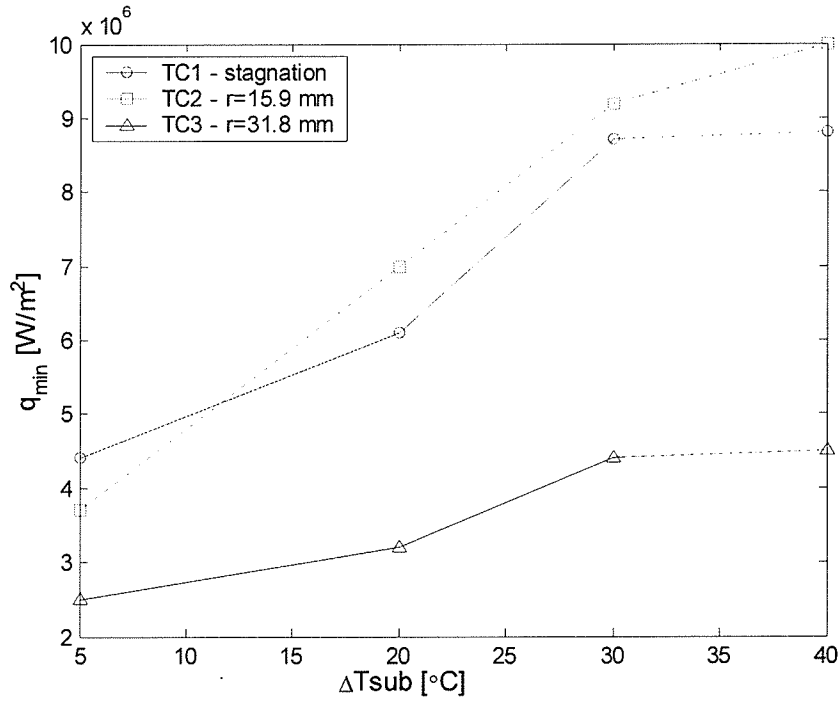


Figure B.7: MHF at different subcoolings [2]

### B.2.3 Effect of Water Flow Rate

Figure B.8 compares CHF's at three different flow rates at a subcooling of 5°C. For flow rates varying from 15 l/min to 30 l/min (jet impingement velocities ranging from 5.5 m/s to 5.7 m/s), the CHF increased. However, it decreased when the flow rate was increased to 45 l/min (impingement jet velocity of 6 m/s).

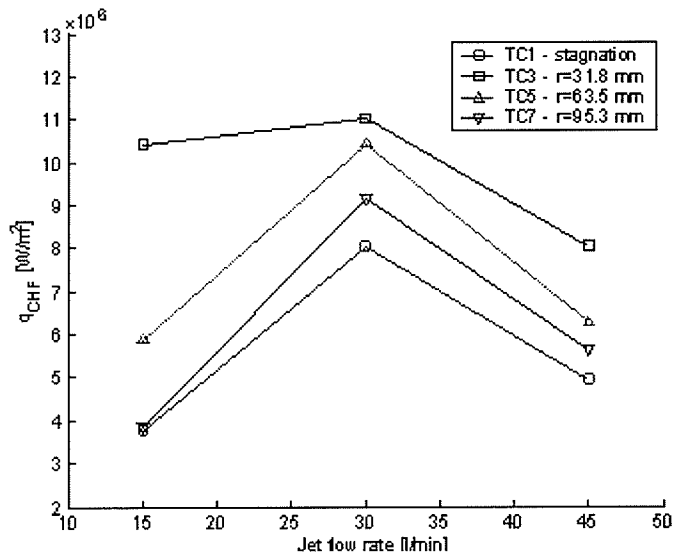
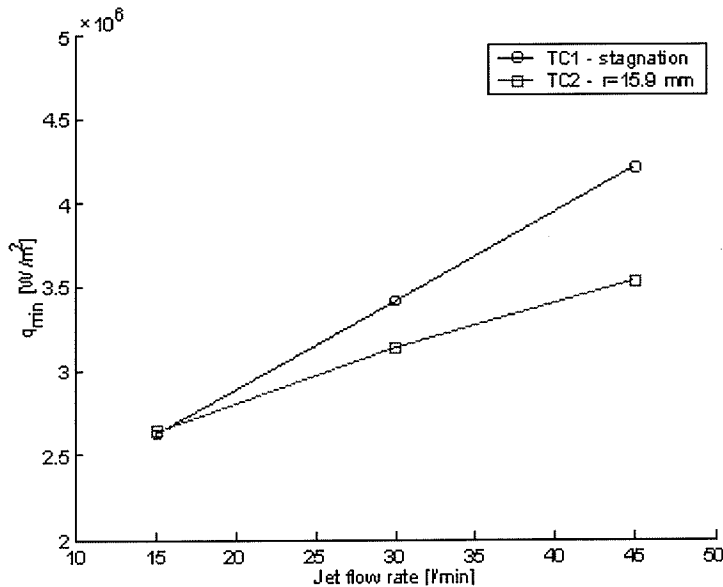


Figure B.8: CHF at different jet velocities at 5°C subcooling [2]

On the other hand Figure B.9 shows the MHF increased with increasing jet velocity at all the jet velocities (or flow rates) tested.



**Figure B.9: MHF at different jet velocities at 5°C subcooling [2]**

#### B.2.4 Effect of Surface Oxidation

Meng also performed experiments to test the effect of surface oxidation.

Figure B.10 shows the boiling curves at locations 1 and 7 at a subcooling temperature of 30°C and water flow rate of 15 l/min. Test 4 was performed with a smooth plate and the plate in test 4a had an oxidized surface. As it can be seen, the effect of surface oxidation had little effect outside the stagnation region. It also had little effect on the CHF and heat transfer for the single-phase convection and nucleate boiling regimes. However, in the stagnation region, having an oxidized surface increased the heat flux in the transition and film boiling regions. These results coincide with the results from Pan et. al [52] cited in Section 2.4.7.

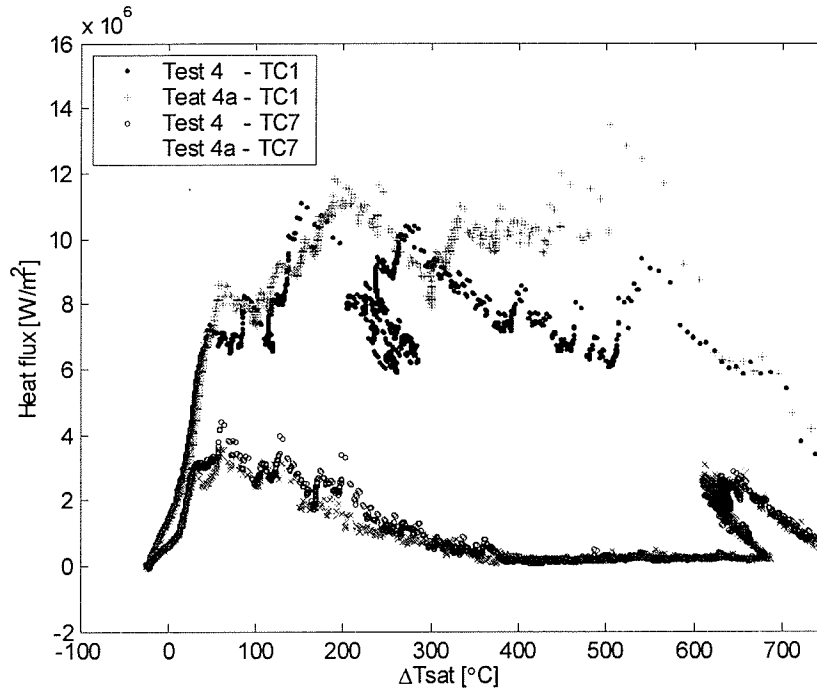


**Figure B.10: Effect of surface oxidation [2]**